Measurements of electric field and dissociated species in nanosecond discharges for kinetic and biological applications

Inna Orel

To cite this version:

Inna Orel. Measurements of electric field and dissociated species in nanosecond discharges for kinetic and biological applications. Plasma Physics [physics.plasm-ph]. Institut Polytechnique de Paris, 2020. English. NNT : 2020IPPAX097 . tel-03118411

HAL Id: tel-03118411
https://theses.hal.science/tel-03118411

Submitted on 22 Jan 2021

INSTITUT
POLYTECHNIQUE
DE PARIS

NNT : 2020IPPAX097

Thèse de doctorat

Measurements of electric field and dissociated species in nanosecond discharges for kinetic and biological applications

Thèse de doctorat de l'Institut Polytechnique de Paris
préparée à l'Ecole Polytechnique

École doctorale n°626 Ecole Doctorale de l'Institut Polytechnique de Paris (EDIPP)
Spécialité de doctorat : Optique, Laser et Plasma

Thèse présentée et soutenue à Palaiseau, France, le 18/12/2020, par

MS. INNA OREL

Composition du Jury :

Khaled Hassouni Professeur, Université Paris-Nord, France	Rapporteur
Timo Gans Professeur, Dublin City University, Irlande	Rapporteur
Gabi Stancu Professeur, École CentraleSupelec, France	Président du Jury
Pierre Tardiveau Maître de conférences, Université Paris-Saclay, France	Examinateur
Guilhem Gallot Directeur de recherche, École Polytechnique, France	Examinateur
Simon Dap Maître de conférences, Université de Toulouse, France	Examinateur
Svetlana Starikovskaia Directeur de recherche, École Polytechnique, France	Directeur de thèse
Halima Kerdjoudj Professeur des Universités, Université de Reims Champagne-Ardenne, France	Co-directeur de thèse

Contents

Acknowledgements

The present chapter is dedicated to the people who had become an essential part of this three-years long journey. It is not possible to list all the reasons behind my recognition and keep it short at the same time so please don't get deceived by laconic formulation. Rest assured that I genuinely acknowledge your impact on me and I am grateful for your presence in my life.

I would like to express my sincerest gratitude...

To my supervisors, Svetlana Starikovskaia and Halima Kerdjoudj, for supporting me and providing numerous opportunities to learn from you. It's been a pleasure to work with you on both personal and professional level.
To Khaled Hassouni and Timo Gans for agreeing to be reviewers of my thesis.
To Gabi Stancu, Pierre Tardiveau, Guilhem Gallot and Simon Dap for becoming members of the jury for my defense.
To Nikita Lepikhin and Tat Loon Chng whom I fully owe my practical knowledge of nanosecond discharges and laser diagnostics, for friendly support and professional advice while constantly being available for me. I will never forget your kindness.
To old team members, Sergey Shcherbanev and Yifei Zhu, for your honest advice and help when it was really needed.
To the current team, Chenyang Ding, Mhedine Ali Cherif and Georgy Pokrovskiy, for scientific, administrative and friendly daily support.
To my first intern, Youssef Haouchat, for being capable to conduct a great job while never meeting your supervisor in person during COVID19 lockdown.
To our teams' collaborators: to Igor Adamovich, for bringing the novel technique to our laboratory, and to Nikolai Popov, for everlasting plasma kinetic simulations support.
To former LPP PhD students, Ana Sofia Morillo-Candas, Constance Duchesne, Abhuday Chatterjee, Bo Liu and Xianjie Wang, for constructive talks and urgent help.
To LPP scientific permanents: to Cyril Drag, for fruitful scientific discussions and giving a side opinion, to Olivier Guaitella, for always helping me with vacuum system problems, to Christophe Blondel, for kindly helping me to specify the spacial location of my supervisor, to Jean-Paul Booth, for constantly and yet kindly providing us with equipment.
To LPP's temporary employees, Alexandra Alexandrova and Lilia Solovyeva (former), for encouraging and at the same time girly pep-talks.
To LPP administrative team, Cherifa Ighoud, Maryline Bazin, Catherine Jegu and

Edouard Bouchet, for ensuring financial and administrative functioning of the laboratory and being kind at the same time.
To LPP informatics team, Veronique Bouzid, Bruno Katra, Nicolas Marsac and Stephane Ravenel, for continuous maintenance of vitally important Ethernet and Internet connection and rapid bugfixes.
To LPP mechanical team: Ali Mahjoub (former), Bruno Dufour and Pascal Pariset, for designing the setups used during the present work, to Garret Curley, for helping with laser external water cooling circuit, to Phillipe Auvrai, for organizing the work with respect to safety regulations.
To LPP higher direction, Pascal Chabert, Dominique Fontaine and Anne Bourdon, for ensuring the work of the laboratory overall and for regularly checking up on PhD students in particular.
To biological collaborators from Reims, Sandra Audonnet, Loic Scomazzon, Sevde Celik, Marie Dubus, Frederic Velard, Florian Lebras, Marie-Paule Gelle, Sophie Gangloff, for warm welcome and patience while bearing with two particular plasma physicists.
To former EDOM, current IPP administration, Audrey Lemarechal, Emmanuel Fullenwarth, Elodie Lelaidier, Alexandra Belus and Adriana Tapus, for well-timed addressing our questions and organizing the "paper side" of a PhD student.
To my elder colleagues from Bachelor Course, Jean-Charles Vanel, Yannis Laplace, Fabian Cadiz and Steffen Backes, for warm and constructive pedagogical discussions.
To EM2C scientific staff, Christophe Laux, Ciprian Dumitrache and Arnaud Gallant, for fruitful discussions within ANR ASPEN community meetings.
To Russian experimental colleagues, Sergey Zyryanov and Dmitry Lopaev, for precious support in data acquisition automation and warm company.
To my de-facto first math and physics teachers, Iryna Volodymyrivna Sydorenko and Lidia Mykhailivna Holvinska, for setting the foundation to achieve such goal.
To supervisors of my first internship, Andrei Ivanovych Momot and Anatoliy Glibovych Zagorodniy, for being the first to introduce me to plasma physics.
To my dear friends, Anastasiya Alexandrovna Andreychenko, Dmytro Vadymovych Gedz, Dmytro Anatolijovych Dmytriev, Tatyana Zadora, Elda Yablonova, for always being there for me.
Special thanks to Dr Herve Bourdonnais who helped me with my critical health situation during the hard period of pandemic.

And to my parents, Tetyana Danylivna Orel and Serhii Ivanovych Orel, who made more than everything to ensure that their only child would get an opportunity to get higher education of international level. I miss you greatly. We will meet again very soon and it’s a promise.

Abstract

The present thesis combines work on absolute and time resolved measurements of O and N atom densities and electric field as a function of specific deposited energy in nanosecond pulsed discharges at high reduced electric fields (above 100 Td) that develop in form of fast ionization wave (FIW).

Ground state O-atom number density, [O], in capillary discharge in 28 mbar air with specific deposited energy of $0.5 - 1$ eV/molecule was measured by optical actinometry technique with Ar as an actinometric admixture. Ar actinometric signal was corrected for N_2 first positive system's background emission. The experiment was highly supported by modelling of kinetic processes in plasma. It has been revealed that in conditions of both high reduced electric field and high specific deposited energy, reactions between charged and/or excited species become important. In particular, the 3-body recombination of O^+ and Ar^+ ions with electron as a third body become dominant in the early afterglow. The peak measured [O], $7.5 \cdot 10^{16}$ cm^{-3}, corresponds to 23% dissociation fraction.

Longitudinal electric field was measured by electric field induced second harmonic generation (E-FISH) technique with picosecond laser in tube discharge in $20 - 100$ mbar pure N_2 with low specific deposited energy at the level of 10^{-3}-10^{-2} eV/molecule during the propagation of FIW and quasi-steady-state discharge. Despite ns-scale laser jitter, temporal resolution as high as 200 ps was attained with help of developed shot-by-shot data treatment procedure that also performed statistical analysis. The electric field in FIW was shown to have a pressure-independent peak value of about 10 kV/cm and $1 - 3$ ns FWHM that increases with pressure. The peak reduced electric field reaches the value of 2 kTd at 20 mbar. It has been concluded that the second harmonic signal originates from the quartz of the discharge tube which disables the possibility of Laplacian field calibration. The calibration against electric field measured by back current shunt and capacitive probe was applied instead.

Ground state N-atom number density, [N], in capillary and tube discharges was measured by two photon absorbed laser induced fluorescence (TALIF) technique. For 1 eV/molecule at capillary discharge, [N] reaches the peak value of $1.3 \cdot 10^{17}$ cm^{-3} at about 1 μs after the initiation of the discharge. [N] stays at the peak value up to 1 ms and then decreases exponentially until reaches the detection limit at 20 ms. The [N] peak value corresponds to 10% dissociation fraction and to effective N-atom production energy cost of almost 10 atoms/100 eV. Such high efficiency is governed by additional population process between charged and excited species, namely, electron impact dissociation of N_2(A,B,C) triplet states. For 10^{-3}-10^{-2} eV/molecule at tube discharge, [N] shows rather constant $5.5 \cdot 10^{12}$ cm^{-3} value for up to 80 μs and further decreases.

The thesis also discusses the interest of ns discharges in biological applications on the example of plasma-assisted regenerative medicine. Cold atmospheric plasma (CAP) device was developed for treatment of dental pulp derived mesenchymal stem cells. CAP effect on cells was assessed by morphological cell analysis, viability test, cytotoxicity test, proliferative test, labelled flow cytometry for measurements of intracellular ROS accumulation and fluorescence microscopy for cytoskeleton and nuclei imaging that had led to establishment of non-toxic protocol of cell treatment by CAP.

Résumé de thèse

La présente thèse combine des travaux sur les mesures absolues et résolues en temps des densités d'atomes O et N et du champ électrique en fonction de l'énergie déposée spécifique dans des décharges pulsées nanosecondes à des champs électriques réduits, supérieurs à 100 Td, qui se développent sous forme d'onde d'ionisation rapide (FIW).

La densité d'atomes O à l'état fondamental, notée [O] a été mesurée dans une décharge capillaire dans l'air, à 28 mbar avec une énergie spécifique déposée de $0,5-1$ eV/molécule par actinométrie optique à l'aide d'argon. Les signaux actinométriques ont été corrigés pour l'émission de fond du premier système positif de N_2. L'expérience a été associée à une modélisation des processus cinétiques dans le plasma. Il a été révélé que dans des conditions à la fois de champ électrique réduit et d'énergie déposée spécifique élevés, les réactions entre les espèces chargées et/ou excitées deviennent importantes. En particulier, la recombinaison à 3 corps des ions O^+ et Ar^+ avec les électrons en tant que 3ème corps devient dominante au début de l'afterglow. Le pic mesuré d'[O], $7,5 \cdot 10^{16}$ cm^{-3}, correspond à un taux de dissociation de 23%.

Le champ électrique longitudinal a été mesuré par génération de deuxième harmonique induite par champ électrique (E-FISH) avec un laser picoseconde dans une décharge de tube de $20-100$ mbar de N_2 pur et une faible énergie spécifique déposée ($10^{-3}-10^{-2}$ eV/molécule) lors de la propagation du FIW et de la décharge quasi-stationnaire. En dépit du jitter du laser à l'échelle ns, une résolution temporelle de 200 ps a été atteinte à l'aide d'une procédure de traitement des données tir-par-tir développée qui a également effectué une analyse statistique. Le champ électrique dans le FIW s'est avéré avoir une valeur de crête indépendante de la pression d'environ 10 kV/cm et $1-3$ ns FWHM qui augmente avec la pression. Le champ électrique réduit de crête atteint la valeur de 2 kTd à 20 mbar. Il a été conclu que le signal de deuxième harmonique provient du quartz du tube à décharge, ce qui rends impossible la calibration par champ Laplacien. Des calibrations par sonde capacitive et par technique de "back current shunt" ont été effectuées.

La densité d'atomes N à l'état fondamental, notée [N], dans les décharges capillaires et tubulaires a été mesurée par la technique de fluorescence induite par laser à absorption à deux photons (TALIF). Pour 1 eV/molécule pour la décharge capillaire, [N] atteint la valeur de crête de $1,3 \cdot 10^{17}$ cm^{-3} 1 μs après le début de la décharge. [N] reste constante jusqu'à 1 ms, puis diminue exponentiellement jusqu'à atteindre la limite de détection à 20 ms. La valeur de crête de [N] correspond à une fraction de dissociation de 10% et à un coût énergétique de production effectif de N

de 10 atomes/100 eV. Une telle efficacité élevée est régie par un processus de population supplémentaire entre les espèces chargées et excitées, à savoir la dissociation par impact électronique des états triplets N_2(A,B,C). Pour $10^{-3} - 10^{-2}$ eV/molécule pour la décharge tube, [N] montre une valeur constante de $5,5 \cdot 10^{12}$ cm^{-3} jusqu'à 80 μs et puis diminue.

La thèse aborde également l'intérêt des décharges ns dans les applications biologiques à l'exemple de la médecine régénérative assistée par plasma. Un dispositif à plasma atmosphérique froid (CAP) a été développé pour le traitement des cellules souches mésenchymateuses dérivées de la pulpe dentaire. L'effet CAP sur les cellules a été évalué par analyse morphologique des cellules, test de viabilité, test de cytotoxicité, test prolifératif, cytométrie en flux marqué pour les mesures de l'accumulation intracellulaire de ROS et microscopie à fluorescence pour l'imagerie du cytosquelette et des noyaux qui ont conduit à l'établissement d'un protocole non toxique de traitement cellulaire par CAP.

Chapter 1

Literature review

1.1 Introduction to nanosecond pulsed discharges

Low temperature plasma (LTP) takes a special place among all plasmas mastered by mankind. As a rule, it is a non-magnetized ionized gas of a small ionization degree that contains an important fraction of chemically reactive species: atoms and molecules, radicals, excited species, ions and electrons. One of the key features of LTP is a significant deviation from thermodynamic equilibrium with electron temperature being much higher than the bath gas temperature. It is also a reason why LTP requires less power for operation compared to thermalized plasma. The possibility to deliver reactive species through the gas phase at room temperature represents LTP's main benefit.

This combination of properties makes LTP very interesting for applications, especially in temperature-sensible cases. LTP is actively used in a number of fields: plasma assisted ignition and combustion [1], deflagration-to-detonation transition control [2], plasma flow re-entry control [3], plasma lithography [4], etching [5], deposition [6], surface activation [7], space propulsion [8], surface sterilization [9], wound healing [10], cancer treatment [11], enhanced seed germination [12] and many others. As for today, LTP installations work in a wide range of different parameters such as gas (composition, presence or absence of flow, pressure), power source (amplitude, repetition frequency, continuity: AC, DC or pulsed periodic), electrode configuration (open or closed) and volumic character of the plasma produced (homogeneous or filamentary).

The development of LTP-based technology is largely constrained by understanding of elementary processes occurring in plasma. In order to optimize plasma source for a particular application and to generally improve the understanding of fundamental LTP problems, detailed studies of elementary plasma processes are needed. At this point, pulsed periodic LTP come into play. In pulsed periodic discharges, because of alternated time intervals of presence and absence of applied voltage, discharge and afterglow phases are separated. Therefore, it is easier to identify the processes responsible for radical's production and loss, to measure kinetic-related values, to account for indirect plasma-related processes such as heat expansion, wall recombination *et cetera*. Strong non-equilibrium produced in nanosecond pulsed plasmas [13–16] have recently gained interest due to their potential use in plasma-assisted fields: aerodynamics [17], combustion and ignition [18–20], biology and medicine [21].

What exactly makes nanosecond pulsed plasmas interesting? Electrons, as the least massive particles among charged species, are the main carriers of the energy retained from acceleration in electric field. During the discharge, reactive plasma species are mostly created in inelastic collisions between electrons and bath gas. Thus, the reaction rates of these processes are strongly dependent on electron energy distribution function (EEDF), which is in its turn highly dependent on E/N.

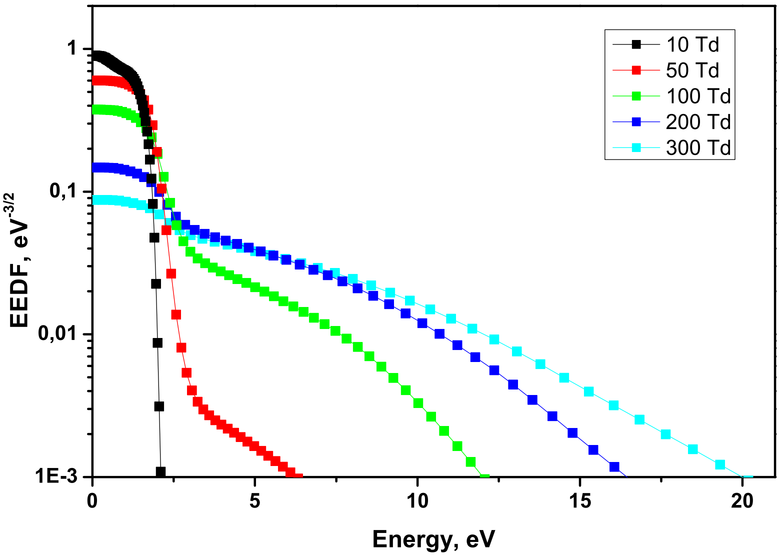

Figure 1.1 – Electron energy distribution function calculated by BOLSIG+ for air discharge. Cross-sections of interaction of electrons with molecules taken from [22] for N_2 and [23] for O_2, respectively.

Figure 1.1 illustrates the effect of the reduced electric field value on EEDF. The curves were calculated using BOLSIG+ software [24,25] for air discharge with cross-sections of interaction of electrons with molecules taken from [22] for N_2 and [23] for O_2, respectively. As it is apparent from Figure 1.1, the higher the E/N, the bigger the mean electron energy and the bigger the concentration of high-energy electrons. From the point of view of reactive species it would mean that the more and more high-energy states can be excited by increasing E/N. In addition, under certain conditions, the interaction between these high-energy states become dominant and consume the majority of energy deposited into plasma.

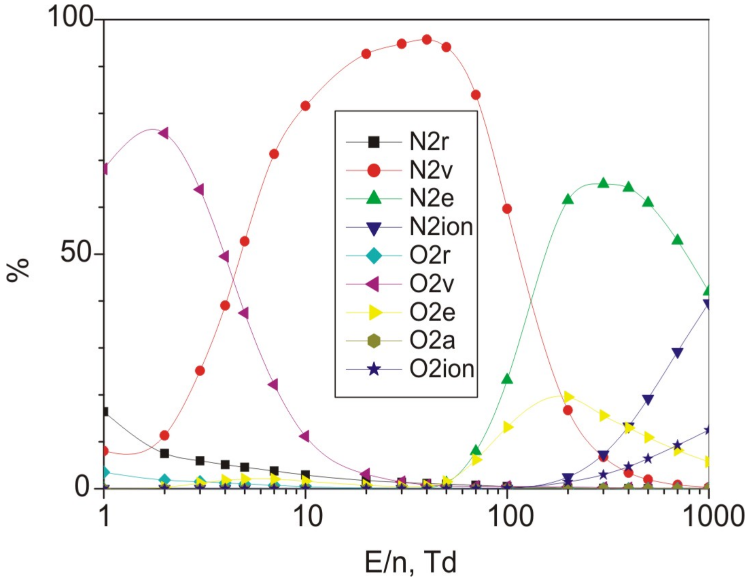

Figure 1.2 – Energy branching of reduced electric field value calculated for the discharge in air. Abbreviations r, v, e, a, ion stand for rotational, vibrational, electronic states excitation, attachment, and ionization processes, respectively. Taken from [26].

Figure 1.2 shows energy re-partition (energy branching) among rotational, vibrational and electronic degrees of freedom as well as energy fraction spent on dissociation and ionization of different N- and O-containing species calculated in [26] for weakly ionized plasma of dry air. Figure 1.2 clearly illustrates that dominant N_2 and O_2 species in plasma depend on reduced electric field value: rotationally and vibrationally excited at $E/N \leq 100$ Td, electronically excited at $100 \leq E/N \leq 700$ Td and ionized at $700 \leq E/N \leq 1000$ Td. The elastic collisions with electrons determine many properties of the plasma medium including electron transport coefficients and the rates of elementary processes [27].

The E/N-dependent behavior of energy branching is not unique for air and is observed for other molecules. For example, calculations of energy branching for hydrogen:air, methane:air and ethane:air mixtures can be found in [28]. From the point of view of applications, it means that the production of desired species in the discharge can be optimized by tuning the E/N value.

Nanosecond pulsed discharges developing in form of fast ionization wave are characterized by E/N as high as of the order of hundreds of Td. Such distinctive feature, according to Figure 1.2, makes nanosecond pulsed discharges interesting from the point of view of effective radical creation, *id est* excitation of electronic states, dissociation and ionization.

1.2 Fast ionization waves: main parameters

For the first time, sub-light speed ionization waves were observed during study of pulsed electric breakdown in 1893 [29]. Discharge in 5 mm diameter, 15 m total length tube filled with air at ≈ 0.5 mm of mercury (≈ 0.7 mbar) pressure was initiated by inductance coil connected to the electrodes at the ends of the tube. The velocity of propagating glow wave was measured by rotating mirror to be rather more than half the velocity of light. In 1937 it has been found that in this type of breakdown, the glow wave is accompanied by potential gradient wave, both waves propagating from the high voltage to the low voltage electrode with the same speed [30]. Ten years later, in 1947, in experiments with a tube surrounded by a metal grounded shield [31] it has been established that the amplitude of current in the wave is determined by charging the capacitance of the discharge device to the potential of high voltage pulse.

The general features of the propagation of this type of discharge were established based on experimental data in 1965 [32] where the discharge was named as "ionizing waves of the potential gradient". Later on, in 1974-76, a review on wave breakdown was made in [33] [34] where this type of discharge was called as "nonlinear electronic acoustic waves". All the works mentioned above experimentally studied integrated electrodynamic characteristics of breakdown and did not discussed their temporal evolution nor kinetic processes occurring in plasma.

In the 1990s, there was a qualitative breakthrough in studies of high-speed ionization waves caused by the widespread use of the latest nanosecond pulsed technology for the generation and diagnostics of ionization waves. Fundamentally new data were obtained on the current, amplitude and velocity of the ionization wave as it moves along the discharge tube. Figure 1.3 plots these parameters as a function of gas pressure for N_2, He and air FIW discharges [35]. Each parameter shows pressure dependence in form of a smooth curve with single extremum that happens at roughly unique pressure value for all three parameters. Extrema pressure value lies within range from tens to hundreds of mbar and depends on the gas composition. Some insight was as well gained concerning the mechanisms of the formation of the wave front, in particular in view of appearance of high-energy electrons. The well-established term "fast ionization wave" was formed and has been widely used since then. A review devoted to studies of a discharges in long discharge tubes at low pressures and moderate voltage rise rates is suggested [37].

Since the 2000s, nanosecond pulsed discharges are more and more studied from the point of view of plasma kinetic processes, in particular, the influence of high values of reduced electric fields on plasma kinetics [38]. Experimental data is gath-

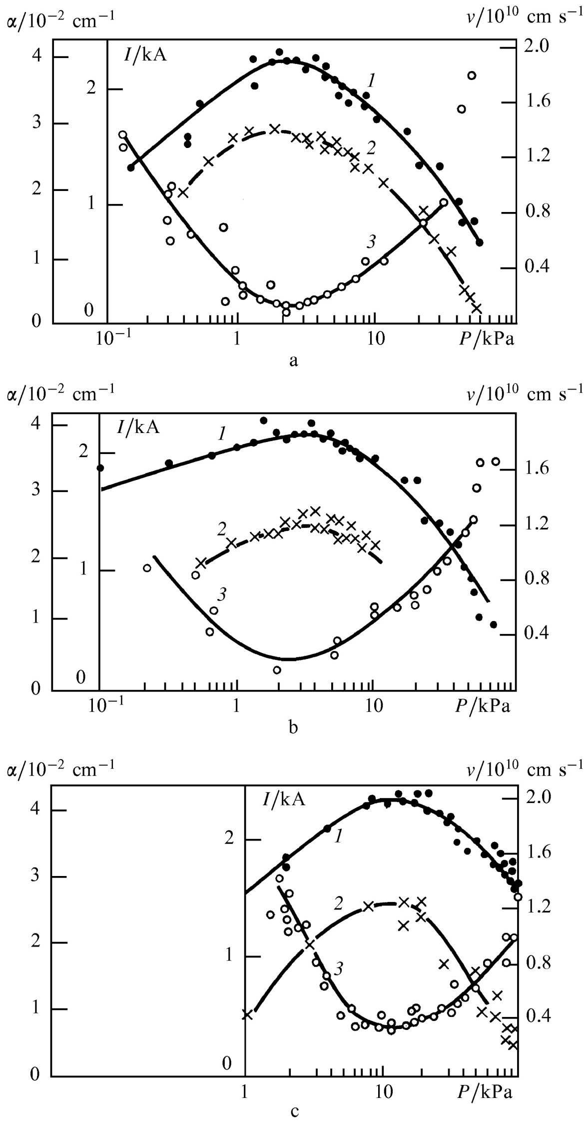

Figure 1.3 – Dependencies of the ionization wave velocity (1), current (2), and damping coefficient (3) on the gas pressure. a - N_2, b - air, c - He. The voltage amplitude is 250 kV. Tube 47 cm long, 0.4 cm in diameter. N_2 insulator. Figure by [35], taken from [36].

ered concerning number density of excited and ground state species, effective and radiative lifetimes, quenching rates, rotational, vibrational and transnational temperatures with temporal and spatial resolution. Modeling efforts are put to describe the interactions between plasma components during the discharge and in the afterglow taking into account measured electrodynamic properties - reduced electric field E/N, current I, specific deposited energy ω.

The generalized scheme of the discharge tube to study nanosecond breakdown can be represented as follows (Figure 1.4). Discharge happens in a quartz or glass

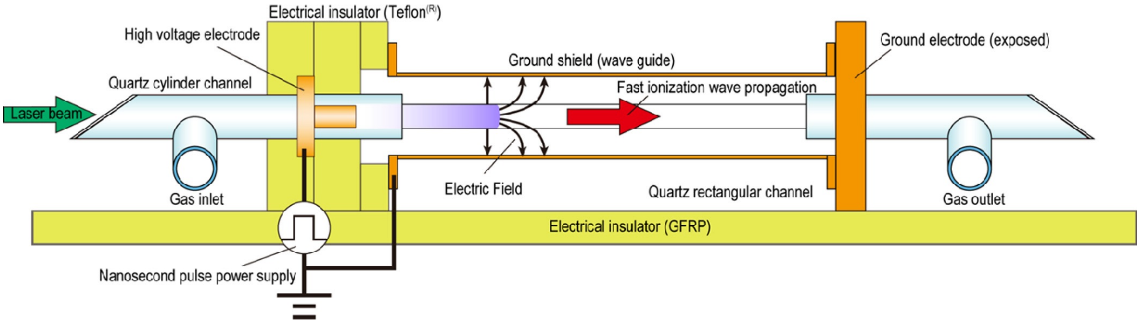

Figure 1.4 – Schematic of a typical fast ionization wave discharge apparatus. Taken from [39].

tube of L length and d diameter so that $L >> d$. The tube is surrounded by a metal coaxial shield; the space between the tube and the screen is filled with a dielectric (air, oil, water, *et cetera*). Electrodes are located at the edges of the tube. High voltage pulses from the nanosecond pulse power supply are transmitted *via* coaxial line to the high voltage electrode of the discharge device. The fast ionization wave forms in proximity of high voltage electrode and propagates towards the low voltage one. The low voltage electrode can be grounded, disconnected from the screen, or connected to a load of a certain value. The choice of the low voltage load would define the amplitude of reflected voltage pulse and, consecutively, the value of specific deposited energy ω. In the case of studying high energy electrons, the low voltage electrode can have a window for radiation output. The window can be made of tube material or of polyethylene terephthalate film of a certain thickness that would act as a high-pass energy filter for electrons accelerated in FIW. FIW can be initiated in discharge tubes with and without flow; the setup depicted at Figure 1.4 shows an example of inlet and outlet gas flow organization.

Fast ionization wave, glow and streamer discharges are plasmas initiated by different breakdown processes. For a given inter-electrode gap filled with neutral gas, the steepness of the front of incident voltage applied to the electrodes defines the discharge that will take place.

If the voltage increases slowly, about 1 kV/μs [40], at a certain value U_{br}, approximately indicated by Paschen's curve, Townsend's breakdown occurs. Primarily determined by ionization efficiency and secondary electron emission from cathode's surface, Townsend's breakdown leads to development of the glow discharge that usually diffusely fills the entire volume of the inter-electrode gap.

When voltage increases faster, inter-electrode gap can endure the overvoltage U, superior to the U_{br}. In this case, Townsend's mechanism does not have enough time to establish. The overvoltaged breakdown develops in form of a perturbation wave and is independent from cathode's secondary electron emission and is defined by the value of $K = (U/U_{br} - 1)$ parameter.

If the overvoltage K is moderate, a few tens of percent, space charge of a single electron avalanche increases considerably compared to glow discharge case. The electric field inside the avalanche becomes comparable to the external electric field while the field in avalanche's head and tail become stronger as well. Thus the breakdown develops in form of a weakly conductive channel that propagates towards one (or both) of the electrodes with a typical velocity of $10^7 - 10^8$ cm/s. This type of discharge is known in literature as streamer. Once the inter-electrode gap is closed, further energy deposition in the small volume of streamer's conductive channel would lead to plasma thermalization and formation of a spark.

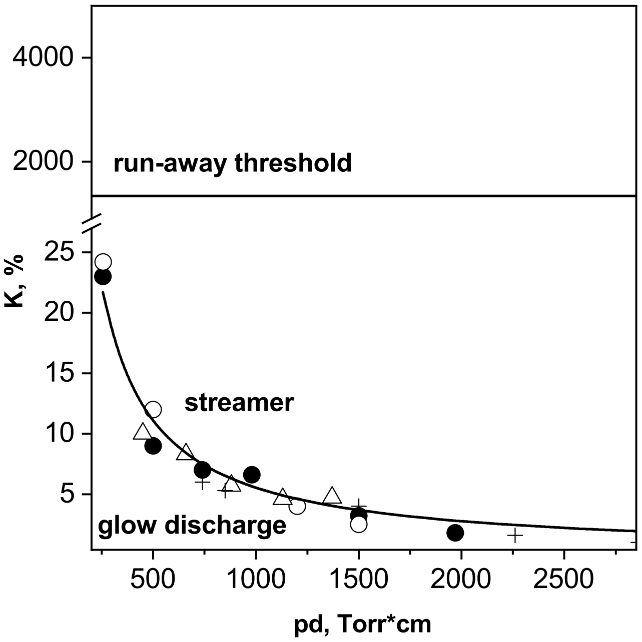

Figure 1.5 – Breakdown development depending upon the overvoltage in air. The curve that separates the glow discharge and the streamer is taken from [41]. Various points designate different experimental data. The horizontal line represents the run-away threshold for a uniform stationary electric field obtained in [42]. Taken from [43].

For more important overvoltages K of hundreds of percent, an additional process appears. The reduced electric field in the front of the avalanche wave becomes sufficient for some electrons to continuously gain energy despite losses *via* electron impact ionization. These electrons contribute to the homogeneous volumic pre-ionization in the front. Herewith, the discharge would propagate with characteristic speed of 10^9 cm/s or higher, hence the title - fast ionization wave (FIW). Figure 1.5 plots the curve that separates the regions of glow and streamer discharge formation, taken from [41], together with the high energy electron threshold from [42].

Overall, streamer and fast ionization wave discharges are very similar one to another. First, their development is way less dependent on cathode's secondary electron emission compared to glow discharge. Second, elementary processes responsible for their formation are gas photoionization in the front and electron impact ionization behind the front. The only difference is that high energy electrons become equally important for front's pre-ionization in case of FIW due to more important overvoltage in FIW compared to streamer's one. Pre-ionization in the front of propagating wave is also what differs homogeneous fast ionization wave from finely structured micro-discharge dielectric barrier discharges (DBDs).

1.3 Electric field measurements in plasma

A few most popular electrical and optical techniques of electric field measurements in view of their applicability to nanosecond pulsed discharges are discussed.

Electrical methods: back current shunt and capacitive probe

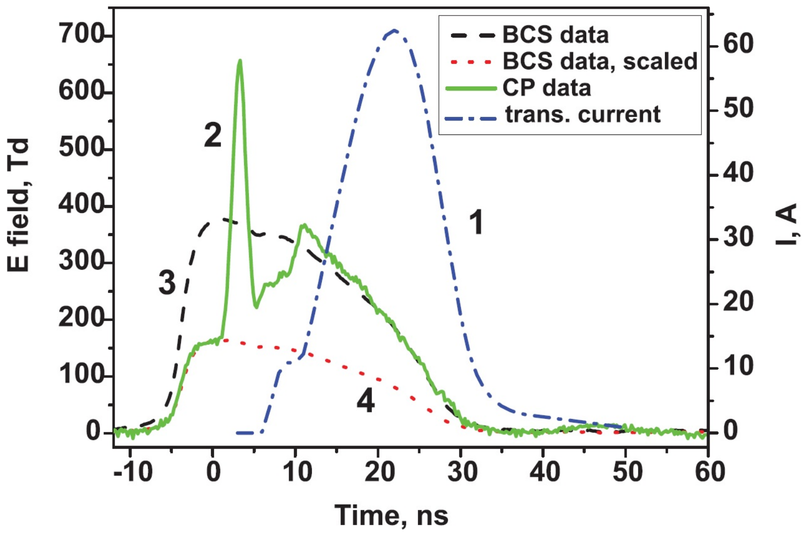

Figure 1.6 – Experimentally measured electric field in nanosecond pulsed capillary discharge: by capacitive probe (2) and by back current shunt (3). Curve (1) is for transmitted current. Capillary tube 70 **mm long,** 1.5 **mm in diameter,** 27 **mbar, N_2. Taken from [44].**

The use of coaxial cable lines for delivery of high voltage pulse to the electrode enables installation of calibrated back current shunts in cable's shielding. Due to conductivity current passing through it, BCS provides a scaled voltage waveform of the high voltage pulse that propagates along the line. BCS thus allows time-resolved reconstitution of essential plasma parameters: transmitted current, electric field, specific deposited energy. However, BCS, being an integral electrical tool, is insensitive to spatial distribution of potential along the tube. BCSs are thus inapplicable for electric field measurements in fast ionization wave. This drawback is devoid of electrical differential method called a capacitive probe. Due to elongated shape of a typical nanosecond pulsed discharge setup, a capacitive divider placed at different positions along inter-electrode gap permits to calculate a longitudinal electric field based on the measured voltage waveform at any time. Capacitive probe is most conveniently calibrated by BCS. BCS and CP are first introduced in 1990s [36, 45, 46] and are used since then [44, 47–50]. Figure 1.6 shows an example of electric field measured by BCS and CP methods together with transmitted current waveform during fast ionization wave and quasi-steady-state discharge in 1.5 mm inner diameter and 70 mm inter-electrode distance capillary at 27 mbar in N_2 [44]. Both tools are described in more detail in [51].

Optical methods: passive and active techniques

Optical approaches of electric field measurements make use of, apparently, optical signals received from plasma. Because of simplicity in experimental use and during calibration, optical emission spectroscopy is more popular compared to optical absorption spectroscopy. Given the indirect method, for electric field reconstitution, there's a need in an at least one electric field dependent elementary kinetic plasma process that entails an experimentally detectable optical transition. The concerned transition itself can be naturally present during the discharge and/or afterglow or stimulated by laser radiation. The value of electric field is then reconstituted from experimentally acquired data based on the assumed kinetic process behind the transition. The calculated E is thus as valid as applied plasma kinetic assumption behind. This is without doubt the biggest drawback of the technique because kinetic knowledge is often limited.

Stark splitting

The splitting and broadening of electronic terms of atoms in an external electric field E_{ext} was first observed in 1913 [52] by Stark for H_β, H_γ and a few He lines in the glow discharge placed in external electric field of $13 - 31$kV/cm value [53]. The effect was soon successfully explained by means of perturbation theory of quantum mechanics [54]. There, interaction of E_{ext} with an atom dipole moment d_a is introduced as a negligibly small additional term (perturbation) to the initial (unperturbed) Hamiltonian. From the point of view of group theory, the perturbation term that holds information about the direction of E_{ext} breaks spherical symmetry of the initial system and thus eliminates the degeneracy of multiplet levels. Due to significant contribution to development of quantum theory, the discovery was marked by Nobel Prize in Physics in 1919 [55].

The value of energy level splitting is proportional to $E_{ext} \cdot d_a$ product which is defined by the atom. Atom dipole moment d_a is a sum of its intrinsic dipole moment d_{int} and electric field induced dipole moment $d_E = \alpha_a \cdot E_{ext}$, where α_a is atom polarizability. For Rydberg atoms, *id est* for H and H-like atoms, $d_{int} \neq 0$ and the Stark effect is the strongest since $E_{ext} \cdot d_a$ contains linearly dependent E_{ext} term. Quadratic term is usually omitted compared to linear one; for H atom, quadratic Stark effect becomes important only if $E_{ext} \approx 100$ kV/cm [56]. In the case of $d_{int} = 0$ (for example, He), only quadratic E_{ext} term defines the line splitting value. Apart from line splitting, line broadening appears as a result of interaction between charged particles. In terms of E_{ext} behavior, the Stark effect can be stationary or alternative (DC or AC, respectively). The paper [57] is suggested for familiarizing with mathematical derivation of Stark effect in AC/DC cases for weak and strong E_{ext} from the point of view of quantum field theory.

This link between the electric field outside the atom and splitting of atomic spectral lines was used to form an electric field diagnostics in plasmas. Theoretical discussions that led to formation of the technique had begun not later than 1972 [58]. The technique itself is applied to electric field measurements in plasma *via* linear [59, 60] and quadratic [61, 62] Stark effects since 1990s.

For electric field measurements by Stark effect in gases with low electric dipole moment and low polarizability, a small H_2 or He admixture can be introduced to the gas. This approach was used in [63] for study of the near-cathode region of an atmospheric pressure 98% Ar-2% H_2 microplasma jet. Figure 1.7 illustrates (a) the experimental setup from the discharge and up to the spectrometer entrance, (b) experimentally measured $H_{\beta-\sigma}$ emission intensity as function of distance to the cathode and (c) space resolved electric field restored from Lorentzian fit. The measured electric field reaches 55 kV/cm in vicinity of the cathode and decreases quasi-linearly by half at 4 cm.

The addition of H_2 or He to the initial mixture for the application of Stark spectroscopy must be done with care. In the case of hydrogen, the vibrational and rotational levels of the molecular gas can absorb a significant fraction of the energy through inelastic collisions and thus affect the EEDF. For He, even the addition of a noble gas in small quantities can be intrusive. Thus such a possibility must either be excluded or taken into account. On the other hand, in media with no electrical dipole active carrier Stark effect is difficult to observe, let alone quantify, against

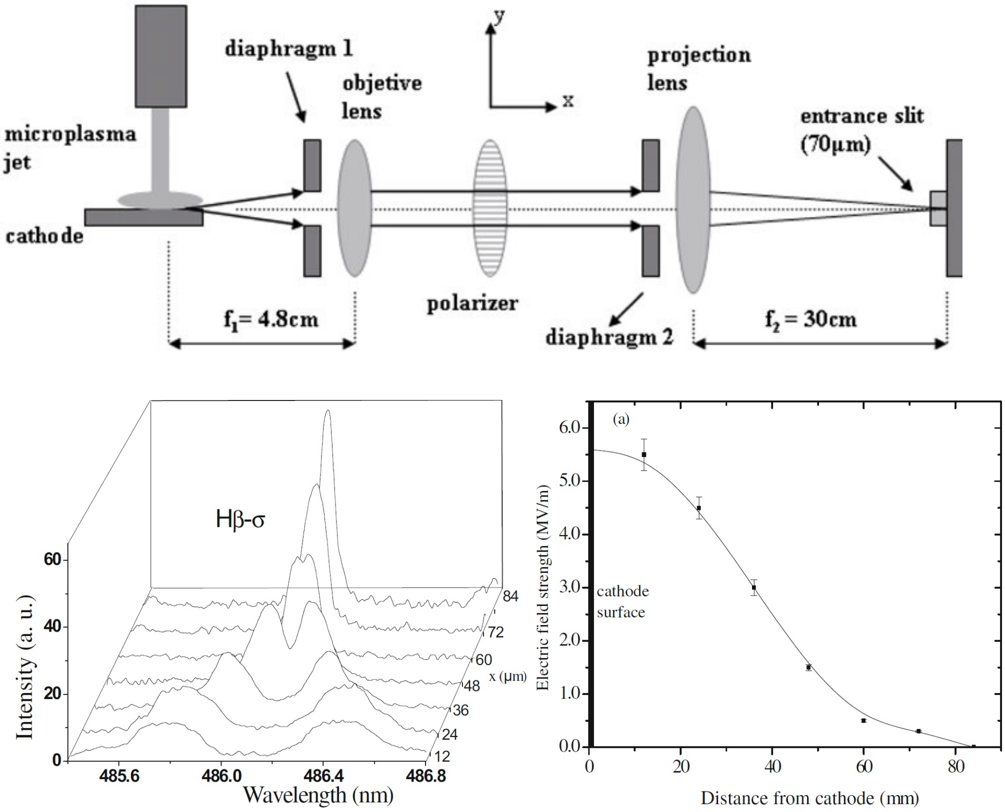

Figure 1.7 – (a) Experimental setup of atmospheric pressure 98% Ar-2% H_2 microplasma jet mounted to investigate the cathode layer region, (b) measured $H_{\beta-\sigma}$ experimental spectrum as a function of distance x from the cathode surface, (c) electric field strength in the sheath restored from Lorentzian-fitted $H_{\beta-\sigma}$ Stark-split lines. Transmitted current value 30 mA. Taken from [63].

the background of Doppler and collisional broadening mechanisms. A published example of Stark line broadening in plasma of a non-polar molecule has been observed under extreme conditions through a transition of N^{3+} ion in laser-generated nitrogen plasma with electron density as high as $1.4 \cdot 10^{18}$ cm^{-3} [64].

Fluorescence dip spectroscopy

If plasma contains an electric field sensitive carrier but the Stark-splitted state is not excited on its own during discharge of afterglow, it can be populated artificially by laser excitation. In this case, two challenges arise: (i) to excite the high-lying Rydberg state from, as a rule, ground state, and (ii) to detect weak fluorescence of a long-lived Rydberg state. A technique called fluorescence dip spectroscopy (FDS) first developed for H_2 molecule [66] serves to overcome both problematic aspects. Figure 1.8(a) shows an example of energy level scheme used during the application of

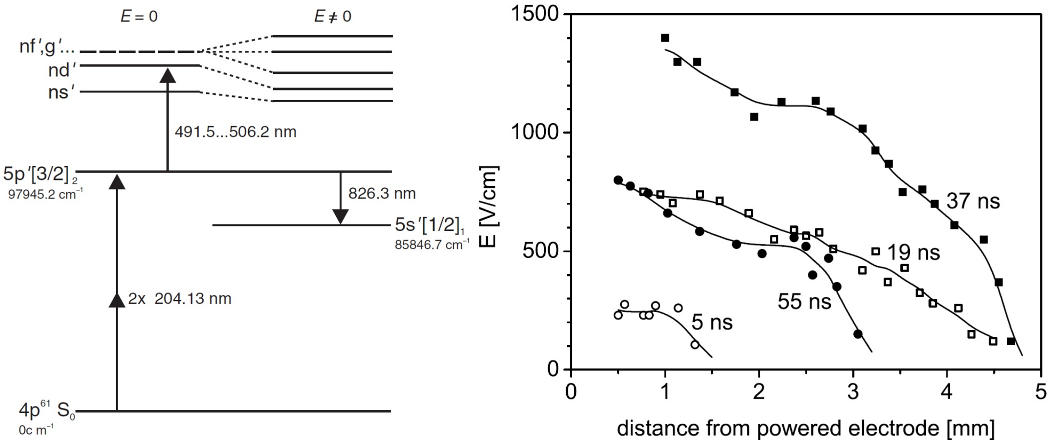

Figure 1.8 – (a) Excitation scheme in Kr. The intermediate state $5p'[3/2]_2$ is two-photon 2×204.13 nm excited from the ground state. The 826.3 nm fluorescence from the transition to $5s'[1/2]_1$ state is depleted when the one-photon $(491.5, 506.2)$ nm excitation is resonant with a Stark-split Rydberg state, (b) space-resolved electric field measurements in a pure Kr, 10 Pa, 8 W CCP at 13.56 MHz; the solid lines serve as eye guidelines. Taken from [65].

FDS technique to sheath region of a capacitively coupled RF discharge in Kr at 10 Pa pressure [65]. The technique is based on a two-photon UV excitation to a short-living intermediate state that undergoes strong fluorescence in the visible wavelength range. High Rydberg states can be excited from this intermediate state by a one-photon excitation in the visible to near-IR wavelength range. One- and two-photon excitation happen instantaneously. Apart from radiative decay, the intermediate level gets additionally depleted when one-photon excitation matches an energy gap to any Stark-splitted Rydberg state. Relative decrease in the fluorescence intensity as a function of one-photon excitation wavelength would thus allow to reconstruct Stark-split fine structure and calculate the electric field shown on Figure 1.8(b).

Coherent Anti-Stokes Raman Spectroscopy (CARS). Four-wave mixing

Coherent Anti-Stokes Raman Spectroscopy (CARS) is another active spectroscopic technique that is sensitive to the electric dipole moment. The total electric dipole moment d_m of a vibrationally excited molecule is not a constant value due to atoms vibrating at ω_m. If the molecule is placed in an electric field of ω frequency, d_m can be expressed as a sum of four oscillatory terms of the following frequencies: ω_m, ω, $\omega + \omega_m$ and $\omega - \omega_m$ (two term Taylor series expansion approximation [68]). The latter two represent elastic (Rayleigh) and inelastic (Raman) scattering, respectively. In an inelastic collision, a molecule can either gain energy (Stokes Raman)

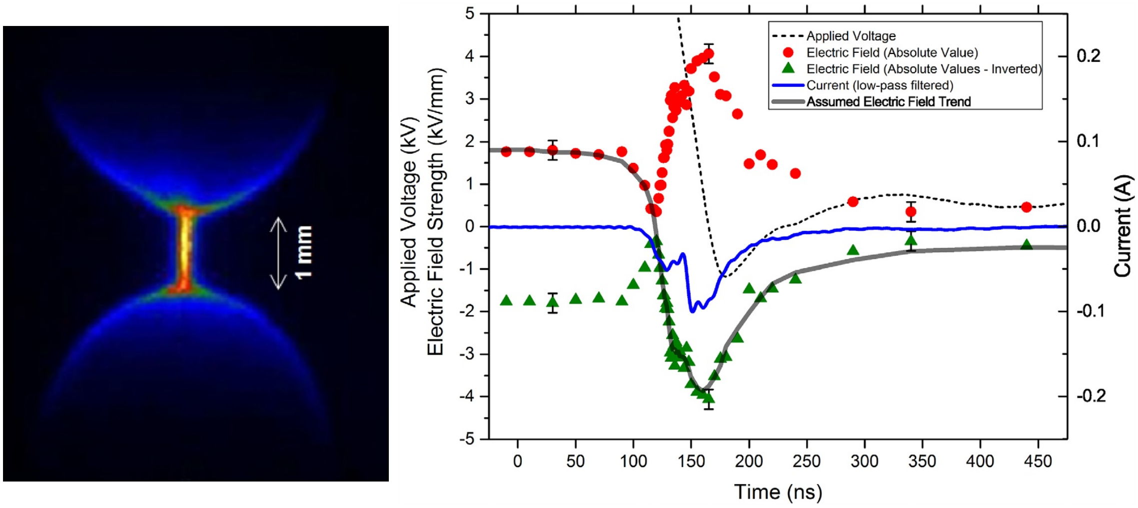

Figure 1.9 – (a) Alumina-covered electrodes with DBD filament in the 1 mm gap: ICCD image with accumulated discharges, (b) Development of the electric field strength at the breakdown process. Taken from [67].

or lose it (anti-Stokes Raman). The change in the vibrational state of the molecule would be thus displayed at scattered radiation.

Naturally present $\omega \pm \omega_m$ lines are too weak for detection on their own and happen in 4π solid angle due to radiative origin of the scattering. Laser pumping of the media is thus used (i) to enhance probability of the transition and (ii) to obtain a coherent signal that would propagate in a predictable way (along the laser beam). Details concerning CARS mathematical derivation and energy scheme can be found in review [69].

Four-wave mixing technique based on CARS technique has been applied to determine the electric field strength of a pulsed-driven filamentary DBD of 1 mm gap using 10% H_2 as a tracer medium in N_2 at atmospheric pressure [67]. Figure 1.9(a) shows the DBD setup under study whilst Figure 1.9(b) presents the measured electric field as a function of time during the breakdown. The authors underline that one of the advantages of the CARS technique over emission-based methods is that CARS do not require emission and thus can be applied when emission is absent.

Electric field induced second harmonic generation (E-FISH)

The methods for measuring the electric field presented above either require the development of complex two-beam laser diagnostics, or are only applicable to a specific atom or molecule. From this perspective, a technique that uses a single laser beam and is potentially applicable to any gas or gas mixture appears very appealing. Electric field induced second harmonic generation (E-FISH) technique possesses both these properties. It has been first observed in 1975 that second harmonic light is generated in focused laser beam in presence of DC electric field [70]. The phenomenon of second harmonic generation has been since used to determine the polarizability tensors in different media for many years (for gases see [71] and numerous references therein) and the functional dependence was oriented towards determination of the electric field only recently [72]. This method takes advantage of the asymmetry in polarizability induced by an applied electric field, which enables the otherwise forbidden second-harmonic generation in homogeneous media. Since no resonant process is needed, laser of any wavelength λ can be used as an input while the output signal would be $\lambda/2$. The spatial resolution of the measurement is defined by laser focusing and is usually submillimetric. The temporal resolution is limited by either laser pulse duration or the sampling rate of the oscilloscope and can be even sub-picosecond [72].

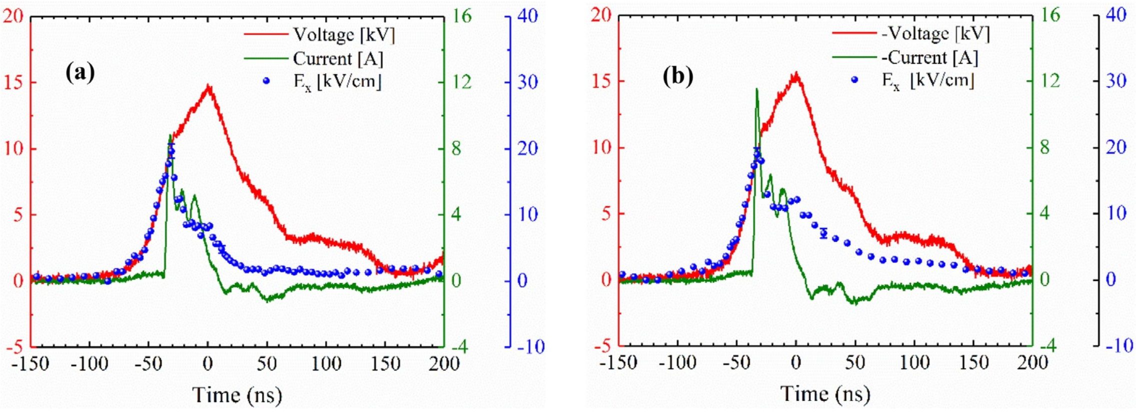

Figure 1.10 – Horizontal electric field in a nanosecond pulsed DBD plotted together with pulse voltage and current waveforms, during (a) positive and (b) negative polarity pulses (inverted axes). Hydrogen flow rate 1.5 slm, pulse repetition rate 20 Hz, discharge gap 4.5 mm. Taken from [73].

Apart from excellent spatio-temporal resolution, another benefit of E-FISH is that the calibration required for absolute electric field measurements can be done within the framework of the technique by measuring Laplacian (pre-breakdown) electric field as suggested in [73]. In [73], time-resolved electric field in DBD atmospheric pressure H2-flown diffusion flame driven by ns pulse or AC sine wave was measured by picosecond E-FISH below the flame. Electric field measurements in a ns pulse discharge have been shown as self-calibrating, since until the breakdown, the field is Laplacian and follows the applied voltage, as shown in Figure 1.10. In the AC discharge, the electric field is calibrated by measuring a Laplacian electric field between two parallel cylinder electrodes.

Initially developed with use of femtosecond and picosecond lasers, a possibility of E-FISH application with wider duration nanosecond lasers has been investigated in [74]. Paper suggests to slice the laser pulse to a duration of 3 ns in order to avoid important energy deposition into media by using Pockels cell (addressed as "electronic wave plate"). The duration of reduced pulse is defined by the duration of the Pockels cell's driving high voltage pulse that is commercially available as short as 100 ps [75].

The techniques versatility had been illustrated in numerous applications from nanosecond pulse discharges for understanding fast ionization wave development [76], surface dielectric barrier discharges [73] and atmospheric pressure plasma jets [77,78], to DC corona discharges [79]. Most recent developments include the probing of 1-D electric fields [77, 80, 81] by line focusing with a cylindrical lens, as well as obtaining simultaneous electric field vector information through the use of a polarizing beam splitter on the detection end [82].

Theoretical derivation of second harmonic generation, used in quantifying of E-FISH technique measurements, suggests plane-wave approximation while in reality focused laser beams are almost always used. The consequent effects of focused beam's use on the E-FISH signal are investigated in [83] by comparing Laplacian electric field measurements by 3 ns duration sliced [82] focused Gaussian beam with predictions of theoretical analysis. Both the length and shape of electric field profile were found to have a distinct effect on the second harmonic signal generation which adds complexity in interpretation of the signal. As a consequence, paper suggests increasing the Rayleigh range of the probe beam to ensure compliance with the plane-wave approximation, or utilizing two crossed laser beams to localize the measurement and eliminate any signal dependence on the spatial profile of the external electric field beyond the intersection volume.

1.4 Measurements of species number density

Electrostatic probes for electron density measurements

One of the most popular methods of plasma diagnostics consists in application of electric (sometimes named in literature as electrostatic) probes. Developed by Langmuir in 1924 and thereupon called after his name, it is an *in situ* tool used to determine plasma potential, electron energy distribution function, and plasma density by measuring the voltage-current characteristic of a thin metallic wire introduced into the plasma. The possibility to measure spatially-resolved electron-related parameters essentially draws attention of experimental community. It was widely applied in a variety of plasma including laboratory low-temperature plasma [84], ionosphere [85] and magnetized plasmas such as Hall thruster [86] and tokamaks [87].

A brief acquaintance with the tool can leave a deceiving impression of its ease of use. In reality, an effort is required to recover meaningful plasma characteristics from the received voltage-current signal. Probe users should be fully aware of the limitations of theoretical approach used and of the sources of error in the experiment that are usually caused by the intrusive nature of the probe. Under these conditions, probes can yield useful data, particularly if used on a comparative basis. Two reviews [88, 89] can be consulted for more details concerning accurate Langmuir probe use and entailed complications.

In case of nanosecond pulsed discharges, the use of *in situ* sensors becomes challenging. Transmitted current in such plasma is at least $1 - 10$ A and can reach values up to ~ 220 A [90] or even a few kA. When this value is compared to at most few tens of mA current in glow discharges where Langmuir probes are used, a question concerning possible tool's damage rises. The majority of probes is developed for relatively low frequencies (typically MHz range of RF band) and thus do not possess sub-ns resolution (> 1 GHz) required for FIW study. The construction of Langmuir probe would also require some modifications for application to ns pulsed discharges. In particular, high inductance of typically thin probe wire would affect dramatically the received signal on ns-scale events. Capacitive charging by electrons accelerated at high reduced electric fields is also to consider while interpreting probes current-voltage characteristic.

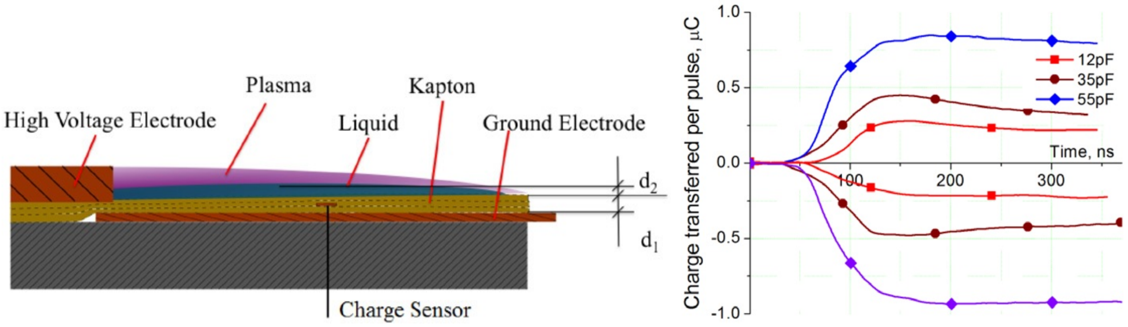

Figure 1.11 – (a) Schematic of DBD assembly with a layer of liquid on top of dielectric surface, used to control surface conductivity (not to scale); $d_1 \sim 0.1$ mm, $d_2 \sim 1$ mm. (b) Comparison of surface charge accumulation measured for different electrode overlaps (capacitance values) and different pulse polarities of alternating polarity pulse trains; $t = 0$ corresponds to the beginning of pulse voltage rise. Taken from [91].

Due to these complications, sensors that come into direct contact with nanosecond plasma are rarely used. On the other hand, sensors that are placed somewhat at a distance from the ionization channel of ns discharges (as the above mentioned capacitive probe) can be successfully applied. The paper [91] presents an example of a ns pulsed atmospheric DBD experimental study with a capacitive divider sensor placed within the dielectric at 1 mm distance from plasma. In general, the approach is valid for both solid and liquid dielectrics. Figure 1.11(a) shows the schematic of the assembly. The work in particular studied the dielectric surface charge accumulation as a function of high voltage pulse polarity and inter-electrode capacitance varied by electrodes mutual disposition shown at Figure 1.11(b).

Optical absorption spectroscopy

A recent review [92] reuniting optical techniques suitable for measurements of numerous and various low-temperature plasma characteristics is suggested.

Optical absorption spectroscopy techniques are based on the measurement of the intensity decrease of a light beam that passes through a medium as a function of time, wavelength or a plasma parameter. If only linear effects are considered and the system is homogeneous, the intensity decrease can be written an exponential function whose argument is a product of through-medium path length, absorption cross-section and density of absorbent species (Beer-Lambert law). The technique's greatest advantage consists in the following: if the absorption cross-section is known, the density of absorbing species can be directly determined from the ratio of intensities before and after passing the media with no calibration. On the other hand, the measurement is line-of-sight integrated thus provides no spacial resolution and is best applied to spatially uniform systems. In addition, the technique consists in measurements of light's decrease that is quite small comparing to the incident light. It is also a non-zero background technique so the use of photo-sensitive equipment (*exempli gratia*, photomultiplier tubes) should be done with care because of possible saturation issues (non-linear equipment's response or damage).

In view of technique's simple one-formula math and typically affordable equipment, it has been adapted for countless measurements of low-temperature plasma. This great variety of mounts can be roughly divided into two piles with respect to the light source used - a broad band or a narrow band one.

The use of a broadband light source (deuterium or tungsten lamp or laser pumped plasma light source) requires spectral isolation of the transition of interest which can done by a narrow-band filter, a monochromator (also called dispersion technique) [93,94] or a Fourier transform spectrometer [95]. In a FT spectrometer, a collimated input beam is split in two sub-beams that constructively or destructively interfere as a function of an optical path difference creating an interferogram. The difference between interferograms recorded with and without the studied absorbent media reveals its absorption spectrum. The benefit of having a FT spectrometer instead of monochromator for OAS technique lies in (i) improved spectral resolution due to application of an interferometric technique and in (ii) the included feature of automatized full spectra recording which is not there for monochromator-PMT pairs.

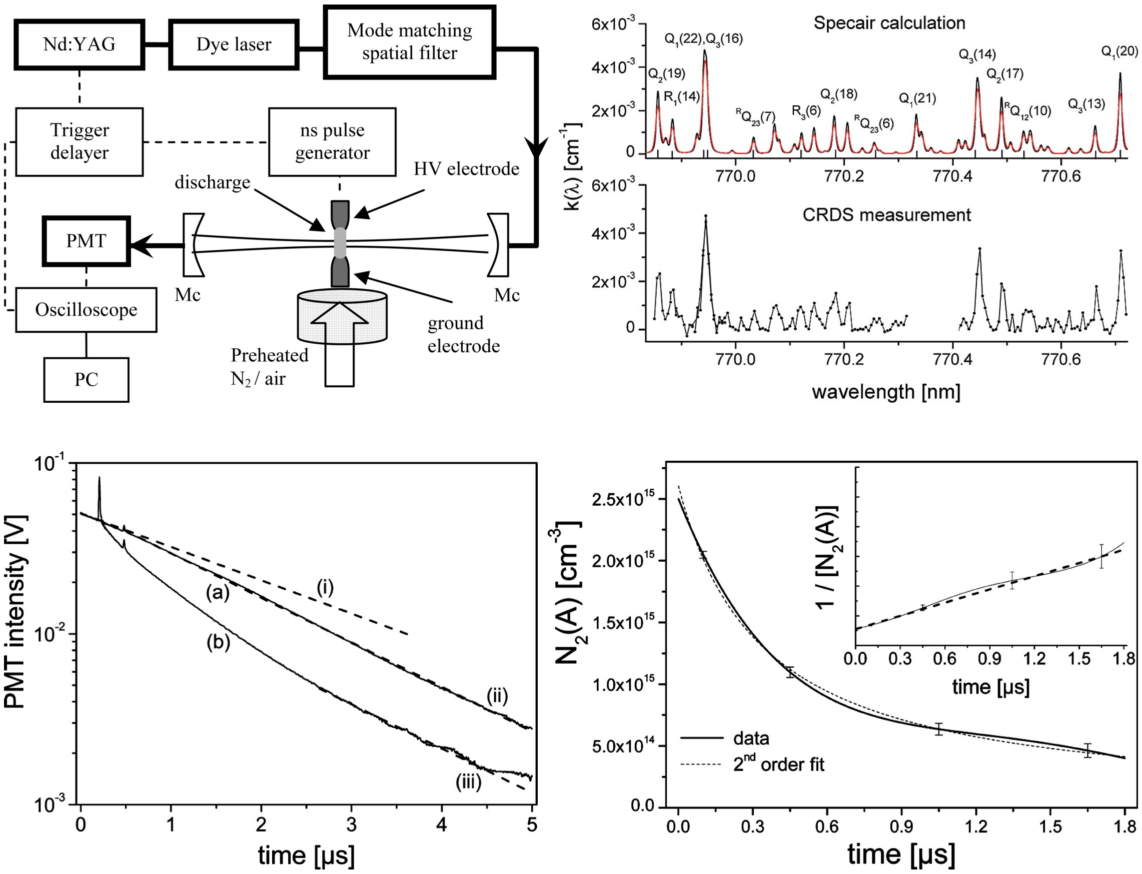

Figure 1.12 – (a) Schematic of the atmospheric pressure nanosecond repetitively pulsed discharge with CRDS experimental setup (Mc stands for cavity mirror). (b) Comparison of the spectral absorption coefficient measured by CRDS and calculated by Specair with spectrum convolved with the instrumental profile in red. (c) Typical measured ring-down signals in nitrogen in log scale. Curves (*a*) and (*b*) are recorded at 770.012 nm (off-resonance) and 769.945 nm (on-resonance), respectively. Curves (*a*) and (*b*) are identical before the pulse (slope (*i*)) and after 2.5 μs (slope (*ii*) = slope (*iii*)). Curve (*b*) has a nonlinear variation after the pulse, indicating temporal change in N_2(A) density. (d) Time evolution of the N_2(A) density and its reciprocal in N_2 plasma. Taken from [96].

In case narrow band tunable lasers, the laser itself acts as the wavelength selective element. Recent developments of tunable pulsed dye lasers in the visible and infrared range had enabled OAS application of high sensitivity (typically 10^{12} cm^{-3} in single path) and high time resolution (few μs) for relatively short optical paths without the need for signal accumulation [97]. Attention should be given to avoid any non-linear absorption-related processes such as absorbing level depletion induced by intense laser radiation. In addition, the pulsed lasers very often suffer from large pulse-to pulse intensity fluctuations.

This drawback is avoided in the ultrasensitive absorption technique called Cavity Ring Down Spectroscopy (CRDS) first suggested in late 1980s [98]. CRDS is a multi-pass technique applied in a closed optical cavity with a high Q-factor attaining extremely long effective path lengths (kilometer scale). The technique is based upon the measurement of the absorption rate rather than the absorption value whence light source intensity fluctuations insensitivity.

In terms of application of OAS technique to nanosecond pulsed discharges, many options are possible. If temporal resolution of $\mu s - ms$ is acceptable (for afterglow studies, for example) then the spectral nature of the light source is indifferent. If one aims to study ns-timescale events, the reference light source itself should be suitable. Elaborating previous statement, for broadband light sources it would mean high ns-scale stability while narrow band light sources should be of ns-scale duration.

A temporal resolution of 50 ns was reached in CRDS technique application to measurement of $N_2(A^3\Sigma_u^+)$ metastables number density produced by nanosecond repetitively pulsed discharges in nitrogen and air preheated at 1000 K and atmospheric pressure [96]. Figure 1.12(a) illustrates the schematic of CRDS experiment. Figure 1.12(b) compares spectral absorption coefficient measured experimentally and calculated by Specair [99]. The gas temperature 1600 K obtained from the rotationally resolved CRDS spectrum was shown to be the same as the rotational temperature obtained from the emission spectra of the second positive system of N_2. Figure 1.12(c) shows the decay of multi-pass absorbed laser light for $\approx 5\mu s$. The slope variation of on-resonance signal indicates temporal change in $N_2(A^3\Sigma_u^+)$ number density. Finally, $N_2(A^3\Sigma_u^+)$ number density temporal dependence is demonstrated at Figure 1.12(d). The measured characteristic lifetime of the metastable was about 600 ns at in nitrogen and less than 100 ns in air. In nitrogen, the main depletion process of the metastable is the energy pooling, whereas in dry air, the main process is quenching by O and O_2.

Optical actinometry

In a low density plasma, the number density of atoms is low enough to safely neglect excited-state atom-atom and excited-state ion-atom collisions. Furthermore, in a weakly ionized plasma the electron and ion densities are low in comparison with the atomic density. Thus, the primary channels for excitation/de-excitation of atoms involve photons and electrons [100]. In corona equilibrium model, applicable at very low electron densities, atomic excitation is solely through electron impact excitation of ground state atoms and de-excitation is solely through photon decay.

Optical actinometry is a number density diagnostic that has formed as a plasma diagnostic technique in early 1980s [101, 102]. At current state of art, the main idea of the method can be described as follows. In order to measure the density of an unknown specie (as a rule, ground state specie, inaccessible to optical emission spectroscopy), a chemically stable admixture (noble gas) is introduced in the gas in a small percentage. This admixture is called an actinometer. According to corona model, it is presumed that both the searched specie and the actinometer are dominantly excited by direct electron impact to their respective excited states that further fluoresce performing an allowed optical transition.

The number density of the specie of interest can be found from the ratio of radiation intensities of the atomic lines. Quenching by bath gas can be taken into account as well. Knowing the reaction rates of the considered processes and spectral sensitivity of optical system at fluorescence wavelengths, actinometry allows to obtain absolute number density value of the specie of interest. The actinometer has to be introduced in a controllable amount, negligible to significantly affect studied plasma kinetics and parameters.

Overall, actinometry is an active optical emission spectroscopy method, term "active" due to necessity of actinometer admixture. Allowing access to ground state species number density data while being non-invasive and experimentally inexpensive and simple as OES, actinometry technique gathered quite an interest in plasma community. The appealing idea of introduction of an indicator inert specie into the studied media was kept in numerous adaptations of the technique. So, actinometry was developed in various discharge conditions for measurements of different radicals, *exempli gratia*, O [103–107], N [108–110], H [110], F [111]. For more details, a quite recent review [112] that discusses the applicability of actinometry for measuring the absolute concentration of O, N and F atoms in discharge plasma is suggested.

The simplicity of the kinetic scheme considered in classical actinometry limits the applicability of the technique as it has been formulated initially. Classical actinometry doesn't include dissociative excitation, radiative cascading population or collisional quenching from higher states to the emitting level that might occur in conditions of high E/N (increase of EEDF tail) or high pressure (from tens of mbar). Therefore, the use of such a seemingly simple and powerful technique as actinometry without checking its applicability to particular system is fraught with incorrect conclusions. A particular importance of dissociative excitation while applying actinometric approach has been shown in [103] and [104].

The authors of [103] have compared measurements of spatially resolved optical actinometric emission intensities with measurements of TALIF technique (the technique would be introduced further in the text) in O_2-CF_4 RF plasmas with $2-3\%$ Ar admixture. The following transitions were used: O(^{3}P-^{3}S) 844 nm, O(^{5}P-^{5}S) 777 nm, Ar($2p_l$-$1s_2$) 750 nm, Ar($2p_9$-$1s_5$) 811.5 nm and F($^2P^0$-^{2}P) 703.7 nm. It has been shown that the $O_{844.6}/Ar_{750.4}$ emission intensity ratio qualitatively follows the O-atom concentration, but the $O_{777.4}/Ar_{750.4}$ ratio does not. The discrepancy is due to the dissociative excitation that populates the O(^{5}P) state in addition to direct electron impact. The evidence for this process was provided by observations of broad emission line shapes. Direct excitation of O-toms was concluded to be favored: (i) when the $[O]/[O_2] > 5\%$, *id est*, for strongly excited discharges, and (ii) when the cross section for direct atomic excitation is much larger than the cross section for dissociative excitation, *id est*, for $O_{844.6}$ but not $O_{777.4}$.

In another study [104], actinometry technique has been applied to determine the absolute O-atoms number density in DC O_2 flowing glow discharges at $0.36-2$ Torr pressure, $5-80$ mA current in Pyrex tubes of $4, 7$ and 16 mm diameter. Considered kinetic processes were those of classical actinometry: electron impact excitation, radiative decay, quenching with molecular species with addition of dissociative excitation. The following transitions were used: O(^{3}P-^{3}S) 844 nm, O(^{5}P-^{5}S) 777 nm and Ar($2p_1$-$1s_2$) 750 nm. Cross-sections were validated by comparing actinometric measurements to VUV absorption spectrometry. Under these experimental conditions where $[O]/[O_2] < 1\%$ and $E/N > 90$ Td, dissociative excitation is a significant source of excited oxygen atoms, especially in the O(^{5}P) state.

The authors of [104] have reached the same conclusion as [103]: the transition O(^{3}P - ^{3}S) at 844 nm is a better choice for actinometric measurements since dissociative excitation is not dominant for $40-110$ Td. Furthermore, it has been shown that E/N can be deduced from the rate constants ratio obtained from measurement of actinometric intensity ratio. The actinometry-obtained E/N was validated against electric probe measurements.

Classical actinometry presumes that the admixed gas acts as a non-invasive EEDF indicator. In general case, this statement requires confirmation, as discussed in [105] where particle-in-cell (PIC) actinometry simulations were validated through comparison with [O] TALIF measurements in RF O_2:Ar=96:4 100 mTorr discharge. Research [103–105] highlights the necessity of accurate kinetic description that allow to carefully select actinometric transitions to extract reliable information concerning ground state number density of the specie of interest from actinometric emission lines especially in conditions of high ionization fraction and E/N.

Two photon absorbed laser induced fluorescence (TALIF)

The possibility of determining the number densities of fluorescent states through absolute passive emission spectroscopy is limited by the states naturally excited in the medium. With the discovery of laser radiation in 1960 [113] and its adaptation for research purposes in the following decade, many ideas have come to improve the existing diagnostics, including emission spectroscopy. Laser radiation has been used to artificially stimulate the transition of an atom from the ground state to a fluorescent state. The collected fluorescence was then used to restore the number density of the ground state using available spectroscopic data on the probability of both transitions. One of the first reviews on laser induced fluorescence (LIF) technique was published in 1977 [114].

The term TALIF, two-photon absorbed LIF, speaks for itself. It is an extensive development of the LIF technique in which the energy required to stimulate the transition to the fluorescent state is delivered by two photons of the same energy. The probability of two photon stimulated transition is lower compared to a single photon one, however, for species such as O and N atoms, all dipole-permitted excitation from the ground state are in the vacuum ultraviolet (VUV) range [115], making one-photon measurements challenging.

TALIF diagnostic is usually used in the so-called "linear regime", when the dependence of the collected fluorescence signal on laser energy is quadratic [116,117]. Physically the regime corresponds to a low laser energy perturbation of the ground state population and to an absence of any parasitic processes that are entailed with high laser energies such as depletion of the ground state, photoionization [118], amplified stimulated emission [119–121] and photo-dissociation [122–125]. How these accompanying processes affect the fluorescent signal, as well as how to avoid them and ensure operation within "linear regime", is methodically and in detail described in recent paper [126].

In actual applications of TALIF technique, absolute number density values are obtained *via* calibration in a noble gas of a known number density with a spectrally close two-photon resonance. The first suggested calibration schemes were in Xe for O-atom measurements [127] and in Kr for N-atom [128] measurements. The noble gas calibration approach requires the use of the same setup for studied media and noble gas and thus benefits from shared laser and optical equipment.

Xe-calibrated TALIF technique with 10 ns long laser beam has been applied to O-atom number density measurements in the afterglow of a nanosecond capillary discharge with reduced electric field in range of $150-300$ Td and specific deposited energy of the order of 1 eV/molecule in $24-30$ mbar air. The work uses an improved

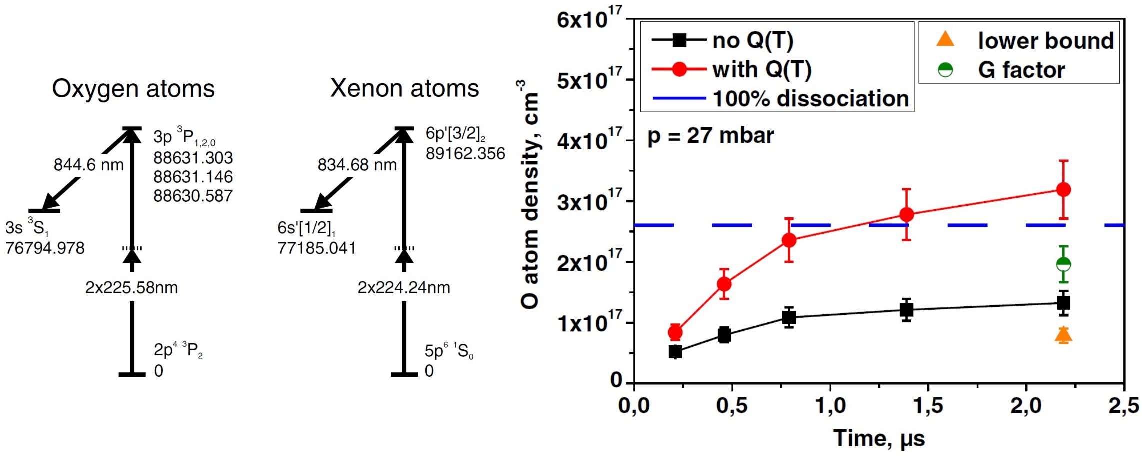

Figure 1.13 – (a) Energy diagram of Xe-calibrated O-atom TALIF measurements, (b) O-atom number density measured by Xe-calibrated TALIF technique in 27 mbar air nanosecond capillary discharge with corrections to temperature independent (black symbols) and dependent (red symbols) quenching coefficients. Complete dissociation limit is shown in blue. Lower bound was estimated based on O-atom fluorescence decay rate. G-factor was estimated from calculations. Taken from [129].

scheme for Xe calibration from [116] shown at Figure 1.13(a). In three subsequent discharges initiated by a train of nanosecond pulses, the O-atom number density was found to increase progressively up to $1.9 \cdot 10^{17}$ cm^{-3} for 27 mbar. Complete dissociation was achieved at about 2 μs after the first discharge for all studied pressure conditions.

When restoring the absolute number density values, one has to account for quenching of fluorescent states by media. Complications are to arise if quenching coefficients are not well known. In [129], the concern gravitated around temperature dependence of quenching coefficients, since the rotational gas temperature measured by emission spectroscopy of the second positive system of N_2 showed an increase from ambient temperature to $2000-3000$ K at 2 μs. Two corrections based on temperature dependent and independent quenching coefficients were applied, as shown at Figure 1.13(b). At times after 1.5 μs, the temperature dependent correction shows a non-physical O-atom production that is superior to total available number of O-atoms that can be obtained after full O_2 dissociation. The authors conclude that the reliability of absolute O-atom number density value can be improved if, in particular, temperature dependence of quenching rate constants is verified.

The uncertainty in the quenching rate of any measured fluorescent specie (the specie of interest or the calibration specie) produces a large uncertainty in the measured number density value. Therefore it is preferred to work in the conditions where fluorescence decay is rather known in advance of can be measured experimentally. The problem is not so pronounced in the case of measurements in hydrogen or oxygen, where the cross sections are already well studied in numerous conditions, but becomes noticeable in case less studied gases such as nitrogen. An alternative way to deal with unknown quenching rates is to avoid dealing with them. Such idea had lead to development of picosecond and femtosecond laser-driven TALIF whose examples can be found in [130, 131].

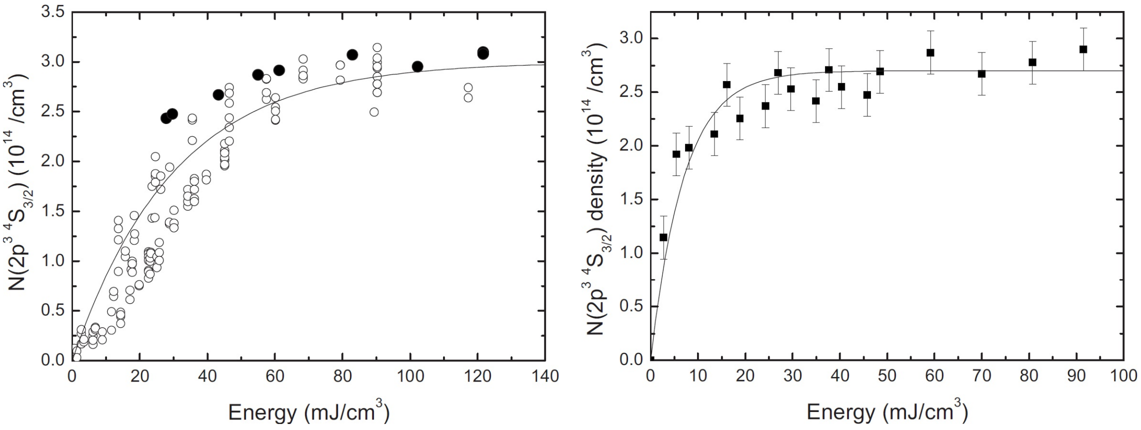

(a) Variant travel time x/v at a given mean energy (empty symbols) and *vice versa* (solid symbols).

(b) Variant mean energy together with variant N_2 gas flow Q and/or the position of measurement x.

Figure 1.14 – N-atom number density measured in atmospheric pressure nanosecond DBD in N_2 as a function of mean deposited energy in (a) homogeneous Townsend and (b) filamentary regimes. Here x the discharge entrance to measurement location, Q the N_2 flow rate. Varied conditions are indicated below each plot. Taken from [132].

TALIF technique can be equally applied for absolute number density measurements at atmospheric pressure as it has been done for Kr-calibrated TALIF N-atom number density measurements in pulsed dielectric barrier discharge (DBD) in flown N_2 [132]. In [132], N-atom production was measured 100 μs after the end of the high voltage pulse at variant position from the discharge entrance to measurement location x, flow rate Q and mean deposited energy in two DBD regimes: homogeneous Townsend regime and filamentary regime. A few results are presented at Figure 1.14. Unfortunately, no information about the value of electric field is provided in the paper. Authors note that the same peak N-atom number density, $3 \cdot 10^{14}$ cm^{-3}, was measured for both regimes. This correspond to N-atom production energy cost of 600 eV/molecule and 170 eV/molecule for Townsend and filamentary regimes, respectively. The dissociation N_2 fraction can be estimated as $(3 \cdot 10^{14})/(2 \cdot 2.46 \cdot 10^{19}) \approx 5 \cdot 10^{-6}$, where denominator is N_2 number density at atmospheric pressure expressed in cm^{-3} from [132]. As one of the explanations, authors associate the increased N-atom production efficiency with electron density difference: 10^{13} cm^{-3} in filamentary channel *versus* 10^{8} cm^{-3} in the Townsend discharge.

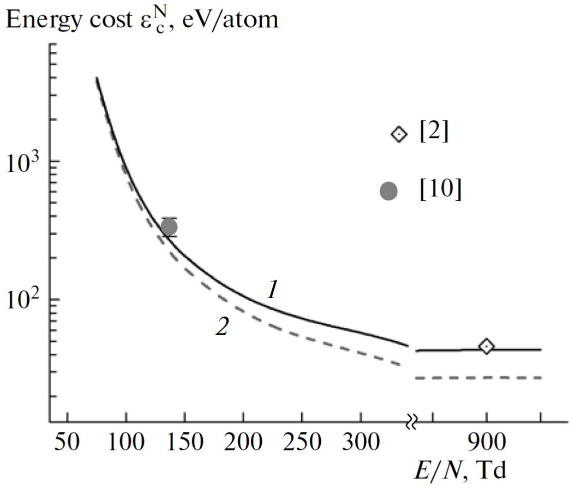

Figure 1.15 – Energy cost of electron-impact dissociation of N_2 as a function of reduced electric field calculated with (1) cross sections from [133], (2) cross sections for electronically excited N_2 with energies above 13 eV from [22]. Experimental data: [2] is [134], [10] is [135]. Taken from [136].

On the one hand, as shown experimentally in [132], for a given discharge regime, the N atom density depends strongly on the energy dissipated in the plasma whatever the other parameters are (Figure 1.14). On the other hand, kinetic parametric calculations performed for atmospheric pressure dielectric barrier discharge in N_2 with low specific deposited energy of about $\sim 10^{-4}$ eV/molecule [136] illustrate a strong dependence of N-atom production on reduced electric field (Figure 1.15). The calculated N-atom production energy cost was found to be in agreement with two experimental measurements, namely, [134,135]. In [136], atomic nitrogen is produced solely by electron impact dissociation of N_2 and the energy cost of N-atom production is predicted to have an asymptotic value of 43 eV/atom at reduced electric fields of about 900 Td. The N-atom production efficiency in case of discharge at both high reduced electric fields and specific deposited energy was not investigated.

1.5 Interest of nanosecond pulsed discharges for biological applications

Low temperature plasma have recently found their way in numerous biological applications as a novel approach in surface sterilization [137], foods decontamination [138], wound and skin decontamination, improved wound healing [10], cancer remission [11, 139], control of wound-resident multidrug resistant bacteria, both *in vitro* and *in vivo* [21]. Cold atmospheric plasma (CAP) applications present a particular interest for medical purposes due to possibility of operation in the surrounding air without heating the living target. CAP consists of a complex media containing ions, electrons and free radicals in conditions of strong localized electric field, UV radiation, and neutral molecules. Nowadays CAP devices exist in numerous variations of pressure (low to atmospheric), gas used (He, Ar, N_2, air), electrode configuration (DBD, plasma jet), power source (AC/DC, microsecond/nanosecond pulsed repetitive). It can be applied directly on the target or to be used indirectly by treating the media that would be later put in contact with biological target.

Despite the variety, they are applied in the same way: produced species are put in interaction with the molecules of the surrounding air, mostly O_2, N_2 and H_2O, and with the biological target which has usually a wet surface (diluted cells, human skin, tumor ou wound surface). Consequently, whatever the CAP gas is, during the operation a part of energy deposited to plasma gets dissipated in the surrounding humidified air producing reactive hydrogen, oxygen and nitrogen species that are known to participate in basic cell functions, such as proliferation, differentiation, and survival [140]. Given the complexity of CAP, a considerable effort was put to identify key processes behind observed CAP-induced effects, in particular, with respect to reactive species, and to measure these species.

CAP characterization from the point of view of produced reactive species is a challenging task since many types of RONS are present in the media at the same time. The simultaneous presence of numerous RONS as well as rich kinetics involved results in loss of sensitivity of existing measurement methods. The issue is discussed in more detail in [141]. Paper analyses available methods in application to RONS measurements in plasma-air-water systems and highlights limitation of the methods in view of complex CAP-produced media.

Figure 1.16 presents $O_2(^1\Delta_g)$ number density in two He atmospheric jets as a function of O_2 admixture measured by infrared optical emission spectroscopy. It is suggested that $O_2(^1\Delta_g)$ is produced mainly in direct electron impact excitation with O_2 and removed in quenching by O_3. At a given deposited energy, increase in O_2 admixture linearly reduces the amount of produced $O_2(^1\Delta_g)$. At a given O_2 admixture, the number density of produced $O_2(^1\Delta_g)$ increases with increasing deposited energy. The energy dependence is however not linear: for 0.2% O_2 admixture, the measured $O_2(^1\Delta_g)$ number density roughly increases for 8 times when the applied power increases by 40% from 32 W to 46 W. Authors also associate more effective $O_2(^1\Delta_g)$ production to the smaller plasma volume in case of RF plasma jet compared to kHz plasma jet.

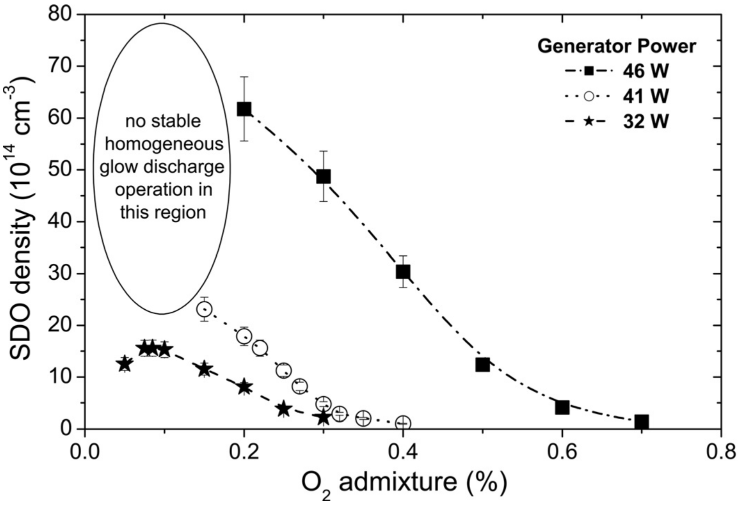

(a) RF plasma jet (13.56 MHz) at He flow of 1 slm.

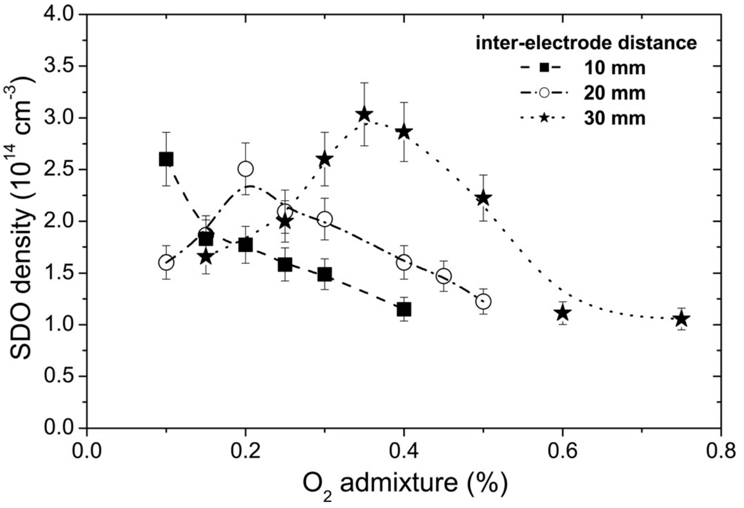

(b) kHz plasma jet (20 kHz) at He flow of 2 slm.

Figure 1.16 – $O_2(^1\Delta_g)$ number density as a function of the O_2 admixture in different He jets. Taken from [142].

In [143], among other results, CAP was shown to produce an effect on cells in dilution that can not be reduced to the effect of hydrogen peroxide of the same amount as CAP produces. Figure 1.17 presents the cell viability following CAP helium jet treatment and H_2O_2 exposure of normal primary skin fibroblasts cells (NHSF) and cancerous human melanoma cells (LU1205) after 24h of culture. Cell viability for both types of exposure exhibit a monotonous decrease. Plasma treatment in both cell lines show a lower survival rate compared to H_2O_2 for any equivalent exposure condition. In cancerous cells the additional effect of CAP compared to H_2O_2 is more pronounced than for normal cells suggesting CAP selectivity between cell lines.

The monotonously decreasing cell survival as a function of CAP treatment time as shown at Figure 1.17 is a commonly observed behavior of cell response with

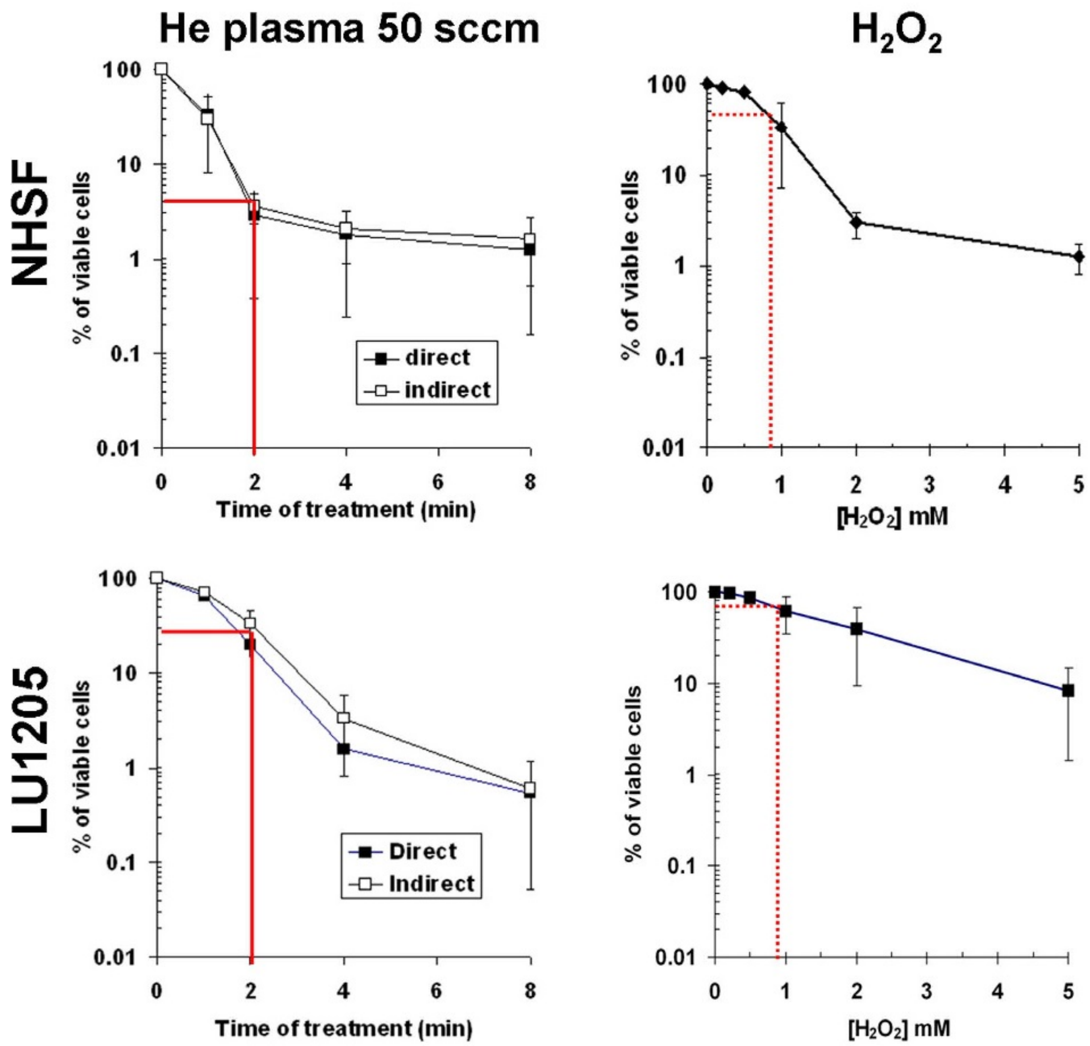

Figure 1.17 – Cell viability following plasma treatment (4 tests) or H_2O_2 exposure (8 tests) after 24h of culture. Top line - normal (NHSF) cells, bottom line - cancerous (Lu1205) cells. Left column - direct and indirect He plasma treatment for $1, 2, 4$ and 8 min, right column - H_2O_2 exposure of corresponding concentration. The continuous and dashed red lines indicate the percentage of viable cells after 2 min of He plasma and after CAP-equivalent 800 μM H_2O_2 exposure, respectively. Taken from [143].

respect to a stimulation that is generally addressed as "dose". The complexity of CAP effect on the target does not permit to clearly define the term yet, but it is applied to exposure time, reagent concentration or deposited energy. In [139], dose-depended cell response was observed *in vitro* in glioblastoma (U87MG) and colorectal carcinoma (HCT-116) cancerous cells as a function of energy deposited in the plasma per unit surface. Figure 1.18 plots cancer cell viability following CAP treatment after 24h of culture, normalized to unexposed control. Paper [139] also presents results of *in vivo* study of anti-tumor CAP effect on treating glioblastoma in mice and report significant tumor volume decrease from 400 cm^3 in control to 233 cm^3 in CAP-treated specimens.

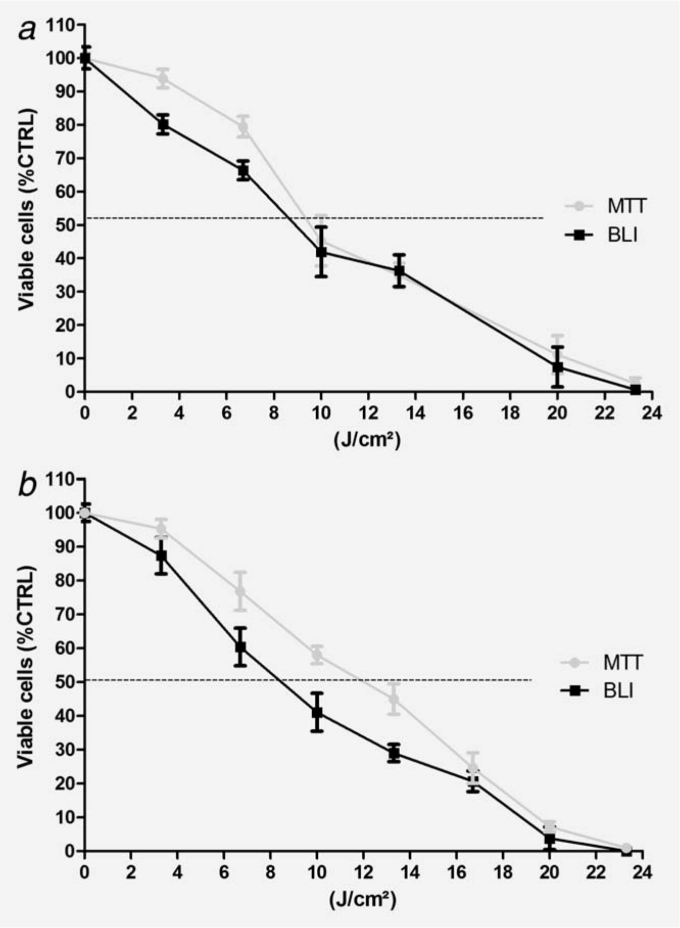

Figure 1.18 – Anti-tumor responses to NTP treatments normalized to unexposed cells. U87MG (a) and HCT-116 (b) cells were treated by increasing doses of CAP. Cell viability was determined 24h after treatment by biological assays (noted as MTT and BLI). Taken from [139].

Interesting to note that from both research and application interest, apart from high reduced electric fields and consecutively significant RONS production, one more appealing feature of nanosecond pulsed discharges is a possibility of fine control over the applied dose. This becomes possible due to low duty cycle of pulsed periodic discharges that can be as low as 10^{-3} *versus* of about 30% in a typical AC discharge.

As a particular application for purposes of regenerative medicine, stem cells are currently considered given their ability to transform into the needed tissue and to improve tissue healing [144]. Stem cell therapy is a novel and promising option for on-site tissue regeneration enabling repair of damaged or filling the missing tissue and organs as reported in [145, 146]. Given the recency of the approach itself, its sub-division that studies plasma treatment of stem cells is even more of a *rara avis*. Despite, some research records can be found.

Plasma effect on human peripheral blood mesenchymal stem cells (hPB-MSC) diluted in culture media was investigated in [147]. The effect of plasma needle differed in three regions of the treated area: the central circle with dead cells, the annular region with no cell debris and the outside region consisted of the viable cells. Since the region with dead cells could be controlled by defined plasma parameters (power, duration of treatment), their optimization can lead to refined cell removal. Additionally, the concern of whether liquid shields treated sample from plasma-generated species was addressed on the example of *Staphylococcus aureus* (ATCC 25923) and *Escherichia coli* (ATCC 25922) bacteria. It was found that noticeable plasma effect may be expected for a wide range of initial densities and plasma operating conditions causing destruction of several orders of magnitude even under the protection of a liquid. Heating was excluded from the reasons behind observed plasma effect.

In latter study [148] of the same research group, the influence of non-thermal atmospheric plasma on human mesenchymal stem cells isolated from periodontal ligament (hPDL-MSCs) in view of possibility of periodontal regeneration was studied. Plasma needle (analogous way to name plasma jet) He-flown configuration powered by sinusoidal RF signal of 13.56 MHz frequency with < 2 W power was employed. Few plasma effects have been demonstrated. Plasma treatment inhibited the migration of treated stem cells and induced some detachment without affecting their viability. Additionally, plasma significantly attenuated cellular proliferation but promoted their osteogenic differentiation. The results of this study indicated that a non-thermal plasma offers specific activity with non-destructive properties that can be advantageous for future dental applications.

Summarizing, CAP treatment was found to illustrate selectivity with respect to biological target. CAP delivers effects varying from destructive necrosis and DNA damage to anti-inflammatory response, arrest of cell proliferation, controlled apoptosis and RONS intracellular accumulation increase. The observed biological effects are usually linked to plasma parameters such as RONS production and delivered energy, both presented in high values in nanosecond capillary pulsed repetitive discharges. Nowadays stem cells present a great potential to regenerative medical applications, and to author's best knowledge, nanosecond CAP treatment of stem cells has not been reported so far.

Chapter 2

Problem formulation

The distribution of energy though internal degrees of freedom, *id est* energy branching, was shown to be highly dependent on the value of reduced electric field. Nanosecond pulsed discharges propagating in form of fast ionization wave are inherently characterized by high reduced electric fields whose measurements present a complicated experimental task. At such fields, the electron energy distribution function becomes substantially populated with high-energy electrons. In this case, the efficiency of electronic excitation, dissociation and ionization of neutral gas molecules increases significantly. And if the qualitative consequences of a change in the EEDF are not in doubt, the question regarding the quantitative effect of this change on plasma kinetics remains.

It was shown earlier that in a nanosecond discharge with reduced electric fields of about 200 Td and specific deposited energy of the order of 1 eV/molecule, the excited and charged particles are produced in such number densities that reactions between them determine plasma behavior. If those conditions are met, common plasma kinetics model for weakly ionized plasma that considers all upward transitions being only due to electron collisions while downward transitions occurring only by radiative decay, essentially becomes invalid and so do every common model based diagnostic.

Nanosecond discharges with high reduced electric fields and specific deposited energy had also declared oneself as an excellent dissociation source on the example of O_2 discharge where an almost 100% O_2 dissociation was achieved within 2 μs from the beginning of the discharge. However, dissociation of more stable molecules, for example, N_2, was found to be a very energy-demanding process. Kinetic simulations performed for atmospheric pressure dielectric barrier discharge in N_2 with low specific deposited energy of about $\sim 10^{-4}$ eV/molecule predict a limit value of N_2 dissociation efficiency to be at least 43 eV/atom. Possible increase in dissociation efficiency of N_2 by nanosecond discharges in conditions of high specific deposited energy is not yet addressed.

The reactive species in important number densities produced during efficient dissociation present an interest for numerous applications in view of their high chemical reactivity, in particular, for biology, where reactive oxygen and nitrogen species were reported as advantageous for maintenance of basic stem cell functions, such as proliferation, differentiation, and survival. However, before proceeding to mass production, any biologically-related tool should first satisfy the criteria of non-toxicity validated over a numerous samples.

The problematic described above had lead to formation of a few guidelines that have constituted the aim of the present thesis. In view of expanding the understanding of elementary plasma kinetic processes in nanosecond repetitively pulsed discharges, the following tasks were set:

- To provide self-consistent experimental data set including electric field, transmitted current, specific deposited energy and spectrally resolved actinometric transitions required to test the applicability of optical actinometry technique in discharge in conditions of both high reduced electric fields and specific deposited energy;
- To apply recently developed sub-nanosecond time and sub-mm space resolved non-intrusive diagnostic of electric field for measurements of the absolute electric field values in the front of fast ionization wave;
- To measure absolute number density of N-atoms as a function of specific deposited energy value using two nanosecond pulsed periodic discharges with the same ~ 200 Td reduced electric field value but different specific deposited energy values: as low as $10^{-3} - 10^{-2}$ eV/molecule and as high as 1 eV/molecule;
- To investigate the possibility of cold atmospheric plasma treatment of stem cells that would meet the criteria of toxicity.

Thesis content

The thesis contains 10 chapters.

In Chapter 1, literature review is presented. First, nanosecond pulsed discharges are briefly overviewed underlining their most distinct features. Then, fast ionization waves are characterized through a historical overview. Next, electric field and species number density measurement techniques are presented in view of application to nanosecond pulsed discharges. Finally, the potential use of nanosecond pulsed discharges in biological applications is discussed.

In Chapter 2, the main goal of thesis and formulated tasks are presented.

In Chapter 3, used materials and methods are listed. "Materials" part comprises description of discharge setups, electrical (back current shunt, capacitive probe) and optical (spectrometer, camera, calibration light source) equipment used. "Methods" part comprises theoretical descriptions of methods applied: electric field second harmonic induced generation (E-FISH) and two photon absorbed laser induced fluorescence (TALIF) and lists N-atom TALIF-related timescales.

In Chapter 4, a self-consistent experimental data set acquired for O ground state number density measurements by Ar optical actinometry technique is presented. The data set consisted of five waveforms: reduced electric field, transmitted current, O and Ar actinometric transitions and $(0-0)$ vibrational transition of second positive system on nitrogen and was taken in nanosecond capillary discharge with 1 eV/molecule of specific deposited energy.

In Chapter 5, longitudinal electric field in the front of fast ionization wave and quasi-steady-state discharge measured by E-FISH technique is presented. Different calibrations: by Laplacian electric field, by capacitive probe and by back current shunt, are applied and discussed. The origin of the second harmonic signal based on calibration results is suggested.

In Chapter 6, the details of organization of TALIF experiment common for both discharge setups such as laser beam alignment, triggering scheme and data treatment are listed.

In Chapters 7 and 8, time-resolved N atom ground state number density measured by Kr-calibrated TALIF technique, is presented and discussed for cases of specific deposited energy of 1 eV/molecule in capillary and 10^{-3} eV/molecule in tube, respectively.

In Chapter 9, preliminary biological results of the impact of the developed cold atmospheric plasma device on stem cells are presented.

In Chapter 10, general conclusions of the present work are given together with future perspectives.

Chapter 3

Materials and methods

3.1 Nanosecond capillary (nCD) and tube (nTD) discharge setups

Common aspects between used setups

Both nanosecond capillary (nCD) and tube (nTD) discharge setups were designed by Ali Mahjoub, former design engineer at Laboratory of Plasma Physics, Ecole Polytechnique, in collaboration with Dr. N Lepikhin and Dr. A Klochko with a perspective of further studying the FIW's propagation. Thus both discharge setups have an elongated shape with inter-electrode gap well superior than the electrode diameter. Pointed brass electrodes are surrounded by tubes made of fused silica to allow optical emission spectroscopy at wavelengths shorter that $\sim$ 300 nm (in particular, for confident observation of Second Positive System of N_2 whose strongest line is located at 337.1 nm). Electrodes are connected to the main wires of the 50 Ohm coaxial single-shielded line used to deliver high voltage pulses from FPG 12-1NM (FID GmbH) high voltage generator at typical repetition rate of 10 Hz. Tubes are surrounded by metal screens connected to the shielding of the cables. Metal screens act as a Faraday cage, they cut off the electro-magnetic noise produced by the discharges and thus protect the surrounding equipment. Electrical diagnostics are performed by means of back current shunts installed in coaxial lines and capacitive probe placed at the metal screen. The general scheme of the electrical supply is shown at Figure 3.1.

Setups are usually operated at moderate pressures of the values between few mbar and up to 100 mbar at flow values varying from units of sccm up to 50 sccm. Gas flow is controlled by Brooks Instruments 5850TR mass flow controller operated from Brooks Instruments Model 0254 control panel. The flow-through configuration is chosen to facilitate pressure tuning and to avoid accumulation of leaking air from the surrounding atmosphere. With no gas inlet and primary vacuum pump connected to

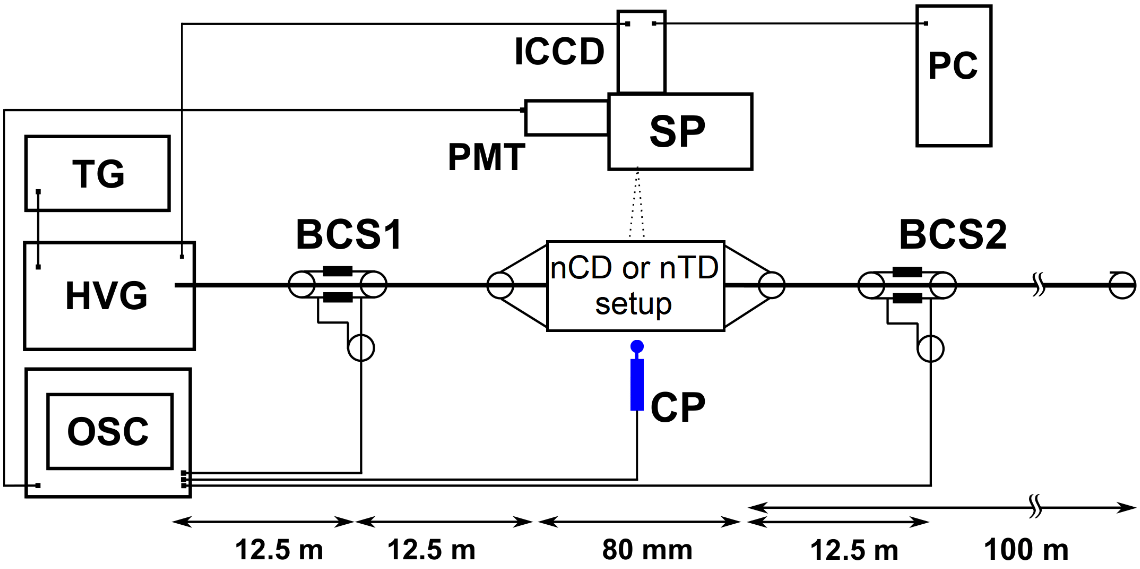

Figure 3.1 – A general scheme of the experimental setup with the basic experimental equipment. TG is triggering generator, HVG is high voltage generator, OSC is oscilloscope, BCS is back current shunt, CP is capacitive probe, PMT is photomultiplier tube, ICCD is intensified charge-coupled device (camera), SP is spectrometer, PC is personal computer. Figure was obtained by editing the Figure 3.3 from [149].

the outlet of the gas supply system, both setups can be pumped out to 10^{-2} mbar. The leak rate was estimated in a following way: once the gas path is pumped out, primary vacuum pump is turned off and separated from the path by a low leak rate valve (in the present case, VAT series 230), and then an average leak rate during the first accumulated ~ 50 mbar is calculated. Both setups show pressure-independent leak rate at the level of $3-5$ mbar/hour. N_2:O_2 mixtures of tunable proportions are obtained by merging air and nitrogen flows delivered from Air France gas cylinders of 99.9% purity. Mixing happens ~ 3 m upstream to arrival at the discharge tube to ensure homogeneous flow's blending. Pressure in the center of the discharge tube is monitored by a pair of Pfeiffer Vacuum capacitive-type CMR 261 pressure gauges located symmetrically up- and downstream from the center of the tube. Prior numerical study [51] had shown that the mean value of these two readings accurately depicts the pressure at the center of the tube even in case of high hydrodynamic resistance of ~ 1.5 mm diameter capillary of nCD setup. The gas emergent from the discharge tube is evacuated by primary vacuum pump to surrounding atmosphere. A schematic view of gas flow system is presented at Figure 3.2.

As would be shown in greater detail further in the chapter, emission of the discharge carried out in nCD or nTD setups shows a non-uniform radial profile. In pure N_2, it exhibits rather a predominantly parietal (close wall) radial structure. At

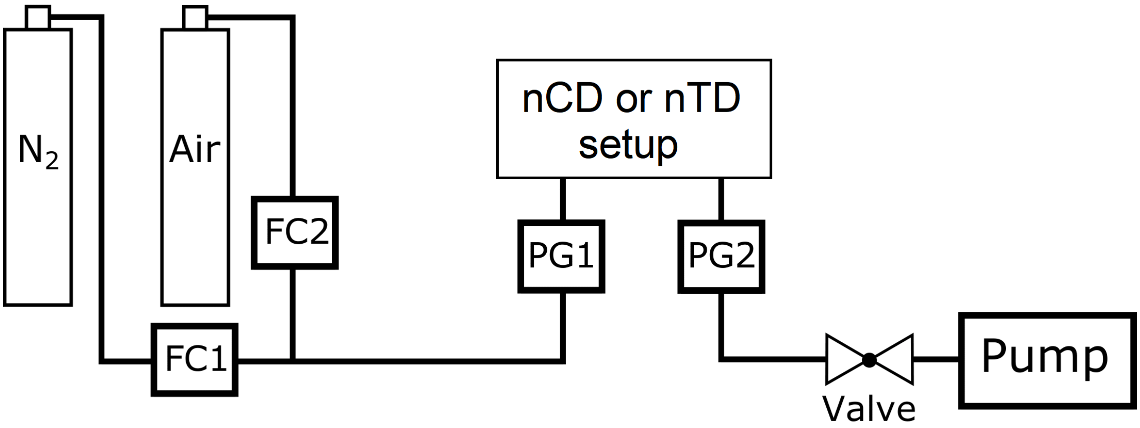

Figure 3.2 – Schematic view of the gas flow system used in the experiments. FC is flow controller, PG is pressure gauge. Figure was obtained by editing the Figure 3.2 from [149].

the same time, even the 2% O_2 admixture modifies the emission's radial distribution towards the inter-electrode axis. A pressure decrease in the same manner acts on the radial distribution.

The important issue of plasma emission spectral overlap with N-atom fluorescence signal within the band-pass of used filter is present in both nCD and nTD setups and would be discussed in related chapters. Such issue is by definition absent during Kr noble neutral gas calibration.

Nanosecond capillary discharge (nCD) setup

Note that all data for nanosecond capillary discharge was taken from PhD thesis of Dr. N Lepikhin [149].

The schematic view of nanosecond capillary discharge and electrode assembly technical drawing are shown on Figure 3.3. The discharge was initiated in the quartz capillary tube with the internal diameter of 1.5 mm and the external one of 3.45 mm. The flow controllers maintain the total constant flow rate equal to 50 sccm and pressure of 28 mbar. The gas renewal time at ambient temperature (300 K) is thus 4 ms. The repetition rate of 10 Hz used in the experiments is way lower than 1/(4 ms) = 250 Hz, so one can be sure that each new discharge does not depend on the previous one. Since the gas renewal time depends inversely proportionally on the gas temperature [150], any gas heating would only reduce the gas renewal time.

The total and specific deposited energy values as a function of pressure and transmitted current are shown at Figure 3.4. As it can be seen, in nCD, specific deposited energy can be as high as 1 eV/molecule.

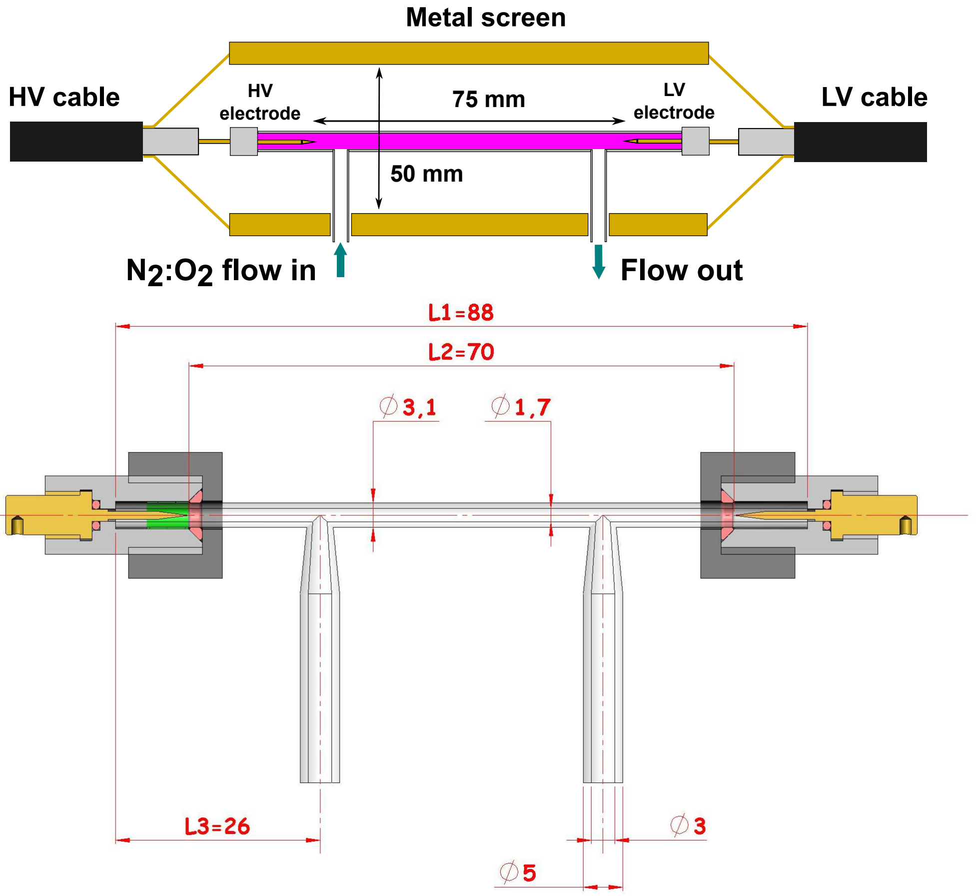

Figure 3.3 – Technical drawing of nCD: general schematic view and electrode assembly technical drawing. $L1$ is the length of the quartz capillary, $L2$ is the distance between electrodes, $L3$ is the distance between capillary edge and gas inlet tube junction. Taken from [149].

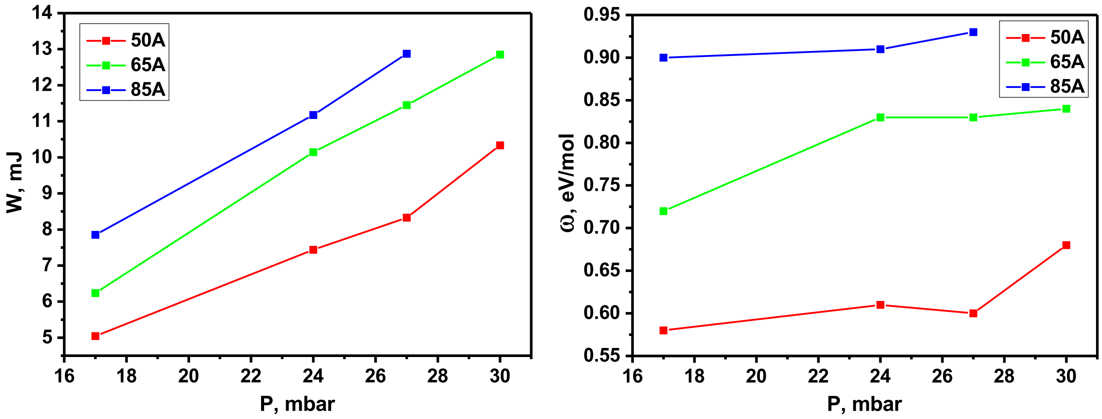

Figure 3.4 – The total (a) and specific (b) deposited energy for different transmitted currents and pressures of pure N_2 in nCD. Taken from [149].

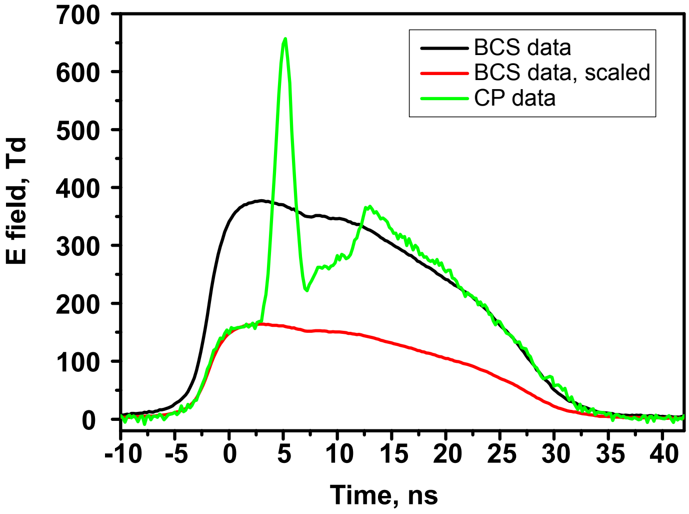

Figure 3.5 – Longitudinal electric field measured by CP (green curve) and by BCS techniques (black curve) together with synchronization curve (red curve). First pulse, N_2, 27 mbar, $I_{tr} = 65$ A. Taken from [149].

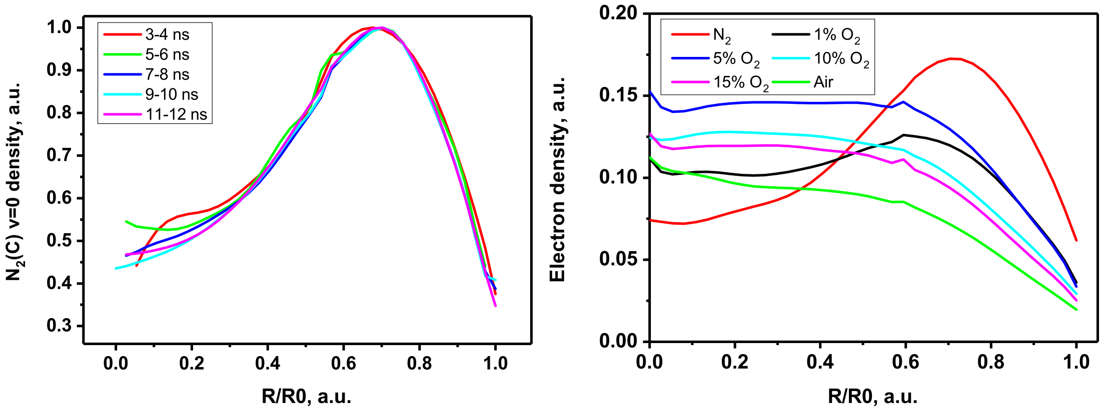

Figure 3.6 – Experimentally measured radial distribution profiles of $N_2(C^3\Pi_u$, v'=0) state at 27 mbar, positive polarity high voltage pulses (amplitude 9.3 kV, 30 ns FWHM) in nCD: (a) taken during first 12 ns in N_2, peak normalized, (b) initial distribution in N_2:O_2 mixtures. Taken from [149].

The electric field in nCD was measured by capacitive probe and back current shunts as shown at Figure 3.5. The E/N reaches 650 Td during FIW and gradually decreases from 350 Td to detection limit during 15 ns of quasi-steady-state discharge.

At such high reduced electric fields and high specific deposited energy, the electron number density as well as the fraction of high-energy electrons increases significantly. These electrons efficiently excite electronic levels of bath gas molecules through collisions. The number density of excited species increases to an extent when collisions between charged and/or excited species become dominant. In particular, two effects has been already observed. First, fast quenching by electrons of 10^{14} cm^{-3} number density that reduce the effective lifetime of $N_2(C^3\Pi_u)$ state from usual ≈ 30 ns to ≈ 10 ns [44]. Second, fast gas heating (up to 2000 K during the 600 ns after the first pulse from initial ambient temperature) due to pooling reaction between N_2(B) molecules that was numerically shown to provide 61% of the heat due to the high density of N_2(B) in the near afterglow [151].

The initial radial distribution of electrons defines the radial map of produced excited species thus its knowledge is of importance for spatially-resolved measurements (such as TALIF). Evaluated from emission imaging with 1 ns resolution, the initial radial profile of electrons was found to stay constant during the FIW propagation and quasi-steady-state discharge (Figure 3.6(a)). The influence of gas mixture composition was studied as well. In N_2, radial distribution shows a parietal structure with a maximum located closer to the wall then to the center of the capillary. But even with 1% O_2 admixture, the tubularity significantly decreases, leading to a flatter distribution in the center. From the O_2 volumic admixture of about 10%, the radial profile can be considered centered. In general, even in N_2, the radial profile maximum-to-center ratio had barely exceeded the value of ~ 2. Radial distributions for six N_2:O_2 mixtures can be found at Figure 3.6(b).

Nanosecond tube discharge (nTD) setup

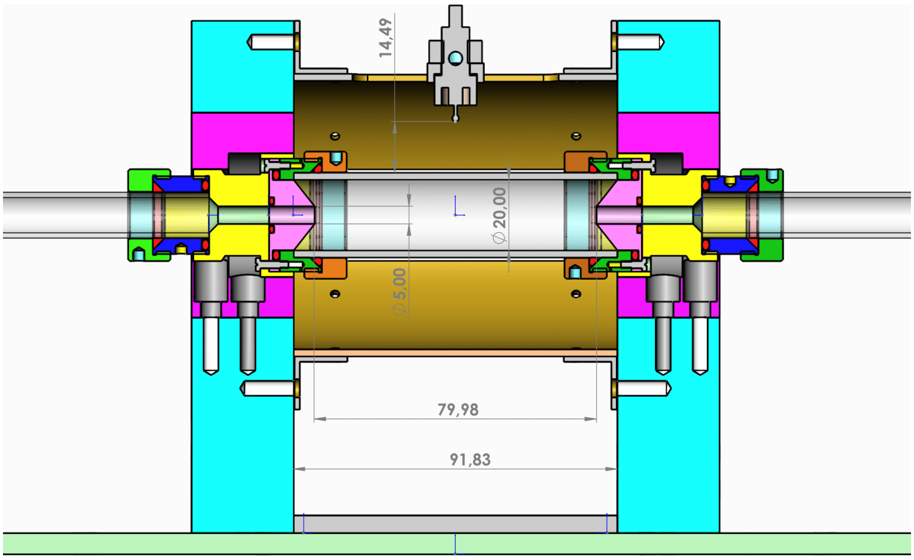

Figure 3.7 – Schematic drawing of nanosecond tube discharge setup in axial section. Quartz tube inner diameter 20 **mm, electrode orifice diameter** 5 **mm, inter-electrode distance** 79.98 **mm, copper screen length** 91.83 **mm, distance from the tip of capacitive probe to quartz tube** 14.49 **mm.**

The schematic drawing of nanosecond tube discharge containing the general assembly view with details on electrode assembly is shown on Figure 3.7.

Specific deposited energy measured in the first pulse in air by a pair of back current shunts as a function of pressure is presented on Figure 3.8. On the plot, nTD data is shown together with nCD to underline the order of magnitude difference in specific deposited energy between the setups. At such low ω, production of excited and ionized species is expected to be small so that collisions between excited and/or charged particles would be negligible compared to collisions between electrons and bath gas molecules (weakly ionized plasma model).

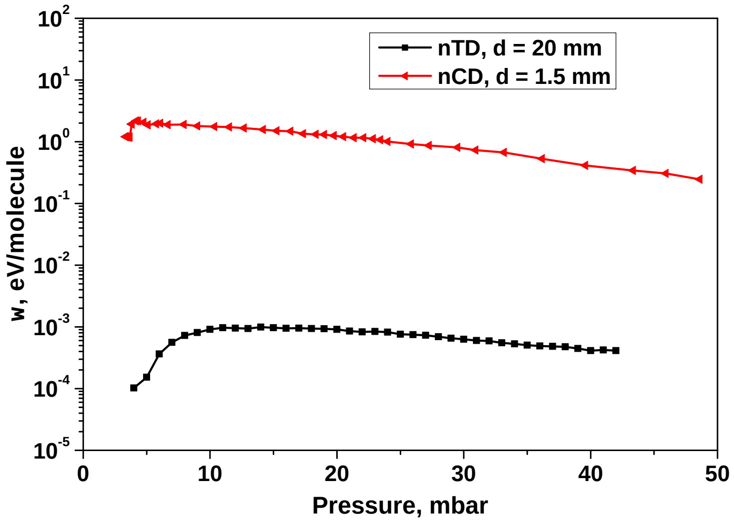

Figure 3.8 – Specific deposited energy measured in the first pulse in air in nTD and nCD.

All the work concerning electric field measurements in nTD at the present moment can be read in detail in Chapter 5 that presents longitudinal electric field in nTD measured from three methods: by electric field induced second harmonic generation (E-FISH) laser technique, by back current shunts and by capacitive probe.

Figure 3.9 shows integrated emission recorded by PiMax4 ICCD camera together with radial profile restored by code described in [149] for the discharge in 10 sccm 20 mbar N_2 in nTD. Two features can be noted. First, even though integrated profile shows the maximum to center ratio of about 2 : 1, radial profile reveals more sharp ratio of 50 : 1. Second, the restored radial emission profile exhibits oscillatory behavior in proximity to the center. This is due to exact expression of direct Abel transform that mathematically cannot be inversed for an arbitrary integrated profile [152]. Such ill-posed inverse problems are characterized by an extreme sensitivity to measurement noise and modeling errors. This numerical artifact introduces uncertainty to definition of emission intensity at the axis where TALIF diagnostic is applied. It would influence the reliability of kinetic simulations that use initial

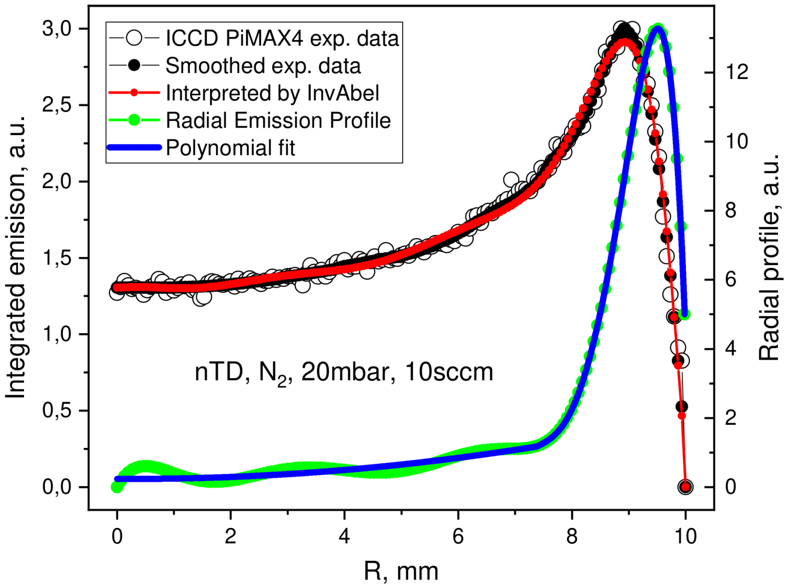

Figure 3.9 – Integrated emission profile together with radial profile restored by code [149] for 10 sccm 20 mbar N_2 nTD discharge. Black hollow circles - integrated emission experimental data, black scatter - smoothed experimental data, red scatter - code fit, green - restored radial emission profile, blue - radial emission profile without parasitic oscillations.

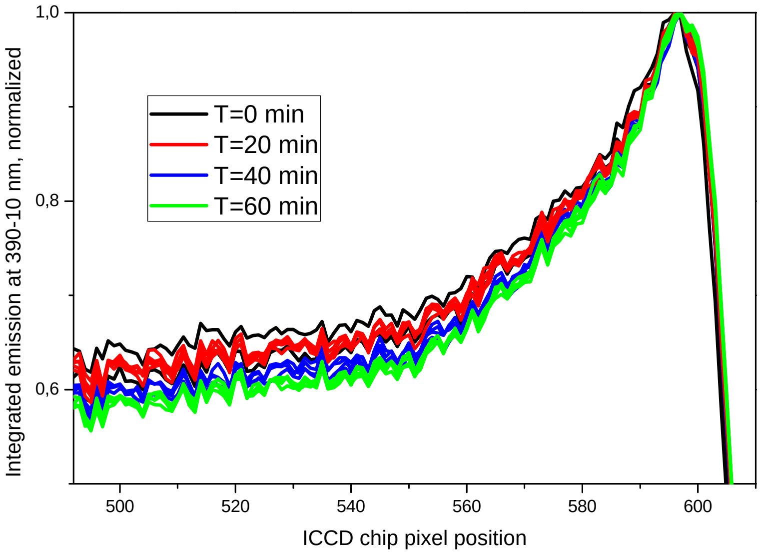

Figure 3.10 – Integral emission reproducibility within 390 – 10 nm bandpass filter at ∼ 1 h scale at nTD setup, 10 sccm 20 mbar N_2.

electron radial profile as an input parameter. Since amplitude of oscillations is independent from the radial profile value at the center, one of the ways to improve the reliability of restored radial profile is to select a more centered discharge.

At the same conditions as of the Figure 3.9, plasma emission was recorded at

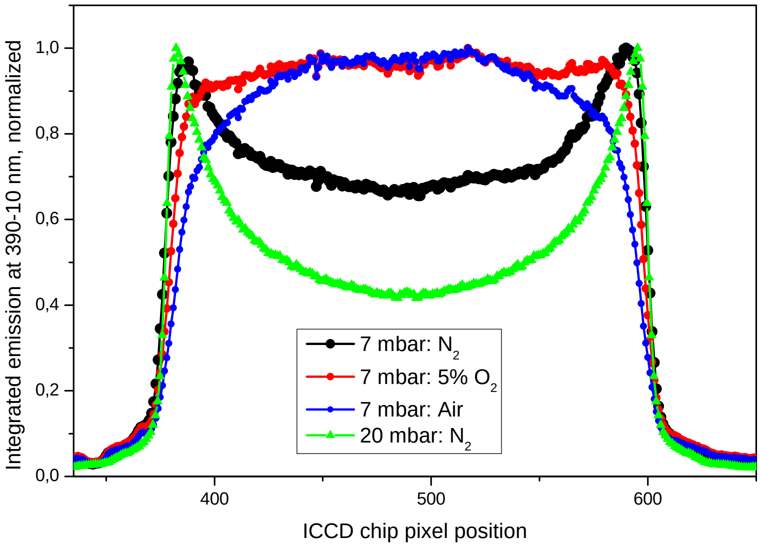

Figure 3.11 – Integral emission within $390 - 10$ **nm bandpass filter at nTD setup in different conditions of pressure and gas mixture. Flow** 10 **sccm.**

different times from turning the setup on and plotted on Figure 3.10. Slight decrease in signal from the central tube's region in observed during about 1 h run. The difference between profiles decreases with time, and at 40 min and 60 min profiles are quite close. It was thus accepted that 40 min is a stabilization time required for nTD to go into working mode. This event, probably because of the heating of high voltage electrode, is apparently linked to the accumulation of species between the pulses due to flow rate that is too low to ensure gas renewal. Because of this point, flow decrease was not considered for the following study.

In view of importance of initial electron radial distribution profile and the issue with its retrieval, a separate study in view of definition of better conditions was conducted. The integral emission in nTD was acquired for different conditions of gas mixture, pressure, flow, repetition rate and voltage pulse polarity. Due to the beforehand known impossibility to have gas renewal between two consecutive discharges, tested flow values were limited a few tens of sccm. Few dependencies were identified. First, frequency modification did not lead to significant profile change. Second, flow increase contributed to more tubular discharge structure. Third, negative polarity pulsed discharges in average showed more centered profile but they suffered from important start time jitter and had different volumic development from shot to shot compared to positive polarity pulsed discharges. Summarizing, only two parameters were found to improve the radial profile: pressure and gas composition. Figure 3.11, similarly to nCD's Figure 3.6(b), illustrates the effect of O_2 pressure decrease for centralization of the discharge in tubes.

The issue of parasitic discharge developing in the side tube upstream to the HV

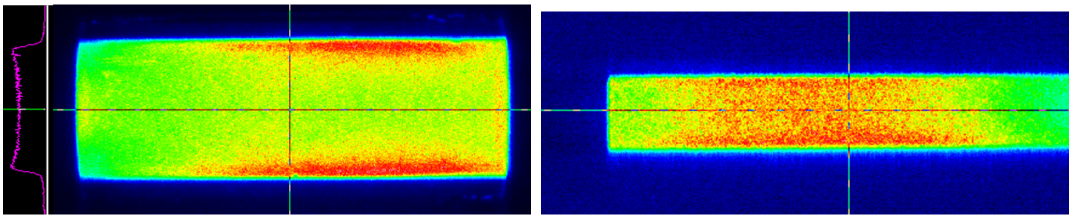

(a) N_2, 7 mbar: $8 : 1$

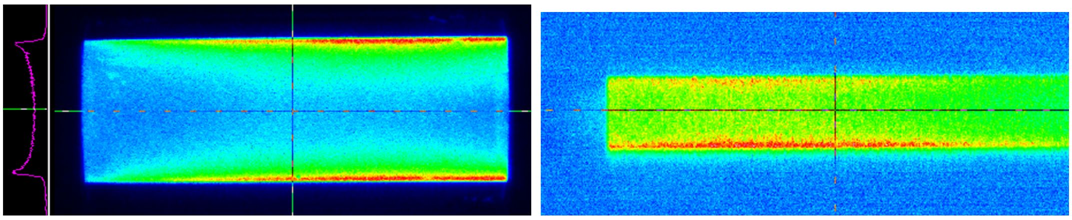

(b) N_2, 20 mbar: $23 : 1$

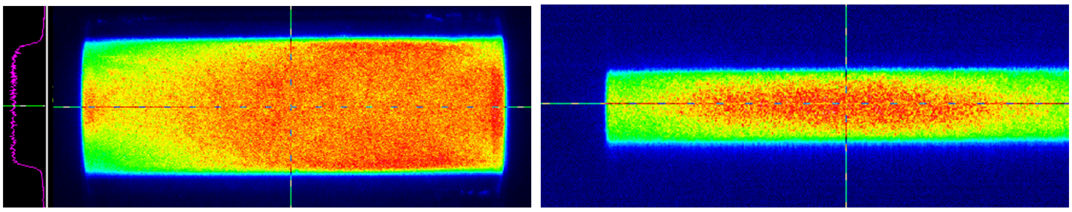

(c) N_2:O_2 $95 : 5$, 7 mbar: $7 : 1$

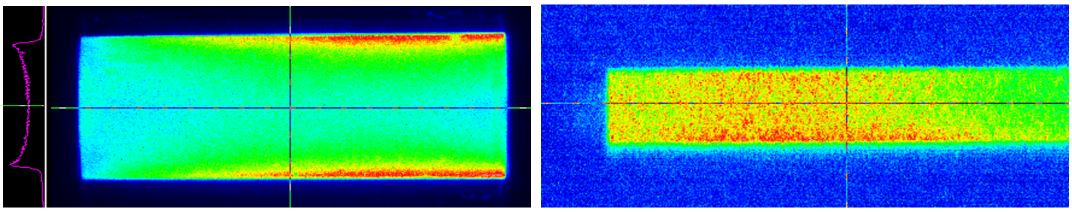

(d) N_2:O_2 $95 : 5$, 20 mbar: $22 : 1$

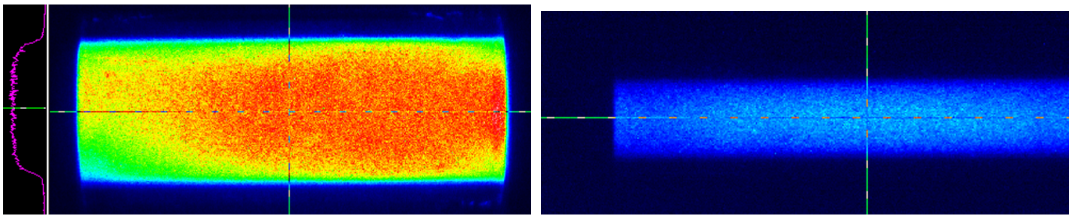

(e) Air, 7 mbar: $9 : 1$

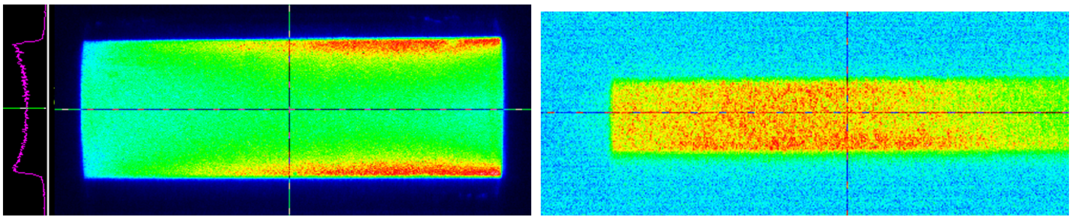

(f) Air, 20 mbar: $16 : 1$

Figure 3.12 – Integrated emission images by PiMax4 ICCD, 45 ns gate, 390 ± 10 nm filter, 300 accumulations. Left: nTD tube, right: side tube.

electrode was addressed as well. Figure 3.12 show integrated emission images of the main tube of nTD setup and side tube taken by PiMax4 ICCD camera from the same distance 20 cm to the axis of the tube, with 45 ns gate, 390 ± 10 nm filter (FNS of N_2, $(0-0)$), 300 accumulations in different gas mixture and pressure conditions keeping flow at 10 sccm and repetition rate at 10 Hz. Images are in false rainbow-palette colors that linearly represent the signal intensity: violet for the smallest and red for the biggest photon count, palette re-partition defined independently for each image. The ratio under each pair of images is the photon count ratio between main and side tubes taken in at a position marked on the image by intersecting vertical and horizontal lines. The lower the pressure, the more parasitic discharge is an issue whatever the gas mixture. In terms of an estimate from the photon count ratio, side tube energy loss is about 12% for 7 mbar and about 6% for 20 mbar. More accurate accounting would require comparison of radial emission profiles from both regions.

Summarizing the above, the following conditions were concluded to be the most suitable for nTD N-TALIF experiment: pressure of 7 mbar, flow rate of 10 sccm, positive polarity HVG in all considered N_2:O_2 mixtures in order to analyze the O_2 influence in more detail.

Different aspects between used setups

Despite all the shared characteristics evoked above, still there are a few important differences that have to be kept in mind.

Laser focusing and plasma radial profile

Due to millimetric scale of nCD setup's transverse section, it was technically challenging to realize a demountable configuration of electrodes that would at the same time allow through-electrode gas introduction and evacuation *via* the tube. Thus in nCD, another approach was realized: quartz side tubes used for gas flow guidance are alloyed to the capillary in between the whole pin-like electrodes that enter the capillary from its ends. Such side tube's disposition immediately causes a question concerning possible effect of flow vorticity on the pressure distribution along the capillary. This concern was addressed numerically in [51] by solving the Navier-Stokes hydrodynamic equation for the exact nCD geometry by commercial solver COMSOL Multiphysics. Calculations have confirmed the presence of laminar flow and linear drop of pressure along the capillary of nCD. Consequently, the use of a pair of symmetrically placed pressure gauges for determining the pressure at the center of the discharge tube was validated for tubes of internal diameter as small as up to 1.5 mm.

From point of view of optical access, the nCD allows only a side and a bottom views at the capillary through a pair of openings done in the metal screen as shown at Figure 3.13. Due to millimetric scale of the transverse section of the nCD's tube, a laser beam focused to nCDs center might be intense enough to break the fused silica wall of the discharge tube because of important non-local heating process. In case of nCD TALIF application, laser beam had to be focused few mm posterior to the tube in order to avoid damaging of the tube.

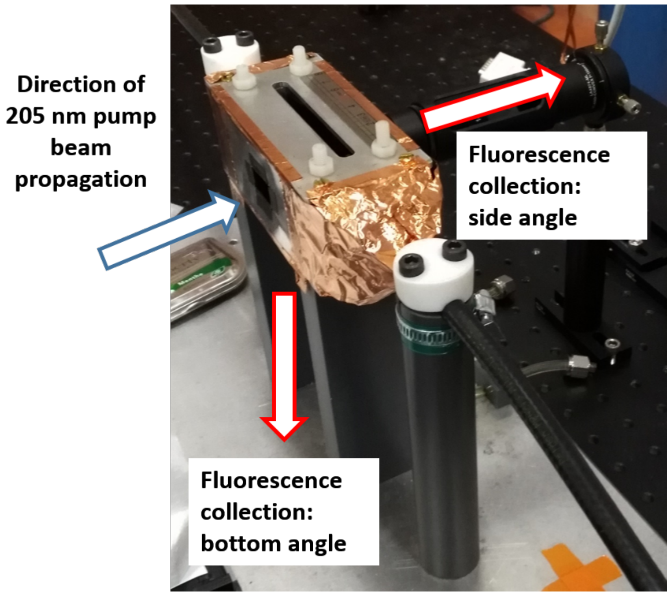

Figure 3.13 – Laser beam input and fluorescence collection views for nCD.

Since the capillary is located some distance upstream of the focus of the probe laser, the exact measurement volume of the TALIF signal is not clearly defined. Such mutual disposition of laser beam and discharge tube has a number of consequences. The nCD tube's volume where laser beam can potentially excite an atom to a fluorescent state can be estimated as a cone-cylinder intersection. In the same time, because of laser beam focusing, since entering the tube and before leaving the tube, laser beam monotonously shrinks and thus its intensity I increases. In these conditions, it is quite likely that the TALIF signal originates from a finite radial extent of the capillary cross-section of radial-dependent number density $n(r)$ where the $n(r) \cdot I^2$ product is the biggest, rather than just from the center.

While noble gas calibration approach partially mitigates this uncertainty by using the same experimental mount as during the discharge, it is believed that the difference in radial profiles of the N and Kr atoms within the capillary will constitute a certain amount of systematic error. In particular, a previous study in the same discharge noted a "U"-shape distribution of $N_2(C^3\Pi_u, \text{v} = 0)$ molecules over the capillary cross-section during the discharge pulse [151]. The consequent N-atom production is expected to be strongly influenced by this initial distribution. In contrast, the laminar flow of Kr noble gas is likely to be uniformly distributed over the entire section of the capillary. Due to complexity of the issue, radial profile related systematic error was not estimated. Other sources of error include the imperfect shot to shot repeatability of the discharge as a random error, as well as the uncertainty in the ratio of the N and Kr two-photon cross sections as a systematic error (would be discussed further).

Generally, the application of on-axis laser focused techniques on nCD setup is probably possible for the techniques that require lower laser energies than TALIF does (for example, single photon techniques as LIF) and if handled with special care.

On its turn, the nTD setup is designed in view of producing nanosecond pulsed discharges with low values of specific deposited energy. The goal was achieved by making its tube a bigger volume (comparing to nCD) by increasing the diameter up to centimetric scale at transverse section. Tube diameter this big freely enables manufacture of demountable through-holed electrodes. Thus in nTD, the gas supply is organized *via* Pyrex side tubes that are co-axially connected to the hollow truncated conically shaped electrodes. Other end of each of the side tubes is sealed with round quartz window. Quartz windows add a possibility of a longitudinal view in addition to the side view through a pair of gaps between upper and lower parts of copper two-piece screen as shown at Figure 3.14.

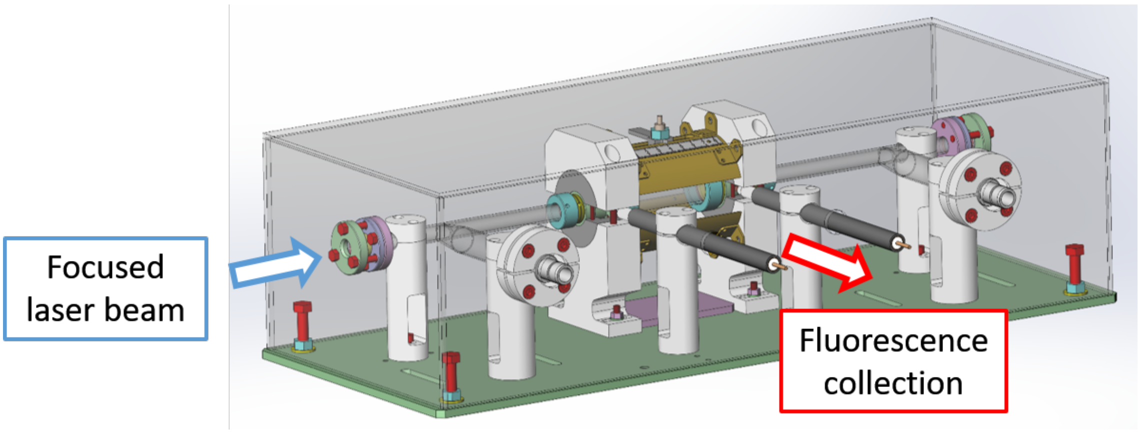

Figure 3.14 – Laser beam input and fluorescence collection views for nTD.

Parasitic discharge in the side tubes

A discharge setup operated at moderate pressure in gas flow is prone to development of parasitic discharges within side tubes intended for gas delivery. In order to have an accurate estimate of energy deposited to plasma between the electrodes, *id est* within the tube, the energy losses spent on discharge at side tubes should be evaluated. The calculations based on voltage waveforms are space-insensitive and represent the total deposited energy value. One of the ways to estimate a fraction of energy spent for development of side tube parasitic discharge is to compare side view integral emission images taken from the discharge tube and the side tubes during the quasi-steady-state discharge. In case of nCD setup, the side tube's imaging was not possible due to design features. More precisely, the nCD setup's metal screen connected to shielding of coaxial cable should expand up to a centimeter-scale transverse section in order to avoid short-circuiting between the screen and the electrode connected to cable's core. The distance between the cable's shielding and the core would effect the FIW's propagation in the nCD so the transverse section should be kept constant. As a result, starting from the alloy point at the capillary, few cm of side tubes are hidden from optical access by metal screen. The issue would hopefully be addressed in future study involving minor re-design of the nCD setup.

Species accumulation between consecutive pulses

The nCD setup is ran at 10 Hz repetition rate at flow values above 5 sccm that allow gas renewal before the next incident high voltage pulse arrives to the discharge tube. The 10 Hz value is a repetition rate of the in-lab available nanosecond dye system used for laser diagnostics on nCD and nTD. Because of $20.2/1.5 \approx 13.5$ time larger diameter of nTD tube compared to nCD's one, the nTD tube volume is $(13.5)^2 \approx 181$ times bigger compared to nCD's. Then the flow value required for gas renewal in nTD for the same repetition time is at least $181 \cdot 5$ sccm$= 905$ sccm. This value cannot be accepted for nTD operation because of a number of reasons. If to order them by increasing importance: (i) incompatibility with the higher working limit of mass flow controller, 100 sccm, (ii) operation at moderate pressures becomes unlikely and (iii) the minimal possible pressure is probably too high for development of FIW discharge in principle. Consecutively, nTD setup has to run in a more sophisticated regime than nCD where gas renewal is possible.

The absence of full gas renewal before another incident high voltage pulse means that temporal evolution of discharge parameters such as energy branching, radial distribution, species number density, temperature *et cetera* are dependent on discharge parameters achieved at the end of the previous pulse. In short, nTD is a feedback-looped system where the next discharge depends one the previous one. At many real systems with a feedback loop, the difference between output parameters of i^{th} run and $(i+1)^{st}$ run decreases with increasing of the i such that the system iteratively converges to a stabilized reproducible regime where temporal evolution of parameters is independent from the i, sequence number of the run. In application to the nTD, after a significant number of incident pulses, the development of the next discharge would become independent from the previous one. Such behavior was experimentally observed during integrated plasma emission imaging, as already described in detail in the chapter. Plasma emission imaging was also used for determining the time needed for nTD to reach the stabilized reproducible regime. The nTD's flow and pressure values leading to homogeneous and axially-distributed plasma with low-intensity parasitic side tube discharges were established based on comparison between different stabilized reproducible regimes.

3.2 Electrical and optical equipment used

Back current shunt, capacitive probe

The waveforms of incident, reflected and transmitted voltage pulses are monitored *via* two calibrated, high bandwidth back current shunts (BCS) installed in the shielding of coaxial transmission lines at a distance of 12.5 m from each electrode. A single BCS is an approximately 2 cm long insertion into the coaxial cable's shielding consisting of several low induction resistors soldered in parallel. The voltage drop across the BCS is directly proportional to the current in the line and thus is a time-accurate and amplitude-scaled waveform of the actual high voltage pulse moving along the line. For a discharge cell installed in the break of the cable, a pair of BCSs inserted before and after the cell allow correct reconstitution of the axial electrical field after the closure of the discharge gap. The temporal resolution of such tool is limited by inductance of resistors used and usually is of the order of 1 ns.

The capacitive probe is a low inductive charge detector installed underneath the discharge tube's shielding and connected to the oscilloscope. Capacitive probe provides a current induced by the changes of electric potential in tool's proximity of about 2 cm with typical response time of 1 ns. Moved along the discharge tube, it allows to access data on charge distribution, electric potential and field propagation as well as the velocity of propagation of fast ionization wave. The tool is calibrated against the signal received from known field which is obtained by filling the insides of the tube by a conductive material (metal needle, tube or cylinder).

More details concerning these tools can be found in [51, 149].

Calibrated sensitivity spectrometer-camera pair

The sensitivity curves of optical equipment given by manufacturers are typical reference-use-only characteristic functions that overall give a fair estimate of the average response of the product within manufactured batch ignoring its piece-to-piece variations which might be important in more specific parameter range. Individual calibration is always welcomed if such a possibility is available.

Knowing that, ISTEQ XWS-65 absolute laser pumped broadband ultrabright plasma light source has been used to calibrate the spectrometer-camera pair. Initial plasma of the X-rays wavelength source (XWS) device is produced by a high voltage electrical discharge in high pressure Xe gas and further is sustained in the optical breakdown state by focused continuous laser radiation. XWS light sources have been developed as a replacement for traditional gas discharge lamps (D, W or Xe lamps) and LEDs. Compared to these, XWS sources have a wider spectral range and higher spectral brightness. Compared to arc lamps, laser plasma has higher spatial and temporal stability, higher brightness, smaller dimensions of emitting volume and considerably longer operation time without lamp replacement due to absence of the wear of lamps and electrodes [153]. The present model has an option of a remote control *via* Ethernet connection by standard RJ45 port.

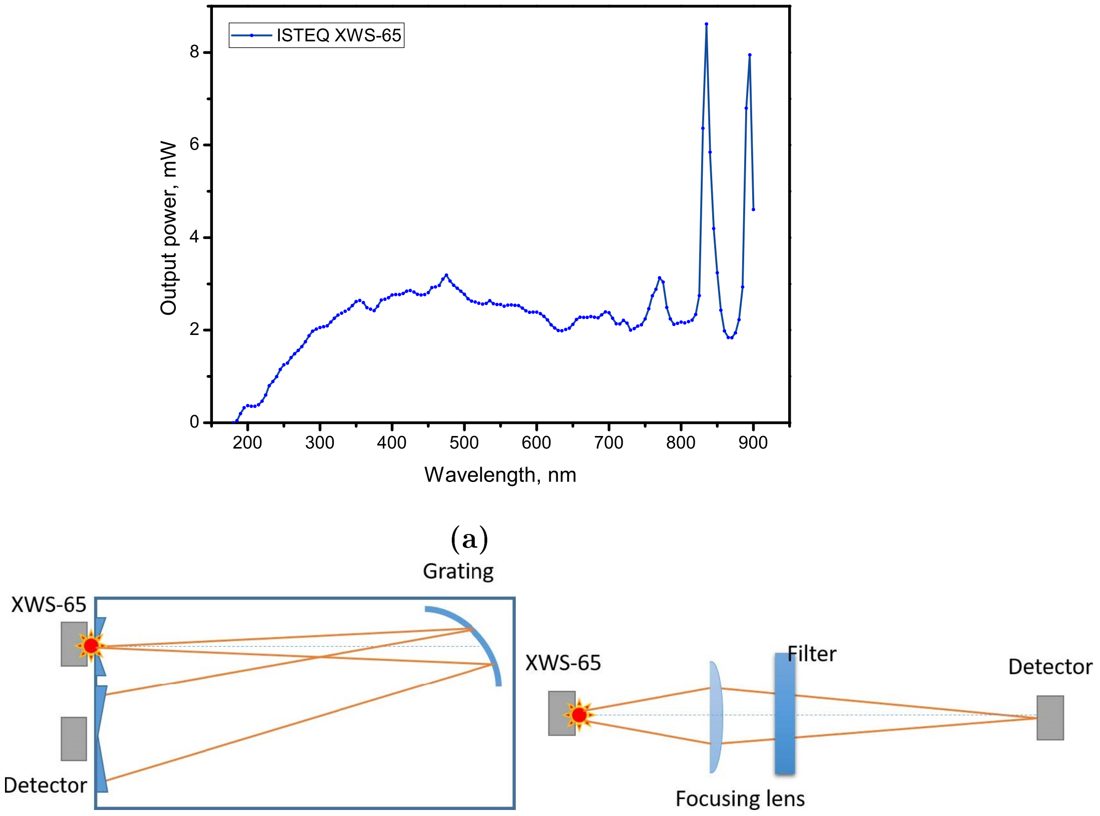

(a)

(b)

(c)

Figure 3.15 – (a) The spectral output power of the ISTEQ XWS-65 lamp. Scheme of the (b) relative and (c) absolute intensity calibration, respectively. Provided by [153].

Figure 3.15 (a) shows the manufacturers' spectral profile of the XWS-65 calibration light source taken with a 5 nm resolution. According to manufacturer, the source has been calibrated in two steps. First, relative calibration allowing to establish the shape of the sensitivity curve (Figure 3.15 (b)). XWS-65 as a point light source was placed instead of the input slit of monochromator with concave diffraction grating 600 lines/mm and curvature radius of 1000 mm. Reflection coefficient of the diffraction grating for a spectral range of $250-1000$ nm was previously measured. IRD SXUV-100 photodiode as an absolutely calibrated detector was placed at the output slit with a width of 5 mm providing a spectral resolution of 8 nm. Second, absolute calibration in order to properly label the relative calibration curve (Figure 3.15 (c)). A well-defined solid angle of XWS-65 point-line light source was focused with a lens of measured reflection through a spectral filter with a known transmission to Ophir sensor used as a detector. Interesting to note that the source's intensity within the region of our main interest, $300-800$ nm, exhibits relatively modest intensity variations not exceeding the factor of two.

The circular 1" diameter output window of the light source was placed in front of the 100 μm width spectrometer slit at the distance of 225 cm. The light arrival's plane angle is less than 1° (to synchronize with diameter of the output window or lamp bulb). As checked by laser level alignment, light from the source arrived perpendicularly to the surface of the slit. The distance of light's propagation from one device to another was fully confined in a box of an approximately 40 cm width, 30 cm height. This over 2 m long confining cage was obtained by gluing three smaller boxes in series and perforating necessary windows of about 5 cm × 5 cm along the light propagation. Such build represents itself a sequence of diaphragms that cut off stray light reflections from internal surfaces.

In the first place, the box was installed in order to isolate the source's light from the rest of experimental space due to its non-negligible intensity within Hartley absorption band at $220-280$ nm. At this wavelengths, O_2 predominantly photodissociates into O-atoms that further recombine with remaining O_2 to form hazardous ozone gas O_3. The box-collected ozone-enriched air has been evacuated with a help of a home air ventilation fan *via* a 10 cm hole made in the bottom of the carton box where O_3 as a heavier than air molecule is expected to accumulate. As O_3 production is dependent on the intensity of the light that decreases with the distance from the source as $1/r^2$, the hole was placed slightly closer to the source, more precisely, at about 80 cm distance. Even with these precautions applied, calibration had to be remote operated for the staff safety reasons. The level of produced ozone was way above the threshold of human odour perception and a prolonged presence in experimental piece concluded to appearance of light ozone poisoning symptoms.

The light source's spectra was used to calibrate the camera-spectrometer pair for three available diffraction gratings in ambient air. In order to eliminate diffraction of the 2^{nd} and 3^{rd} order, the whole light source's spectrum was recorded in three parts: (i) as-it-is in $180 - 430$ nm range, (ii) *via* Thorlabs FGL400S filter (high-pass from 400 nm) in $370 - 630$ nm range and (iii) *via* colored glass filter (Electrosteklo Orange Glass #14) (high-pass from 600 nm) in $570 - 900$ nm range. The overlap in 60 nm between the areas was taken to assure their mutual correspondence. Since each part of the light source's spectra is way larger than the spectral range within one camera shot, Step-n-Glue procedure within WinSpec camera software allowing to reconstitute full continuous image from a sequence of consecutive acquisitions was applied. Used parameters were: 10 accumulations per grating's position, gain equal to 25, camera gate of 3 ms and minimal shot-to-shot overlapping of 20% to ensure proper superposition between the shots.

Obtained areas of spectra for each diffraction grating used have been corrected by transition function of the appropriate filter if applicable, vertically shifted to match the tail of the previous area's spectra, divided by spectral output power of the light source, normalized to unity and further inferred as experimental sensitivity of camera-spectrometer pair for a chosen diffraction grating.

Figure 3.16 shows the experimental sensitivity *versus* expected sensitivity of camera-spectrometer pair for three diffraction gratings. As discussed above, the calibration has been performed in presence of ambient air. This means that due to Hartley absorption band of O_2, experimental values at wavelengths below 300 nm cannot be interpreted as a characteristic feature of the devices and only give an underestimate of its actual sensitivity. For this reason the experimental curves on Figure 3.16 withing the above mentioned region are plotted in grey to empathize its evaluative character.

Obtained experimental curves generally follow the expected trend with a few important deviations such as lacking right slope of the peak at 280 nm at Figure 3.16 (a) or for about 1.5 times underestimated peak at 375 nm at Figure 3.16 (c). Two regions with value's discrepancy of around 2 times are present at 330 nm and 625 nm at Figure 3.16 (b) as well. The abrupt fall of sensitivity from 630 nm to 700 nm at Figure 3.16 (c) is caused by mechanical limit of light's reception of the rotated grating in the spectrometer. Peak at 824 nm observed at Figure 3.16 (a, b) is most probably due to slightly inaccurate wavelength definition of the light source's output emission spectra in the near IR region since no such resonance-like behavior is expected from neither camera chip, diffraction grating or two reflective mirrors installed at the input and the output of the spectrometer. For future use, it is suggested to ignore the 824 nm peak and replace the lacking data by linearly joining the remaining points. Data was smoothed by Adjacent Averaging method with 5 nm width window to eliminate noise spikes. The width of the window corresponds to

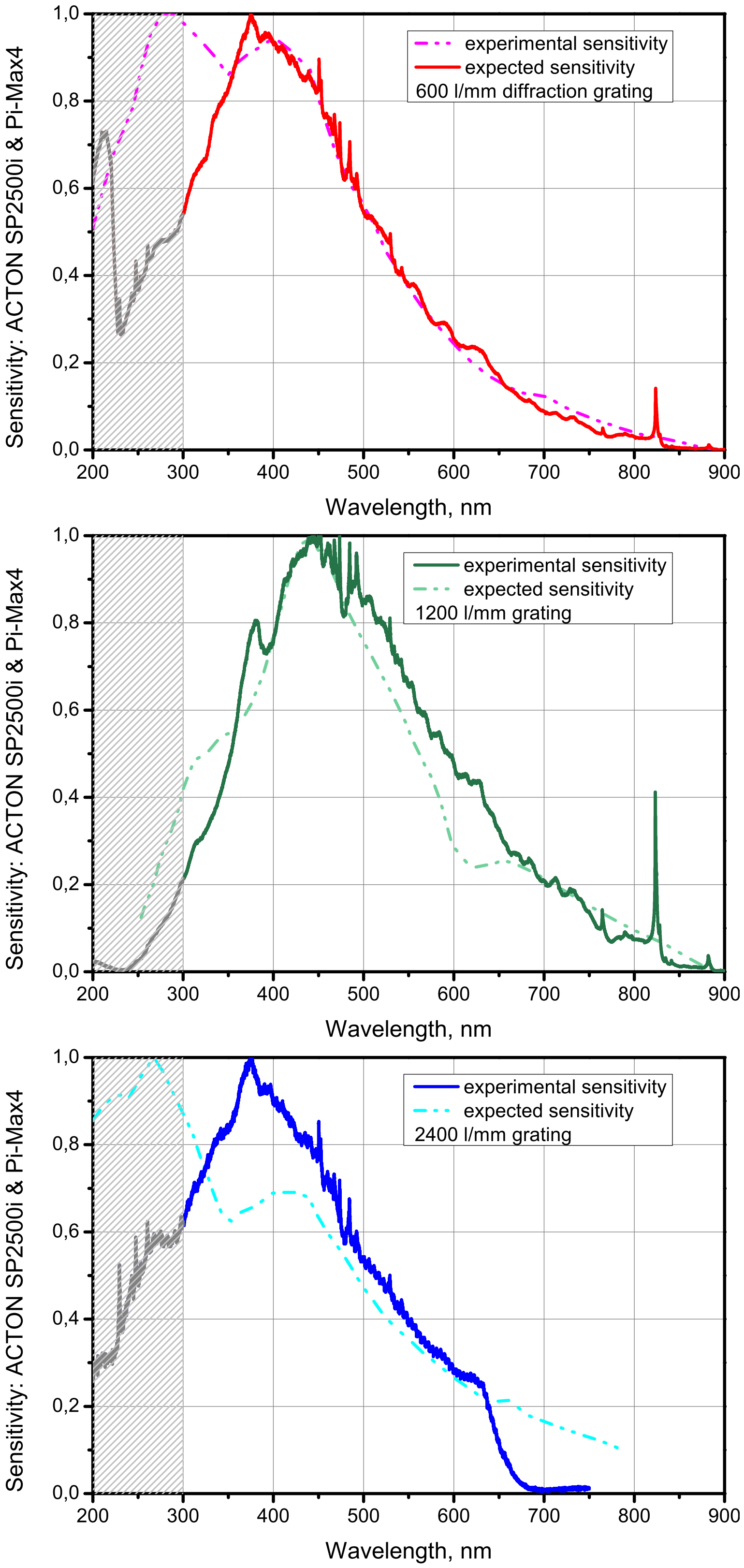

Figure 3.16 – Experimentally reconstituted sensitivity *versus* expected sensitivity of Princeton camera-spectrometer pair for (a) 600 l/mm, (b) 1200 l/mm, (c) 2400 l/mm diffraction gratings. For grey areas and peak at 824 nm at (a, b) see text.

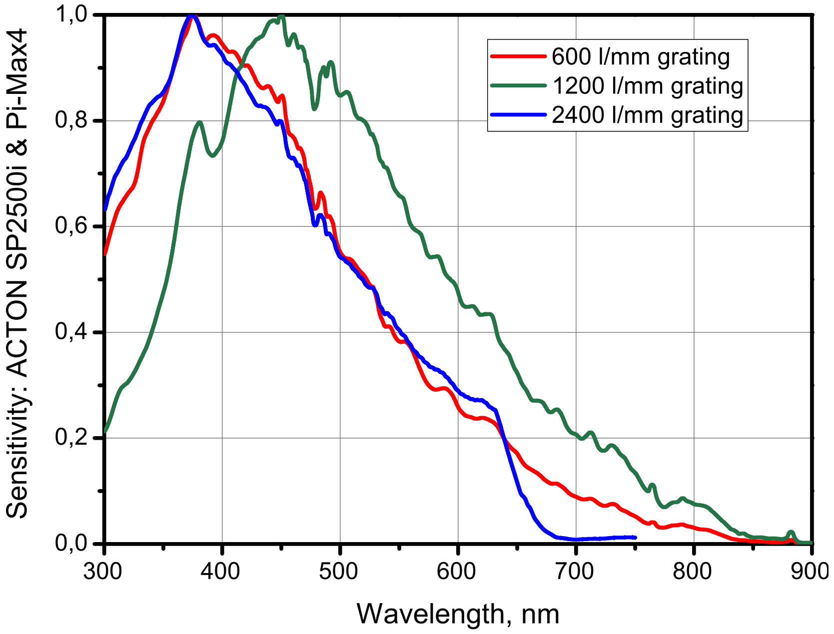

Figure 3.17 – Established calibrated sensitivity curves of Princeton camera-spectrometer pair for 600 **l/mm,** 1200 **l/mm and** 2400 **l/mm diffraction gratings, obtained using ISTEQ XWS-65 light source.**

the sampling step of provided spectral output power of the ISTEQ XWS-65 lamp.

Contemplating the considerations listed above, it is further considered that the camera-spectrometer pair have been calibrated for all three available diffraction gratings with sensitivity curves shown at Figure 3.17.

3.3 Methods applied in the work

3.3.1 Electric field induced second harmonic generation (E-FISH)

The longitudinal electric field in the front of fast ionization wave initiated in nanosecond tube discharge was measured by electric field induced second harmonic generation technique in the approximation of plane wave.

The ability of the media (solid, liquid, gas, plasma) to generate second harmonic is strictly linked to its $\chi^{(3)}_{ijkl}$ third order non-linear hyperpolarizability, a material-dependent 4^{th} order polarizability tensor. The second harmonic light is generated during propagation of a collimated laser beam of fundamental frequency ω and electric field $E^{(\omega)}$ along z axis in the media with N number density in an electric field E_{ext} (external with respect to the field of the laser beam). Second harmonic is a coherent light that propagates along the fundamental laser beam, and a disperse prism can be used to spatially separate the second harmonic light from the laser fundamental. Under conditions described above, the intensity of second harmonic can be expressed as:

$$I_i^{(2\omega)} \propto \left(\chi_{ijkl}^{(3)} \cdot N \cdot (E_{ext})_j \cdot E_k^{(\omega)} E_l^{(\omega)}\right)^2 \left|\int_{-L}^{L} e^{i\cdot\Delta kz} dz\right|^2 = \tag{3.1}$$

$$= \left(\chi_{ijkl}^{(3)} \cdot N \cdot (E_{ext})_j \cdot E_k^{(\omega)} E_l^{(\omega)} \cdot \frac{2 \cdot sin(\Delta k \cdot L)}{\Delta k}\right)^2 \tag{3.2}$$

where Δk is the difference between the fundamental and second harmonic wave vectors, wave vector mismatch, and $2L$ is the region of presence of E_{ext}. The Δk-containing term accounts for the interference of second harmonic signal generated along the laser beam. For a collimated laser beam, the distance $2L$ effectively defines the spatial resolution of the technique, or region of overlap between E_{ext} and $E^{(\omega)}$. This expression is valid if the second harmonic conversion is weak and there is no depletion of probe beam and the laser beam intensity can be presumed constant throughout the interaction.

The $I_i^{(2\omega)}$ expression of plane wave approximation is frequently applied to focused Gaussian laser beams as well. Since second harmonic generation process depends quadratically on the laser intensity, it is presumed that the dominant contribution to the second harmonic signal would be produced from the close focal region. In that case, the spatial resolution is often defined as the confocal beam parameter, or twice the Rayleigh range, $2z_R$, of the beam. More accurate mathematical expression of $I_i^{(2\omega)}$ for Gaussian fundamental laser beam would require accounting (i) to the phase variation within the focused beam and (ii) to an additional interference of second harmonic signal because of its Gaussian profile.

3.3.2 Two-photon absorbed laser induced fluorescence (TALIF)

Two-photon absorbed laser induced fluorescence technique was applied for time-resolved N-atom absolute number density measurements in nanosecond capillary and tube discharges in rate equation regime, also called "linear regime".

This approach is applicable if laser electric field is considered as a small perturbation compared to electric field within the system of interest, atom. In this case, the laser stimulated transitions from ground state g to upper fluorescent state u do not deplete the ground state. This means that the number of transitions $g \rightarrow u$ holds (i) linear relation with respect to g state population and (ii) quadratic relation with respect to laser photon energy due to two-photon absorption process. The upper fluorescent state u performs an allowed optical transition to the lower fluorescence state l and this fluorescence is tracked during experiment by photomultiplier tube and is further used for g state number density computation.

Other processes apart from the tracked transition that happen to u state are considered as losses and have to be accounted. The u state can have optical transitions to other states than l or be quenched by surrounding species, usually by bath gas molecules or self-quenched. Both processes can be taken into account by a certain scaling factor (optical branching ratio and quenching rate). The absolute number density of the specie of interest is concluded from comparison of fluorescence signals with a noble gas of a know number density with spectrally close two-photon transition. Other processes such as ionization or cascading are not included in the applied approach.

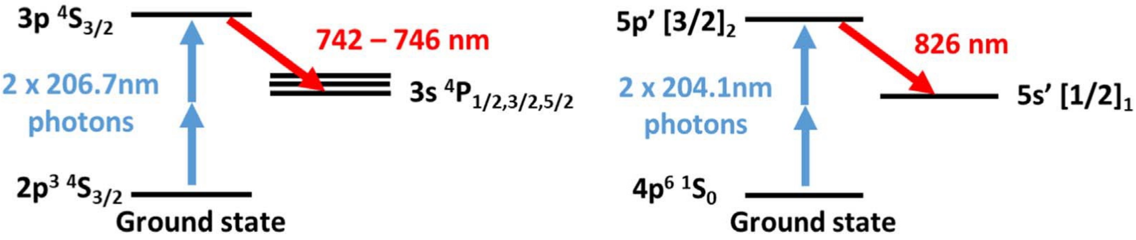

(a) (b)

Figure 3.18 – Two photon excitation scheme (taken from [128]) used for (a) atomic nitrogen and (b) krypton.

The N and Kr TALIF schemes used are shown in Figure 3.18 and are taken from [128]. The two-photon N(3p $^4S_{3/2}$) resonance is accessed *via* a pair of 206.7 nm photons and subsequently fluoresces to three different fine structure levels, emitting light respectively at 742.6 nm, 744.4 nm and 747.0 nm [154]. To obtain quantitative atomic nitrogen number densities, signal calibration is performed against a noble gas, Kr, which has a spectrally close two-photon resonance at 204.1 nm from the Kr(4p^6 $^1S_0$) ground state to the Kr(5p' [3/2]$_2$) resonance. This population subsequently relaxes to the Kr(5s' [1/2]$_1$) state accompanied by the emission of 826 nm light. Given that only the 826 nm fluorescence from the Kr(5p' [3/2]$_2$) excited state is monitored, the optical branching ratio is thus less than unity, and is assigned a value of 0.962 based on an average of the values in [128, 154].

The choice of Kr as a calibration gas is advantageous since it has a two-photon resonance close to that of N. However, Kr fluorescence does not exhibit similarly good overlap with N fluorescence. Therefore, transmission efficiencies of the various components within the light collection system at these different fluorescent wavelengths must be accounted for. Following [128], the time and spectrally integrated fluorescence S of two gases may be written respectively as:

$$S_{\mathrm{N}} = \Gamma_{\mathrm{N}} \cdot n_{\mathrm{N}} \cdot \sigma_{\mathrm{N}} \cdot \left(\frac{I_{\mathrm{L}}}{h\nu}\right)^2_{\mathrm{N}} \cdot \frac{A_{\mathrm{N}}}{A_{\mathrm{N}} + Q_{\mathrm{N}}} \cdot F_{\mathrm{N}} \cdot (\mathrm{PMT})_{\mathrm{N}} \tag{3.3}$$

$$S_{\mathrm{Kr}} = \Gamma_{\mathrm{Kr}} \cdot n_{\mathrm{Kr}} \cdot \sigma_{\mathrm{Kr}} \cdot \left(\frac{I_{\mathrm{L}}}{h\nu}\right)^2_{\mathrm{Kr}} \cdot \frac{a_{\mathrm{Kr}}}{A_{\mathrm{Kr}}} \cdot \frac{A_{\mathrm{Kr}}}{A_{\mathrm{Kr}} + Q_{\mathrm{Kr}}} \cdot F_{\mathrm{Kr}} \cdot (\mathrm{PMT})_{\mathrm{Kr}} \tag{3.4}$$

where Γ represents the two-photon statistical factor at a relevant laser wavelength, n is the number density, σ is the two-photon absorption cross-section, I_{L} is the laser intensity, h is the Planck constant, ν is the laser frequency, a is the natural radiative rate for a specific observed fluorescence transition, A and Q are the natural radiative and quenching rates of the two photon excited state while F and (PMT) represent the transmission efficiencies of the filters and photomultiplier at the respective fluorescent wavelengths, respectively. Rearranging terms in (3.3) and (3.4), one arrives at the following expression for n_{N}, the number density of N-atoms:

$$n_{\mathrm{N}} = \frac{\sigma_{\mathrm{Kr}}}{\sigma_{\mathrm{N}}} \left(\frac{\nu_{\mathrm{N}}}{\nu_{\mathrm{Kr}}}\right)^2 \frac{\mathrm{PMT}_{\mathrm{Kr}}}{\mathrm{PMT}_{\mathrm{N}}} \frac{a_{\mathrm{Kr}}}{A_{\mathrm{Kr}}} \cdot \frac{A_{\mathrm{Kr}}}{A_{\mathrm{N}}} \frac{F_{\mathrm{Kr}}}{F_{\mathrm{N}}} \frac{A_{\mathrm{N}} + Q_{\mathrm{N}}}{A_{\mathrm{Kr}} + Q_{\mathrm{Kr}}} \cdot \left(\frac{I_{\mathrm{L,Kr}}}{I_{\mathrm{L,N}}}\right)^2 \frac{S_{\mathrm{N}}}{S_{\mathrm{Kr}}} n_{\mathrm{Kr}} \tag{3.5}$$

Given that both the N and Kr resonances lie within close spectral proximity, it is assumed that their respective photon statistical factors are invariant within this wavelength range and therefore cancel out. The various parameters on the right hand side of n_{N} expression in (3.5) have been grouped as follows: the first four terms represents quantities or ratios which have not been measured in this study but referenced from the literature or operating manuals, the next three terms contain parameters which have been measured in this work but are also available in the literature, while the remaining terms consist of only measured quantities.

N-atom related characteristic time scales

This sub-section lists six characteristic time scales of the processes that play role in N-atom temporal evolution in view of further interpretation of TALIF data.

First, the laser and high voltage repetition rate of 10 Hz gives the τ_{rep} time between two consecutive laser or high voltage pulses:

$$\tau_{\mathrm{rep}} = \frac{1}{10\ \mathrm{Hz}} = 100\ \mathrm{ms} \tag{3.6}$$

Second, the gas renewal time τ_{gas} can be obtained as a ratio of discharge tube's volume V to volumic flow through the tube v. The expression written for volumic flow v expressed in standardized units is by definition independent from pressure and temperature conditions in the discharge tube. The actual volumic flow v expressed in cm^3/min at P and T conditions of the discharge tube can be obtained by multiplying v expressed in sccm by P_0T/PT_0 factor where P_0 and T_0 are standard conditions:

$$\tau_{\text{gas}} = \frac{V}{v, \text{sccm}} = \frac{V}{v, \text{cm}^3/\text{min}} \cdot \frac{T_0}{T}\frac{P}{P_0} \tag{3.7}$$

Third, acoustic timescale which is a typical travel time τ_{ac} of the sound wave from the point of sound creation to the measurement location. In fluids (gases or liquids) the longitudinal sound wave is the only possible type of the sound wave. Its velocity can be estimated as $\sqrt{\gamma RT/M}$ where γ is the adiabatic coefficient of the media, R is the gas constant, T is media's temperature and M is the media's molar mass. For the case of pure N_2, $\gamma_{N_2} = 1.470$, $M_{N_2} = 28.0 \cdot 10^{-3}$ kg/mol [155]. It is presumed that the tip of the high voltage electrode during discharge initiation and development can be a source of acoustic waves. Accordingly, the acoustic timescale may be expressed as a ratio of half of inter-electrode distance L to wave's velocity:

$$\tau_{\text{ac}} = \frac{L/2}{\sqrt{\gamma RT/M}} \tag{3.8}$$

Fourth, gas expansion due to the local heating. Typical cooling time τ_{heat} with the wall based on thermal diffusion can be expressed with temperature-dependent thermal heat conductivity $\lambda(T)$, gas isochoric specific heat capacity C_V, the gas density ρ and the radius of the tube, r:

$$\tau_{\text{heat}} = \frac{\rho \cdot C_V}{\lambda(T)} \left(\frac{r}{2.4}\right)^2 \tag{3.9}$$

Fifth, N-atom radial diffusion. Electron impact reactions during the voltage pulse may produce N-atoms directly from dissociation of N_2 or *via* excitation to pre-dissociative states. Keeping in mind the link between initial electron number density distribution and plasma emission at uniform field, an assumption can be done concerning the link between the plasma emission and N-atom produced during the voltage pulse [151]. Plasma emission in N_2-containing mixtures is usually of a parietal structure [151]. The $\tau_{diff_{\text{N}}}$ time scale represents the N-atom diffusion from the near-wall radial position to the axis of the tube and is expressed as a function of the mass diffusion coefficient of N(^{4}S) in pure N_2, D_{N}, and the tube radius, R:

$$\tau_{diff_{\text{N}}} = \frac{1}{D_{\text{N}}} \cdot \left(\frac{r}{2.4}\right)^2 \tag{3.10}$$

Sixth, heterogeneous recombination of N(^{4}S) at quartz walls expressed as a function of the coefficient of heterogeneous recombination of atomic nitrogen on the wall of the capillary tube γ_{N}, the thermal velocity u and the N-atom diffusion time $\tau_{diff_{\text{N}}}$:

$$\tau_{\text{het}} = \frac{2}{\gamma_{\text{N}}}\frac{r}{u} + \tau_{diff_{\text{N}}} \tag{3.11}$$

Chapter 4

O-atom number density measurements in nanosecond capillary discharge (nCD) by optical actinometry technique

Recent two-photon absorption laser-induced fluorescence (TALIF) measurements in nCD in air [129] at $24-30$ mbar with specific deposited energy value of about 1 eV/molecule had shown the progressively increase in oxygen density, approaching practically complete dissociation at about 2 μs after the first pulse. Gas temperature in the capillary reached $1500-2500$ K at the time scale $1-2$ μs, confirming a significant role of the fast gas heating due to the energy release from electronically excited species [136]. Time-resolved optical emission spectroscopy of the second positive system of N_2 in nCD at similar parameters in pure N_2 coupled with modeling efforts revealed that starting from deposited energies of about 0.1 eV/molecule, the $N_2(C^3\Pi_u)$ state is additionally quenched by electrons, and the effective lifetime of the $N_2(C^3\Pi_u)$ state depends on specific deposited energy [44]. The high electron density in the afterglow in [44] is sustained by associative ionization *via* $N_2(A^3\Sigma_u^+)$ and $N_2(a^{'}\Sigma_u^-)$ electronically excited molecules.

Classical actinometric kinetic scheme contains only electron impact excitation and radiative decay and neglects every other process such as quenching, dissociation, stepwise excitation, cascading, excitation transfer *et cetera*. However, the idea of using an inert admixture to the gas as a reference for determining an unknown specie's number density can be used even in case of more rich kinetic scheme. The studies [44,129,136] illustrated that in case of high specific deposited energy, plasma kinetics is dominated by collisions between excited species that are negligible at low specific deposited energies. The aim of the present work is to test the limits of classical O-atoms actinometry is under conditions typical for short pulsed discharges with high specific deposited energy.

The chapter contains experimental measurements required for application of actinometry technique to $O(^3P)$ atom number density measurements in N_2:O_2 nanosecond capillary discharge with $Ar(2p_1)$ as actinometric specie. Two self-consistent experimental data sets were taken for 0.5 and 1 eV/molecule conditions of specific deposited energy. The number density of O(^{3}P) ground state was reconstructed using the adapted actinometric kinetic scheme developed by Dr. Y Zhu and described in greater detail in his PhD thesis [156]. Chapter focuses mainly on the manuscript author's contribution, namely experimentally measured nCD discharge parameters and actinometric optical transitions, O(3p^{3}P$_{1,2,0}$) → O(3s^{3}S$_1$) at $\lambda_{\mathrm{O}} = 844.6$ nm or Ar(2p$_1$) → Ar(1s$_2$) at $\lambda_{\mathrm{Ar}} = 750.4$ nm. This chapter's content was partially published in [157].

4.1 Development and validation of actinometric kinetic scheme

0D model ran by ZDPlaskin code was specifically developed to study the temporal evolution of N$_2$(C$^3\Pi_u$), O(3p^{3}P) and Ar(2p$_1$) species of N$_2$:O$_2$:Ar mixture during the quasi-steady-state discharge in nCD in high specific energy deposition case. The key points of the study were (i) to investigate the main processes in nanosecond pulsed discharges at high specific energy deposition and (ii) to respectively adjust the actinometric expression used to calculate the ground state number density of the O(3p^{3}P), the specie of interest.

Governing equations of the fluid model

The plasma was described in terms of fluid approach built on 0^{th} (continuity equation) and 2^{nd} (energy conservation equation) moments of Boltzmann equation with non-zero collisional term. The 1^{st} moment (momentum balance equation) was rewritten in terms of drift diffusion approximation (DDA) and thereby replaced by provided closure relations for the truncation at 2^{nd} moment: particle and energy flux expressions. Transport coefficients and rate coefficients that appear in particle and energy flux expressions are EEDF-dependent coefficients.

Drift diffusion approximation

Physical meaning of DDA is that the collisional contribution (*id est* of chemical reactions) to diffusion is dominant compared to other processes such as ionization, particle flow due to external electric field or diffusion because of pressure gradient. These conditions are realized in a low ionization degree plasma whose behavior is defined locally (absence of nonlocalities, isotropic pressure expressed as $p = nkT$). DDA's applicability was approved with the help of BOLSIG+ code based on two-term approximation of Boltzmann electron equation. DDA is valid for reduced electric fields E/N below 2 kTd at pressures above few mbar.

2D nonPDPsim model

nonPDPsim is a developed by the group of Prof. Mark Kushner [158] 2D plasma hydrodynamics model that solves Poisson's and radiation transport equations in an automatically simulated and meshed 2D area. The 2D rectangular-like area accurately replicates the longitudinal section of nCD including electrode system except the absent side flow arms. Boundary conditions were assigned according to equations and materials. For transport equations, a flux boundary condition account for surface interaction (adsorption and desorption). The initial electron density was set to be uniformly distributed in the capillary with the value of 10^9 cm^{-3}. Initial plasma spot of Gaussian profile is located at the tip of HV electrode with electron density distributed according to the electric field. The source term of photoionization is accounted for using a propagator method of VUV photon emission.

0D ZDPlaskin model

Due to the high value of time required for a single simulation in 2D nonPDPsim, less time-consuming 0D ZDPlaskin [159] simulation was developed. 0D approach is valid in case of a uniform discharge which seems to be rather realistic assumption for nCD [151]. In ZDPlaskin, the source function includes gain and loss terms due to gas phase reactions (neutral chemistry, ion-molecule reactions and electron impact processes) and contributions associated with wall chemistry including electron emission from surfaces. Electric field and initial electron density are considered as input parameters. The latter is calculated from initial electric field using BOLSIG+ calculated electron mobility.

0D ZDPlaskin vs 2D nonPDPsim

Apart from different computation time and dimension, nonPDPsim and ZDPlaskin use different approaches to calculate collision frequency and reaction rate coefficients. Local mean energy approach used in nonPDPsim is a better method for nCD simulation than local electric field approximation used in ZDPlaskin because the experimental electric field is more susceptible to EM noise compared to experimental specific deposited energy. Overall, the 2D nonPDPsim model's simulations were used as benchmark cases for 0D ZDPlaskin.

Selection of electron impact reactions

Since the electron energy distribution function (EEDF) defines plasma behaviour, its correct definition is a primary task in quantitative gas chemistry simulations. The reactions responsible for EEDF formation should include all electron-related processes. nonPDPsim's incorporated kinetic module originally contains about 70 atomic and molecular species containing N and/or O in around a few hundred of electron impact reactions (elastic collisions, momentum transfer collisions, electronic, vibrational and rotational excitation, recombination, attachment, ionization). It was exposed to two modifications in order to correspond better to specific condition of high deposited energy. First, cross sections of electron impact excitation of N_2(v=0-8), $N_2(A^3\Sigma_u^+)$, $N_2(B^3\Pi_g)$, $N_2(W^3\Delta_u)$, $N_2(B'^3\Sigma_u^-)$, $N_2(a^1\Pi_g)$, $N_2(a'^1\Sigma_u^-)$, $N_2(W^1\Delta_u)$, $N_2(C^3\Pi_u)$, $N_2(E^3\Sigma_g^+)$, N_2(sum) and O_2(4.5 eV) states were updated based on Phelps [22]. Second, $e + N_2(B) \rightarrow e + N_2(C)$ reaction and it's reverse reaction, $e + N_2(C) \rightarrow e + N_2(B)$ were added with cross sections from [160].

Validation of electron impact cross sections against swarm parameters

The cross sections of electron-impact reactions of modified nonPDPsim's kinetic module were used for calculations by both 0D and 2D models of experimentally accessible swarm parameters: ionization rate and electron drift velocity. The EEDF was calculated by BOLSIG+ for ZDPlaskin and by proper intrinsic module for nonPDPsim. The ratio of obtained swarm parameters was validated against the experimentally measured one in N_2 and air, as shown on Figure 4.1 [156]. Thereby the selected set of cross sections is considered to be self-consisting for EEDF recreation.

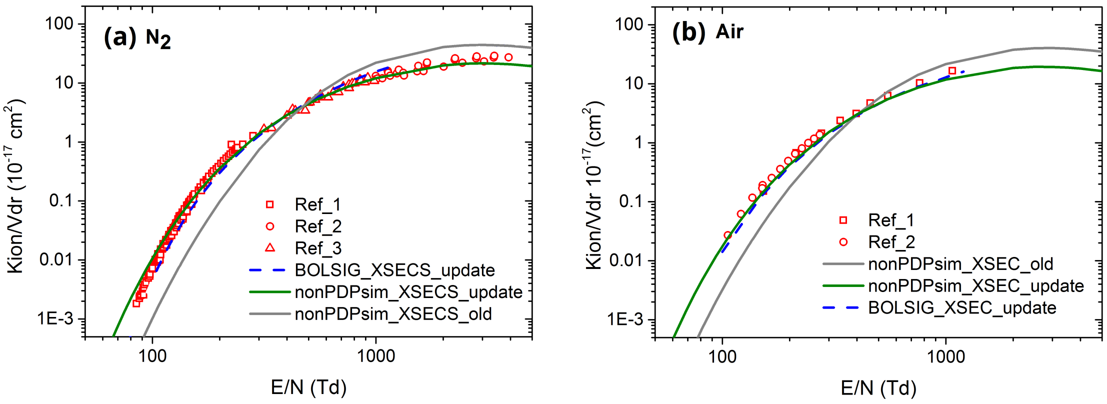

Figure 4.1 – Validation of updated cross section data sets in (a) pure N2 and (b) air by swarm parameters (ionization rate and electron drift velocity) comparison. Solid lines show nonPDPsim calculations with default cross sections (in grey) and with updated sets (in olive). Dashed lines are results from BOLSIG+ with updated sets. Experimental scatters in (a) are from [161–163], in (b) are from [164, 165]. Taken from [156].

Full actinometric kinetic scheme

A well-known and validated kinetic scheme [166] suggested by Flitti and Pancheshnyi for N_2:O_2 mixtures, based on air kinetics of Kossyi [115] and Cappitelli [167], was taken as a basis. The presence of Ar was accounted by a minimum necessary number of reactions including Ar, Ar^+, $Ar(2p^1)$, $Ar(1s^2)$ species as well as one

Ar(11.55 eV) specie for both metastable Ar($1s^3$) and Ar($1s^5$) levels together. The reactions included those for Ar($2p^1$) used in traditional actinometry analysis and supplementary reactions, important for Ar($2p^1$), O($3p^3P$) and $N_2(C^3\Pi_u)$ states at typical conditions of nCD. Electron impact reactions used for EEDF calculation with validated cross sections were included as well. For electron collisions with N_2, O_2 and Ar, the self-consistent sets of cross sections [22], [168] and [169] respectively were used. Quenching by electrons was concluded to be negligible for O($3p^3P$). Overall, the full actinometric kinetic scheme contains about 700 reactions between over 60 species.

Validation of 2D model against experimentally measured nCD data

Reduced electric field E/N, electron density n_e and N_2(C) decay profile were calculated by nonPDPsim at the center of the modelled tube. Calculated axial E/N shows a good qualitative reproduction of all three stages of development of the discharge in nCD. Quantitatively, the peak value of the calculated FIW is however higher than the CP measured value. The possible reasons for the observed discrepancy probably are (i) the improved spatio-temporal resolution of the calculations compared to such of CP and (ii) different location of the measurement point. The axial potential field calculated by nonPDPsim from CP's position was validated compared to experimental data [170] including FIW's front velocity value reproduction. The N_2(C) decay profile accurately reproduces such an abnormally fast decay observed previously in nCD experiment in N_2 [44].

Validation of 0D model against 2D

Calculated by nonPDPsim profiles of E/N and n_e were used as input parameters for 0D ZDPlaskin. The ZDPlaskin calculated N_2(C) decay profile accurately reproduces such of nonPDPsim that shows the validity of 0D approach.

Sensitivity analysis and reduced actinometric kinetic scheme

Once the full actinometric kinetic scheme was validated, it was reduced to the most important reactions using a specifically developed separate module of sensitivity analysis. For each reaction, reaction rate was varied by a factor of 1.5. If the following percentage change in Ar($2p^1$), O($3p^3P$) or $N_2(C^3\Pi_u)$ species number density was above 10%, the reaction was considered as important for the reduced kinetic actinometry scheme. The established scheme [157] comprises 47 reactions between 22 species. Due to computational time limitations, nonPDPsim was ran only with the reduced actinometric kinetic scheme.

Limitations of the models

The current model does not account for gas heating nor for temperature gradient induced hydrodynamic motion of neutrals. These processes were omitted as such that would not become dominant in ns-timescale of studied quasi-steady-state discharge. In addition, the values of photo-ionization, absorption cross section and absorption length are rather roughly estimated based on available nCD experimental data. Still they are considered reliable for the studied quasi-steady-state discharge case because (i) nCD operational conditions were held the same as during validation and (ii) the processes mentioned above are not considered to be important.

4.2 Simultaneous three angle observed emission spectroscopy experiment

Gas flow was composed of 50.3 sccm of synthetic air (impurity below 3.5 ppm) and of 2.1 sccm of Ar (impurity below 1 ppm) mixed $\approx$ 3 m prior to enter nCD setup. Thereby Ar admixture to the air flow was on the level of 5.3%. Gas pressure in the middle of the capillary was kept at the value of 28.5 mbar. Voltage pulse was kept at its maximum amplitude of 9.3 kV. Two cases of specific deposited energy, 0.5 eV/molecule and 1 eV/molecule, obtained in nCD of inter-electrode gap of 70 mm and 55 mm, respectively, were studied. For each case, 10 Hz repetition frequency of the discharge pulses ensured full gas renewal before the arrival of the next pulse.

The experimental setup for actinometry technique at nCD is presented in Figure 4.2. Plasma at the center of the capillary was viewed in the direction perpendicular to the tube axis from three different observation angles - two side views and one bottom view. For each view, plasma emission was collected by Thorlabs LB1471-B bi-convex lens, then focused on entrance of the PMT or on entrance slit of a spectrometer and finally guided to a detector.

The following pairs of spectrometer-detector were used: ANDOR Shamrock 303i spectrometer with mounted Hamamatsu H7422-50 photomultiplier tube and Princeton Instruments ACTON SP-2500i spectrometer with mounted Princeton Instruments Pi-Max4 ICCD camera. Both spectrometer input slits were set to 150 μm. The output slit of ANDOR spectrometer that preceded PMT's entrance was set to 50 μm. Used diffraction gratings were 1200 l/mm with blaze at 500 nm. Thorlabs FEL0500 filter was placed before ANDOR spectrometer input slit while colored glass filter (Electrosteklo Orange Glass #14) was placed before ACTON spectrometer input slit to block the second order of diffraction grating. The first spectrometer-detector pair was used to track the waveform of one of the actinometric optical transitions, $\mathrm{O(3p^3P_{1,2,0})} \rightarrow \mathrm{O(3s^3S_1)}$ at $\lambda_\mathrm{O} = 844.6$ nm or $\mathrm{Ar(2p_1)} \rightarrow \mathrm{Ar(1s_2)}$ at $\lambda_\mathrm{Ar} = 750.4$ nm, while the second pair served to verify emission's spectral composition in proximity of the tracked transition.

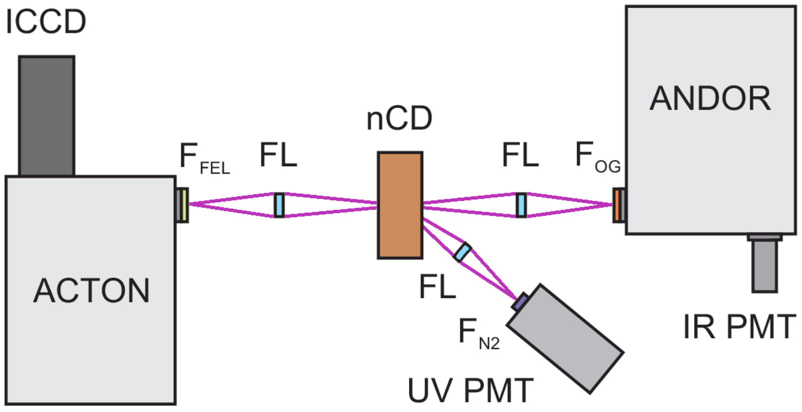

(a) Top view

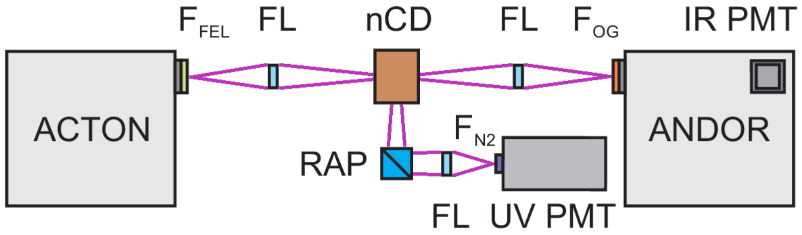

(b) Side view

Figure 4.2 – Scheme of actinometry experiment setup. ICCD: Pi-Max4 ICCD camera; UV PMT - Hamamatsu H6610 photomultiplier tube; IR PMT - Hamamatsu H7422-50 photomultiplier tube; ACTON - Princeton Instruments ACTON SP-2500i spectrometer; ANDOR - ANDOR Shamrock 303i spectrometer; F_{FEL} - Thorlabs FEL0500 filter; F_{OG} - Elektrosteklo Orange Glass #14 filter; F_{N_2} - Thorlabs FB340-10 filter; FL - Thorlabs LB1471-B bi-convex lens; RAP - right angle prism.

The spectral overlap of each actinometric transition with other atomic lines or molecular systems was studied in two ways: (i) in time-resolved mode with camera gate equal to 2 ns and variable time delay with respect to the discharge and (ii) in time-integrated mode with camera gate of 70 ns from the beginning of the incident pulse. The number of frame accumulations varied from 10 to 50. No spectral overlap was observed for either of transitions. It becomes clear however that λ_{Ar} transition is located close to one of the rotational transitions within $(4-2)$ vibrational band of the first positive system (FPS) of N_2 ($N_2(B^3\Pi_g, v''=4) \rightarrow N_2(A^3\Sigma_u^+, v''=2)$). Both these transitions would be captured by PMT when spectrometer is tuned to λ_{Ar}. Since these transitions are independent, N_2 FPS contribution to λ_{Ar}-close PMT signal can be considered as an ofsset and subtracted. It was thus measured separately from the plasma emission of an Ar-less gas mixture with N_2:O_2 flow and thus partial pressure conditions unchanged. Finally, the waveform of $\mathrm{Ar}(2p_1) \rightarrow \mathrm{Ar}(1s_2)$ transition was deduced as a difference between the PMT-captured waveforms of plasma emission at λ_{Ar} proximity in the gas mixture with and without Ar.

Emission collected from the bottom view was reflected by right angle prism and sent onto the entrance of Hamamatsu H6610 photomultiplier tube. This PMT was used to track the waveform of the strongest optical transition of the second positive system (SPS) of N_2, $\mathrm{N_2(C^3\Pi_u, v' = 0) \rightarrow N_2(B^3\Pi_g, v'' = 0)}$ at $\lambda_{\mathrm{N_2}} = 337.1$ nm. Thorlabs FB340-10 bandpass filter was mounted before PMT's entrance to isolate the transition.

For each photomultiplier tube waveform or camera frame, the non-optical noise was acquired under the same conditions as the signal but with blocked optical input and further subtracted. The origin of non-optical noise is believed to be equipment's thermal noise and EM noise from the discharge. The obtained waveforms of the actinometric transitions were corrected for wavelength-dependent sensitivity of each optical element used during the acquisition, namely, lenses, filters, right angle prism, spectrometer's diffractional grating and reflective mirrors and PMT.

4.3 Measured plasma parameters and actinometric waveforms

Figure 4.3 shows synchronized in time experimentally measured (a) reduced electric field and transmitted current, (b) deposited power and specific deposited energy, (c) sensitivity corrected waveforms of actinometric transitions normalized to the maximum of $\mathrm{O(3p^3P)}$ emission and (d) decay of $\mathrm{N_2(C)}$ emission profile for 1 eV/molecule specific deposited energy case. Figure 4.3(a) also presents reduced electric field as interpreted by ZDPlaskin and calculated transmitted current that shows good agreement with measured one. The maximum of energy is deposited to the plasma in period of $10 < t < 25$ ns when the inter-electrode gap is already closed and the electric field has not yet dropped to zero.

Figure 4.4 shows normalized densities of (a) $\mathrm{Ar(2p_1)}$, (b) $\mathrm{N_2}(\mathrm{C}^3\Pi_u)$, (c) $\mathrm{O(3p^3P)}$ and (d) ratio of $\mathrm{Ar(2p_1)}$ and $\mathrm{O(3p^3P)}$ number densities calculated by full and reduced actinometric kinetic schemes in comparison with appropriate normalized experimental emission waveform. Both schemes reproduce the production and loss of $\mathrm{Ar(2p_1)}$ and $\mathrm{N_2}(\mathrm{C}^3\Pi_u)$ reasonably well. The discrepancy between full and reduced description does not exceed $10 - 15\%$ for $\mathrm{Ar(2p_1)}$ and $3 - 5\%$ for $\mathrm{N_2}(\mathrm{C}^3\Pi_u)$ at times after 40 ns. For $\mathrm{O(3p^3P)}$, both schemes give the same result at times before 40 ns. Since then schemes' $\mathrm{O(3p^3P)}$ number density calculations diverge progressively leading to a difference of a factor 2 at the end of the calculation time. It should be noted

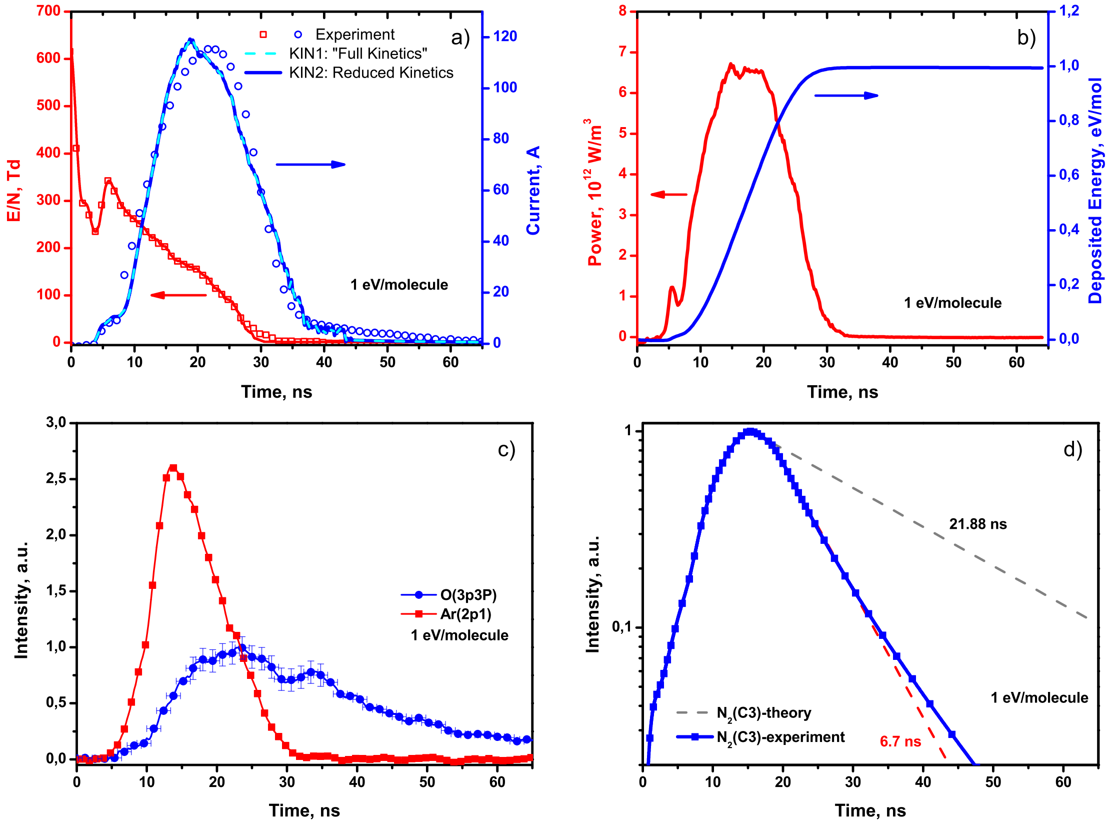

Figure 4.3 – Main experimental results for 1 eV/molecule specific deposited energy case: (a) longitudinal reduced electric field, E/N, in the center of the inter-electrode gap and electric current I_{tr} transmitted through discharge tube; (b) specific deposited energy, ω, and power, P, deposited into the plasma; (c) relative O-atoms emission ($\lambda_{\mathrm{O}} = 844.6$ nm) and Ar emission ($\lambda_{\mathrm{Ar}} = 750.4$ nm) curves, the maximum of the emission of O-atoms is taken to be unity; (d) optical emission of N$_2$ ($\lambda_{\mathrm{N_2}} = 337.1$ nm) superimposed with a theoretical decay curve from [171].

that the experimental data on O(3p^{3}P) emission is the noisiest one among acquired optical signals. Its signal-to-noise ratio is of about 10 because the spectral systems' sensitivity significantly decreases in the near-IR region. In spite of the noise, a dip of the O(3p^{3}P) experimental emission waveform is resolved at 30 ns. At this time, longitudinal electric field drops to the values below detection limit and electric current is at its mid-decay. Similar dip but $3 - 4$ times more profound is observed from calculations. Better near-IR spectral sensitivity of PMT in the present study compared to ICCD camera used in [51] allowed to confirm the presence of O(3p^{3}P) emission tail in the early afterglow.

The ratio of experimentally measured Ar(2p$_1$) and O(3p^{3}P) number densities shown on Figure 4.4(d) was obtained in a following manner. The emission intensity

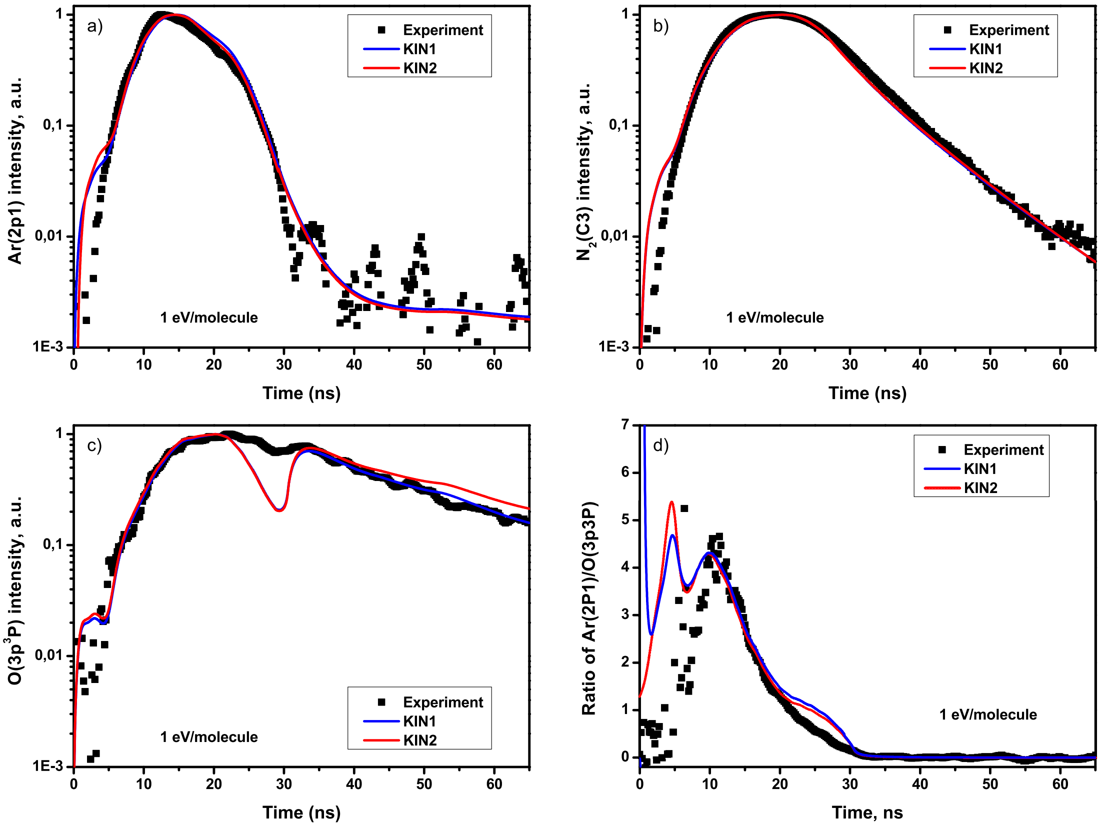

Figure 4.4 – Comparison of the calculated normalized density and the experimentally measured normalized emission intensity for (a) Ar(2p$_1$), (b) N$_2$(C$^3\Pi_u$) and (c) O(3p^{3}P) together with (d) calculated and experimental relative density of Ar(2p$_1$) to O(3p^{3}P) in case of 1 eV/molecule specific deposited energy.

I_X of a transition $i \rightarrow j$ of X^* excited state was expressed by the following formula: $I_X = h\nu_{ij}[X_i^*]A_{ij}$, where $h\nu_{ij}$ is the energy gap between i and j states, $[X_i^*]$ is the number density of the emitting i^{th} state, A_{ij} is the Einstein coefficient for spontaneous emission of observed $i \rightarrow j$ transition. Then, the ratio of Ar(2p$_1$) and O(3p^{3}P) number densities is expressed as

$$\frac{[X^*_{\mathrm{Ar}}]}{[X^*_{\mathrm{O}}]} = \frac{I_{\mathrm{Ar}} \cdot \lambda_{\mathrm{Ar}} \cdot A_{\mathrm{O}}}{I_{\mathrm{O}} \cdot \lambda_{\mathrm{O}} \cdot A_{\mathrm{Ar}}} \tag{4.1}$$

where A_{Ar} and A_{O} are Einstein coefficients for spontaneous emission of Ar and O actinometric transitions, respectively, whose values were taken from [112].

As overall seen from Figures 4.3 and 4.4, the reduced kinetic scheme is capable to reproduce not only the temporal behavior of Ar(2p$_1$), O(3p^{3}P) and N$_2$(C$^3\Pi_u$) emission but the ratio of number densities of Ar(2p$_1$) and O(3p^{3}P) as well.

Figure 4.5 presents the calculated kinetic curves for N$_2$, O$_2$, Ar, O-atoms in

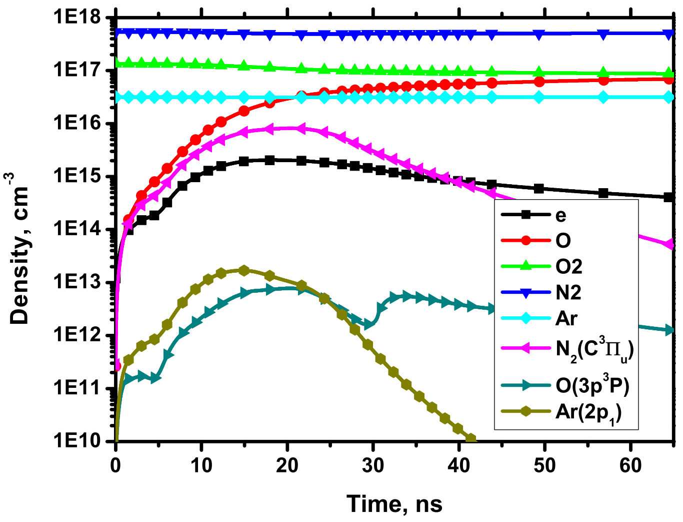

Figure 4.5 – The time evolution of number densities of the calculated main components, namely, electron, O-atoms in the ground state, O_2, N_2, Ar, $N_2(C^3\Pi_u)$, O(3p^{3}P), and Ar(2p$_1$).

the ground state, Ar(2p$_1$), O(3p^{3}P), $N_2(C^3\Pi_u)$, and electron density. The electron number density reaches its maximum value of about $2 \cdot 10^{15}$ cm^3 in about time that corresponds to maximum deposited power. The value is in reasonable correlation with calculations of the FIWs in capillary tubes in air [170] and measurements and calculations of the electron density in capillary discharge in pure nitrogen [44]. Atomic oxygen density reaches $[O] = 3 \cdot 10^{16}$ cm^3 at 20 ns that is almost as big as Ar admixture percentage. In early afterglow, 65 ns after the start of the discharge, $[O] = 7.5 \cdot 10^{16}$ cm^3, which corresponds to 23% dissociation fraction calculated as $[O]/2{\cdot}[O_2]$. The data is in reasonable agreement with nCD O-atom TALIF measurements [129] in air that report the O-atom density increase from $\sim 6 \cdot 10^{16}$ cm^{-3} at 0.2 μs to about $2 \cdot 10^{17}$ cm^{-3} at 2.2 μs. It has to be noted that the peak current value in [129] was about 80 A *versus* 120 A in case of measurements and simulations presented at Figures 4.3, 4.4 and 4.5.

4.4 Rate analysis of experimentally measured species

As stated earlier, rate analysis has been performed to reduced scheme to identify key reactions responsible for production and loss of experimentally monitored Ar(2p$_1$), O(3p^{3}P) and $N_2(C^3\Pi_u)$ species in typical conditions of nCD.

For Ar(2p$_1$), only three reactions (except for radiative decay to Ar(1s$_2$)) schematically shown at Figure 4.6 were found important. During FIW propagation and before establishment of quasi-steady-state discharge, when reduced electric field is

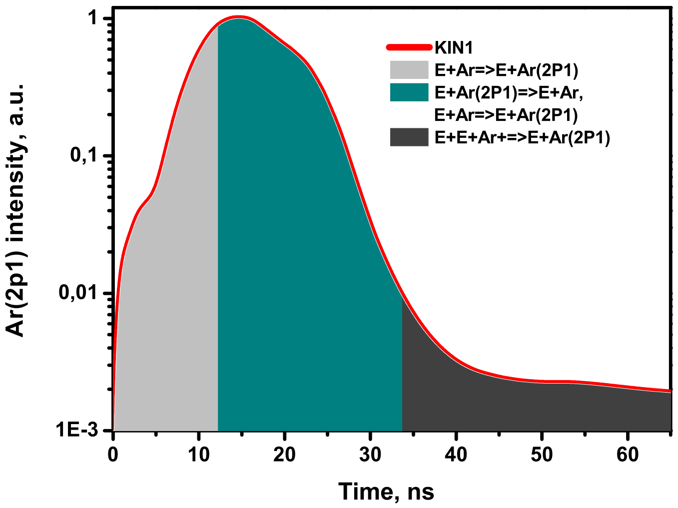

Figure 4.6 – Dominating reactions for production and loss of Ar(2p$_1$).

high and current begins to increase, Ar(2p$_1$) is mainly produced by electron impact excitation of Ar (R16). Then, during the quasi-steady-state discharge, when electric current and electron density are high, electron quenching (R37) becomes important in addition to (R16). Finally, in the afterglow, when external electric field dropped to zero, the tail of Ar(2p$_1$) is caused by 3-body electron-ion recombination (R11) with electron as a third body.

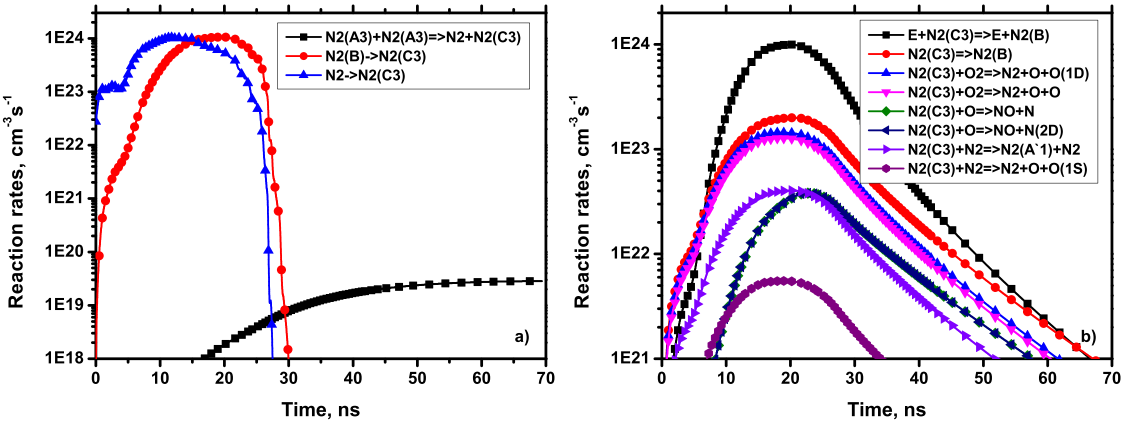

Figure 4.7 – Rates of the main reactions of (a) production and (b) loss of N$_2$(C$^3\Pi_u$).

In case of N$_2$(C$^3\Pi_u$), reaction rates for the most important production and loss reactions are shown on Figure 4.7. Similarly to Ar(2p$_1$), during FIW propagation and before establishment of quasi-steady-state discharge, N$_2$(C$^3\Pi_u$) is mainly produced by electron impact excitation of N$_2$ (R20). During the quasi-steady-state discharge, population by electron impact from N$_2$(B$^3\Pi_g$) (R21) becomes equally important. In the afterglow, population happens *via* pooling reaction between two

$N_2(A^3\Sigma_u^+)$ metastable states. The rate of pooling reaction is four orders of magnitude lower compared to (R20) and (R21) and thus the reaction is not included in the reduced scheme. Decay of $N_2(C^3\Pi_u)$ is caused mostly by quenching in collisions with the electrons to $N_2(B^3\Pi_g)$ state (R45). Three more less pronounced processes contribute to $N_2(C^3\Pi_u)$ decay: radiative decay to $N_2(B^3\Pi_g)$ (R33) and quenching in collisions with molecular oxygen (R41), (R42). It should be noted that the rate of (R33), (R41) and (R42) reactions together is only a few times lower than the rate of reaction (R45). This indicates that the electron quenching will not play a dominant role in $N_2(C^3\Pi_u)$ decay if the electron density is of an order of magnitude lower.

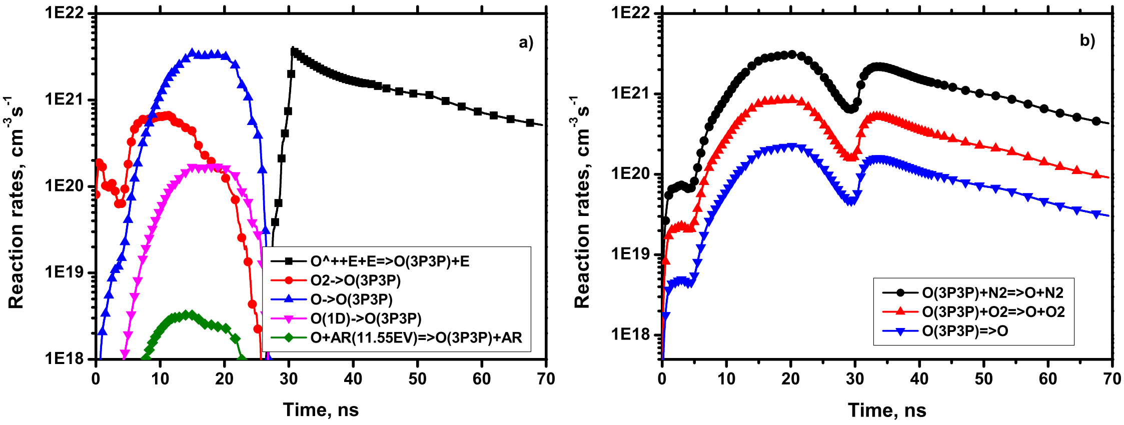

Figure 4.8 – Rates of the main reactions of (a) production and (b) loss of $O(3p^3P)$.

Reaction rates for the most important production and loss reactions of $O(3p^3P)$ are shown on Figure 4.8. During FIW propagation and before establishment of quasi-steady-state discharge, $O(3p^3P)$ is dominantly produced from electron impact O_2 dissociation (R27) and electron impact excitation of O (R28). The (R28) quickly builds up and becomes dominant for $O(3p^3P)$ production during the quasi-steady-state discharge with (R27) and electron impact excitation of $O(^1D)$ (R30) as less important processes. In the afterglow, the 3-body recombination of O^+ ion with electron as a third body solely governs the $O(3p^3P)$ production (R12). $O(3p^3P)$ decay is defined by the collisional quenching on the main mixture components, N_2 (R47) and O_2 (R46), and radiative decay (R34).

For $Ar(2p_1)$ and $O(3p^3P)$ states, the tail of the emission in the afterglow is mainly due to reactions of 3-body recombination with electron as a third body. This observation may question the validity of equation 4.1. However, the ratio of densities of $Ar(2p_1)$ and $O(3p^3P)$ excited atoms was found to be of a non-zero value during the discharge only when quenching and 3-body recombination are inactive.

4.5 Underlining the role of high electron density

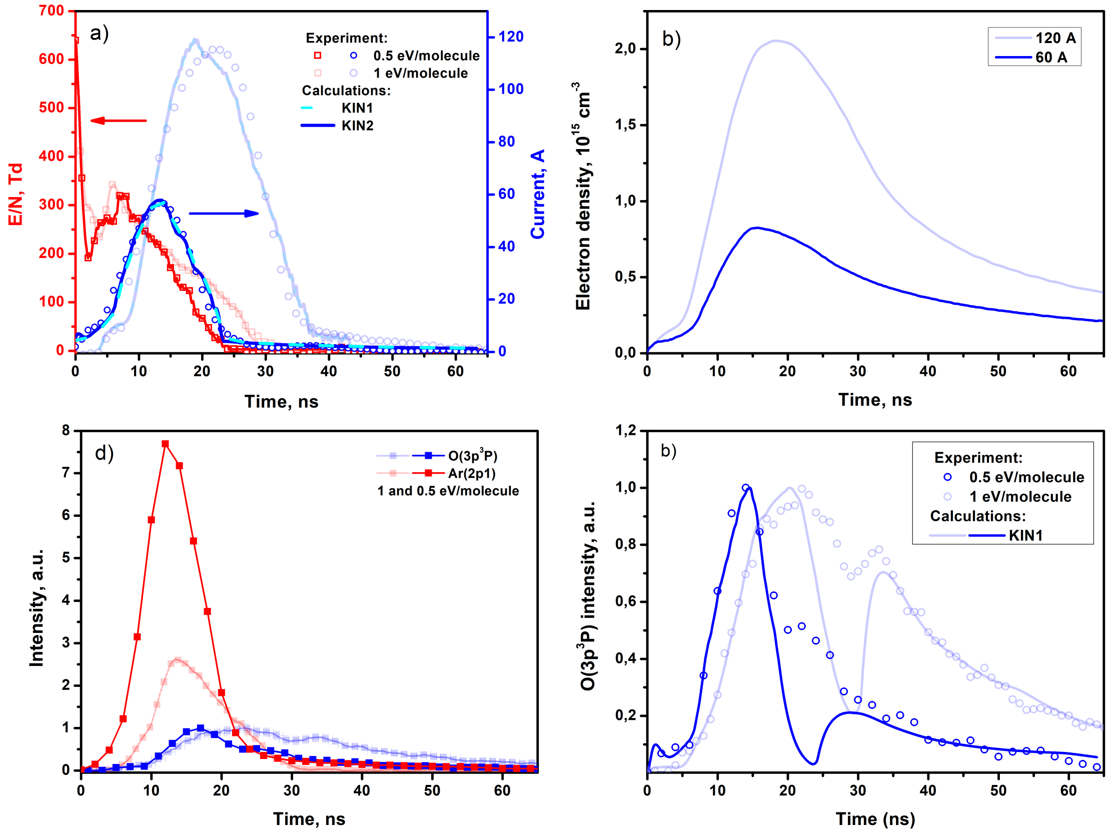

Figure 4.9 – Experimental results: (a) longitudinal reduced electric field, E/N, in the center of the inter-electrode gap and electric current I_{tr} transmitted through discharge tube; (b) relative O-atoms ($\lambda_{\mathrm{O}} = 844.6$ nm) and Ar ($\lambda_{\mathrm{Ar}} = 750.4$ nm) emission curves, the maximum of O-atoms emission is taken to be unity; (c) the calculated density and experimentally measured emission intensity for O(3p3P), normalized. The lines and scatters in the dark solid and light transparent colours represent 60 A and 120 A peak current values cases, respectively.

The data acquired during previous actinometry experiment [51] was used as a benchmark case to the developed kinetic scheme as well. With the inter-electrode distance of 70 mm instead of 55 mm, it was possible to get almost the same electric field in amplitude, while the electrical current and specific deposited energy were different by a factor of two. These data were used to trace a trend in actinometry experiments to verify the validity of the suggestions made in the numerical modeling, at conditions of high electric field and high energy density. For technical reasons, no data on $N_2(C^3\Pi_u)$ was taken during that experiment.

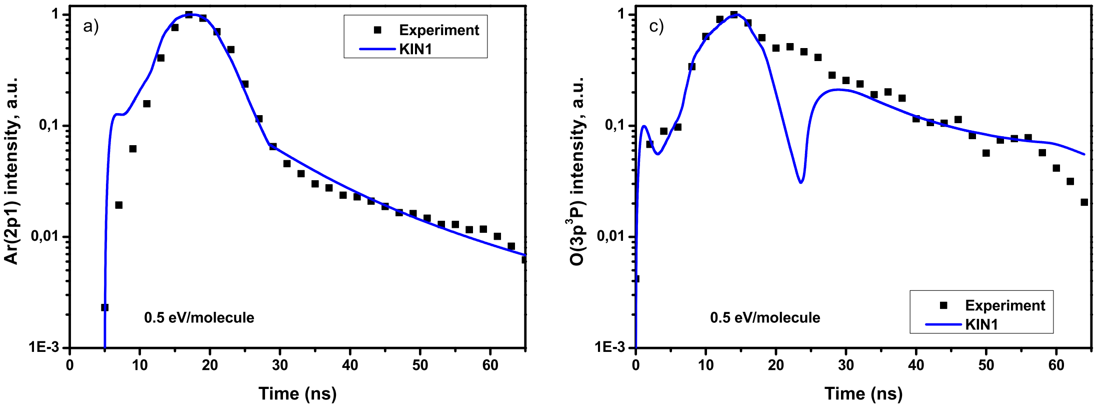

Figure 4.10 – Comparison of the calculated normalized density and the experimentally measured normalized emission intensity for (a) Ar(2p$_1$) and (b) O(3p^{3}P) in case of 0.5 eV/molecule specific deposited energy.

Figure 4.9 represents the actinometric nCD experimental data acquired in case of 60 A peak current value on top of those of 120 A peak current value. Plots of emission of O(3p^{3}P) superimposed with the density of O(3p^{3}P) calculated in arbitrary units for both values of deposited energies, are presented in linear scale. The dip on the experimental curve is clearly seen at 27 ns for the 1 eV/molecule case while for 0.5 eV/molecule case a similar but less pronounced dip appears at 20 ns. It follows from analysis of Figure 4.9(a), that for both cases, the reduced electric field at the position of the dip is equal to 60 Td. In both cases, numerical modeling reproduces the dip only qualitatively. Even so, the population of excited oxygen atom becomes less pronounced with a decrease in the specific energy density.

The density of Ar(2p$_1$) relative to the density of O(3p^{3}P) (the maximum density of excited oxygen is taken as unity) is adequately reproduced for both values of energy. At lower energy, and thus lower electron density, (i) the density of excited Ar is less influenced by quenching, and so is almost three times higher; (ii) the 'tails' of the kinetic curves for both excited species decay faster, according to the idea that the reason for the observed long decay is a reaction strongly dependent upon the electron density. Thus, further decrease in the specific energy density should lead to a decrease in the role of three-body recombination and to higher Ar(2p$_1$) intensity compared to the intensity of O(3p^{3}P).

Summarizing the performed kinetic analysis, it is possible to formulate the simplified kinetics equations for the [Ar(2p$_1$)] and [O(3p^{3}P)] in typical conditions of nanosecond capillary discharge. At the developed discharge stage, when the main production of O(3p^{3}P) is due to excitation from the ground state of the O-atom and when the reaction of recombination is not yet important (10 ns $< t <$ 25 ns for the 1 eV/molecule case), the balance between the production and the decay of the excited atoms can be written as following:

$$\frac{d[\mathrm{Ar(2p_1)}]}{dt} = k_{16}n_e[\mathrm{Ar}] - k_{37}n_e[\mathrm{Ar(2p_1)}] \tag{4.2}$$

$$\frac{d[\mathrm{O(3p^3P)}]}{dt} = k_{28}n_e[\mathrm{O}] - (k_{47}[\mathrm{N_2}] + k_{48}[\mathrm{O_2}])[\mathrm{O(3p^3P)}] \tag{4.3}$$

Selecting on the left-hand side the terms containing the densities of atoms in the ground state, one obtains:

$$[\mathrm{O}] = [\mathrm{Ar}] \cdot \frac{k_{16}}{k_{28}} \cdot \frac{d[\mathrm{O(3p^3P)}]/dt + (k_{47}[\mathrm{N_2}] + k_{48}[\mathrm{O_2}])[\mathrm{O(3p^3P)}]}{d[\mathrm{Ar(2p_1)}]/dt + k_{37}n_e[\mathrm{Ar(2p_1)}]} \tag{4.4}$$

Equation 4.4 can be considered as an actinometry equation for a discharge at high electric fields and specific deposited energy. Atomic oxygen density in the discharge can be found as a function of time at the conditions of known: (i) absolute values and waveforms of the electric field and current; (ii) waveforms and relative intensities of $[\mathrm{Ar(2p_1)}]$ and $[\mathrm{O(3p^3P)}]$ emission. It is recommended to check the validity of equation 4.4 by performing reaction rates analysis at different discharge stages.

4.6 Conclusions

Two experimental datasets measured in $\mathrm{N_2{:}O_2}$ nanosecond capillary discharge with $\mathrm{Ar(2p_1)}$ as actinometric specie were presented. For both 0.5 and 1 eV/molecule specific deposited energies, the following time-resolved quantities were measured during the discharge: reduced electric field, transmitted current, deposited power and specific energy together with $\mathrm{O(3p^3P_{1,2,0})} \rightarrow \mathrm{O(3s^3S_1)}$, $\mathrm{Ar(2p_1)} \rightarrow \mathrm{Ar(1s_2)}$ and $\mathrm{N_2(C^3\Pi_u, v' = 0)} \rightarrow \mathrm{N_2(B^3\Pi_g, v'' = 0)}$ optical transitions. The peak measured value, $[\mathrm{O}] = 7.5 \cdot 10^{16}$ cm^3, corresponds to 23% dissociation fraction. The datasets served as benchmark cases for adjustment and validation of actinometric kinetic scheme described in [156]. Actinometric kinetic scheme reproduced well temporal behavior of (i) all experimentally acquired optical transitions and of (ii) $\mathrm{Ar(2p_1)}$ to $\mathrm{O(3p^3P_{1,2,0})}$ density ratio reconstituted from emission waveforms with help of Einstein coefficients for radiative decay. It was shown that the 3-body recombination of $\mathrm{O^+}$ and $\mathrm{Ar^+}$ ions with electron as a third body become dominant in the early afterglow.

Chapter 5

Longitudinal electric field in fast ionization wave front measured by electric field induced second harmonic generation (E-FISH)

The plasma chemical processes that occur during discharge and afterglow are basically determined by the space-time distribution of electron number density $n_e(\overrightarrow{r}, \overrightarrow{v}, t)$ and the electric field $\overrightarrow{E}(\overrightarrow{r}, t)$. *Grosso modo*, if at a point of time t_0 one knows $n_e(\overrightarrow{r}, \overrightarrow{v}, t_0)$ and $\overrightarrow{E}(\overrightarrow{r}, t_0)$, one can determine reaction rates of all plasma processes at t_0 (reactive species production, dissociation, ionization *et cetera*). This relation makes electric field a vitally important input parameter for simulations. In nanosecond pulsed discharges, the electric field can be conditionally divided into the field of the fast ionization wave and the field in a closed gap. Measurements of electric field in the front of FIW is a complicated task due to the high speed (units of cm/s), short duration (units of ns), and high peak value. Consecutively, selected diagnostic has to have high spatial and temporal resolution in order to fully resolve electric field waveform in a nanosecond pulsed discharge. The chapter presents measurements of longitudinal component of electric field measured in the front of FIW by electric field induced second harmonic generation (E-FISH) laser technique. This chapter's content was partially published in [172].

5.1 Description of the implementation of the experimental technique

The experiment has been performed on the nanosecond tube discharge (nTD) setup. The discharge develops between two brass electrodes produced in a form of hollow truncated cones separated by 80 mm within a quartz tube of internal diameter of 20.2 mm. The surrounding cylinder-shaped two-parts made copper screen leaves a possibility of side optical access that was used during the experiment for laser's beam input-output pathway. The discharge tube can be considered as a break in the high voltage cable line with plasma interconnected cone electrodes as a main line and a copper screen as a ground. The high voltage pulses of positive polarity, 9.3 kV amplitude, 4 ns rise/fall time, and 30 ns FWHM duration are produced by FPG 12-1NM (FID GmbH) high voltage pulse generator at a repetition rate of 10 Hz. The gas input is controlled by Brooks Instruments 5850TR mass flow controller so that N_2 is flown trough the electrode orifices from low voltage electrode to high voltage electrode in amount of 10 sccm at the pressures of 20, 40, 70 and 100 mbar monitored by Pfeiffer Vacuum SAS Pfeiffer CMR 362 capacitive pressure gauges.

The E-FISH diagnostic has been put into practice as schematically shown on Figure 5.1. To study the event of a nanosecond time scale, a picosecond mode-locked laser EKSPLA PL2241B of a pulse duration 30 ps at a repetition rate of 10 Hz has been used. The vertical polarization of 1064 nm fundamental output beam of 6 mJ pulse energy was rotated by a half-wave plate to horizontal to receive the generation of the second harmonic signal from the interaction between the electric field of laser beam and longitudinal component of FIW's electric field in plasma. The beam was then directed horizontally through the quartz discharge tube perpendicularly to inter-electrode axis of symmetry in the middle between the high voltage and low voltage electrodes. The position of the laser beam was slightly (less than 1 mm) misaligned with respect to the height to avoid back reflections. The precision of horizontal and vertical positioning was less than 1 mm. The entering laser beam was focused on the center of the discharge tube by a 20 cm focal distance lens with a confocal parameter estimated to be ≈ 1 mm assuming a Gaussian laser beam. The laser pulse energy was kept sufficiently low, around 6 mJ, to prevent damage of the quartz tube by the laser beam. Since the second harmonic is eventually generated on the air-glass interfaces, a Thorlabs FGL665S long pass filter, placed after the first focusing lens, was used to block the stray 532 nm second harmonic signal generated in the optical systems' components prior to the discharge tube.

After passing the discharge tube (Figure 5.1), the laser beam containing fundamental 1064 nm and second harmonic signal 532 nm was collimated by a second 20 cm focal distance lens. The dichroic mirror placed after the lens reflects 532 nm light and lets pass fundamentals 1064 nm light that was blocked by a beam trap. The light reflected by dichroic mirror contains not only 532 nm of the second harmonic signal, but some fundamental laser's 1064 nm light as well. The co-propagating signals of different wavelengths were spatially separated by a dispersive prism. Assuming negligible depletion of the fundamental, the residual 1064 nm was used to monitor laser's shot-to-shot energy variations by a Thorlabs DET10A/M longpass $(200 - 1100$ nm) 1 ns rise time Si-biased photodiode detector, further addressed as

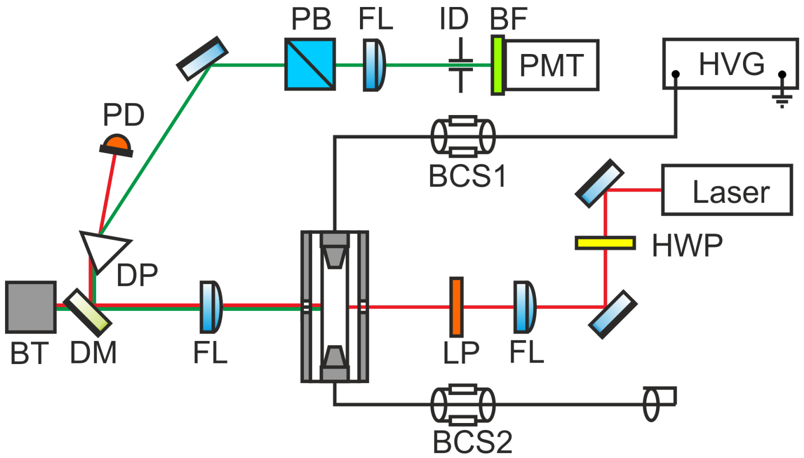

Figure 5.1 – Schematic of nTD setup (top view) and ps E-FISH diagnostic. BT: beam trap; DM: dichroic mirror (532 nm reflecting, 1064 nm transmitting); DP: dispersive prism; PD: photodiode; FL: plano-convex lens; PB: 532 nm polarizer; ID: iris diaphragm; BF: 532 nm bandpass filter; PMT: photomultiplier tube; LP: long pass filter; HWP: 1064 nm half-wave plate; HVG: high voltage generator; BCS1, BCS2: back current shunts before the high and low voltage electrodes, respectively. Fundamental and second harmonic laser beams are depicted in red and green lines, respectively, while black lines indicate electrical wires.

PD. Since the sensing element is small (1×1 mm^2), minute changes in the beam mode or even the beam path could affect the laser intensity registered by the PD. To prevent such inaccuracies from occurring, diffusive glass was mounted on the optical entrance of PD. Neutral density Thorlabs NDUV10A filter mounted before the diffusive glass ensured operation of PD in linear regime. The 532 nm second harmonic beam sent through a polarizer to isolate the horizontally polarized signal proportional to the square of the longitudinal electric field in the discharge, was focused with a 10 cm focal length lens into the H7422-50P Hamamatsu photomultiplier module with a rise time of 1 ns. An iris and FL532-10 532 nm bandpass filter (FWHM 10 nm) were placed at the entrance of the PMT for the purpose of stray light rejection. With the same intentions, the time-resolved plasma emission detected by the PMT during the discharge pulse (emission background) was measured with the laser turned off, and subtracted from the PMT signal measured with the laser on. Such plasma emission background correction has been performed only for the case of the lowest pressure of 20 mbar, where emission was found to be the strongest among studied pressure conditions of 20, 40, 70 and 100 mbar.

The PD and PMT signals are recorded by LeCroy WaveRunner 64Xi-A digital oscilloscope with 5 GHz sampling rate and 600 MHz bandwidth. Oscilloscope triggered from incident pulse monitored by BCS1 saves non-averaged waveforms of incident and reflected pulses, transmitted voltage pulse, laser energy and second harmonic detected by BCS1, BCS2, PD and PMT, respectively.

Additionally, imaging of fast ionization wave's propagation along the discharge tube has been done using a Princeton Instruments ICCD PI-MAX 4 camera. A side-view sequence of integrated plasma emission images (200 – 900 nm) of the shortest possible 1.17 ns gate width were taken every 0.2 ns for 20, 40 and 70 mbar, and every 1 ns for 100 mbar. Delay difference is adapted to match the fast ionization wave's speed. The latter is inferred from the emission images by tracking the time evolution of the wave front development from the moment of initiation at the high voltage electrode until its arrival at the low voltage electrode.

5.2 Absolute calibration: by Laplacian field and electrical alternative

Absolute calibration is the process of establishing a relationship between the outcome of a technique under calibration expressed in arbitrary units and absolute values of a measured quantity expressed in units of a chosen system of measurement. In practice, calibration can be performed in two approaches: (i) by applying the technique under calibration to a known quantity and (ii) by applying the technique under calibration together with an already calibrated technique to an unknown quantity. To ensure validity of a novel technique, calibrations of both types were done. Following the first approach, an electric field of a beforehand known value was measured by E-FISH technique. Following the second approach, the longitudinal electric field under study was measured by calibrated electrical tools - back current shunts and capacitive probe simultaneously with E-FISH experiment.

The E-FISH calibration technique was adopted from [73]. The article suggests to measure the experimental setup's E-FISH response from a known electric field and to presume that the quadratic relation between second harmonic signal and the value of applied electric field holds up to the values of the electric field of the main experiment. A way to create a known electric field in the discharge tube is to run the cell with no plasma, meaning with a Laplacian field at under breakdown conditions. In [73], breakdown voltage of setup used had limited calibration electric field by 20 kV/cm when values of studied electric field reached 140 kV/cm. The reliability of extrapolation to an order of magnitude bigger values was not evaluated nor discussed. At the same time, the calibration approach is the most reliable when conducted under conditions that match those of study, namely the number density, the gas composition and the values of electric field. The following text discusses considerations raised to design a calibration that should cover values of beforehand unknown electric field. Generally, in order to avoid possible complications due to use of newly introduced equipment, it is recommended to calibrate the very same setup as used in main experiment. Note that during the present calibration, all the equipment, its mutual disposition and operating conditions were the same as during the main experiment except one insert modification discussed further in the section.

The generation of second harmonic signal that lies at the heart of E-FISH technique is a result of interaction between three polarized electric fields and is sensitive to the angle between electric fields' polarization planes. The signal is strongest when the polarizations of all electric fields are maintained parallel one to another, hence the choice of polarization of laser probe beam. This implies that the calibration electric field should be of the same polarization as the one probed during the experiment. In the context of the present work where longitudinal electric field is studied, the calibration electric field created inside of the discharge tube should also be aligned to the inter-electrode axis. Laplacian electric field created in the discharge tube with electrodes in form of hollow truncated cones has unknown in advance spatially non-uniform radially dependent distribution. In order to create a homogeneous electric field, both high and low voltage electrodes were symmetrically extended so that new edges form a plane parallel capacitor.

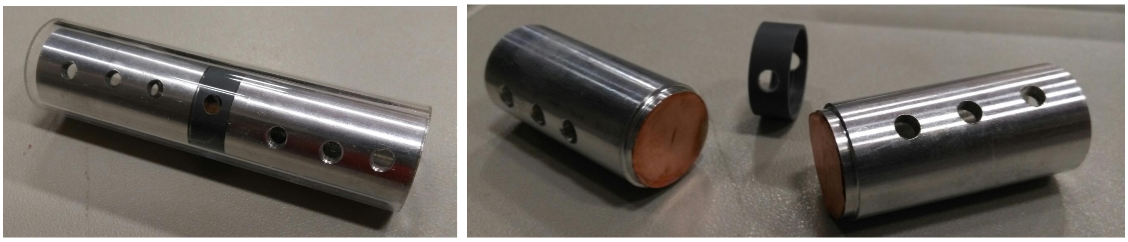

(a) (b)

Figure 5.2 – Hollow alumina perforated electrode extensions with copper flat end and separation PVC ring used during E-FISH calibration: (a) assembled in quartz tube, (b) view on the planes that form plane capacitor when mounted in the tube.

Figure 5.2(a) shows the insert mounted within the quartz tube of the discharge tube while Figure 5.2(b) shows it separately. Each extension's body is made from 44 mm long hollow alumina tube of 20 mm external diameter and ends by round plane copper surface glued to the tube by conductive glue. Plane surfaces are separated by 4 mm distance fixed by PVC ring that was side-holed to allow laser beam's passage. Twelve through holes at side surfaces of the extension tubes allow gas flow across the discharge tube. The insert enters the tube tightly. Electrical contact between electrode and its extension is ensured by matching total length of the insert with length of the quartz tube. During the assembly of the discharge tube due to its design the insert is forced to physical contact with the surface of the electrode once the latter is screwed onto the quartz tube.

These capacitor-like inserts provide a possibility to create axially-aligned homogeneous electric field of the value that equals to ratio of voltage applied to the HV-electrode U to distance between insert's surfaces d. The distance d between plain electrodes was determined on the basis of two considerations. On the one hand, in order to avoid the influence of round plain capacitor edge effect on its central zone, the distance between plates should be much smaller than the plate's diameter. On the other hand, the distance between the plates should ensure confident passage of the laser beam and so has to be at least a few mm. As a compromise, it was decided to spread the 20 mm diameter plates to a distance of 4 mm.

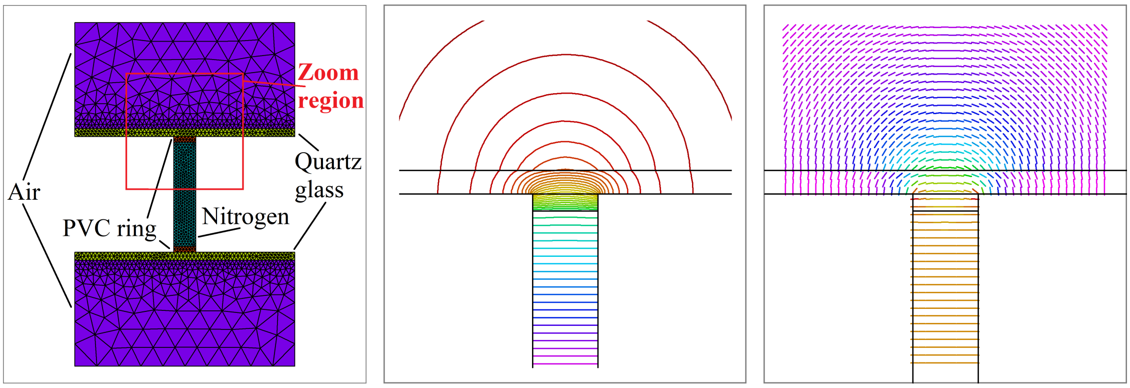

(a) (b) (c)

Figure 5.3 – Laplacian electric field calculations performed using FlexPDE 7.07/W64 solver. (a) Automatically generated mesh. Field of simulation is 20 mm×30 mm. Red square indicates the region 20.2 mm×20.2 mm used to show electric field in greater detail in (b) field lines and in (c) vector field plot representations respectively.

The homogeneity of electric field between two plane parallel 20.2 mm diameter round surfaces separated by 4 mm was estimated by means of FlexPDE 7.07/W64 solver [173]. FlexPDE is a powerful tool for numerical solving stationary and time-dependent systems of differential equations in a 1D, 2D or 3D defined area with initial and boundary conditions by finite elements method. Variables are calculated at the nodes of program-generated triangular cell mesh. Initial cell size is defined by problem's geometry and may decrease to satisfy the acceptable error limit.

Code used to calculate Laplacian electric field consists in solving Gauss's law in differential form, $\nabla \cdot (\epsilon\epsilon_0 \overrightarrow{E}) = 0$, where $\nabla\cdot$ denotes the divergence operator, ϵ_0 -

vacuum permittivity, ϵ - relative permittivity, or dielectric constant, and $\overrightarrow{E}$ - vector of electric field. Gauss's law is solved for the 20 mm × 30 mm region containing axial cross-section of the discharge tube shown on Figure 5.3(a). Extended electrodes are represented as whole conductive pieces on purpose to eliminate accumulation of numerical error in regions that depict alumina tube's voids. Calculation region includes quartz tube and PVC ring presented without laser-passage holes for simplicity, both given an average value of dielectric constant of $\epsilon = 4$. Dielectric constants of N_2 in the discharge cell and of surrounding air are presumed to be equal to $\epsilon = 1$. Figure 5.3(b) and (c) show calculated electric field in field lines and vector field plot representations respectively in more detail at the region indicated by red frame at Figure 5.3(a). Calculations reveal that electric field in the region of inter-electrode gap remains dominantly longitudinal at any position be it N_2 gas or PVC ring.

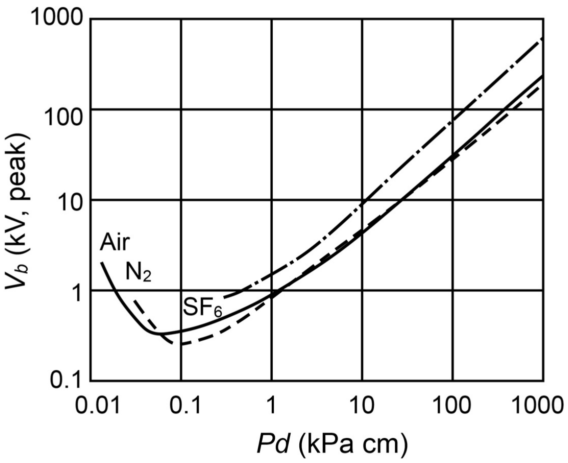

Figure 5.4 – Paschen's curve for N_2, SF_6 and air. Taken from [174].

Based on calculations above, Laplacian electric field is considered to be homogeneous and radially independent in proximity of laser focal point. This discharge tube modification is further used for E-FISH calibration.

Breakdown conditions can be approximately specified by Paschen's law [174], which gives the breakdown voltage between two electrodes in a gas as a function $f(p{\cdot}d)$ of pressure p and inter-electrode distance d. The function f can be understood as following: at a given pressure p and inter-electrode distance d, if the applied voltage is roughly lower than the $f(p \cdot d)$, the discharge will not occur. Figure 5.4 shows Paschen's curve for gas under study, N_2. For all pressure conditions during calibration with parallel plane electrodes separated by 4 mm, the $p \cdot d$ values lie withing $(0.8 - 4)$ range. Obtained voltage threshold at 20 mbar pressure condition was used as an estimate of voltage upper limit for calibration. During calibration, amplitude of applied voltage was adjusted to cause no breakdown that was ensured by zero transmitted current pulse monitored by back current shunt located after the discharge tube. Incident voltage pulse having rectangular-like shape with quasi-linear rise of 4 ns duration allows to measure calibration electric field in range from 0 to U/d with 0.2 ns sampling time resolution of the oscilloscope.

The calibration "in the E-FISH way" benefits from usage of the same discharge cell, optical elements and laser system. With all precautions listed above, it is expected to provide the E-FISH response of the experimental setup up to the breakdown values of electric field. Current calibration approach has however a few drawbacks that have to be listed. An extra effort is needed to construct the custom-made inserts required for sustaining the Laplacian field of appropriate polarization. Introducing these inserts to the discharge tube also involves disassembly of the discharge apparatus which could inadvertently lead to a source of optical alignment systematic error. Such approach means that calibration has to be done separately from the main experiment. Consecutively, it not only requires more time, but also makes impossible to obtain a set of shot-to-shot independent calibrations.

Apart from the E-FISH calibration described above, two electrical calibrations have been applied - by back current shunts and by capacitive probe. As a brief reminder, back current shunts are monitoring the conductivity current within the coaxial line and allow accurate reconstruction of electric field after the discharge gap is closed while capacitive probe is sensible to spacial charge distribution disrespectful to its origin and allows to reconstruct electric field at any time instant: before, during or after FIW. Electric field calibration by BCSs was done using voltage waveforms saved along E-FISH experiment (so-to-say, in parallel with the experiment itself). Data for electric field calibration by CP was acquired independently.

The confidence in absolute calibration of present measurements may well be increased by comparison with kinetic modeling predicting electric field distributions both in the plasma and in the wall of the discharge tube, as has been done previously for electric field measurements using an electro-optic probe [175]. An alternative solution is to perform calibration using the second incident high voltage pulse that is reflected from the HV generator. After the passage of the FIW produced by the first incident HV pulse, the inter-electrode gap is essentially closed and replaced by a conductive medium. The discharge is effectively in a quasi-steady state and a good estimate of the electric field may be simply obtained as a ratio between potential difference across electrodes and inter-electrode gap distance.

5.3 Single laser shot data treatment procedure

Picosecond lasers are known to be subject to shot-to-shot energy fluctuations and time jitter. The laser available for E-FISH diagnostic had a time jitter of approximately 30 ns after arrival of external trigger. The event under study, *id est* the longitudinal electric field created in discharge tube by high voltage pulses of 30 ns duration, has characteristic time scale that matches the time uncertainty of laser system. Despite the unpredictable and uncontrollable arrival time of the laser pulse with respect to the incident voltage pulse, E-FISH diagnostic can still be applied in single laser shot mode, meaning with no pre-averaging during laser run. It means that, for every single laser shot, a set containing (i) photodiode waveform of laser intensity, (ii) photomultiplier waveform of second harmonic generated photon flux and (iii) back current shunt waveforms of incident, reflected and transmitted voltage pulse voltages was saved. This approach results in an ensemble of laser excited second harmonic signals randomly distributed in time with respect to the incident high voltage pulse. Thus time jitter, one of the biggest inconveniences of picosecond laser, was used for the benefit. Each single laser shot probes electric field at a specific time instant and data gathered from totality of single laser shots would allow to reconstruct temporal development of electric field.

Although laser diagnostics are highly influenced by laser intensity waveform and its fluctuations, exact accounting for laser intensity waveform encounters difficulties in terms of complex integro-convolutional mathematical description, specific equipment requests and development of deconvolution algorithms for data post treatment. Generally speaking, diagnostics is a method for determining an unknown parameter through its relations with known parameters, while technique is the adaptation of diagnostics to a specific system with available equipment and data processing capabilities. In other words, technique adjusts accuracy of relations behind diagnostics in order to fit diagnostics' demands to experimental constraints of each particular case. In the framework of the current experiment, laser pulse of 30 ps duration or second harmonic signal of expected duration of tens of ps can not be resolved due to 1 ns rise/fall time of photodiode and photomultiplier. As viewed by photodiode, shot-to-shot fluctuations of laser intensity waveform did not exceed 3%. Due to equipment limitation and stability of observed laser intensity waveform, E-FISH technique was applied with respect to integrated values of laser intensity and second harmonic generated photon flux, meaning, laser energy and total number of second harmonic generated photons. These values are obtained by integration over time of corresponding waveforms viewed by oscilloscope. The temporal resolution of the technique is limited by oscilloscope's sampling rate, 200 ps. For such waveform-independent E-FISH technique, once the photodiode and photomultiplier signals are detectable and noise distinguishable, single shot approach is applicable.

As seen experimentally, the discharge start in nTD powered by nanosecond high voltage generator can have temporal and spacial jitter. Time jitter of ≈ 7 ns becomes clear when several transmitted voltage pulses triggered from the incident pulse are

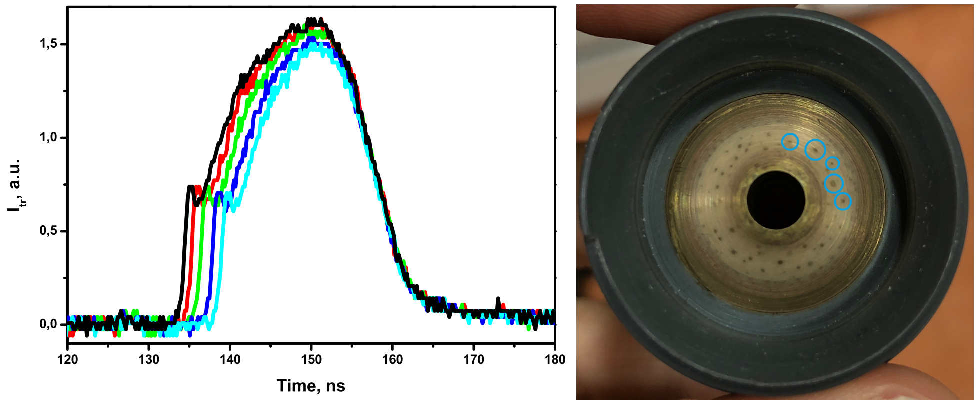

Figure 5.5 – nTD quasi-steady-state discharge time and space jitters: (a) few transmitted pulses plotted together synchronized by the front of the incident pulse show a start time uncertainty, (b) nTD's high voltage electrode, top view. Multiple dark dots on the light circular section on electrode's conical surface are starting points of transmitted current, five of them are indicated by blue circles for clarity.

plotted together as shown at Figure 5.5(a) for 20 mbar N_2. It was also visually observed from repetitive triggering of the discharge that plasma emission originates from multiple points on surface of HV electrode shown at Figure 5.5(b). Presumably, current passing through the discharge start points engaged brass HV electrode into chemical reactions with ionized medium. These reactions had led to light-colored deposit around discharge starting points making the latters visible.

The reason for observed spatio-temporal jitter in discharge start is explained as follows. Discharge avalanche starts from the point at HV electrode surface where sufficient gas pre-ionization caused by collisions of neutrals with accelerated electrons was formed the earliest. Due to axial symmetry of the discharge tube, discharge start point at HV electrode surface is defined by radial non-localities of electron density in vicinity of the electrode at arrival of voltage pulse. Interesting to note that plasma start points appear roughly at unique circular section on electrode's conical surface and not at the truncated edge where surface curvature is the biggest. Such peculiar behavior of the plasma start point is presumed to be associated to the superficial electrode's charge distribution that does not allow decrease in radial position because of electrostatic repulsion. Somewhat similar effect is observed at axisymmetric high pressure dielectric barrier discharge in [176], where maximum number of filaments initiated from HV electrode is limited by Coulomb repulsion between charged filaments. Aerodynamic influence of the gas flown through the electrodes to the effect described above is negligible due to small value of gas linear velocity. At used flow rate of $Q = 10$ sccm, gas within the discharge tube of inner diameter of $d = 20.2$ mm moves with the linear velocity equal to 10 sccm/$(\pi d^2/4) = 0.5$ mm/s, which implies that during ~30 ns of high voltage pulse gas flow can be considered immobile.

Nonetheless, as was observed from time-resolved plasma emission images, for each pressure condition the avalanche develops in the same way whether time jitter has appeared. It means that for each pressure condition, FIW is independent from plasma start and, particularly, independent from time jitter. Further in the text, plasma with a particular time delay of the discharge start with respect to incident pulse is associated to corresponding transmitted voltage pulse and called "a plasma mode". In terms of E-FISH experiment, the time instant when laser probes electric field has to be taken with respect to an electric field related event. As discussed previously, rise of incident pulse can not be a reference time instant due to temporal uncertainty of FIW's start. On the contrary, rise of transmitted voltage pulse is a clear indication of an electric field related event which is arrival of FIW to LV electrode. Thereby in the present work the time instant of each single laser induced second harmonic generation is calculated in relation to the rise of transmitted voltage pulse. Re-synchronization to the transmitted voltage pulse was done at the data post treatment. For each pressure condition, in order to create a common time axis for all single laser shot events, waveforms were time shifted to match the latter start among all. Transmitted current time synchronization would allow accurate tracking of the $1-2$ ns FIW's development at a cost of ≈ 5 ns blurring the falling edge of the electric field.

The development of longitudinal electric field during FIW propagation and in quasi-steady-state discharge has been scanned by two partially recovering 30 ns jitter-scattered laser pulse bunches. For every pressure condition, at least 40000 single laser shots were recorded. To treat single shots data, there is a need in a code capable to calculate laser pulse energy and total number of second harmonic generated photons from saved waveforms. It is also necessary to perform a statistical analysis in order to account for multiple second harmonic measurements acquired at the same time instant with respect to the transmitted voltage pulse. To satisfy these needs, two separate codes were written: SHG (stands for Second Harmonic Generation) code and SSC (stands for Student Statistics Calculation) code. SHG code searches for E-FISH events in recorded data, calculates the time of laser pulse arrival with respect to the transmitted voltage pulse further called as "event time" and creates a list of time-integrated photodiode and photomultiplier waveforms that represent laser energy and second harmonic signal, respectively, together with event time. SSC code sorts these events by user-defined equally spaced time intervals (bins) and returns the mean value and the error of laser energy and second harmonic signal expressed in a.u. for each time bin. The two following sub-chapters contain explanation of logic and functioning for SHG and SSC codes.

Second Harmonic Generation code

The algorithm flow chart of SHG code is shown on Figure 5.6. The code contains two major parts: first part defines the so-called latest plasma mode, second part selects E-FISH events, synchronizes them to the latest plasma mode and creates a table of single-shot events of maximums and integrals of PD and PMT signals.

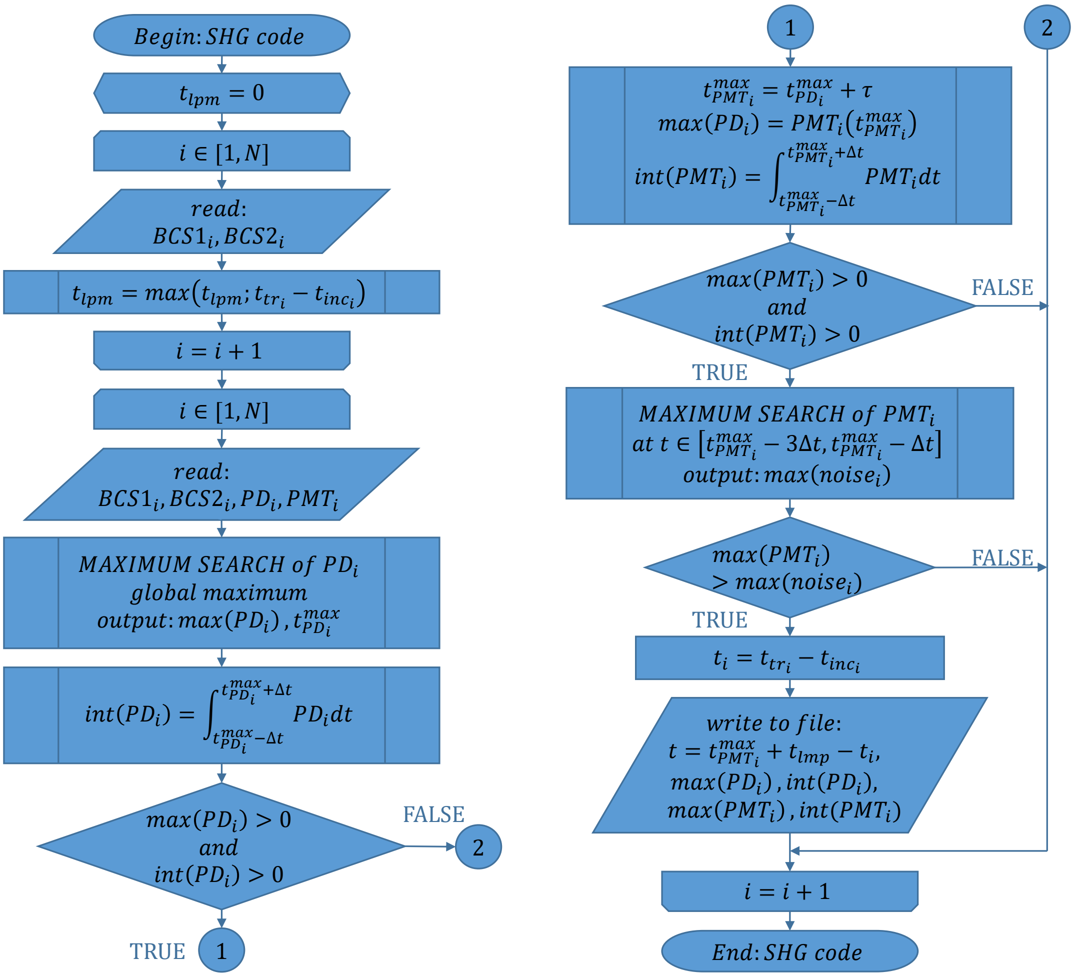

Figure 5.6 – Algorithm flow chart of SHG code. t_{lpm} - time delay of FIW start with respect to the incident pulse for latest plasma mode, i - counter, N - number of single laser shots, t_{tr} - arrival time of transmitted pulse at BCS2, t_{inc} - arrival time of incident pulse at BCS1, Δt - half of integration interval, τ - time delay of PMT maximum with respect to PD maximum, t_i - time delay of FIW start with respect to incident pulse.

For each single laser shot, time instant is saved when BCS1 and BCS2 signals overcome a certain triggering threshold (similar principle as any oscilloscope uses for triggering). The biggest time difference between single shot's BCS1 and BCS2 pair defines the most retarded start (Figure 5.7(a)) further addressed as the latest plasma mode. Further, the events that would pass signal selection criteria will be time-shifted to match the fronts of I_{tr} of the latest plasma mode's start.

Signal selection criteria contains a few checks:

- The PD is almost insensitive to EM noise (at least, comparing to PMT), so its signal can be unmistakably found by a global maximum search. Global maximum of PD waveform (laser intensity) as well as integral under the peak (laser energy) are strictly positive (Figure 5.7(b));

- The time delay between PD's and PMT's signal's maximums is defined only by the difference in optical paths (mutual disposition of optical elements), response functions of the above mentioned devices and lengths of the signal cables. The delay is thus a constant value within the experiment and is reproduced from shot to shot. So, once this delay is defined for an event with a strong, pronounced and well-defined second harmonic signal, it can be applied for all the others events to retrieve PMT's maximum's form PD's one. In present case the delay was equal to 4.2 ns (Figure 5.7(c));

- Similarly to the PD selection, the PMT's maximum (maximum intensity of second harmonic photon flux) as well as the integral under the peak (amount of second harmonic photons) are strictly positive (Figure 5.7(d));

- The noise PMT records is mostly of the EM nature that is due to the discharge ignition just before the laser pulse arrives to the measurement point. Knowing that, the following condition of noise discrimination has been adopted: the PMT's maximum should be bigger than noise amplitude. The noise extremum modulus is determined on a time interval equal to the PMT integration length located immediately before the PMT integration time (Figure 5.7(e)).

Though not observed on the oscilloscope during the run, some PMT waveforms were recorded with an overshoot. The peak was artificially restored by separate procedure if a plateau in near-maximum region is found. The missing peak is modeled as an isosceles triangle with the plateau as a base. The legs of the triangle have the slope defined by the recorded parts of the peak, as Figure 5.7(f) shows.

In terms of E-FISH experiment, any stray light contribution to the second harmonic signal would be misleadingly associated to electric field in the studied medium. Plasma emission in principle can have a transition line(s) in proximity of the wavelength of second harmonic signal within bandpass of the filter mounted before PMT. For studied discharge tube operated with N_2 flow, the presence of such plasma emission has been confirmed. In that perspective, the SHG code contains a procedure

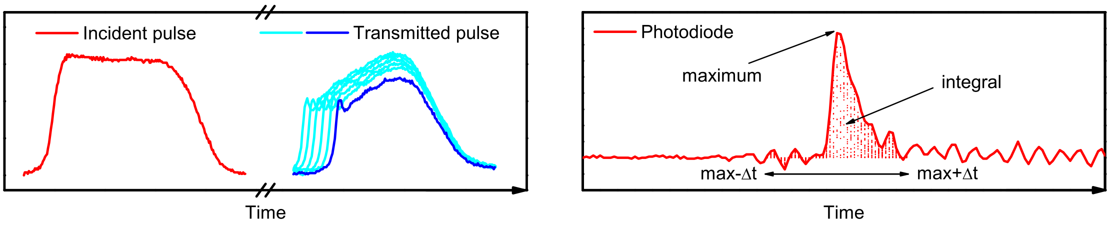

(a) Latest plasma mode **(b) PD maximum and integral values**

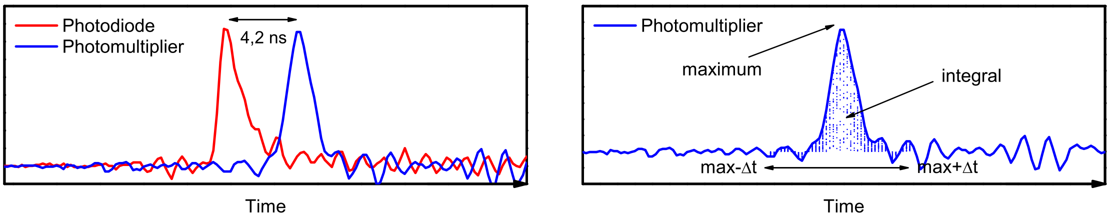

(c) PMT maximum time delay **(d) PMT maximum and integral values**

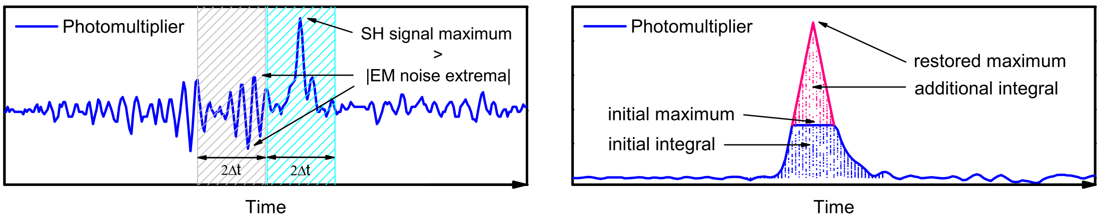

(e) Noise discrimination criteria **(f) Overshoot PMT reconstruction**

Figure 5.7 – Schematic explanation of SHG code selection criteria.

that allows to take into account signal's "contamination" by plasma emission. The procedure uses single shot data acquired in the same way as during the main experiment but with blocked laser beam. Signal waveforms obtained by PMT from plasma emission were synchronized to the latest plasma mode, averaged, smoothed over 10 points by adjacent-averaging method to reduce EM noise and further subtracted from second harmonic signal collected during the main experiment.

The values of maximums and integrals of PD and PMT are saved together with PMT maximum time, further called "event time". Typically, SHG code allows to treat 10000 input events in 30 minutes on an ordinary modern desktop PC.

Student Statistics' Calculation code

For each pressure condition, all single laser shot events are distributed over ∼60 ns because of laser jitter. These ∼60 ns are recorded as ∼300 time instants due to 0.2 ns temporal resolution of the oscilloscope. With at least 40000 single laser shot events recorded at ∼300 time instants it is quite likely to have more than one measurement at a time instant. When taking care of statistics of the N-times experimentally measured value, it is often considered that the measured values follow normal (Gaussian) distribution. Such approach is correct only if number of measurements $N \to \infty$. In a general case of a finite number N of measurements of an experimental quantity, N measurements obey Students' distribution of $(N-1)$ degrees of freedom. When $N \to \infty$, Students' distribution naturally converges to normal distribution. Students' distribution is a useful tool for understanding the statistical behavior of normally distributed population when standard deviation is unknown, *id est* of a small number of measurements. Roughly, it allows to state that with a pre-defined probability the calculated statistical error (confidence interval) from the experiment comprise the true value of the population parameter. Students' distribution is also known in literature as t-distribution due to a t parameter used for determination of a confidence interval. Brief mathematical derivation and analysis can be found elsewhere [177,178].

The SSC code was created to determine mean value and statistical error of experimentally measured time-dependent second harmonic signal using Students' distribution of a chosen confidence interval. As the only user-provided input, the SSC code uses the output file of SHG code containing values of maximums and integrals of photodiode and photomultiplier at corresponding event times of selected single laser shot events. The code creates a sequence of time intervals of unique user-defined width called time bins and attributes each single laser shot event to one of time bins according to the event time. For each time bin, the SSC code calculates mean value and statistical error of the Students' distribution. Time uncertainty is equal to half of time bin width. In the present experiment, the confidence interval was set to 95% and the time bin width was chosen to be 0.2 ns.

5.4 Fast ionization wave velocity deduced from emission images

Figure 5.8(a) shows a 200 shot averaged broadband $200-900$ nm plasma emission image acquired at 20 mbar N_2 at 3.2 ns after the beginning of the voltage rise. The discharge tube was run under the conditions of E-FISH experiment. Camera parameters were: 1.17 ns gate, 1 gain, and the field of view of approximately 2.5 cm×6.8 cm. The camera was placed from the side at the distance of 40 cm from the center of the inter-electrode axis at matching height. In Figure 5.8(a), the high voltage electrode is on the left, the low voltage electrode is on the right, and the flow is left to right. It can be seen that the emission intensity in nitrogen in the range of $20-100$ mbar is significantly higher near the discharge tube walls. It

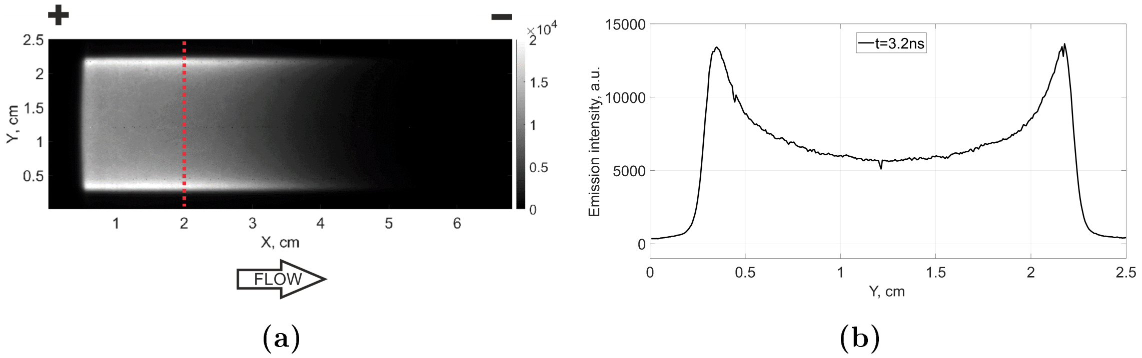

Figure 5.8 – Broadband plasma emission in 20 mbar N_2 at 3.2 ns after the beginning of incident voltage rise: (a) 200 shot averaged ICCD image. + and - depict HV and LV electrodes, respectively. Vertical red dashed line indicates the position of radial integrated emission shown on (b).

is illustrated further by plotting the radial distribution of the emission intensity in Figure 5.8(b), at the axial locations indicated by a dashed line in Figure 5.8(a). This result, which is consistent with previous experimental and kinetic modeling studies of fast ionization wave discharges in nitrogen [39,151], shows that the ionization wave is propagating predominantly near the walls of the discharge tube. Kinetic modeling predictions [39] reveal that this occurs due to higher electric field near the wall, caused by the jump in permittivity, and due to secondary photo-electron emission from the wall irradiated by the UV photons from the plasma. At higher pressures, when the electron transport becomes slower, this effect is more pronounced. It is interesting to note that such radial non-uniformity is also present in a capillary discharge sustained in a significantly smaller diameter quartz tube of 1.5 mm [151].

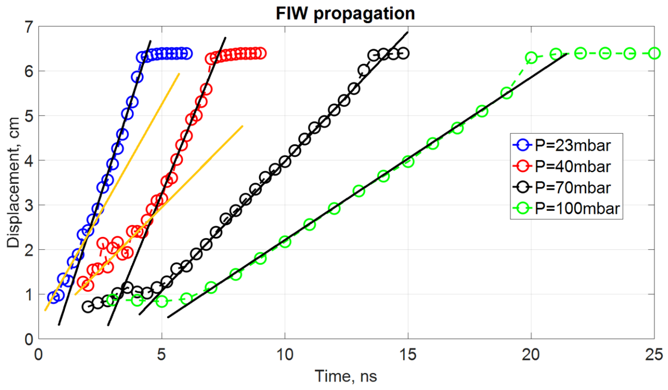

Figure 5.9 – Propagation of FIW front along the inter-electrode axis as a function of time for $20, 40, 70$ and 100 mbar. Experimental points in scatter, linear fit chosen for FIW speed estimate in black solid line, FIW speed in proximity of HV electrode in yellow solid line.

To determine the FIW propagation speed for studied pressure conditions, averaged broadband plasma emission images acquired at different time instants after the arrival of HV pulse were used. For each image, several lines located around the inter-electrode axis were averaged to build emission profile along the propagation of FIW at specific time instant. The x-position of the profile's half-maximum is associated to front of FIW at the time instant of the profile. FIW's front positions plotted against time are shown at Figure 5.9 for 20, 40, 70 and 100 mbar cases. For each pressure condition, the data points of front's displacement between 2.5 cm and 5.5 cm were used for linear approximation by least squares method. The slope of linear fit is thus concluded to be FIW propagation speed of 1.6, 1.2, 0.6 and 0.4 cm/ns for 20, 40, 70 and 100 mbar, respectively.

5.5 Laplacian field calibration. Origin of second harmonic signal

According to E-FISH diagnostics [70], for a laser plane wave approximation and for a uniform electric field, the line-of-sight integrated intensity of the horizontally polarized second-harmonic signal, $I_x^{(2\omega)}$, is

$$I_x^{(2\omega)} \sim \left(\chi_{xx}^{(3)} E_x I_x^{(\omega)} \cdot \frac{sin(\Delta k \cdot L/2)}{\Delta k/2} \right)^2 \tag{5.1}$$

where E_x is the longitudinal component of the electric field, $I_x^{(\omega)}$ is the intensity of the horizontally polarized laser beam, $\chi_{xx}^{(3)}$ is the third-order nonlinear susceptibility (in gases, proportional to the number density n), L is the length of the region where the electric field is applied, in the direction of the laser beam, and Δk is the difference between the fundamental and the second harmonic wave vectors. At the present conditions, the coherence length in nitrogen at $p = 20 - 100$ mbar, $L_c^{\mathrm{N_2}} = \pi/(2k_\omega - k_{2\omega}) \approx 60 - 300$ cm, and in ambient air, $L_c^{\mathrm{Air}} \approx 6$ cm, is very long, such that the phase mismatching is not expected to affect the signal in the plasma or in ambient air. On the other hand, the coherence length in quartz made of fused silica is much shorter, $L_c^{\mathrm{FS}} \approx 10$ μm, such that the wall thickness strongly affects the electric field induced second harmonic signal generated in the wall.

The line-of-sight integrated second harmonic signal $I_x^{(2\omega)}$ is therefore proportional to number density of generating medium squared n^2, electric field in the generating medium squared E_x^2 and laser pulse intensity squared $(I_x^{(\omega)})^2$. To simplify the visualization of quadratic dependence between experimentally measured $I_x^{(2\omega)}$ and n, E_x, $I_x^{(\omega)}$, all Figures in the present chapter are done for $\sqrt{I_x^{(2\omega)}} \sim n, E_x, I_x^{(\omega)}$.

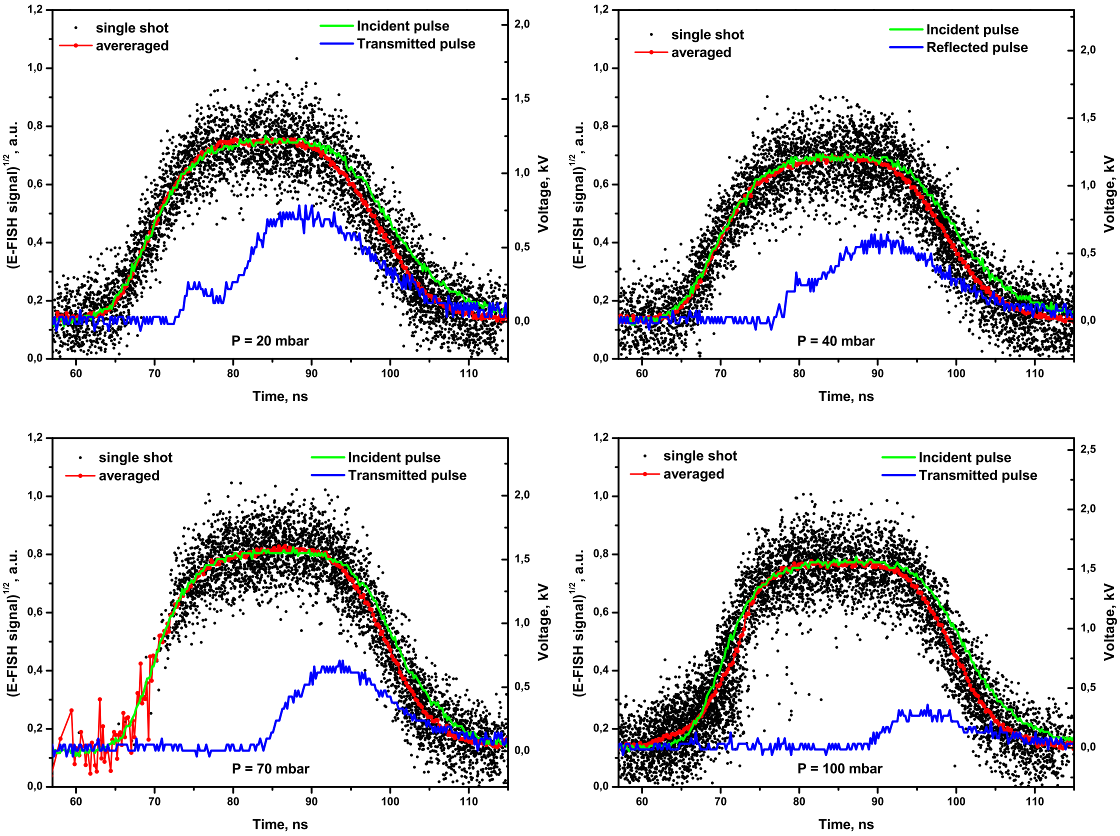

Figure 5.10 – E-FISH signal of calibration Laplacian field calculated by SHG code for $20, 40, 70$ and 100 mbar as a function of time. To ease the visualization, only each 10^{th} single shot data point (black dots) is shown. Red line and dots show signal's average value calculated by SSC code. Incident and transmitted pulses are shown in green and blue, respectively.

For each pressure condition, a care was taken to ensure that discharge does not appear during calibration. With laser beam blocked, the incident voltage pulse amplitude was first set equal to the reference voltage value preliminarily deduced from Paschen's law. The voltage amplitude was then adjusted to its maximum value that does not cause electrical breakdown ensured by absence of the transmitted voltage pulse. Laser breakdown was excluded as well because no spike of laser intensity was observed at photodiode.

Figure 5.10 shows time-dependent square root of second harmonic signals $\sqrt{I_x^{(2\omega)}}$ measured from calibration Laplacian electric field at all tested pressures together with synchronized incident and transmitted voltage pulses. The E-FISH signal accurately captures the shape of incident pulse, especially during rise and plateau indicating that the expected quadratic dependence of the signal on the applied electric field is observed. However, the source of a slight systematic deviation on the falling section is yet unclear but could be due to development of a very weak discharge.

The idea of presence of a weak discharge is supported by the ubiquitously present non-zero transmitted pulse, as seen at Figure 5.10. Breakdown actually occurs during E-FISH calibration when laser pulse enters inter-electrode space under high voltage. Since no signs of laser breakdown were observed at photodiode, a synergetic event of laser assisted breakdown is supposed where laser electric field enhances gas ionization in near high voltage electrode space. Note that no plasma emission was visually ascertained during calibration at any pressure condition. In accordance with Paschen's law, it was observed that the breakdown voltage in a discharge tube with fixed electrode configuration changes with pressure. For each pressure, the breakdown voltage defines maximum electric field accessible during calibration.

For further treatment, only single laser shot events happened before breakdown were taken for calibration with the exception of 70 mbar pressure case. For this pressure, due to memory stock issue at the oscilloscope, the data on the rising edge of the high voltage pulse was lost. As seen at other pressure conditions, if synchronized to the falling edge of the incident high voltage pulse, square root of the second harmonic signal follows it exactly. In view of situation, the data for 70 mbar pressure was taken at the falling edge of the incident high voltage pulse.

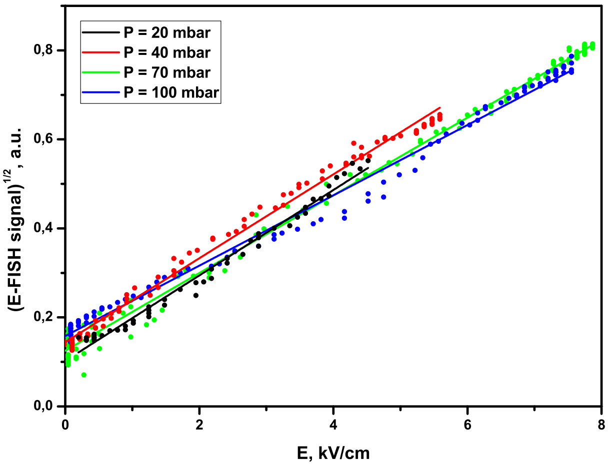

Figure 5.11 – E-FISH signal of calibration Laplacian field calculated by SHG code and averaged by SSC code for $20, 40, 70$ **and** 100 **mbar as a function of applied electric field. Solid lines show linear fits.**

Figure 5.11 plots the square root of calibration pre-breakdown averaged second harmonic signals $\sqrt{I_x^{(2\omega)}}$ together with least squares linear approximation as a function of applied Laplacian electric field at four different pressures. For all four pressures, the square root of the second harmonic signal is proportional to the applied electric field, as expected by E-FISH diagnostics. However, it is readily apparent that varying the pressure in the tube by a factor of 5 has essentially no effect on the signal. This indicates that most of the signal is generated not in the nitrogen within the tube, but in a medium of a constant number density in the line of propagation of laser pulse which is either the quartz wall or the atmospheric pressure air outside the tube. Such side-origin generation is possible due to the electric field extending beyond the space between the electrodes.

The third order susceptibility of fused silica at 1064 nm is nearly 4 orders of magnitude larger compared to that of atmospheric pressure air, $\chi^{(3)}_{\mathrm{FS}} = 2 \cdot 10^{-22}$ m^2 V^{-2} [179,180] *versus* $\chi^{(3)}_{\mathrm{Air}} = 3 \cdot 10^{-26}$ m^2 V^{-2} [71,180]. If laser pulse intensity and electric field are presumed identical, the second harmonic signal from the ambient air would be comparable to that originating within the discharge tube quartz wall only if it is produced over a distance of $L \sim L_c^{\mathrm{FS}} \cdot \chi^{(3)}_{\mathrm{FS}} / \chi^{(3)}_{\mathrm{Air}} \sim 7$ cm. This is extremely unlikely in the conditions of the present experiment, since the laser beam diameter over this distance is increasing from ≈ 0.5 mm at the wall to ≈ 4 mm, and since the electric field outside of the discharge tube is decreasing as $\sim 1/R^2$ with distance R to the HV electrode. It is therefore concluded that at the present conditions, the signal is likely to be generated in the quartz wall.

The estimate above is consistent with the results of [72], which show that for tight focusing configurations, *id est* for the lens focal distance of 15 cm and 30 cm, the second harmonic signal is also generated from regions beyond the confocal beam parameter. This means that at present conditions, the contribution of electric-field induced signal from tube wall could be dominant. Fused silica has no volumic but superficial generation of the second harmonic. Basically, Laplacian electric field calibration indicated that at present conditions, reduction of electric field and of laser pulse intensity at beam focal point with distance from the beam focal point is overcome by much higher nonlinear susceptibility of outlying quartz wall compared to that of N_2 of $20 - 100$ mbar pressure gas at the focal point. At the present discharge tube, the second harmonic signal is presumed to be sensitive to the electric field within the wall of the discharge tube. The conclusion seems more reliable in view that calibration electric field reached its maximum value which is limited by breakdown voltage. As a consequence, the plane-to-plane Laplacian electric field calibration may well be inaccurate. Because of such thought, error bars and linear fit values were omitted from Figure 5.11 to avoid confusion.

For absolute calibration in present experiment, an alternative method using calibrated back current shunts and capacitive probes was employed. The square root of second harmonic signal is matched to the electric field waveform obtained from back current shunt waveforms during incident high voltage pulse's fall, well after the fast ionization wave reaches the low voltage electrode and discharge develops. In case of quasi-steady-state discharge, electric field is lower than such at breakdown because the current passing through the discharge cell lowers the voltage drop between the electrodes. Fortunately, for the present experiment, the validity region of calibration method by quasi-steady-state electric field can be well extended. Though the generating medium was found to be not the gas inside the discharge tube but the material of the tube wall, the Laplacian electric field calibration has revealed that the second harmonic signal measured at the present setup scales quadratically with applied electric field up to the value limited by breakdown voltage. In the present case it means that if for each gas pressure another calibration method (BCSs) provides absolute scaling at sub-breakdown electric field values, this scaling can be safely extrapolated up to the breakdown electric field values shown at Figure 5.11 measured Laplacian electric field calibration. Such combination of two calibration methods allows to solve the issue of unexpected source of second harmonic signal.

5.6 Second harmonic signal: single laser shot and averaged

Figure 5.12 plots square root of the second harmonic signals, single shot and averaged, for all considered pressure conditions. Black symbols indicate second harmonic signals calculated from the so-called events - single laser shots that had passed selection criteria of SHG code. In its turn, red symbols show the average values and statistical uncertainty of second harmonic signals calculated by SSC code for events in each one of 0.2 ns time bins.

From Figure 5.12, different phases of the discharge development are readily identified and well understood, based on the previous lower-fidelity electric field measurements by capacitive probes [45, 181–183], theoretical analysis, and kinetic modeling predictions [39]. During E-FISH experiment, the evolution of electric field was observed at measurement point located in the middle between electrodes. Fast ionization wave initiated in proximity of high voltage electrode propagates along the discharge tube towards the measurement location. Laplacian electric field generated ahead of the approaching fast ionization wave causes the initial gradual rise of the signal. The peak of the signal occurs when the front of the fast ionization wave arrives at measurement point. Then, signal rapidly decreases due to screening in plasma generated behind the front of the wave so that FIW's Laplacian electric field no longer influences the measurement point. The electric field behind the front is reduced considerably, but remains above the detection limit at all pressures tested. The observed electric field is that what makes the electrons created in the wave front to transport in direction to the high voltage electrode, generating initial small

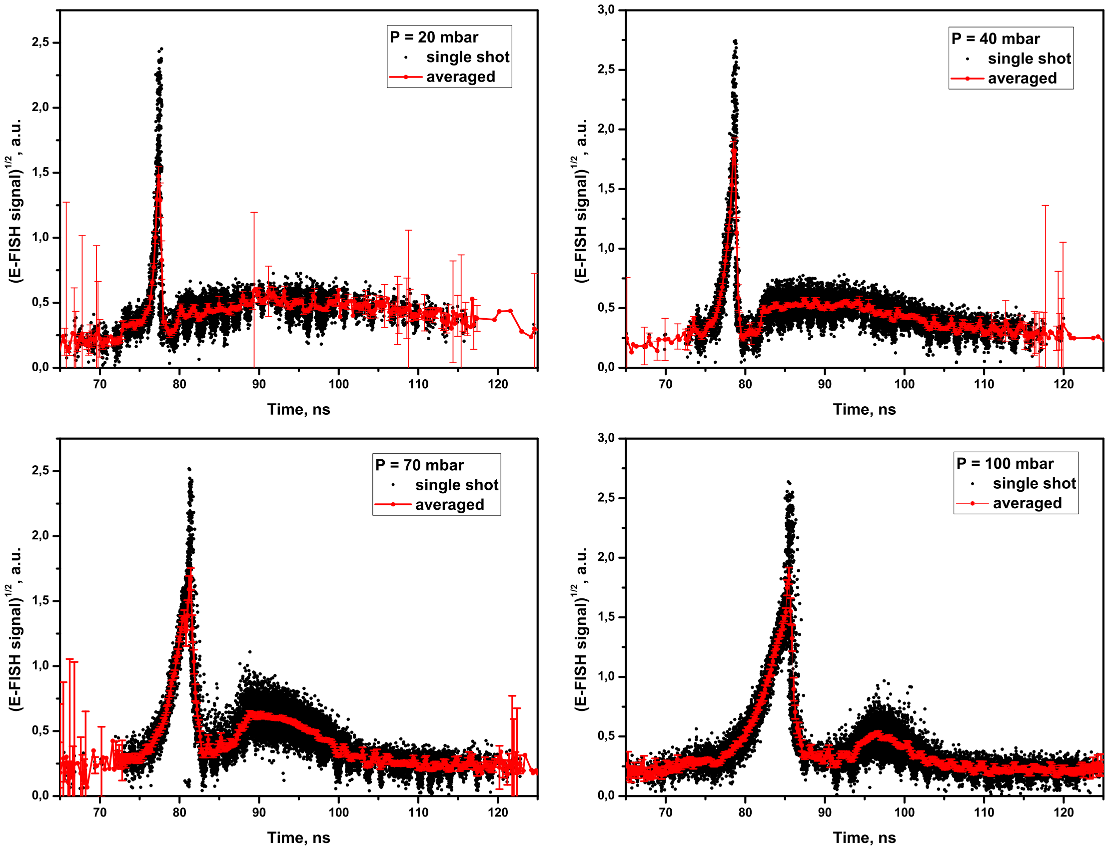

Figure 5.12 – Second harmonic signal as a function of time for $20, 40, 70$ and 100 mbar. Black symbols are single-shot data points calculated by SHG code, red symbols are averaged data points and statistical uncertainty of the data in 0.2 ns time bins calculated by SSC code.

conduction current. Displacement current phase ends when the wave front arrives at cathode embodied by the low voltage electrode. The secondary emission electrons generated from cathode's surface accelerate towards high voltage electrode and close the inter-electrode gap. While the current across the discharge tube reaches its maximum, the discharge develops into a quasi-steady-state regime. The electric field rises for the second time to the value defined by voltage drop over inter-electrode distance. Finally, the electric field decays to near detection limit as the applied voltage falls to zero.

Figure 5.13 shows histograms of selected events *versus* all performed laser shots for each bin together with laser pulse energy taken during the discharge in N_2 at 40 and 100 mbar. The single laser shots that were not selected by SHG code have mostly failed to pass the EM noise discrimination criterion. The EM noise from the touchdown of the FIW to the LV electrode was found to be stronger than during quasi-steady-state phase. Also, the longitudinal electric field before arrival of the

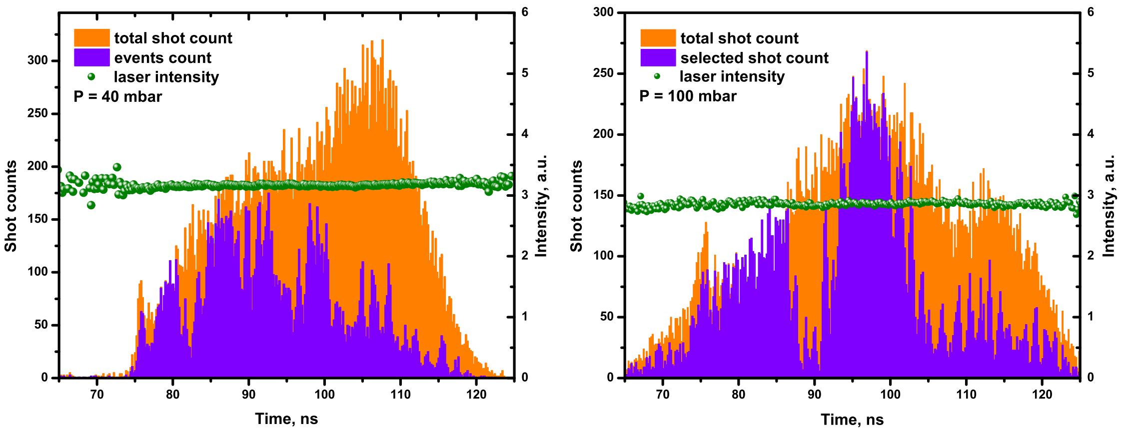

Figure 5.13 – Laser count histograms as a function of time for 40 and 100 mbar. Orange bars are distributions of > 40000 total laser shots, purple bars are distributions of E-FISH events selected by SHG code. Laser pulse energy is plotted on top in green.

FIW to the measurement location and during the falling edge of the high voltage pulse is close to the detection threshold of the technique. Such relation explains decrease in event selection at these times. The event count number beating of an approximately 760 MHz frequency is also associated to EM noise.

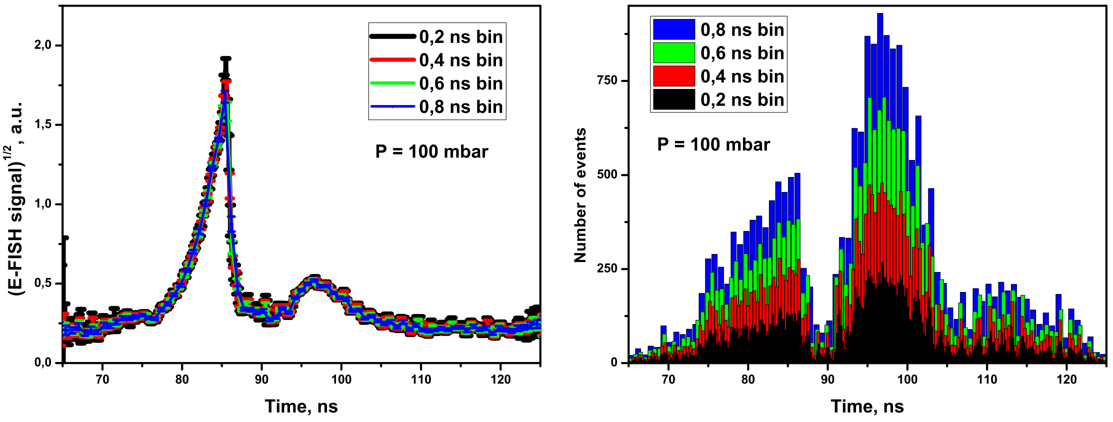

Figure 5.14 – Average E-FISH signal at 100 mbar calculated by SSC code for different time bins: (a) averaged signal's value and statistical uncertainty, (b) bin-distributed histogram of selected events.

Figure 5.14(a) plots averaged single laser shot second harmonic signals over time bins of different widths for 100 mbar pressure case. Figure 5.14(b) plots histogram for each selected bin width. For each pair of widths $t_b > t_a$, the main value of the t_b time bin falls within the expected interval of the t_a time bin. It also shows that the error bar decreases with increase of the time bin width. Such convergent behavior of mean value with an increase of number of averaged events is an indirect indication of reproducibility of an experimentally measured quantity. For the present experiment, smallest possible 200 ps bin width was chosen.

5.7 Background contributions: stray second harmonic and plasma emission

The offset of the second harmonic signal shown at Figures 5.10, 5.12 and 5.14(a) was observed for all pressures tested and does not vary with pressure. Since no electric field is expected at the measurement point at times that are out of duration of the high voltage pulse, the offset is attributed to the stray second harmonic signal generated at glass-air optics' interfaces that are located downstream the discharge tube. For following, this constant offset was removed.

As expected, the electric field starts from zero and drops to zero together with incident pulse as observed for second harmonic signals at 70 and 100 mbar pressures. However, the signal at 20 mbar stays above zero up to the latter available time instant and does not show a decaying behavior. This time-asymmetric effect, though less pronounced, is present at 40 mbar pressure case as well. Plasma emission during the laser run was visually observed to be more intense at lower pressures. This observation led to suggestion of plasma emission origin of residual signal at 532 nm.

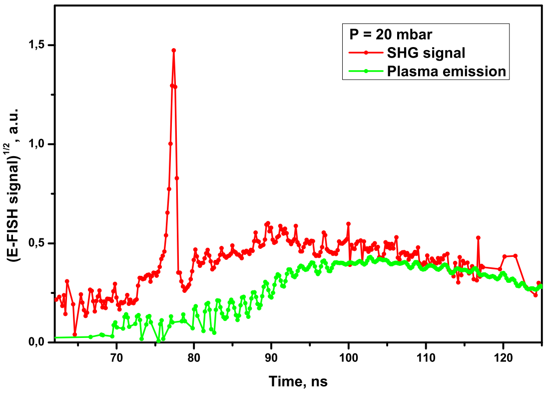

Figure 5.15 – Broadband plasma emission impact on the averaged second harmonic signal shown on the example of 20 mbar case.

For the most affected 20 mbar case, plasma emission was measured separately at the very same E-FISH setup ran at operating conditions unchanged except laser beam being blocked. Figure 5.15 plots the plasma emission second harmonic signal together with second harmonic signal recorded at 20 mbar. Plasma emission within bandpass of the filter before PMT initiates when the fast ionization wave arrives at the low voltage electrode and exhibits a monotonous rise during the presence of the high voltage pulse. Slight oscillatory behavior of plasma emission curve is of electromagnetic origin and stayed after low-pass EM noise filtering at data post treatment. After the FIW touchdown, second harmonic signal asymptotically approaches the curve of plasma emission. For further, this stray plasma emission is subtracted from second harmonic signal for the most affected 20 mbar pressure case. Signals at other pressure conditions also may be improved if similar procedure is performed.

5.8 Calibrated longitudinal electric field waveform

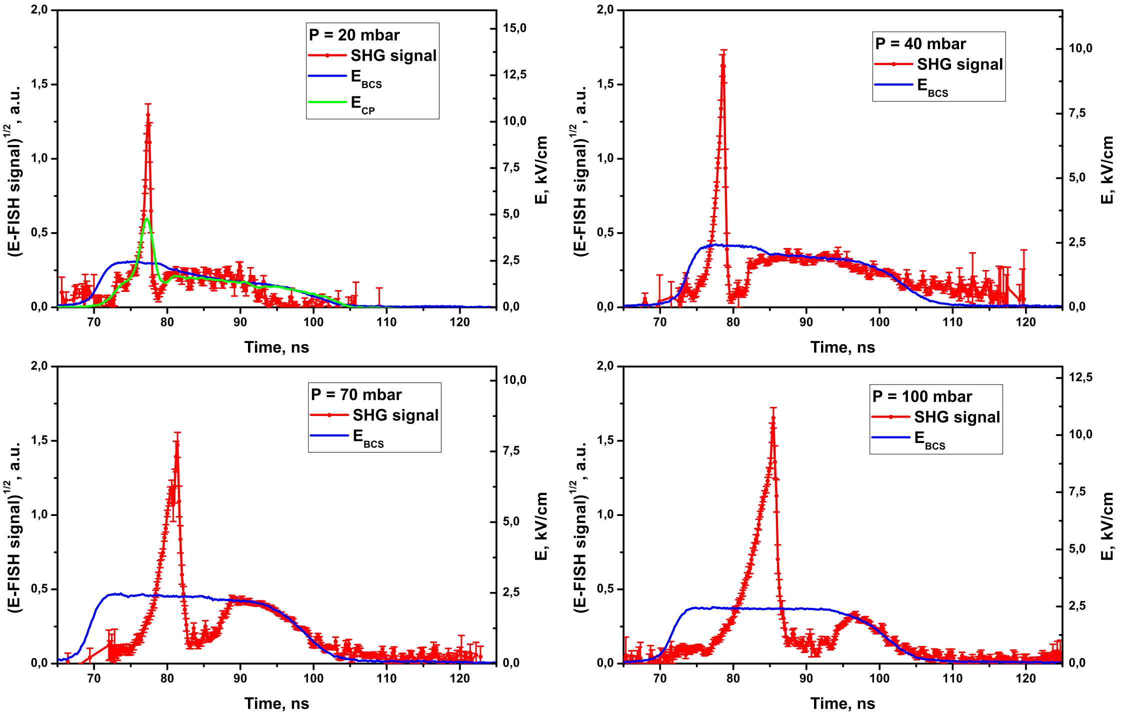

Figure 5.16 – Electric field in a fast ionization wave discharge in N_2 at $20, 40, 70$ and 100 mbar in nTD, plotted together with the back current shunt signal used for absolute calibration. Electric field inferred from the capacitive probe measurements is also plotted for 20 mbar case.

Figure 5.16 plots mean value and error of square root of the events' second harmonic signals averaged over 200 ps time bins together with the electric fields obtained by back current shunts. Capacitive probe data is added to 20 mbar case. It can be seen that according to expectations, the electric field waveform obtained by the E-FISH measurements matches the back current shunt waveform after the moment when fast ionization wave reaches the low voltage electrode for all studied pressures, including at 20 mbar where the signal-to-noise ratio becomes significantly lower that at other pressure conditions. The capacitive probe measurements also

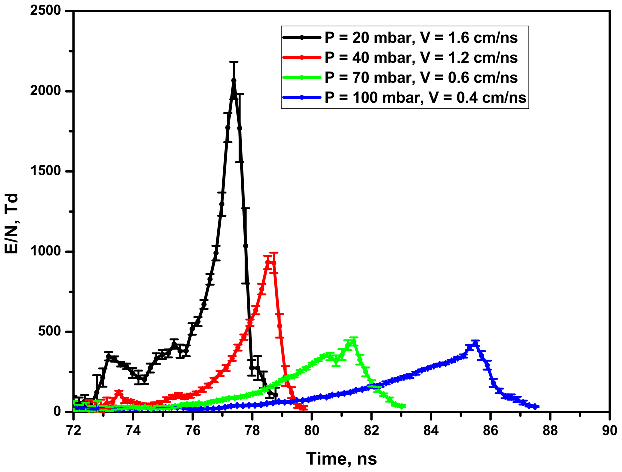

Figure 5.17 – Reduced electric field measured in the front of a fast ionization wave discharge in N_2 at $20, 40, 70$ and 100 mbar in nTD.

match very well the current shunt waveform in the quasi-steady-state discharge. Absolute calibration was possible because such coincidence between E-FISH and BCS waveforms was observed. However, it is readily apparent that the electric field peak in the ionization wave front, measured by the capacitive probe, is not fully resolved compared to the E-FISH data, meaning the apparent peak is wider and the maximum value is lower. This behavior is expected, since the effective time resolution of the capacitive probe (≈ 2.0 ns), limited by its spatial sensitivity, is up to an order of magnitude lower compared to that of the present diagnostic (200 ps).

Comparison of the data taken at different pressures exhibits several dominant trends. First, in the entire pressure range, the peak electric field in the ionization wave exceeds the quasi-steady-state value established after the wave reaches low voltage electrode, by up to a factor of 4 to 5. This is much higher compared to a relatively modest electric field overshoot of ~10% detected in a ns pulse discharge generated in 100 Torr of N_2 across a relatively short gap of 13 mm, where the fast ionization wave does not fully develop [184]. Second, the peak value of the longitudinal electric field in the wave front exhibits a fairly weak pressure dependence, $E_{peak} = 8 - 11$ kV/cm. Figure 5.17 plots the reduced electric field during FIW propagation for tested pressures. It shows that the highest reduced electric field, $E/N \approx 2$ kTd, is produced at the lowest pressure of 20 mbar, as expected. The gas density used in computing the reduced electric field assumes room temperature, which is anticipated given the low deposited energy density of this discharge. Third, reducing the pressure from 100 to 20 mbar, while keeping the discharge pulse voltage waveform the same, steepens the ionization wave front considerably, as illustrated at Figure 5.17. At 100 mbar, the full width at half maximum of the transient electric field peak in the wave front is 3.0 ± 0.2 ns, while at 20 mbar it is reduced to

1.0 ± 0.2 ns, and remains fully resolved by the present diagnostic. This behavior is most likely due to the faster electron impact ionization at a significantly higher reduced electric field in the fast ionization wave, as well as the more rapid electron transport behind the wave front, resulting in plasma self-shielding on a sub-ns time scale. Finally, the wave speed increases considerably as the pressure is reduced, from 0.4 cm/ns at 100 mbar to 1.6 cm/ns at 20 mbar. The wave speed at the present conditions was determined from the time-resolved integrated plasma emission intensity distribution measurements, such as that shown in Figure 5.8, with a relative uncertainty of 2%. The difference between the wave speed measured on the tube centerline and near the wall did not exceed 5%. The wave speed values are indicated in the legend of Figure 5.17. The length of FIW front estimated as a product of wave speed and full wisth at half maximum of FIW peak (Figure 5.17) is equal to ~ 1.5 cm at 20, 40 and 70 mbar and reduces to 1.2 cm at 100 mbar.

5.9 Conclusions

Non-intrusive time-accurate absolute measurements of longitudinal component of electric field in the front of FIW discharge sustained over a wide range of pressures are obtained for the first time. The E-FISH technique was calibrated against recognized electrical techniques such as back current shunt and capacitive probe for the first time as well. The data shows that the contribution of the discharge cell walls into the net electric-field induced second harmonic signal has to be identified and accounted for, *exempli gratia*, by using the electrostatic calibration over a wide range of pressures. Since the signal generated within the wall during the discharge is induced by the electric field, it cannot be easily subtracted from the net second harmonic signal, unlike the zero-field background. The temporal resolution of the present measurements, 200 ps, is limited only by the laser pulse duration, 30 ps, and may be improved by using equipment with higher sampling rate. In low and moderate pressure FIW discharges, E-FISH opens a possibility of detection and analysis of non-local electron kinetics effects in presence of rapidly varying, high peak value E/N. Finally, with additional calibration, the same approach can be used to measure the radial component of the electric field in the ionization wave front. The technique can also be used for assessing the predictive capability of kinetic models of FIWs generating breakdown on ns and sub-ns time scale. The present work where the electric field detection was done within the discharge tube wall demonstrates that ps second harmonic generation may be employed for electric field measurements at discharges with challenging features, *id est*, (i) at low pressure, (ii) in small diameter capillary tubes, and (iii) in gases with very low nonlinear polarizability such as He.

Chapter 6

Organization of N-atom TALIF experiment in nanosecond capillary (nCD) and tube (nTD) discharges

Nanosecond scale high voltage pulses have gained interest recently as a way to achieve high reduced electric fields of about 100 Td or higher. As discussed in greater detail in previous chapter, ns-scale HV pulse applied to the discharge tube causes an initiation of a fast ionization wave initiating in proximity of high voltage electrode. FIW propagates towards the other (grounded or floating potential) electrode with extremely high reduced electric fields reaching the value of $\sim 10^3$ Td at the FIW's front. After arrival of fast ionization wave's front to the other electrode, a quasi-steady-state discharge is sustained with relatively high reduced electric fields of order of ~ 200 Td until the end of the high voltage pulse. The presence of high reduced electric fields in plasma during high voltage pulse efficiently excites electronic levels of atoms and molecules and thus can possibly lead to molecular dissociation.

It has been shown that O_2 can be almost completely dissociated within 2 μs from the beginning of the discharge in nanosecond capillary discharge with specific deposited energy value of 1 eV/molecule. However, most of the current work indicates that it is extremely difficult to achieve a high dissociation degree of N_2 molecules in a gas-discharge nitrogen plasmas. This is primarily because of the very high dissociation barrier of N_2 (9.76 eV), much higher than that of O_2 (5.12 eV) [155]. Thus, some effort has been put to numerically investigate the mechanisms behind N-atom creation [136].

According to calculations done for atmospheric pressure nanosecond pulsed discharges with specific deposited energy at the order of 10^{-4} eV/molecule [136], the quenching of pre-dissociative N_2 states is negligible and the electron impact dissociation of N_2 is the main source of N-atoms. Comparison of calculated N-atom production energy cost with two experimental data points obtained at ~ 140 Td (first reported at [135] and further published in [132]) and ~ 850 Td [134] reveals a good agreement with the results of calculations.

At low values of specific deposited energies, main reactions happen between reactive species and bath gas (sometimes called as "classical kinetics" in literature). In case of high values of specific deposited energies, the probability of interaction among reactive species becomes higher due to increase of reactive species' densities. It is a consequence of more efficient excitation of electronic and vibrational levels of atoms and molecules in a mixture with high values of specific deposited energies. As known from [44], in nitrogen plasma at 27 mbar with high reduced electric field of the order of 150 Td and high specific deposited energy of the order of 1 eV/molecule, electrons reaching number density of 10^{15} cm^{-3} become the main quencher of the $N_2(C)$ state. Though not studied previously, it is only natural to presume that such high electron number density might influence other species's evolution as well, in particular, N_2 dissociation.

The evident lack of experimental verification of calculations [136] and unclear influence of specific deposited energy on the main reaction of N_2-dissociation has motivated the current research. The main objective of this study is to examine the N-atom density and energy efficiency in a moderate pressure high reduced electric field nanosecond discharges of high and low values of specific deposited energies. The main interest gravitates around improving the understanding of reduced electric field's and deposited energy's influence on discharge kinetics by providing experimental data in a variety of high E/N values to support related modeling efforts.

The task was split in two. Existing nanosecond capillary discharge (nCD) mentioned in [44] was used to evaluate the energy cost of N-atom creation in conditions of high reduced electric field and high specific deposited energy. Concerning the case of low specific deposited energy, a separate nanosecond tube discharge (nTD) setup was specifically developed. Additionally, while staying at roughly the same values of high reduced electric fields, nTD setup potentially allows one to modify the value of E/N during discharge's quasi-steady-state regime by changing the inter-electrode distance.

Both nCD and nTD setups were designed for similar needs by the same engineering team and so have a high degree of likeness in construction and shared power and gas supply systems. In order to assess N-atom number density in both setups, it has been decided to perform nanosecond dye laser-driven TALIF measurements with Kr noble gas absolute calibration. Consecutively, apart from the laser system itself, the majority of optics used to shape and deliver the laser beam to measurement location was also shared by the experiments. The same goes with respect to triggering scheme and data collection software. The aim of the present chapter is thus to introduce the organization of N-atom TALIF experimental setup in nanosecond capillary (nCD) and tube (nTD) discharges.

6.1 Description of laser system and fluorescence collection experiment

The laser system used for the TALIF experiments consists of a Sirah Lasertechnik Cobra Stretch dual-grating dye laser driven by a frequency-doubled Spectra Physics Quanta Ray Nd:YAG 532 nm pump laser. Flash lamps of pump laser create a beam that is absorbed by Rhodamin B-101 ethanol-diluted dye mix used as a lasing media and converted to the light within the visible range of interest, namely $612 - 621$ nm. It is then frequency-tripled *via* two successive alpha-BBO nonlinear crystals to yield 3 mJ, wavelength-tunable UV pulses near 206 nm with a FWHM pulse duration of about 6.5 ns. These laser pulses are used for TALIF diagnostic described below. Since there is no O_2 and N_2 absorption bands in $204 - 206.7$ nm wavelength range, it is considered that laser beam suffers no important energy losses while propagating to the measurement location.

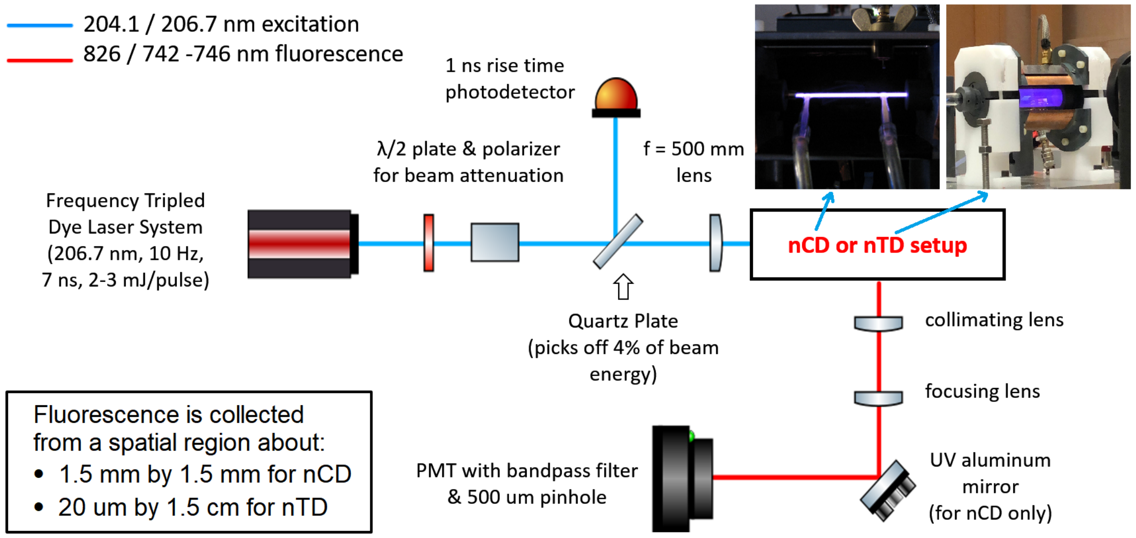

Figure 6.1 – Principal optical scheme of TALIF experiment.

In order to match the height of the laser beam to the height of discharge cell, a pair of right-angle prisms is placed. The height-shifted laser beam then hits the optical system, shown at Figure 6.1. The propagation of the beam within the horizontal plane is ensured by imaging the laser spot at the graph paper card placed perpendicularly to the surface of the optical table along the distance of 2 m following the prisms' output. Subsequently, after each new element introduced to the optical path, the absence of beam's spatial shift is checked in the same manner. In order to modify the energy of the beam's input to the discharge, a pair of two mutually compensating, near-Brewster's angle wave plates followed by a horizontal polarizer are placed. Wave plates rotate the polarization of beam's electric field meanwhile linear polarizer lets pass only its horizontal component and so allows controlled input of the laser energy with a typical values of laser energy of $10-35$ and $85-220$ μJ for Kr and N-atoms measurements, respectively. An iris placed after the linear polarizer (not shown) cuts the undesired upstream reflections from glass-air interfaces already hit by beam.

Then, an approximately 4% of the main beam gets reflected from the air-glass surface of the glass slide introduced at the $\sim 45°$ angle to the axis of propagation of the beam. This probe beam reaches the dispersive prism that spatially separates the residual dye fundamental from the dye-tripled UV light. The UV light is used to monitor shot-to-shot variations of laser energy by Thorlabs DET10A/M longpass ($200-1100$ nm) 1 ns rise time Si biased photodiode detector, for short addressed as PD in following text. To ensure that the arriving light reaches the relatively small (1 mm^2) PD sensor in homogeneous and non-damaging way, diffusive glass and NDUV10A filter are mounted on the optical entrance of PD.

The remaining 96% of the main beam arrives at the 500 mm focal distance plano-convex convergent Thorlabs LA4184-ML lens that shapes the beam to 30 um beam waist along 15 mm in the proximity of the focal point. A $2-3$ mm precision in defining the laser focal point is achieved with the help of a paper card moved along the beam at the proximity of the expected focal point's position.

The optics alignment for fluorescence collection is done with use of a point-like pre-wired micro 0402 SMD red LED light source placed at laser focal point as to imitate the original source of fluorescence. The collection of the fluorescent light is done from side view, meaning perpendicularly to the axis of the propagation of the laser beam at its height. A 3 inch (75 mm) diameter 200 mm focal distance plano-convex Thorlabs LA1353 lens was placed to collect the LED's divergent light and convert it to the collimated beam. It was further received by 3 inch (75 mm) diameter 85 mm focal distance plano-convex Thorlabs LA1740 lens and focused directly to the photocathode of the Hamamatsu Photo Sensor Module H7422P-50 (PMT). The narrow-band filter of the wavelength corresponding to such of the fluorescence collected during the experiment is mounted before the entrance of the PMT as well as an appropriate neutral density filter (Thorlabs NDUV 1 inch set) if needed. To decrease the influence of EM noise, cables used for PMT's gate operation and output signal delivery were double-shielded, and PMT has been put inside of the grounded Faradey cage. Having the fluorescence light collection path prepared, it is only necessary to replace the LED imitation by actual discharge setup with matching spatial disposition according to the laser beam. Since the laser beam is not absorbed completely along its path in the discharge setup, a beam trap is placed at the exiting round quartz window.

6.2 Delay generator triggering scheme

The triggering scheme was built using two BNC Model 575 pulse delay generators. Two time constraints had to be taken into account: (i) the delay between lasers' lamp and Q-switch input triggers and (ii) the delay between high voltage generator's (HVG) input trigger and HVG output synchronization trigger. The first time delay is a manually set parameter, the 180 μs value was found to be the best for the release of the collected lasing excitation after the inversed population has reached its maximum and had not degraded yet. The second time delay of 18 μs is strictly imposed by the internal circuit of the HVG and characterizes the time lag between the incoming trigger to HVG and HVG output synchronization trigger.

Kr-calibrated N-TALIF technique requires two principally different triggering schemes: one including HVG to perform N-TALIF in plasma and one excluding HVG for Kr-TALIF calibration.

For the N-TALIF scheme, BNC1 by Channel A sends a TTL signal to externally trigger laser lamp to start the accumulation of inversed population. Meanwhile, Channel B sends a 7 V pulse to the HVG input to set off the HV pulse to the discharge cell. Following the arrival of the HVG's input trigger, HVG output synchronization trigger is sent to BNC2 input. BNC2 by Channel A sends a TTL signal to externally trigger the Q-switch to release laser shot while Channel B sends a TTL pulse to gated PMT. This scheme allows to synchronize laser pulse release with gated PMT's opening for a controlled time delay of any value within the repetition period, $1/(10\ Hz) = 100\ ms$, related to the plasma ignition. Due to the imposed time delay of 180 μs between lasers lamp and Q-switch input triggers, two triggering orders should be used to perform TALIF on N-containing plasma. For the probing delays related to plasma ignition inferior to 180 μs, HVG is triggered after laser lamp and before Q-switch. For the probing delays related to plasma ignition between 180 μs and 100 ms, HVG is triggered before both laser lamp and Q-switch.

For the Kr-TALIF scheme, measurements are performed in Kr constantly flown directly from the bottle to the discharge cell with no HV pulse applied. Due to time indifference, the laser pulse can be released anytime. Scheme is thus built based on laser's internal 10 Hz triggering and requires only one BNC that is triggered by laser's Q-switch output TTL signal and opens the gate of gated PMT.

The LeCroy WaveRunner 64Xi-A digital oscilloscope with a 5 GHz sampling rate and 600 MHz bandwidth was used to monitor the waveforms from PMT and PD. Oscilloscope was triggered from laser's advanced Q-switch synch-out channel that gives a few μs long TTL signal once Q-switch is triggered and laser beam is released. The acquired files were ported to PC by RJ45 connection for further treatment.

6.3 Data collection and preliminary treatment

It was experimentally established that to obtain the repetitive laser waveform with FWHM fluctuations not exceeding 0.2 ns in time and 3% in amplitude, at least 350 accumulations need to be averaged. Also, it has been seen that fluorescence signal of a single laser shot exhibits an insufficiently low signal-to-noise ratio leading to impossibility of accounting for quenching. Due to these reasons, waveforms of fluorescence signal and laser waveform profile were averaged over 400 single laser shots.

The custom-made LabView program, courtesy of Dr. S M Zyryanov, was used for remote control and automation of data acquisition. The program modifies dye laser's wavelength by adjusting positioning motors of the crystals FCU1 and FCU2, collects the waveforms averaged for a user-defined number of single-shot events from the oscilloscope by RJ45 port, and performs primary data processing such as shown in the table below.

The background light that was subtracted during data acquisition is supposed to be composed of two main contributions: non-resonant plasma emission and the fluorescence of the quartz tube. The latter contribution persists even several hundred picometers away from the peak signal wavelength. Presuming that its value is independent of wavelength within the spectral scan range, the quartz fluorescence was determined by simply tuning the probe laser off-resonance.

Procedure	Why?	How?
Background correction	EM noise, non-resonant plasma emission, quartz tube fluorescence	File acquired with laser beam blocked and automatically subtracted from each following acquired averaged waveform
Offset correction	Variant from shot-to-shot EM noise and optical pollution	Corrects for a manually user-defined baseline region that is physically supposed to have no signal
Signal integration	Provides TALIF data	Is applied after background and offset corrections. Integrated the signal within a manually user-defined region
Laser scan	Provides TALIF data	Performs wavelength scan, plots integrated PD and PMT signals as a function of laser wavelength

Chapter 7

Time resolved N-atom number density measured in nanosecond capillary discharge (nCD) by TALIF technique with Kr calibration

The paragraph introduces reader to organization of the next two chapters that present results and discussion of TALIF experiments performed in nCD and nTD. First, Kr and N fluorescence signals are taken over a span of laser energies in order to define the value required for linear regime. Second, spontaneous emission rate and quenching rate with bath gas are deduced from pressure-dependent signal decay rate and compared with literature. Third, Kr and N fluorescence signals are resolved spectrally in proximity of appropriate fluorescence transition to ensure that PMT signal represents the considered transition. Once the concerns above are addressed, chapter presents time evolution of deduced N(^{4}S)-atom density together with time dependent fluorescence decay rate and discusses the observed trends from the point of view of kinetic processes. This chapter's content was partially published in [185].

7.1 Laser energy value required for TALIF linear regime in N and Kr

To ensure operation within the "linear regime", TALIF signals at resonance are measured for various levels of the laser energy. Plotting the logarithmic values of both the TALIF signal and the laser intensity (given by the integral of the photodiode signal) as displayed in Figure 7.1, yields a slope of about 2 for both the case of Kr (2.11) and N (2.08). Although full spectral scans are not taken for these data, a similar procedure whereby fluctuations in the laser intensity are limited to ±3% of a mean value is still observed. The laser energy used in the case of N was about 85 μJ and the corresponding value for Kr was about 30 μJ.

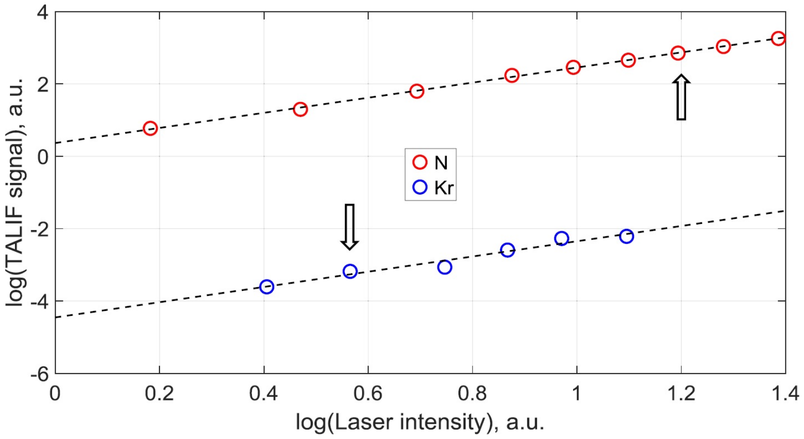

Figure 7.1 – Logarithmic plots of TALIF signals *versus* laser intensity for Kr and N. The laser intensities used in the respective experiments are indicated with black arrows.

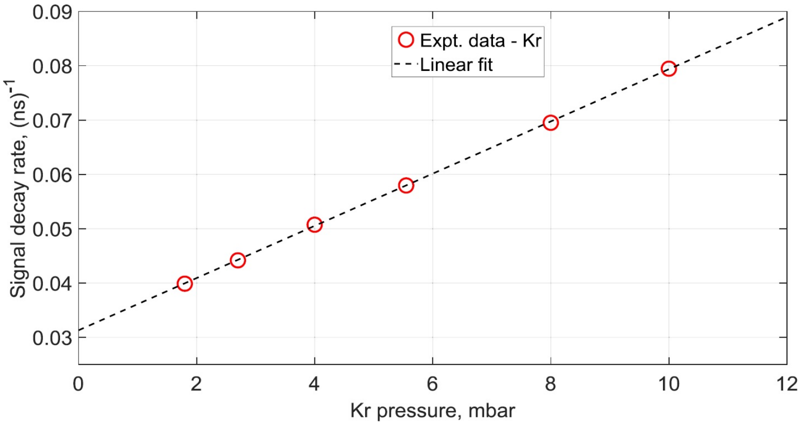

Figure 7.2 – Kr signal decay rate as a function of pressure. The random uncertainty of these measurements is about 3%.

It has to be reminded that the laser focusing was done off the central axis of the 1.7 mm diameter discharge capillary in order to prevent tube's damage. It means that the laser beam arrives to the measurement location being yet unfocused. Consecutively, the laser intensity that caused excitation of Kr and N atoms to respective fluorescent states should not be calculated at the laser's beam waist. It has been thus chosen to express the laser energy in arbitrary units to prevent misinterpreted estimates of the actual laser intensity. As a final note, since the TALIF signals are also dependent on the square of the temporal variation in the laser intensity, the data is also corrected for small differences in the mean temporal profile of the laser pulse for Kr and N. These small differences are believed to arise from the non-uniform lasing efficiency of the dye at slightly different resonant wavelengths.

Figure 7.2 shows the Kr TALIF decay rate as a function of pressure. The values of the natural radiative rate $A_{\mathrm{Kr}} = 3.08 \cdot 10^{7}$ s^{-1} of the Kr 5p$'$ $[3/2]^2$ state and the Kr self-quenching rate $Q_{\mathrm{Kr}} = 1.9 \cdot 10^{-10}$ $\mathrm{cm}^{-3}\mathrm{s}^{-1}$ were obtained from a linear fit to Figure 7.2 data as the y-intercept and the gradient, respectively. The natural radiative lifetime of the Kr 5p$'$ $[3/2]^2$ state was found to be equal to $1/A_{\mathrm{Kr}} =$ 32.5 ns exhibiting excellent agreement with the value 34.1 ns from [128]. However, the measured quenching rate Q_{Kr} only offers relatively modest agreement with the value $1.46 \cdot 10^{-10}$ $\mathrm{cm}^{-3}\mathrm{s}^{-1}$ from [128]. The experimentally measured values of the corresponding natural radiative rate A_{Kr} and decay rate $A_{\mathrm{Kr}} + Q_{\mathrm{Kr}}$ have been used for computing the absolute N-atom density based on rate equation approach. The overall systematic uncertainty due to the difference in A_{Kr} and Q_{Kr} measured values with respect to [128] is estimated to be less than 7%.

N and Kr fluorescence spectral composition

The paragraph presents comparison of experimentally measured transmission function of used band-pass filters with their respective datasheets and discusses the spectral composition of the N and K fluorescence signals. Figure 7.3 shows 1000 laser shots averaged fluorescence spectrum of (a) Kr and (b) N acquired with and without band-pass filter by ANDOR SR-500i-B1 infra-red sensitive spectrometer.

As expected, the Kr spectrum at Figure 7.3 (a) shows the presence of the 826 nm atomic fluorescence. However, an exception is that at higher pressures in excess of 9 mbar, the presence of two other lines at 828 and 830 nm is observed. The source of these extraneous emission lines has not been further examined, but could be associated with either collisional processes or electron-ion recombination into various excited states. It is important to point out that these lines fall within the transmission linewidth of commonly used bandpass filters for the Kr 5p$'$ $[3/2]^2$ to 5s$'$ $[1/2]^1$ transition, and may constitute a source of error when interpreting PMT data, if not taken into consideration. Interestingly, the presence of additional fluorescence features has also been observed in femtosecond-TALIF related research [130, 131].

Figure 7.3 (b) shows that the three fine structure N-atom lines are faithfully captured in experimental fluorescence spectrum. The relative individual linestrengths, computed as spectral integral of each line normalized by total spectral integral, are 0.15 : 0.33 : 0.51 exhibiting excellent agreement with NIST published data 0.15 : 0.32 : 0.53 [154]. Experimentally measured transmission function shows very good agreement with the datasheet values for the filter used for Kr but only fair agreement for that of N. Since the effective transmission given by the product of respective normalized linestrengths with either experimental or datasheet values only differ by 1%, no further attempt was made to understand this discrepancy.

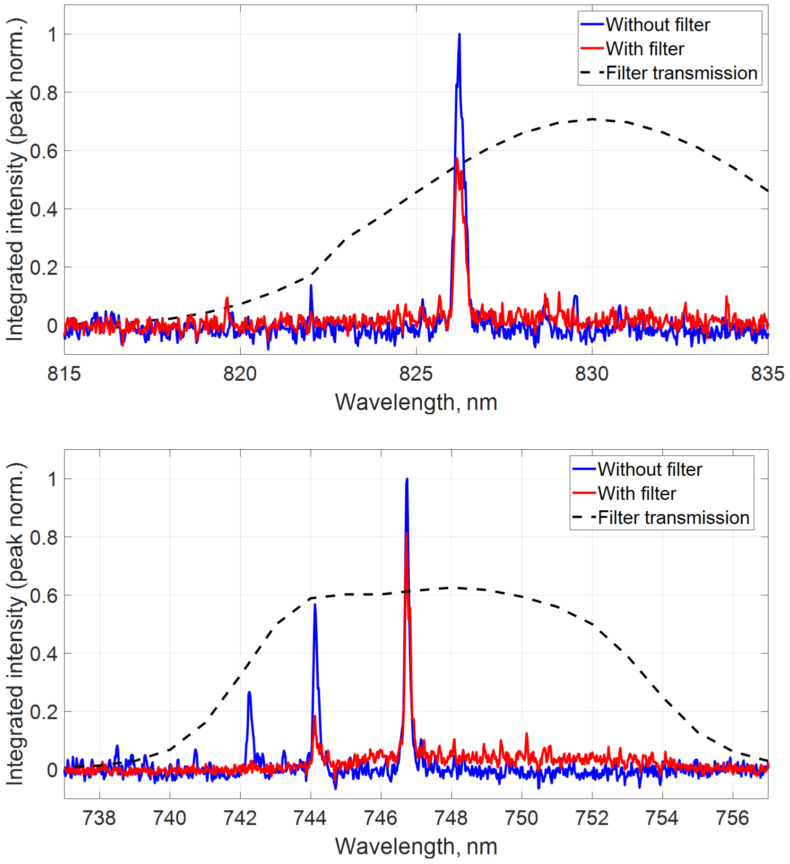

Figure 7.3 – Peak normalized fluorescence spectra of (a) Kr at 2.7 **mbar and (b) N at** 27 mbar **taken with (in red) and without (in blue) the appropriate band-pass filter with datasheet transmission function (dashed). The N-atom spectra are acquired** 160 μs **after discharge initiation.**

7.2 Plasma emission superimposition with N-atom fluorescence signal

Figure 7.4 shows maximum normalized temporal profile of the PMT captured plasma emission in nCD setup. For amplitude comparison, a peak at ≈ 2.5 μs illustrates a typical N-TALIF signal. The main difficulty of time resolved N-TALIF measurements appear in the early afterglow. In accordance with the plasma mode realised, the plasma emission has a slightly different amplitude from shot to shot. This shot-to-shot variation easily drowns the N-TALIF signal during the discharge. In the afterglow though, the variation gets smaller with time. So does the emission amplitude making plasma emissions noise impact on TALIF signal less important. So, the N-TALIF measurements in the early afterglow were possible only at time instant preceding the reflected HV pulse arrival when (i) the emission was the most

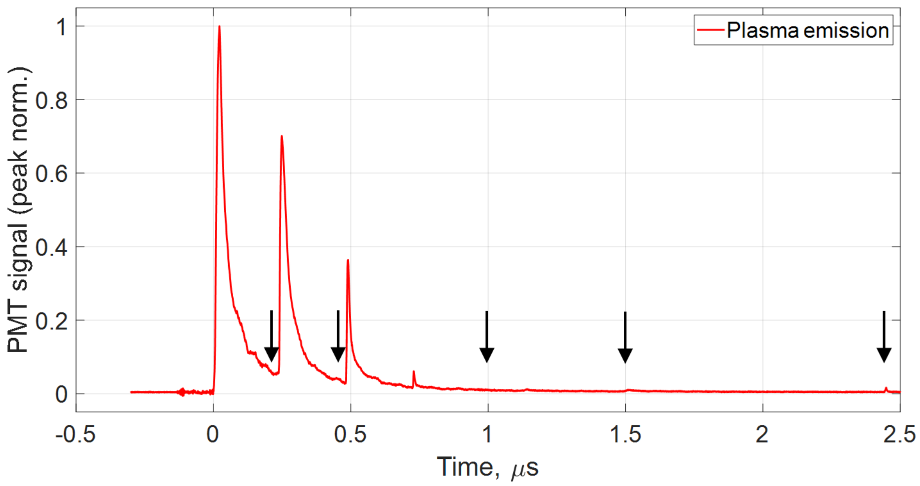

Figure 7.4 – PMT time trace acquired during the early afterglow of the discharge, illustrating the strong background emission from the plasma up to about $t = 1$ μs. The small peak near $t = 2.5$ μs provides an example of a representative TALIF signal. Black arrows correspond to time instants of the TALIF measurements relative to this emission signal.

reproducible and when (ii) the signal-to-noise ratio was the best possible. Totally the N-atom density was tracked from early times at about 300 ns after the first HV pulse and until several tens of milliseconds after the initiation of the discharge.

7.3 Temporal evolution of N-atom number density and decay rate

Figure 7.5 presents the time evolution of the N-atom density in nCD together with the associated characteristic timescales. The error bars at the N-atom number density data indicate random errors obtained as a result of repeated experiments at two different collection angles (side and bottom views) and at reduced laser energies.

The measurements were performed before the laser repetition $\tau_{\rm rep} = 100$ ms and gas renewal $\tau_{\rm gas} = 40$ ms timescales that are equipment-defined only. The acoustic timescale $\tau_{\rm ac} \geq 57$ μs and the typical cooling time $\tau_{\rm heat} = 46$ μs were estimated for $T \leq 1000$ K based on nCD measurements. The N-atom radial diffusion time $\tau_{\rm diff_N} \leq 10$ μs was calculated with the value of $D_{\rm N} \approx 150$ cm^2 s^{-1} at $p = 27$ mbar pressure and $T = 2000$ K temperature. The heterogeneous recombination time $\tau_{\rm het} = 1.5 - 3$ ms was estimated with the value of $\gamma_{\rm N} = (1-2) \cdot 10^{-3}$ for a clean quartz surface at $T_{\rm wall} = 800 - 1200$ K wall temperature [186].

To eliminate the possibility of N-atom production by laser photolysis or from

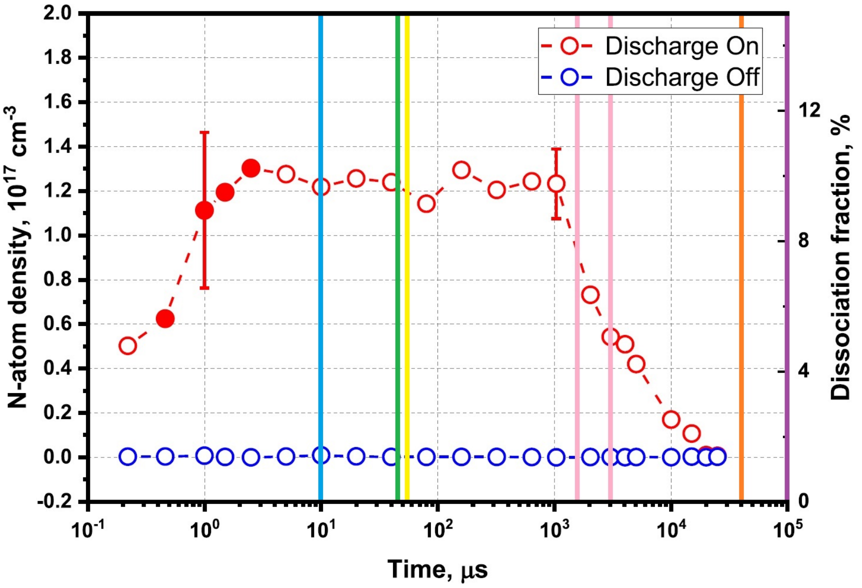

Figure 7.5 – Time evolution of the N-atom number density in nCD measured by TALIF technique with absolute calibration by Kr noble gas. Red filled symbols represent data points where fluorescence decay was limited by laser pulse duration. The quenching corrections for these data points were applied based on observed signal's decay entailing an underestimate of the actual N-atom number density. Vertical lines are timescales: $\tau_{\mathrm{diff_N}}$ in blue, τ_{heat} in green, τ_{ac} in yellow, τ_{het} in pink, τ_{gas} in orange, τ_{rep} in violet.

atmospheric air outside of the capillary, it was confirmed that no TALIF signal was registered with no discharge, as also shown at Figure 7.5 in black symbols.

Wherever possible, quenching corrections were applied using experimentally determined decay rates rather than literature published rates. This approach is deemed prudent given uncertainties surrounding the exact plasma composition at any time.

The dissociation fraction defined as $\beta = n_{\mathrm{N}}/(n_{\mathrm{N}} + 2 \cdot n_{\mathrm{N_2}})$ gives a 10% value in measured peak of N-atom density. Due to the existence of fast quenching processes at early times, the affected data was corrected only for the apparent signal decay limited by laser pulse duration. This in particular means that calculated value of β is a lower estimate of the actual dissociation fraction. The issue of fast quenching would be addressed in greater detail in the next subsection.

Figure 7.6 echoes the time evolution plot of Figure 7.5 for experimentally measured N-TALIF signal decay rates instead. It is observed that at early times, mainly for $t < 5$ μs, the measured decay rates are not resolvable ($1/\tau_{decay} = A_{\mathrm{N}} + Q_{\mathrm{N}} \geq 0.4$ ns^{-1}) and are limited by the duration of the probe laser pulse. For these data points, the N-atom density has been quenching-corrected using the measured signal decay rates, which obviously leads to an underestimation of the actual values.

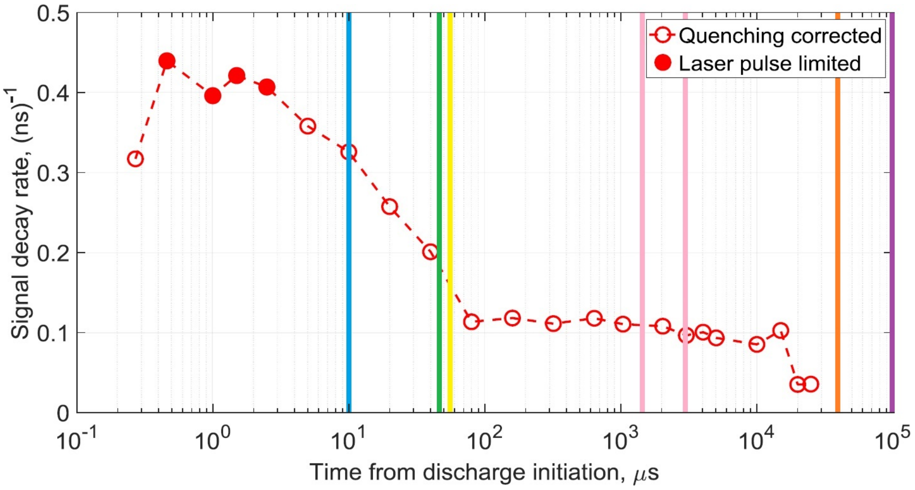

Figure 7.6 – Time evolution of the N-atom signal decay rate in nCD measured by TALIF technique. The maximum uncertainty of these measurements is about 5% and 15% for $t \leq 10$ ms and $t > 10$ ms respectively. Red filled symbols represent data points where fluorescence decay was limited by laser pulse duration. Vertical lines are timescales: $\tau_{\mathrm{diff_N}}$ in blue, τ_{heat} in green, τ_{ac} in yellow, τ_{het} in pink, τ_{gas} in orange, τ_{rep} in violet.

7.4 Possible processes behind measured rapid N-atom decay rates

The analysis of plasma kinetic processes based on known number densities of plasma species and the values of characteristic time scales presented in the chapter were obtained from kinetic calculations performed in 1D-approximation by our collaborator Dr. Sc. Nikolay A Popov.

The N-atom rapid decay rates during the discharge and in the early afterglow are a consequence of N-atom interaction with at least one highly effective quencher. At these times, three different quenching partners are considered.

1. Electrons.

   Electron production and its ensuing impact on the plasma kinetics is a distinctive feature of such high specific deposited energy and high reduced electric fields capillary discharges. As presented in [44], electron number density is estimated as 10^{14} cm^{-3} at about 700 ns after the initiation of the discharge. Given that electrons are known to be very effective quenchers of excited states under present experimental conditions [44], and that the peak of the electron density tends to coincide with time instants where the TALIF decay rates are fastest, suggests that electron quenching could be a reason for this rapid signal decay.

2. N_2 bath gas.

   Another possible reason is that the quenching rate of the N_2 bath gas could be significantly higher due to an increased gas temperature at these early times $t < 5$ μs, even though the gas density remains constant (discussed in the next subsection). An earlier study conducted under identical conditions measured a temperature rise to about 2150 K at $t = 1.5$ μs [128]. The temperature after the first HV pulse ($t \approx 270$ ns) is however, significantly lower (≈ 750 K) [128], and could explain why the TALIF decay rate measured at this time (first point in Figure 7.6) is less rapid.

3. N-atom self-quenching.

   Finally, as a consequence of the large plasma produced N-atom densities on the order of 10^{17} cm^{-3}, the presence of self-quenching from N-atoms could also be a factor in accelerating the fluorescence decay. Evidence in favor of this argument can also be seen later, for instance at $t = 1$ ms, when the gas temperature has probably equilibrated with the ambient but with the N-atom density still reasonably high. The measured decay rate of $1/\tau_{decay} \approx 0.1$ ns^{-1} at $t = 10$ ms is still slightly higher than that predicted by considering the natural radiative rate and N_2 quenching at room temperature (0.06 ns$^{-1} \leq 1/\tau_{\text{decay}} \leq 0.08$ ns^{-1}). The latter is computed based on published room temperature quenching rate coefficients for N_2 [128, 187].

From the Figure 7.5 it becomes evident that the N-atom number density displays a trapezoidal-like shape. This shape consists in, at first, a continuous rise after each of the three HV pulses, lasting up to about $t = 2$ μs, then a plateau until $t = 1$ ms, and finally a drop until $t = 20$ ms. The initial rise in the number density to about $1.3 \cdot 10^{17}$ cm^{-3} is believed to be driven mainly by electron-impact excitation to high lying predissociative states, according to the reaction given in [133, 136]:

$$e + \mathrm{N_2} \rightarrow e + \mathrm{N(^4S)} + \mathrm{N(^2D)} \tag{7.1}$$

Each HV pulse produces additional N-atoms *via* reaction 7.1, of which one atom is in the ground $\mathrm{N(^4S)}$ state, and the other in the electronically excited state $\mathrm{N(^2D)}$.

Another source of ground state N-atoms is therefore derived from the collisional de-excitation of these $\mathrm{N(^2D)}$ atoms with the bath N_2 gas. At gas temperatures between $T = 1700 - 2000$ K typical of such a capillary discharge [151], the rate constant of quenching reaction

$$\mathrm{N(^2D)} + \mathrm{N_2} \rightarrow \mathrm{N(^4S)} + \mathrm{N_2} \tag{7.2}$$

is equal to $k_B = (3-4) \cdot 10^{-12}$ cm^3/s [188]. A typical quenching time of reaction 7.2 at $P = 27$ mbar is equal to $400 - 500$ ns. Thus, at $t > 2$ μs, the density of ground state N(^{4}S) atoms is equal to the total density of N-atoms produced in the discharge.

Timescales that appear on the N-atom number density plateau on the Figure 7.5 are the (i) N-atom radial diffusion time $\tau_{\text{diff}_\text{N}}$, (ii) the typical cooling time τ_{heat} and (iii) the acoustic timescale τ_{ac}. Invariant N-atom number density in proximity of these timescales indicates that the related processes does not have a major effect on N-atom time evolution. Such conclusion leads to a few assumptions, namely: (i) the TALIF signal originates from the entire cross-section of the capillary, (ii) the processes of N-atom production and loss are temperature-independent and (iii) longitudinal compression wave's influence on the plasma media is negligible.

The only timescale that appears at the drop of N-atom time evolution is the heterogeneous recombination time τ_{het}. This indicates that the removal of N-atoms is driven by heterogeneous recombination with fused silica material of the wall. The N-atom density drops to zero at approximately $20-25$ ms after the initiation of the discharge. This implies that in case of present nCD, the accumulation of N-atoms from pulse to pulse will be absent at repetition frequencies below $40 - 50$ Hz.

7.5 Possible mechanisms leading to efficient N_2 dissociation

The present subsection investigates main processes responsible for the production and removal of N-atoms in nCD. Such discussion is of an interest particularly in light of the fact that the measured peak dissociation fraction $\beta = 10\%$ that corresponds to the peak measured N-atom density, $1.3 \cdot 10^{17}$ cm^{-3}, is rarely reported in the literature [108], and surpasses typical values measured in streamer discharges [189].

The specific deposited energy over the three HV pulses, averaged over the discharge volume is about $W = 1.7$ eV/molecule. In this case, the fraction of discharge energy spent on dissociation is equal to 50%, corresponding to an energy efficiency of N-atom production (G-factor) of $G_\text{N} = 10$ atom/100 eV (*id est* 10 atoms of nitrogen per 100 eV of deposited energy). Figure 7.7 presents the results of measurements [132, 190] and calculations [136] of the energy efficiency of N_2 dissociation, G_N, as a function of the reduced electric field E/N. For $E/N = 200 - 250$ Td, the energy efficiency of N(^{4}S) production *via* dissociation of N_2 by electron impact (meaning only *via* reaction 7.1) is equal to $G_\text{N} = 1 - 1.3$ atom/100 eV [136] as shown by the blue curve. This is almost 10 times lower than the value obtained in the present work for the nanosecond capillary discharge, albeit where both the

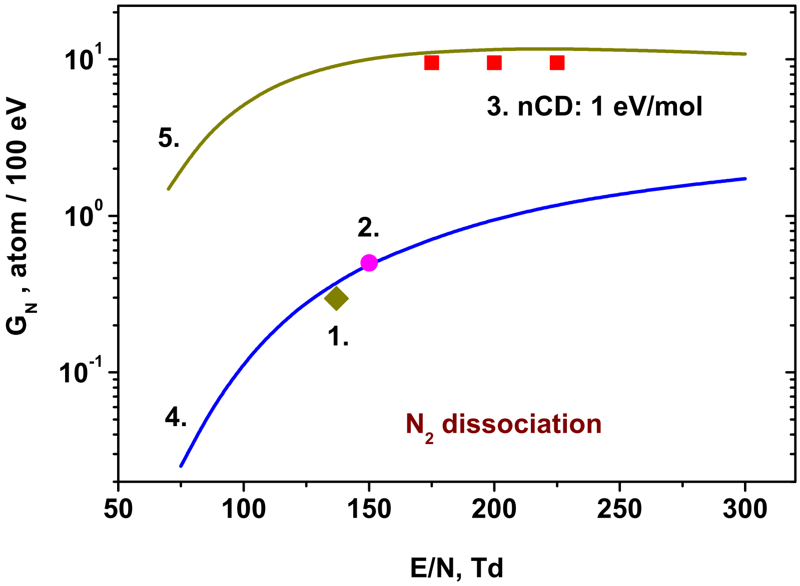

Figure 7.7 – Energy efficiency of dissociation of N_2, G-factor, or G_N, as a function of E/N measured in nCD. Symbols are the results of measurements: 1 - [132], 2 - [190], 3 - the present work. Curves are the calculations: 4 - [136], 5 - the present work taking into account stepwise electron impact dissociation *via* $N_2(A^3\Sigma_u^+, B^3\Pi_g, C^3\Pi_u)$ electronic states.

reduced electric field and specific deposited energy are high. Given such a large difference, we therefore attempt to make further sense of the experimental results in the following section.

One of the immediate consequences of having both a high E/N and large specific energy deposited to the discharge, is a high density of electrons (peak $n_e \geq 10^{15}$ cm^{-3} [44]) and electronically excited N_2 molecules. To this end, we consider the dissociation of electronically excited molecules by electron impact, such as:

$$e + N_2(A^3\Sigma_u^+, B^3\Pi_g, C^3\Pi_u) \rightarrow e + N(^4S) + N(^4S,^2D) \tag{7.3}$$

As will be seen, reaction 7.3 provides a significant input of N-atoms under the conditions of the present work. Calculated rate constants of the $N_2(A^3\Sigma_u^+, B^3\Pi_g, C^3\Pi_u)$ excited states electron impact dissociation as a function of E/N are presented in Figure 7.8. The data are obtained by solving the Boltzmann equation in a two-term approximation, using BOLSIG+ [24]. Self-consistent sets of the cross-sections for elastic and inelastic electron collisions with N_2 molecules have been taken from the SIGLO database [191], and cross-sections for reaction 7.3 from [160]. It should be emphasized that for typical conditions of electron number density $n_e \geq 10^{15}$ cm^{-3} and reduced electric field $E/N \geq 75$ Td during the HV pulse, reaction 7.3 is faster than the relevant depletion processes involving quenching of the $N_2(A^3\Sigma_u^+, B^3\Pi_g, C^3\Pi_u)$ states to the $N_2(X^1\Sigma_g^+)$ ground state, given by:

$$e + N_2(A^3\Sigma_u^+, B^3\Pi_g, C^3\Pi_u) \rightarrow e + N_2(X^1\Sigma_g^+) \tag{7.4}$$

$$N_2(A^3\Sigma_u^+, B^3\Pi_g, C^3\Pi_u) + N_2 \rightarrow N_2(X^1\Sigma_g^+) + N_2 \tag{7.5}$$

$$N_2(A^3\Sigma_u^+) + N_2(A^3\Sigma_u^+) \rightarrow N_2(B^3\Pi_g, C^3\Pi_u) + N_2(X^1\Sigma_g^+) \tag{7.6}$$

As an illustrative comparison, the quenching rate constant of the $N_2(B^3\Pi_g)$ state to the $N_2(X^1\Sigma_g^+)$ ground state by electron impact is shown in Figure 7.8. Clearly, for $E/N \geq 75$ Td, this reaction is much slower than the dissociative quenching pathways in reaction 7.3. A similar argument applies as well for the quenching rate constants of the $N_2(A^3\Sigma_u^+)$ and $N_2(C^3\Pi_u)$ states. Likewise, at $n_e > 10^{15}$ cm^{-3}, the frequency of dissociative quenching in the discharge exceeds $2 \cdot 10^7$ s^{-1}, which is $5 - 6$ times higher than the frequency of $N_2(A^3\Sigma_u^+)$ quenching in the pooling reaction. Thus, at $E/N > 75$ Td the total N_2 dissociation rate is given by reaction 7.3 and is equal to the total rate of $N_2(X^1\Sigma_g^+)$ electron impact excitation to triplet states. It should be added that while fast transitions between the $N_2(A^3\Sigma_u^+, B^3\Pi_g, C^3\Pi_u)$ triplet states through collisions with electrons are possible [44], this exchange does not change the gross population of the triplet states.

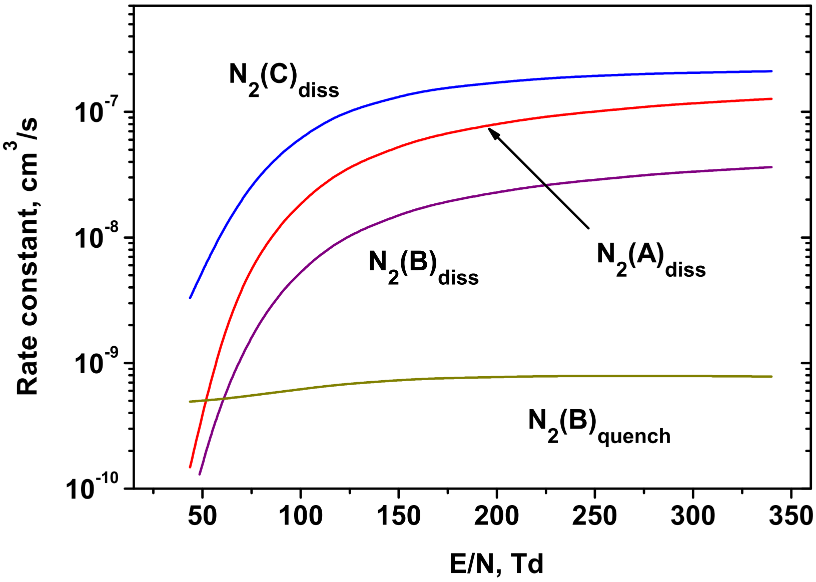

Figure 7.8 – Rate constants of dissociation of $N_2(A^3\Sigma_u^+, B^3\Pi_g, C^3\Pi_u)$ by electron impact and for the quenching of $N_2(B^3\Pi_g)$ to the $N_2(X^1\Sigma_g^+)$ ground state by electron impact as a function of E/N. The data are calculated on the basis of cross-sections obtained from [160].

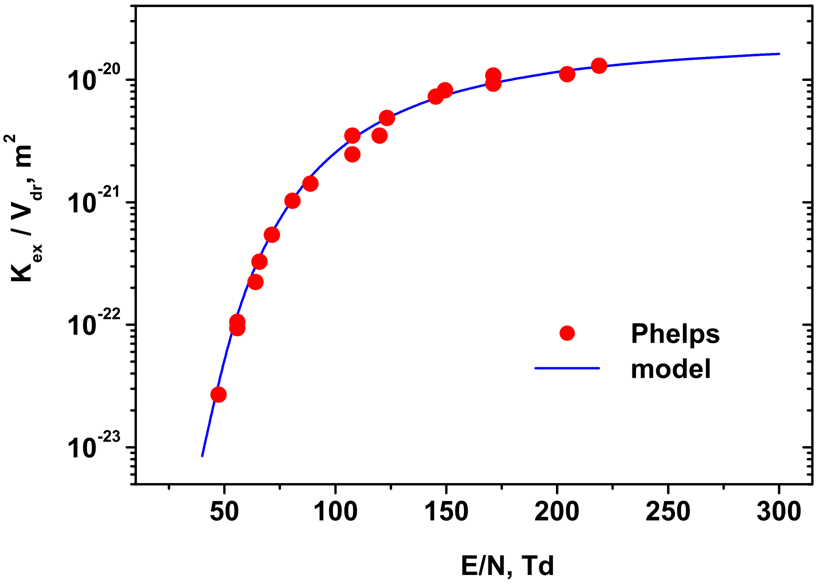

Figure 7.9 – Effective coefficient of electron impact excitation of the triplet states of nitrogen $N_2(A^3\Sigma_u^+, B^3\Pi_g, C^3\Pi_u)$ as a function of E/N. Symbols are for the experimental data [22], the line is the result of the calculation of the present work.

Figure 7.9 presents the swarm parameters check of the calculated and measured excitation coefficients K_{ex}/V_{dr} for the $N_2(A^3\Sigma_u^+, B^3\Pi_g, C^3\Pi_u)$ excited states, where $K_{ex} = k_A + k_B + k_C$, and V_{dr} is the drift velocity of electrons for a given E/N. The measured excitation coefficients are shown as points and are assumed to include the contributions of cascading from all of the triplet states $N_2(A^3\Sigma_u^+, B^3\Pi_g, C^3\Pi_u)$. These data are in turn used to estimate the energy efficiency of N_2 dissociation, given by:

$$G_N = \frac{2 \cdot K_{ex}}{V_{dr} \cdot E/N} \tag{7.7}$$

The results of calculations according to formula 7.7 are given in Figure 7.7 by the curve №5. Comparison of these numerical results with the experimental data prove that the energy efficiency of N_2 dissociation in the nCD is close to the maximum possible value. In particular, the $5-10$ times larger production of $N_2(A^3\Sigma_u^+, B^3\Pi_g, C^3\Pi_u)$ molecules (due to the high reduced fields and electron densities associated with the capillary discharge) compared with conventional electron impact dissociation of ground state molecules given in reaction 7.1, implies that the corresponding N-atom production is also $5-10$ times more efficient.

Summarizing, the key to maximizing the dissociation efficiency as experimentally observed in the present work, is as follows: (i) the ionization degree should be high enough to ensure that reaction 7.3 is the main pathway for the dissociative quenching of nitrogen triplet states $N_2(A^3\Sigma_u^+, B^3\Pi_g, C^3\Pi_u)$ and (ii) the duration of the discharge pulse is much longer than the characteristic dissociation time due to reaction 7.3 so that the electrons are maintained at sufficiently high energies.

7.6 Conclusions

N-atom density measurements have been conducted in a pure N_2 nanosecond pulsed capillary discharge with specific deposited energy at the level of 1 eV/molecule at a pressure of 27 mbar by TALIF technique with Kr gas absolute calibration. The data was taken at laser energies where fluorescence signal exhibits quadratic dependence on the laser energy. A peak N-atom density of about $1.3 \cdot 10^{17}$ cm^{-3}, corresponding to an exceptionally high dissociation degree of about 10%, has been measured using two-photon absorption laser induced fluorescence. The energy efficiency of the N-atom production reaches approximately 10 atoms/100 eV, and suggests the existence of alternative pathways for the generation of these atomic species. In order to justify these experimental observations, kinetic modeling was performed. A stepwise dissociation mechanism *via* electronically excited $N_2(A^3\Sigma_u^+, B^3\Pi_g, C^3\Pi_u)$ triplet states is suggested to complement the more well-known pathway of electron impact dissociation of $N_2(X^1\Sigma_g^+)$ ground state molecules. The present study supports the development of the capillary discharge as an efficient source of N-atoms.

Chapter 8

Time resolved N-atom number density measured in nanosecond tube discharge (nTD) by TALIF technique with Kr calibration

The chapter presents the first N-TALIF preliminary experiment done in nanosecond tube discharge in 20 mbar N_2 before COVID19 lockdown. Similar to the previous chapter, N-atom number density and decay rate measured by TALIF technique are presented after (i) determination of laser energy value required for linear regime operation in N and in Kr and (ii) performing a spectral study on N fluorescence. The measured values are discussed with respect to literature.

Improved fluorescence collection efficiency compared to nCD

As explained previously, because of millimetric scale of nCD's capillary cross-section, laser beam had to be introduced perpendicularly to axis of symmetry of the capillary. Such choice entangles complicated interpretation spacial resolution of the experiment, laser intensity value and influence of radial profiles between the gas under study and calibration gas. The nTD setup was deprived of these inconveniences due to centimetric scale of nTD's tube cross-section.

Figure 8.1 plots Kr TALIF signal from PMT within the bandpass filter in nCD and nTD setups at 2.5 mbar at about 30 μJ laser energy, (a) peak normalized and (b) in semi-log scale. Normalized signals exhibit similar trends with decay rate value 0.0413 ns^{-1} in nTD and 0.0430 ns^{-1} in nCD that agree with [128]. Semi-log plot reveals approximately 100 times more efficient fluorescence collection in nTD compared to nCD which is partially due to bigger diameter (3” for nTD *versus* 1” for nCD experiment) collimating and focusing lenses used and their closer positioning.

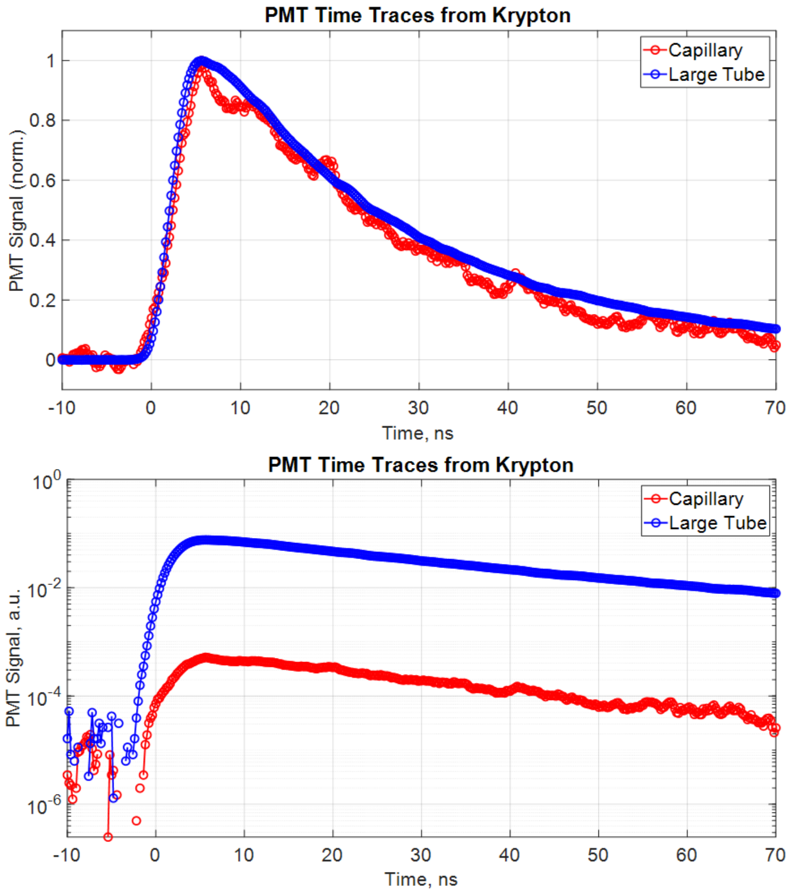

Figure 8.1 – Kr TALIF signal in nCD and nTD setups at 2.5 mbar, 1.5 sccm: (a) normalized, (b) in semi-log scale. Laser energy about 30 μJ.

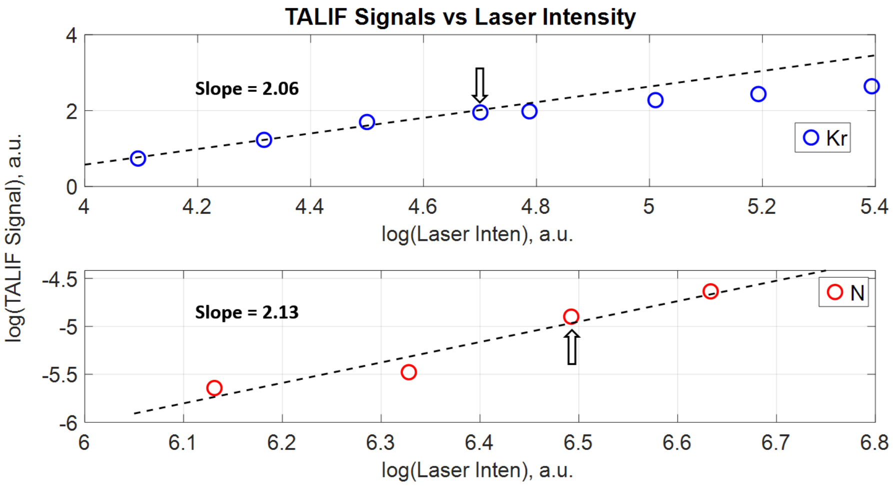

Figure 8.2 – Logarithmic plots of TALIF signals *versus* laser intensity for Kr and N. The laser intensities used in the respective experiments indicated with black arrows: 40 μJ fo Kr and 200 μJ for N.

8.1 Laser energy value required for linear regime in N and Kr

Figure 8.2 plots the logarithmic values of both the TALIF signal and the laser intensity for Kr and N. Linear fits yield to slope value of about 2 for both the case of Kr (2.06) and N (2.13). Despite the higher energies used in the N experiments, signals appear to be still within the linear regime. The laser energy used in the case of N was about 200 μJ and the corresponding value for Kr was about 40 μJ.

8.2 Plasma emission superimposition with N-atom fluorescence signal

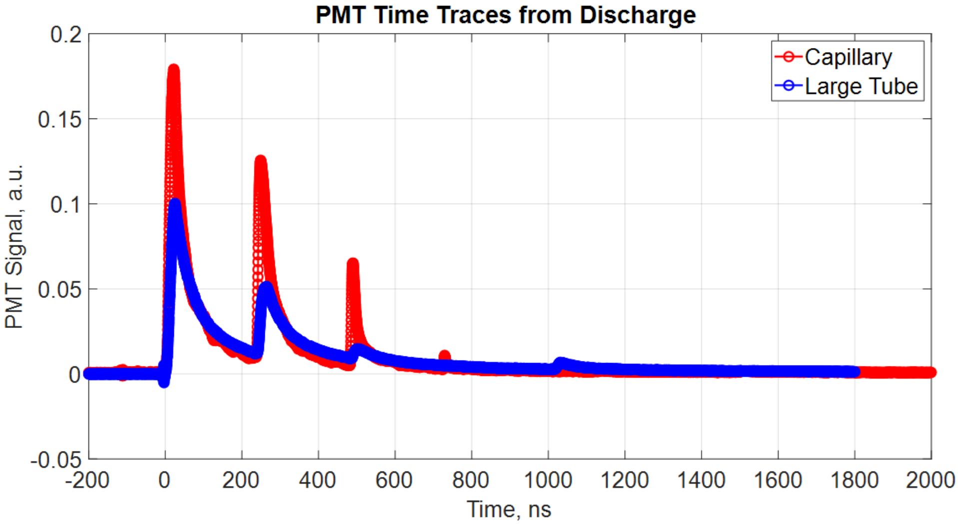

Figure 8.3 – Plasma emission at nCD (27 mbar), and nTD (20 mbar), setups during first 2 μs as seen by PMT within the bandpass filter during N-TALIF experiment. Pure N_2, 10 sccm.

Figure 8.3 illustrates plasma emission at nCD, 27 mbar, and nTD, 20 mbar, setups during first 2 μs as seen by PMT within the bandpass filter. Peak plasma emission in nTD is only a few times lower than in nCD meanwhile afterglow is of about same amplitude. Figure 8.4 plots N-TALIF signal as seen a PMT within the bandpass filter in nCD (27 mbar) and nTD (20 mbar) setups taken at 160 μs after the 1^{st} pulse at about 85 μJ laser energy, (a) in linear and (b) in semi-log scale. The decay rate trend is noticeably slower while the peak fluorescence value is $\sim$ 10 times weaker in nTD compared to nCD.

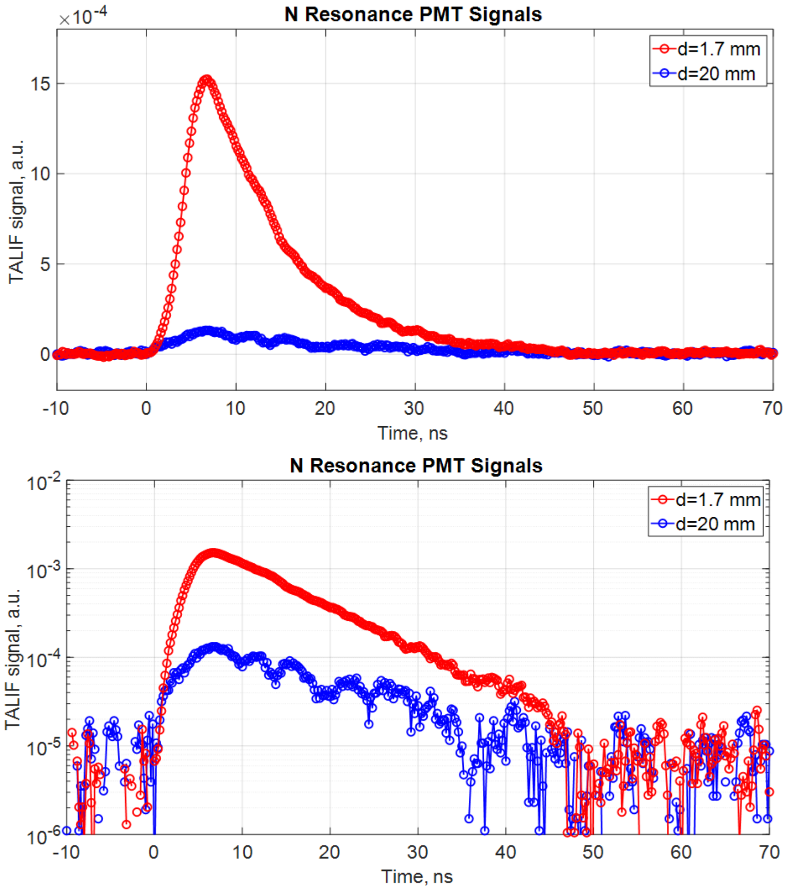

Figure 8.4 – N TALIF signal in nCD (27 mbar) and nTD (20 mbar) setups: (a) linear scale, (b) in semi-log scale. Laser energy about 85 μJ. Pure N_2, 10 sccm. Taken at 160 μs after the 1st pulse.

The spectral composition of background plasma emission was addressed. Figure 8.5 shows spectrally resolved plasma emission at nTD setup during the 1st pulse and during first 2 μs of the afterglow in 730-770 nm wavelength range for different N_2:O_2 mixtures. Emission has been recorded with Princeton camera-spectrometer pair of calibrated spectral sensitivity and the light was guided by single-leg optical fiber bundle LG-255-020. The input of the optical fiber has been put from the side to nTD at the distance of 17 cm from the axis of the discharge tube, its output was mounted to the spectrometer's input 500 μm slit. Acquired spectra was corrected for spectral sensitivity of camera-spectrometer pair assuming that fiber's response in 730-770 nm range is constant. The first positive system of N_2, $N_2(B^3\Pi_g$, v')→$N_2(A^3\Sigma_u^+$, v"), is easily identified at Figure 8.5, more precisely, $(5-3)$, $(4-2)$ and $(3-1)$ vibrational bands from left to right.

The data above concludes that the overlap between fluorescence signal and plasma emission is a major issue for N-TALIF measurements in nTD. In comparison to nCD, despite two orders of magnitude increased collection efficiency, at a comparable pressure conditions N-TALIF signal in nTD is one order of magnitude weaker while plasma emission background contribution is comparable. Such relation decreases dramatically the temporal range of TALIF signal detection. As seen at Figure 8.5, with increasing O_2 admixture, plasma emission and TALIF signal bith decrease in intensity because of quenching with molecular oxygen. The fluorescence signal is thus first detected at earlier times but drowns earlier in background emission, too.

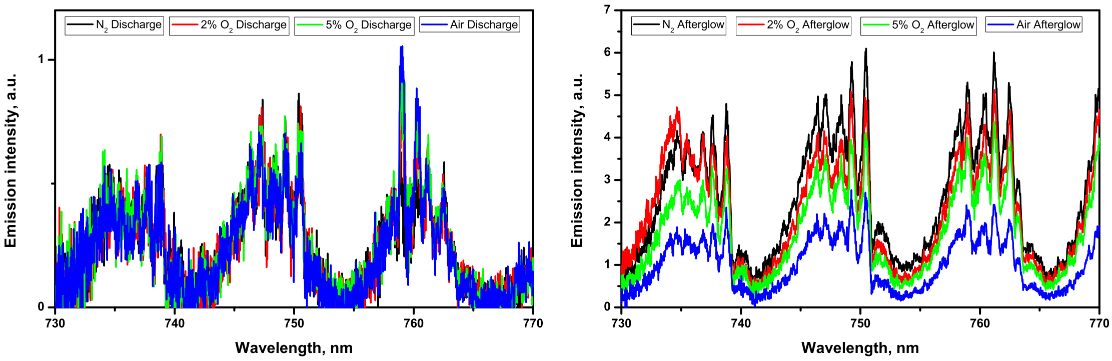

Figure 8.5 – Plasma emission at nTD setup during the 1st pulse and during first 2 μs of the afterglow in 730-770 nm wavelength range taken by Princeton camera-spectrometer pair for different N_2:O_2 mixtures.

8.3 Temporal evolution of N-atom number density and decay rate

Given the weak signal, it was not possible to acquire signals earlier than 5 μs after the discharge initiation. At earlier times, the noise floor is higher due to the background plasma emission. From the other end, signal reached the detection limit at approximately 1 ms after the discharge initiation.

Figure 8.6 shows N-TALIF signal's decay rate as a function of time from the discharge. The grey-shaded region from 0.054 ns^{-1} to 0.072 ns^{-1} with an average value of 0.063 ns^{-1} represents the estimations from literature for 300 K temperature at 20 mbar N_2. The lower boundary is obtained using data on $N(3s^4P_{3/2})$ state from [128]: the natural lifetime of $\tau = 29.6$ ns and N_2 quenching rate of $0.41 \cdot 10^{-10}$ cm^3/s. The upper boundary estimate is obtained using data on $N(3s^4S_{3/2})$ from [187] where the natural lifetime is $\tau = 26.2$ ns, and N_2 quenching rate is $0.68 \cdot 10^{-11}$ cm^3/s. So, unlike in the capillary, decay rates are quite constant and mostly fall within that predicted by room temperature quenching rates. This also indirectly suggests that the gas temperature in nTD is at around 300 K value.

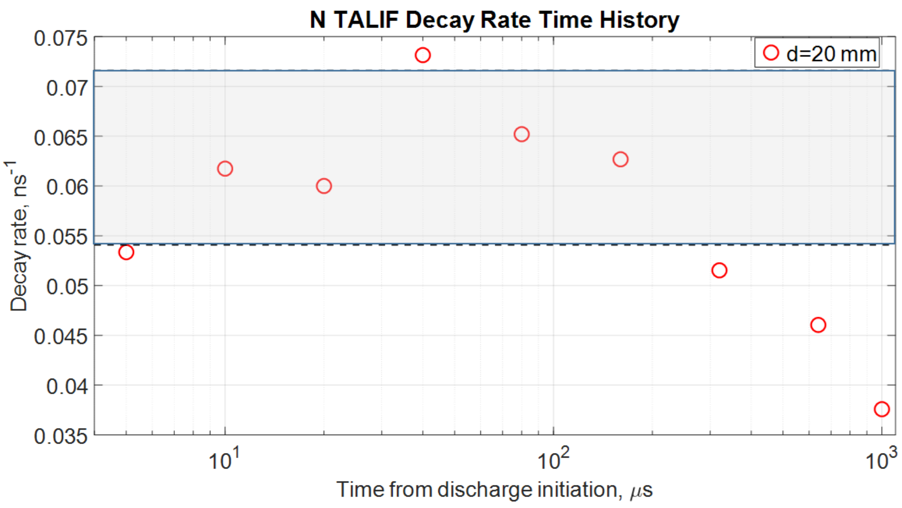

Figure 8.6 – Time evolution of N-atom signal decay rate measured by TALIF in nTD. Grey area represent the range of decay values found in literature with the lower [128] and upper boundaries [187].

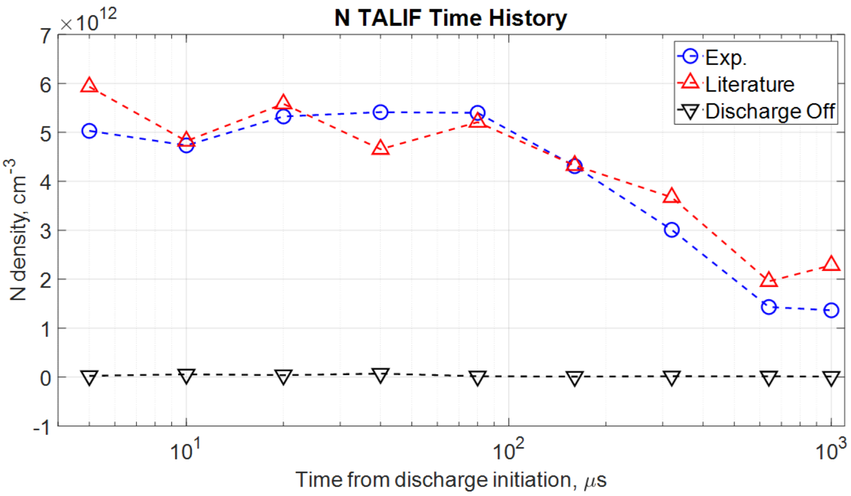

Figure 8.7 – Time evolution of N-atom number density measured by TALIF in nTD with absolute calibration by Kr noble gas. Quenching corrections: for experimentally measured decay in blue, for the average value from [128] and [187] in red. Black scatter indicated TALIF signal acquired with discharge off.

Figure 8.7 presents the data on N-atom number density as a function of time. The measured peak value of N-atom number density, $5.5 \cdot 10^{12}$ cm^{-3}, corresponds to dissociation fraction of 10^{-5}. Black symbols represent the noise level of PMT recorded when discharge was off (*id est*, when laser beam enters the discharge tube with pure N_2 flow). No N-signal in the absence of discharge implies that the laser intensity is low enough to prevent laser interferences (photolysis) from occurring. Due to poor signal-to-noise ratio, there was a considerable uncertainty in the measured decay rates used for quenching corrections (used to obtain the blue symbols in Figure 8.7). Thus correction to an average value from literature [128, 187], 0.063 ns^{-1}, has been applied as well (red symbols in Figure 8.7). The absence of important discrepancy between the data points calculated with different quenching correction suggests that the experimentally measured quenching rates are correct.

8.4 N-atom production efficiency compared to modeling prediction

Figure 8.8 updates the Figure 7.7 with the energy efficiency of N_2 dissociation measured in nTD in blue scatter to be 0.67 atoms/100 eV. The value was obtained suggesting that generated N-atoms follow the initial plasma radial distribution of presented at Figure 3.9. Measured G-factor shows a rather good agreement with modeling predictions [136] performed for discharges such as nTD, meaning with high reduced electric field and low specific deposited energy, indirectly confirming radial-dependent behavior of N-atom generation.

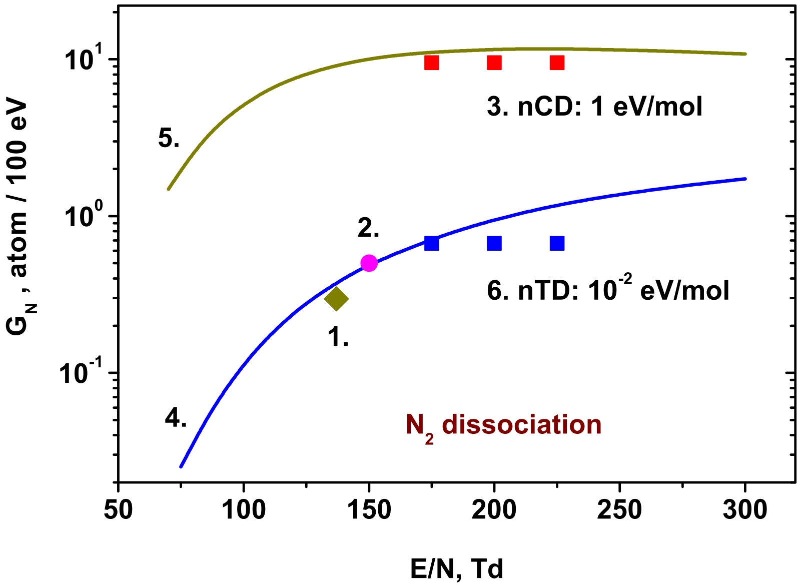

Figure 8.8 – Energy efficiency N_2 dissociation, G-factor, or G_N, as a function of E/N measured in nCD and nTD. Symbols are the results of measurements: 1 - [132], 2 - [190], 3 and 6 - the present work. Curves are the calculations: 4 - [136], 5 - the present work taking into account stepwise electron impact dissociation *via* $N_2(A^3\Sigma_u^+, B^3\Pi_g, C^3\Pi_u)$ electronic states.

In nTD, the value of reduced electric field during energy deposition to plasma equals to $E/N = 150 - 200$ Td. At such E/N, the rate constant of the total population of all $\mathrm{N_2(A^3\Sigma_u^+, B^3\Pi_g, C^3\Pi_u)}$ triplet states is about 10 times greater than the rate constant of $\mathrm{N_2}$ electron impact dissociation (as seen at Figure 7.7 from the previous chapter). It is thus logical to assume that immediately after the discharge, the $\mathrm{N_2(A)}$ to $\mathrm{N(^4S)}$ number density ratio would be of about 10. If one estimates the $\mathrm{N(^4S)}$ number density at the end of the discharge as the value $5 \cdot 10^{12}$ cm^{-3} measured by TALIF in nTD at closest available time instant, 5 μs, the expected $\mathrm{N_2(A^3\Sigma_u^+)}$ number density would be of about $5 \cdot 10^{13}$ cm^{-3}.

According to recently accepted manuscript [192], pooling reaction between two $\mathrm{N_2(A^3\Sigma_u^+)}$ molecules can be one of the main channels of $\mathrm{N_2}$ dissociation. The rate constant of this process is expected to be up to 70% of the total rate of $\mathrm{N_2(A^3\Sigma_u^+)}$ self-quenching ($4 \cdot 10^{-10}$ cm^3 s^{-1} according to [193]). Under the conditions of nTD, the characteristic time of the pooling reaction is about 50 μs. Thus, if the pooling reaction suggested by [192] took place with sufficiently large rate constant, at times $t > 50$ μs, a significant (up to 5 times) increase in the number density of atomic nitrogen should have been observed. According to Figure 8.7, no such increase was observed, which may indicate that the rate constant of the pooling reaction is way more modest, no more than 10% of the total pooling reaction rate, that is, less than $4 \cdot 10^{-11}$ cm^3 s^{-1}.

8.5 Conclusions

N-atom density measurements have been conducted in a pure $\mathrm{N_2}$ nanosecond pulsed tube discharge with specific deposited energy at the level of 10^{-3} eV/molecule at a pressure of 20 mbar by TALIF technique with Kr gas absolute calibration at the center of the discharge tube. Due to weak signal, it was not possible to acquire signals earlier than 5 μs after the discharge initiation. The measured peak value of N-atom number density, $5.5 \cdot 10^{12}$ cm^{-3}, stays rather constant from 5 μs to up to 100 μs and then drops to $\sim (1 - 2) \cdot 10^{12}$ cm^{-3} at 1 ms. Measured quenching was found to overall fall withing the range of values expected by literature. Measured peak N-atom production corresponds to dissociation fraction of 10^{-5}.

Chapter 9

Preliminary biological results on nanosecond plasma exposed stem cells

Recently, the application of cold atmospheric plasma (CAP) had gained an increasing interest in numerous biological applications: wound healing [10], blood coagulation [194], cancer treatment [195, 196]. Because of its complexity, cold plasma has a simultaneous effect on the target from many factors such as reactive species production, electrical field effect (polarization), electrification (passing of electrical current through the target), UV, visible and IR radiation. Up to now the beneficial effect of these factors and the underlying mechanisms are still difficult to elucidate because of the multidisciplinary character of the approach. On the other hand, ease of use, typically short exposure times, and experimentally observed healing effects have riveted the community's interest in CAP.

Regenerative medicine is aiming for efficient treatment or even potential replacement of damaged tissues and organs. Stem cells are currently investigated as a source for regenerative medicine because of their vast differentiation potential (possibility to develop into the needed tissue), high proliferation rate and ability to orchestrate tissue healing through the secretion of suitable factors [144]. In adult, stem cells are found in bone marrow, adipose tissue, synovial membrane, dental pulp. On the other hand, tissue conditions are deleterious for cell survival and therefore preconditioning is necessary. Thus a development of a pre-conditioning approaches is an essential action preceding stem cell's administration to the damaged site.

Reactive oxygen and nitrogen species (RONS) play a fundamental key role in inducing specific biological responses. The effect of excessive accumulation of RONS depends on the ability of certain cells to produce, accumulate, and/or release RONS into the extracellular environment and may also lead, in some cases, to the release of growth factors that induce beneficial effects, like angiogenesis for example. Oxidative stress damage can also induce lipid peroxidation and protein cross-linking, and lead to protein inactivation and breakage of DNA, as well as to the pathogenesis.

Nanosecond pulsed discharges with high specific deposited energy have proved to be efficient sources of RONS and thus are particularly interesting for biological applications. In order to address the possibility of stem cells plasma pre-conditioning for the purpose of regenerative medicine, the collaboration has been established between cold plasma research group of S. Starikovskaia and stem cell research group of H. Kerdjoudj. The objective of this collaboration within the framework of current PhD was (i) to develop a cold atmospheric plasma (CAP) device that would meet the criteria for non-toxicity and (ii) to investigate CAP's action on stem cells.

9.1 Cold atmospheric plasma (CAP) device

During current PhD, two generations of CAP device have been developed. In both, the discharge is initiated in a capillary with an internal diameter of a few mm, between a high voltage needle at the axis of capillary and the ground wrapped around capillary slightly below the needle's end. Helium is flown through the capillary at the flow rate of 28 sccm through a side tube. The discharge in the tube is initiated using positive polarity high voltage nanosecond pulses of 6 kV amplitude, 4 ns pulse rise/fall time, 30 ns pulse duration (FWHM), at 300 Hz repetition rate, produced by an FPG 12-1NM (FID GmbH) high voltage pulse generator. Cells in suspension were placed in the plasma flowing afterglow at nozzle-surface distance of $3-4$ mm. The CAP device can be set for a custom height thanks to vertical rail.

Figure 9.1 presents the first generation CAP device, CAP-1. It was constructed based on the 1.5 mm inner diameter capillary of nCD discharge tube discussed in previous chapters of the thesis, with a copper needle as high voltage electrode. The biggest inconvenience of CAP-1 was O_3 production that had exceeded the threshold value of human sensory perception in less than an hour of operation. Because of high hazardous and cancerogenous activity of O_3, such setup is likely to cause undesired complications to the treated cells (such as DNA damage) as well as to the staff (short and long term ozone poisoning). Fortunately, the characteristic smell of ozone begins to be organoleptically felt already at concentrations of $0.004-0.015$ mg/m^3, *id est* significantly below the hygienic standard [197].

From this perspective, a possibility to reduce ozone production while keeping the features of high E/N and high ω of nanosecond pulsed capillary discharges has been investigated. He co-flow of the same value as He plasma flow has been suggested as a way to reduce the mixing between plasma afterglow and surrounding atmospheric air that contributed to ozone production. Gas inlet connector was made from hollow 1/16" inner diameter stainless steel tubing that served as high voltage electrode as well. The capillary material was changed from quartz to glass in order to reduce O_2 dissociation from UV plasma radiation. Due to specifications of Pyrex tube fabrication, glass capillary wall is ≈ 1.5 times thicker than the quartz one. Glass

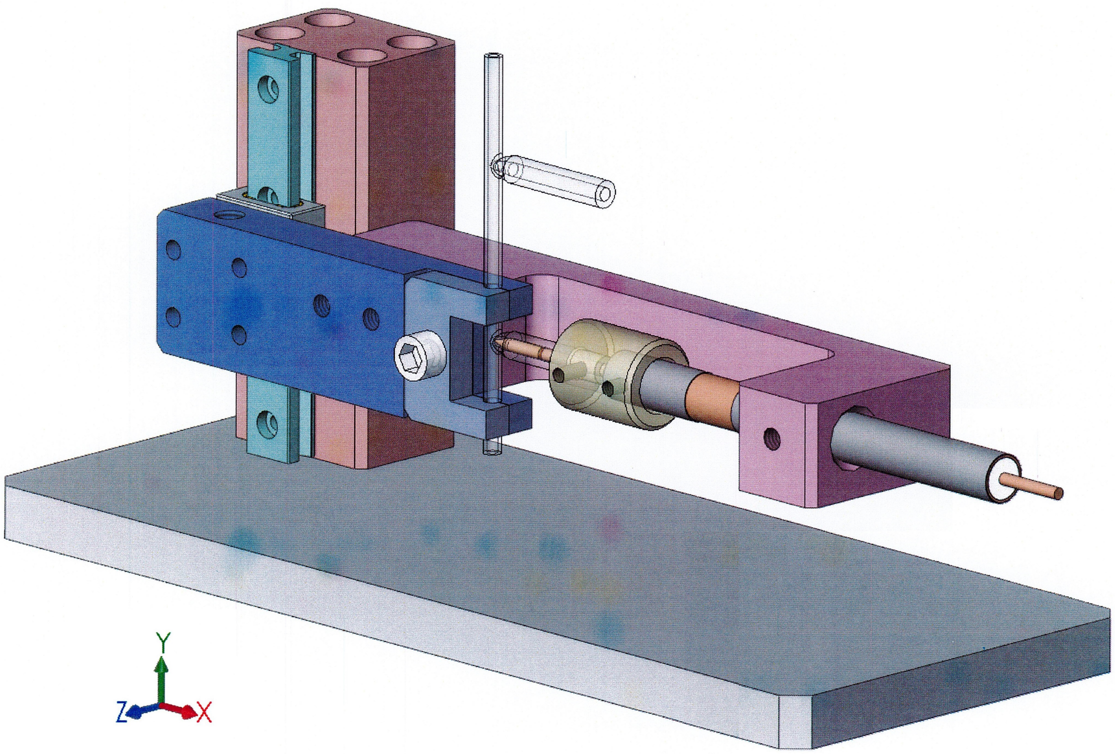

(a) General view on CAP-1 device.

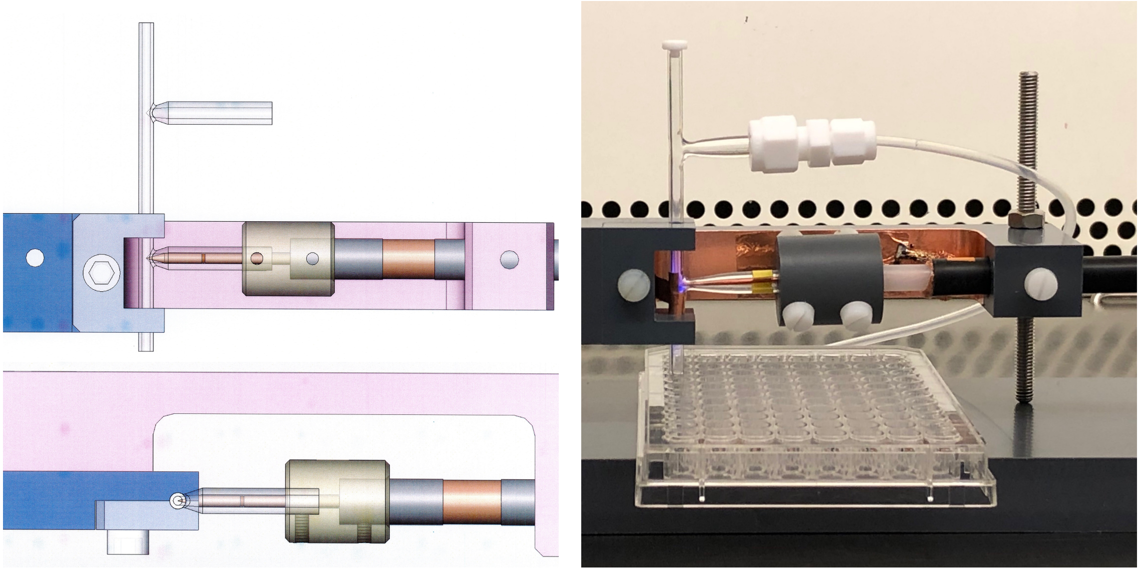

(b) Side and top view on the electrode system of CAP-1.

(c) Photo during CAP-1 operation, side view.

Figure 9.1 – First generation CAP device, CAP-1, technical drawings and photo. Ground was guided by the plastic support and connected to a 5 mm high copper ring wrapped around the capillary as shown at (c).

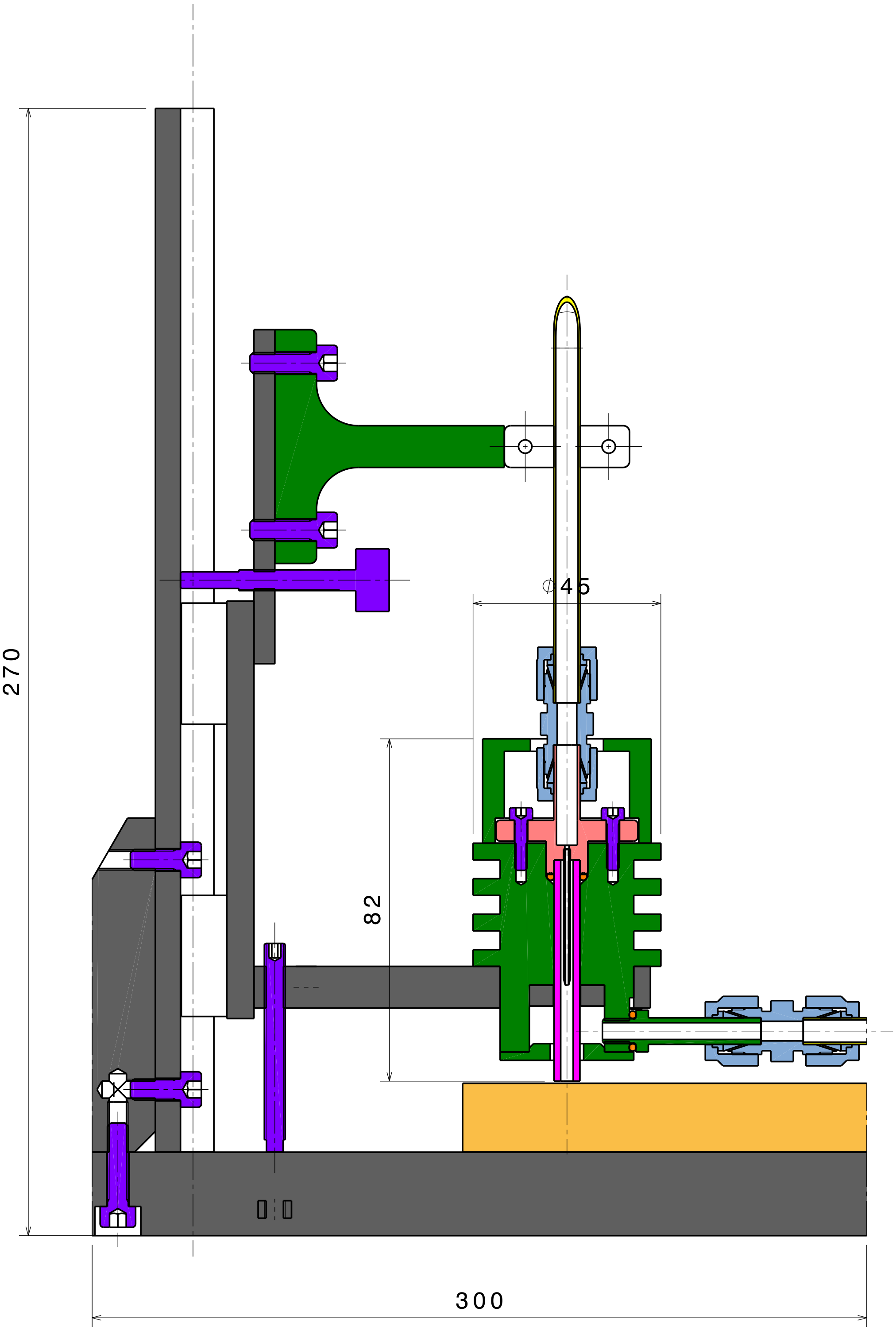

Figure 9.2 – Second generation CAP device, CAP-2, schematic: general view. Ground electrode is a ring (in gray) around the capillary (in pink).

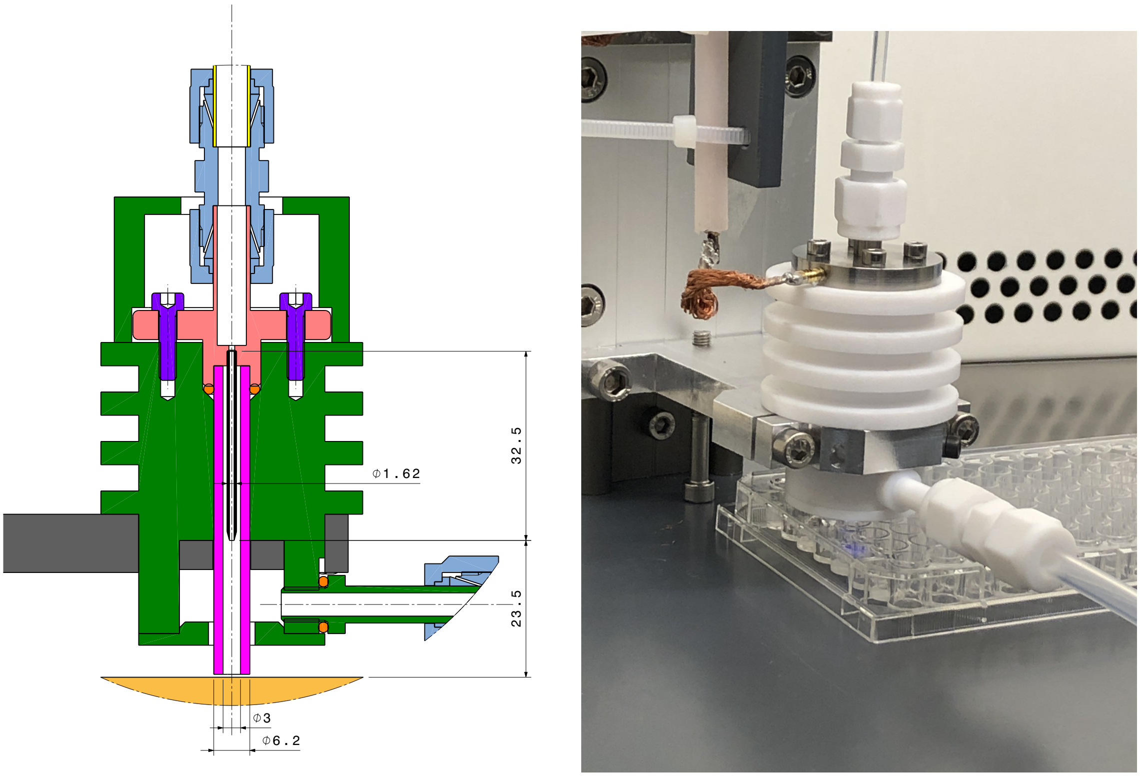

(a) CAP-2 electrode system side view. (b) Photo during CAP-2 operation.

Figure 9.3 – Second generation CAP device, CAP-2, closer look on the electrode system. Ground electrode is a ring (in gray) around the capillary (in pink).

capillary internal diameter was set to 4 mm to match the inter-electrode distance of CAP-1. All considerations above had lead to the second generation CAP device, CAP-2, presented at Figures 9.2 and 9.3. Dielectric (shown on Figures 9.2 and 9.3 in green) had been given a ribbed shape in order to prevent short circuit. Unlike CAP-1, CAP-2 does not overpass the perceptible ozone production threshold concentration within $2-3$ hours of use.

It has to be noted that despite ozone's generally known toxic influence on the human and cell culture, the impact of ozone produced by CAP-1 and CAP-2 on stem cells has not been isolated nor evaluated. Since few recent works suggest that one of plasmas main benefit for biomedical applications is efficient RONS production, one should not discard any RONS specie beforehand. Over-threshold concentrations of O_3 have undoubtedly poisonous effect on both human and cell culture if experienced for long time (several hours and more). However, the suggested CAP treatment time for a single well was at most 3 min long. Additionally, plasma afterglow gets in contact only with the surface of the solution liquid without causing perturbations on its surface. Hence results from both CAP-1 and CAP-2 devices are presented.

9.2 Description of biological targets and development of treatment protocol

In this study stem cells derived from dental pulp were used. Healthy pulp tissues were isolated from non-fully erupted third molars. The procedure was ethically and methodologically approved by local Research Institution associated to the BIOS laboratory and was conducted with informed patients (written consent, non-opposition) in accordance with the usual ethical legal regulations (Article R 1243-57). All procedures were done in accordance with our authorization and registration number DC-2014-2262 given by the National "Cellule de Bioéthique". Following the enzymatic digestion of pulp in collagenase and trypsin mixture, the extracted DPSCs were cultured in α-MEM supplemented with 10% decomplemented fetal bovine serum (FBS), 1% Penicillin/Streptomycin/Amphotericin-B and 1% Glutamax$^{©}$ and maintained in a humidified atmosphere of 5% CO_2 at 37°C. Reaching sub-confluence, DPSCs were seeded at density of 3×10^3 cell/cm^2 until the third passage.

In order to investigate the CAP effect on release of proinflammation mediators, THP-1 cells, a pro-monocytic cell line, were purchased from the American Type Culture Collection. Cells were cultured at a density of 2×10^5 cells/mL in a 75 cm^2 flask in RPMI 1640 medium supplemented with 10% heat-inactivated FBS, 1% Penicillin/Streptomycin (v/v, Gibco, Villebon-sur-Yvette, France) and maintained in a humidified atmosphere of 5% CO_2 at 37°C.

To treat the surface of 10^5 cells in 150 μL of suspension per well in a homogeneous manner, 96-well culture plate (example shown at Figure 9.3(b)) that matched the best the size of plasma nozzle was selected. Two solutions, isotonic phosphate saline buffer (PBS) and cell culture media with antibiotics, were tested as a dilution media for cell treatment. It has been observed that serum presence in culture media causes CAP-treated cells to adhere to the plastic bottom of the well directly after treatment. Thus, a treatment in PBS was preferred. Treated cells were further centrifuged at 250 g for 10 min and set in 24-well cell culture plate in nutritive media for culture.

To ensure the same environmental impact within a CAP treatment session, PBS-diluted cells were distributed to cell culture at the same time and used as a control. Being a neutral media, PBS is acceptable as a cell temporal solution on the scale of a few hours but further presence in PBS increases cells mortality rate due to lack of nutrients and impossibility for cell to adhere to the culture substrate. To account for change due to presence in PBS solution, a separate control well (addressed as "unexposed cells") is kept. The effect of He flown through the device was accounted by 3 min He flow exposure with device off. In addition, care has been taken to plan CAP treatment sessions no longer than 2 h.

9.3 Biological methods used to assess the effect of CAP treatment

Labeled flow cytometry

Although microscopy provides a visually convincing evidence, it can not be used to represent the average state of whole population. According to the law of big numbers [198], the larger the number of events (in current context, observed treated cells), the closer the observed average value to the expected value. If to reformulate the law in the opposite direction, it would sound as "the less events one has, the less reliable conclusions one can get".

Flow cytometry is a common statistical approach in modern cellular biology. The method makes use of a collimated laser beam projected on a capillary tube. Cells in a solution are passed individually through the capillary meanwhile transmitted and scattered laser light are registered. After data treatment, transmitted laser radiation ("forward scatter") provides information concerning cell size, and scattered radiation ("side scatter") - about cell's granularity (density of organelles). The data is presented in a form of a diagram where every point represents a cell. In diagrams, forward scatter ("FSC") and side scatter ("SSC") are usually plotted as x and y axis, respectively.

Flow cytometry should be "labeled". It requires use of a reagent (label) that would undergo into a fluorescent chemical reaction with the compound of interest (organelles, some reactive species *et cetera*). The registered fluorescent signal allows to study abundance and spatial distribution of the compound of interest.

Quantitative measurements of a particular ROS, namely superoxide radicals in CAP-stimulated DPSCs undergoing oxidative stress, were performed using the Muse Oxidative Stress kit (Millipore, Bedford, MA, USA) in accordance with the manufacturer protocol. Briefly, following CAP exposure, cells were re-suspended at a concentration assay buffer and incubated in oxidative stress working solution for 30 min at 37°C.

Enzyme-linked immunosorbent assay (ELISA)

Enzyme-linked immunosorbent assay (ELISA) is a another statistical method for the qualitative or quantitative determination of various low molecular weight compounds (macromolecules, viruses) using a colorimetric assay (spectrophotometer). The method is based on a specific antigen-antibody reaction. The detection of the formed antigen-antibody pair is carried out using an enzyme, a protein that acts as a biological catalyst, as a label for signal registration. The theoretical foundations of ELISA are based on modern immunochemistry and chemical enzymology, knowledge of the physicochemical laws of the antigen-antibody reaction, as well as on the basic principles of analytical chemistry.

ELISA is one of the most actively developing areas of chemical enzymology. This is due to the fact that in ELISA the unique specificity of the immunochemical reaction (that is, antibodies bind exclusively to specific antigens, and not to any others) is combined with a high detection sensitivity of an enzymatic label (up to 10^{-21} mol in a sample).

The quantification of released proinflammatory mediator tumor necrotic factor alpha (TNF-α) by CAP-stimulated THP-1 cells in culture media was assessed using DuoSet© ELISA Kit for human TNF-α (R&D Systems, Lille, France). Absorbance was measured at 450 nm with correction of non-specific background at 570 nm according to the manufacturer's instructions.

Water-soluble tetrazolium salts (WST-1) release assay

The WST-1 assay provides a sensitive means for performing a quantitative cell proliferation assay, cell viability assay, or cytotoxicity assay in mammalian cells. The WST-1 assay protocol is based on the cleavage of the tetrazolium salt to formazan by cellular mitochondrial dehydrogenase. The amount of the dye generated by activity of dehydrogenase is directly proportional to the number of living cells. The formazan dye produced by viable cells can be quantified by microplate reader by measuring the absorbance of the dye solution at 440 nm. WST-1 cell proliferation assay (Roche Diagnostics, France) was performed after 24h and 6 days of culture. Absorbance was measured at 490 nm using a FLUOstar Omega microplate reader (BMG Labtech) against a background control as blank. A wavelength of 750 nm was used as the reference wavelength.

Lactate deshydrogenase (LDH) release assay

LDH is a cytoplasmic enzyme released in cell culture media when plasma membrane of cells is damaged (cell death indicator). Extracellular LDH can be quantified in the media by a coupled enzymatic reaction, in which LDH catalyses the conversion of lactate to pyruvate *via* NAD+ reduction to NADH. Then NADH is used to reduce a tetrazolium salt to a red formazan product, whose absorbance can be measured at 490 nm. The level of formazan formation is directly proportional to the amount of LDH released into the cell supernatant, indicative of cytotoxicity. Following the 24h post-treatment, LDH activity was evaluated through DPSCs conditioned media analysis with the cytotoxicity detection kit (Roche, France) following the manufacturer's instructions. Absorbance was measured at 490 nm with correction at 700 nm using a FLUOstar Omega microplate reader (BMG Labtech) against a background control as blank.

Visualization of cellular cytoskeleton and nuclei

After 7 days of culture the morphology of adhered DPSC were examined by fluorescent microscopy. For that, cells were fixed with 4% (w/v) paraformaldehyde (Sigma-Aldrich, Saint-Quentin Fallavier, France) at 37°C for 10 min and permeabilized with 0.5% (v/v) Triton X-100 for 5 min. Alexa© Fluor-488 conjugated-Phalloidin© (1/100 dilution in 0.1% Triton X-100) was used to stain F-actin for 45 min at room temperature. Nuclei were counter-stained with 4,6-diamidino-2-phenylindole (DAPI, 100 ng/mL, $1/10,000$ dilution) for 5 min. Stained cells were mounted and imaged by confocal laser scanning microscopy (CLSM, Zeiss LSM 710 NLO, 10× objective, Numerical Aperture 1.4, Carl Zeiss Jena, Germany).

9.4 Validation of CAP device in application to stem cells

Changes in cellular morphology immediately after treatment

Stem cells can exist *in vitro* if a specific range of parameters is respected: (i) presence of a hydrophilic surface to adhere and proliferate to form a cell population, (ii) nutritive solution in access, (iii) 5% CO_2 admixture to air atmosphere of around 37°C temperature, and (iv) in absence of any mechanical stress such as shock. Under these conditions, a single stem cell would adhere to the surface and its cytoskeleton would take an elongated shape.

Stem cell can tolerate a short-term deviation from comfort zone conditions. For example, it can be resettled to another surface following the sequence of actions: (i) detachment from current surface by enzyme action (trypsine), (ii) trypsine neutralization by culture media, (iii) centrifuging the solution to enable liquid elimination and finally (iv) setting on the new surface in a nutritive media. When detached from a surface and re-suspended in a suitable buffer media (isotonic solution), stem cell takes a round shape form with a regular structure. If one of the parameters

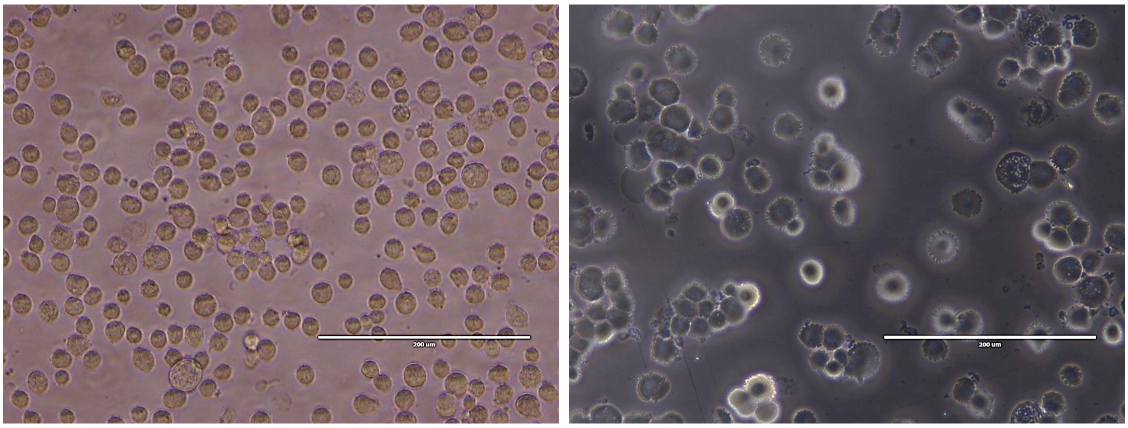

(a) Unexposed cells **(b) CAP-1 3 min**

Figure 9.4 – Microscopy imaging for morphological cell analysis. Scale represents 200 μm.

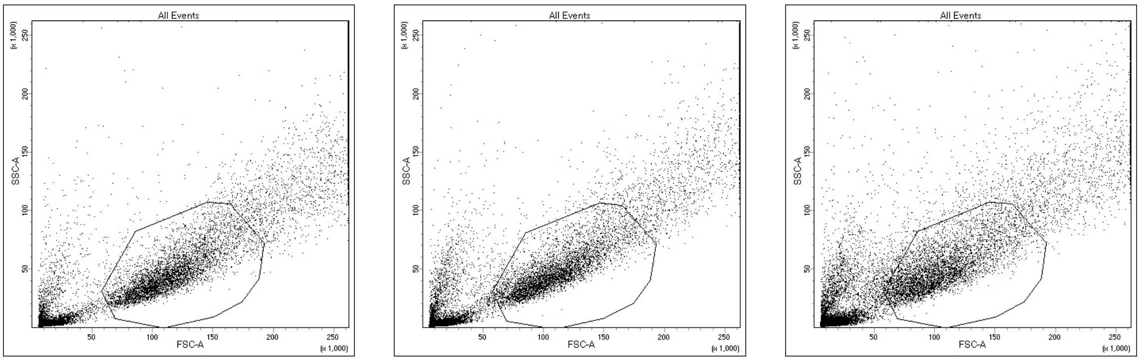

(a) Cells kept overnight at 4° C **(b) 1 min of CAP-1 to (a) cells** **(c) 3 min of CAP-1 to (a) cells**

Figure 9.5 – Flow cytometry diagrams. Horizontal axis represents stem cell's size, vertical – granularity.

of cell's surroundings do not match the comfort zone values for too long (several hours), the cell can either cease part of one's activity (*exempli gratia*, proliferation) or even trigger apoptosis, programmed death mechanism. In this case the cell do not attach to the surface or detaches from the surface and takes the round shape form on its own. During apoptotic process, the cellular membrane shrinks and folds around different organelles, causing cells morphology to have a more irregular form.

Some severe trauma on the cell (hypotonic osmotic pressure, extreme temperature conditions) can result in necrosis, *id est* expulsion of damaged cell's organelles into the extracellular space. Necrosis is a highly undesirable death path since associated with inflammation and propagation of damaged genetic information. On microscopic images, signs of necrosis can be seen as small scale remnants in extracellular media.

Figure 9.4 presents two microscopic images, of the unexposed dental pulp derived stem cells (on the left) and of CAP-1 treated for 3 min (on the right), taken immediately after treatment. The scale on both images is kept the same. The unexposed cells, as expected, have a round regular shape. Meanwhile, CAP-1 treated DPSCs compared to the unexposed show a few trends: (i) cell size increase, (ii) irregular membrane shape with finger-like formations, (iii) important cell clustering. The presence of immediate morphological changes was the first obtained evidence of CAP-1 device's action stem cells in suspension. Additionally, the irregular shape some treated DPSCs seems similar to apoptotic cells behavior.

Slight increase in cells granularity immediately following CAP-1 treatment was confirmed by flow cytometry. Figure 9.5 presents flow cytomery diagrams for (a) cells kept overnight at 4°C addressed as unexposed DPSCs, (b) cells after 1 min CAP-1 treatment and (b) cells after 3 min CAP-1 treatment. The region selected by black solid line closed figure depicts normal cellular population. The scatter to the left of the figure represents cellular remnants (way to small to be a cell), the scatter to the left - probably apoptotic cells (slightly bigger and more granular that a normal cell is). CAP-1 treatment of 1 min shown at Figure 9.5(b) does not present an important morphological shift in size nor in granularity. However, 3 min of CAP-1 treatment shown at Figure 9.5(c) increases the cellular granularity to an appreciable extent. The reason behind can be increased organelles activity (mitosis or apoptosis) within the cell induced by CAP-1 treatment.

Changes in cellular morphology after 24h of culture

Figure 9.6 presents DPSCs after 24h following (a) 10 sec and (b) 3 min CAP-1 treatment together with (c) unexposed DPSCs and (d) 3 min He flow control. All cases show adhered cells to the plastic culture substrate except for 3 min CAP-1 treatment that were rounded and lost their adhesive properties; these cells are probably dead. Combined with data from unlabeled flow cytometry from the previous subsection, it can be suggested that increased granularity of the cells observed for 3 min CAP-1 treatment case (Figure 9.5(c)) was associated to triggered apoptosis.

Cytotoxicity of the device and effect of treatment on following cell proliferation

Figure 9.7(a) shows cells viability after 24h after CAP-1 of 10 sec, 30 sec, 1 min and 3 min treatment together with unexposed cells and 3 min He flow control. The

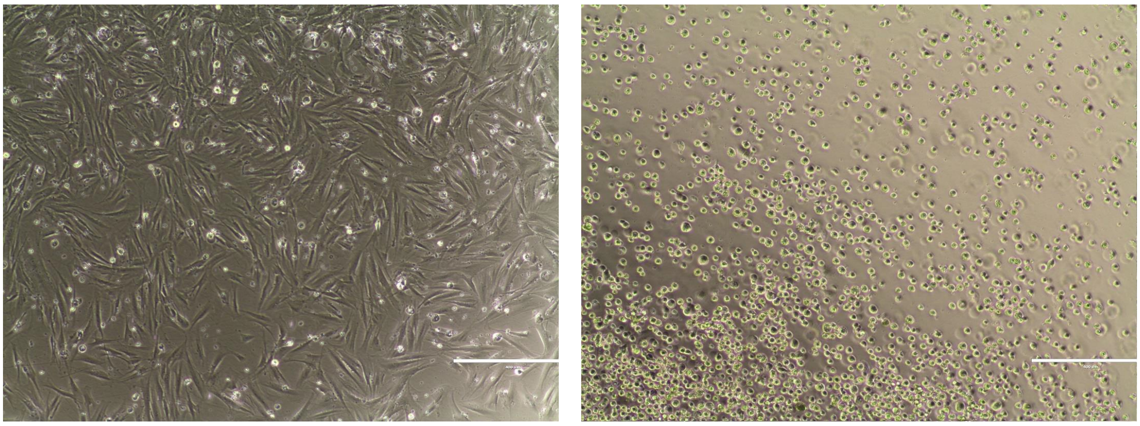

(a) **CAP-1** 10 **sec** (b) **CAP-1** 3 **min**

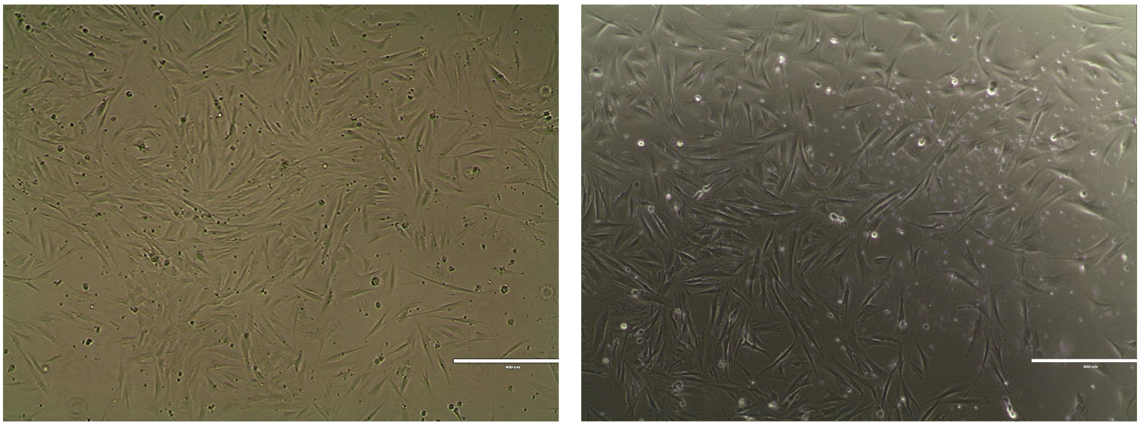

(c) **Unexposed cells** (d) **He** 3 **min**

Figure 9.6 – Optical microscopy imaging of DPSCs after CAP-1 treatment followed by 24h of culture. Scale represents 400 μ**m.**

CAP-1 3 min exposure presents toxic conditions - only about 20% of cells compared to unexposed cells had survived the treatment after 24h. Value below the 70% of cell viability threshold is considered as an indicator of cytotoxic phenomenon according to ISO standard (ISO/EN 10993 part 5 guidelines). Figure 9.7(b) illustrates cells proliferation after 6 days after the same treatment. As it follows, CAP-1 treatment of 30 sec and longer is toxic for cells in the long term perspective.

Change in inflammation level after 24h of culture

Figure 9.8 illustrates monocyte activation level after 24h following the CAP-1 of THP-1 cells of 10 sec, 30 sec, 1 min and 3 min treatment together with unexposed cells and 3 min He flow control. Overall, CAP-1 treatment shows slightly anti-inflammatory response.

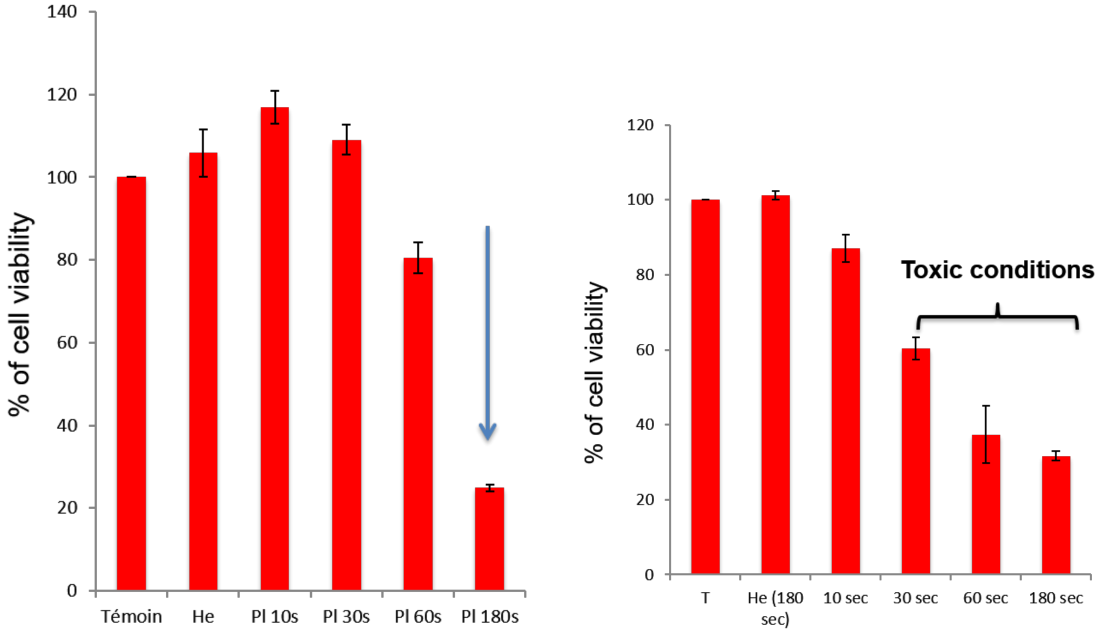

(a) Cytotoxicity test (H24)

(b) Proliferation test (D6)

Figure 9.7 – Cell viability and proliferation tests assessed by WST-1 after CAP-1 treatment of different duration.

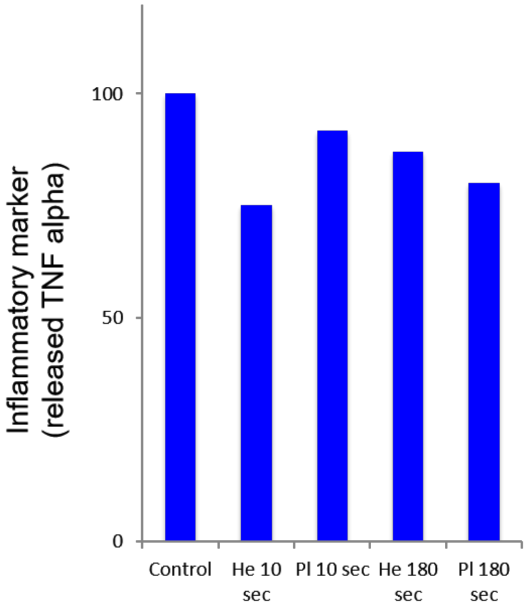

Figure 9.8 – Inflammation test assessed by ELISA assay with TNF-α reagent after CAP-1 treatment of different duration and 24h culture.

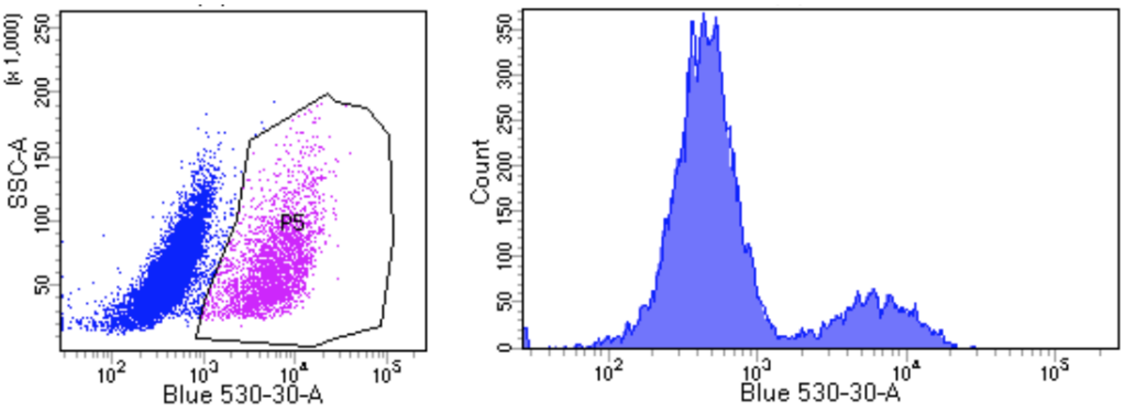

(a) **Unexposed cells**

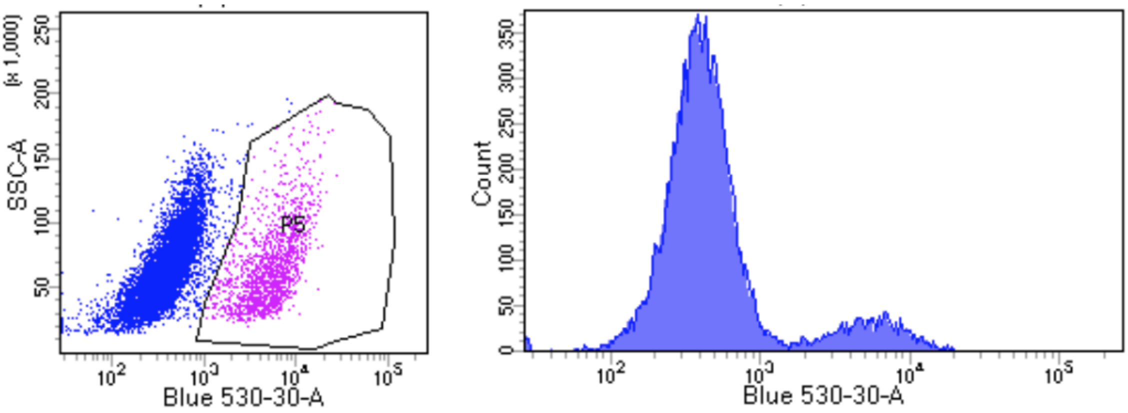

(b) **He** 3 **min**

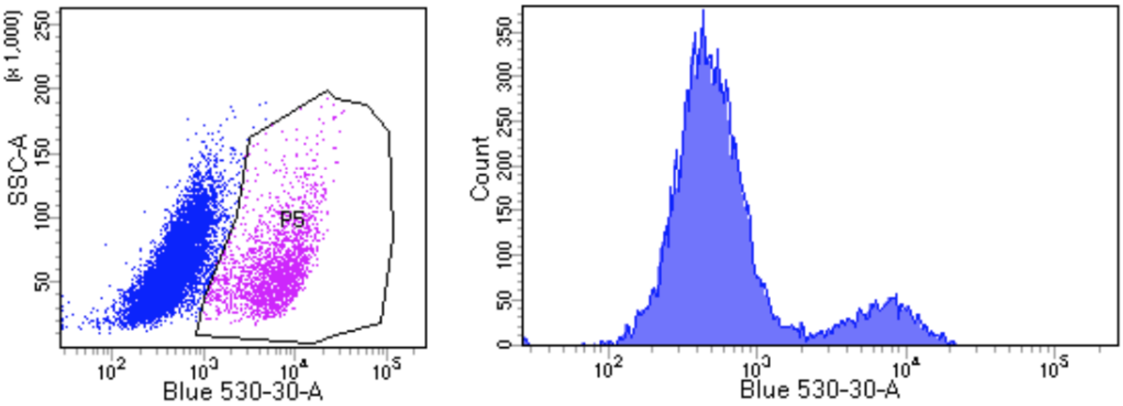

(c) **CAP-1** 3 **min**

Figure 9.9 – ROS intracellular accumulation assessed by flow cytometry, donor 1.

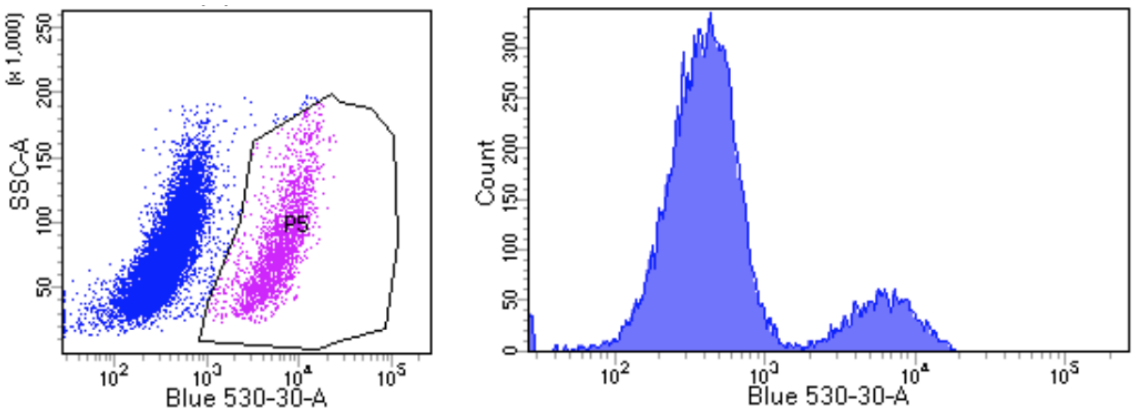

(a) **Unexposed cells**

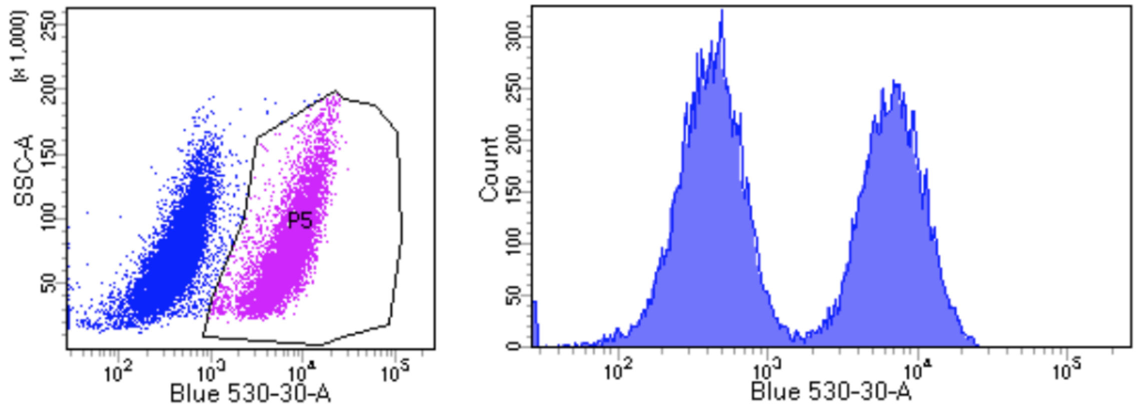

(b) **He** 3 **min**

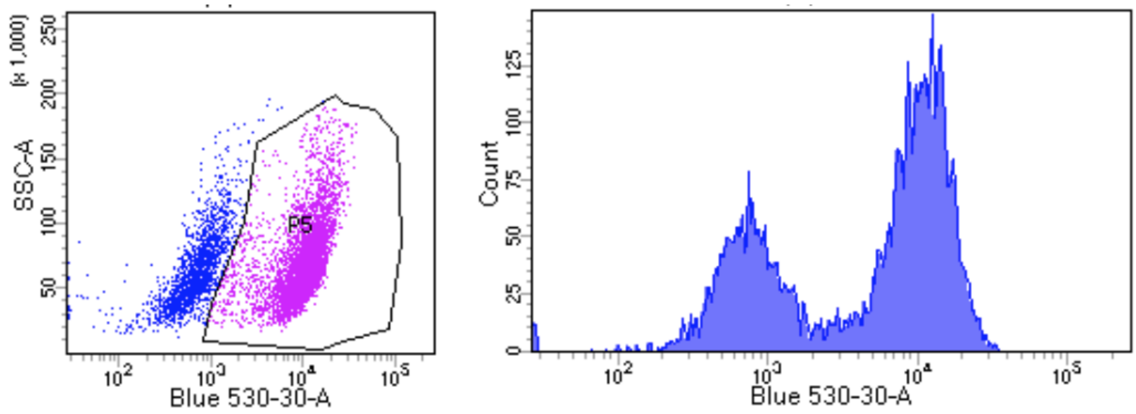

(c) **CAP-1** 3 **min**

Figure 9.10 – ROS intracellular accumulation assessed by flow cytometry, donor 2.

Donor-dependent reactive oxygen species (ROS) intracellular accumulation immediately after treatment

Figures 9.9 and 9.10 present intracellular reactive oxygen species (ROS) levels assessed by flow cytomery from two donors evaluated immediately after CAP-1 3 min exposure of DPSCs together with unexposed cells and 3 min He flow control. The donor 1 (Figures 9.9) does not show any change in ROS accumulation compared to the unexposed and He flow control. However, the donor 2 (Figures 9.10) illustrates an important increase in the accumulation of intracellular ROS after 3 min of He flow already. If the CAP-1 is on, donor 2 shows (i) an overall decrease of signal intensity and (ii) a noticeable change in distribution of the signal. Thus, ROS intracellular accumulations seems to be patient-dependent.

Influence of tubing material (PTFE or PMMA) on device's cytotoxicity

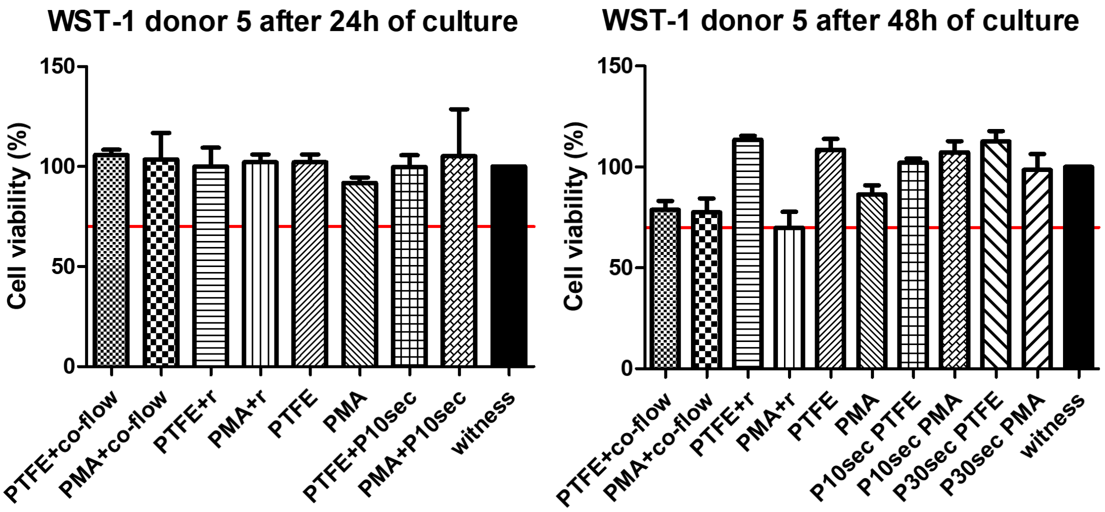

Figure 9.11 – Cellular viability after CAP-2 treatment assessed by WST-1 for different exposure time and tubing plastic after 24h and 48h of culture. The red line indicates the toxicity threshold set at 70% of unexposed control survival.

Figure 9.11 presents cytotoxicity of CAP-2 treatment of different duration and conditions after (a) 24h and (b) 48h, according to ISO standard (ISO/EN 10993 part 5 guidelines). On the Figure 9.11, PTFE (Polytetrafluoroethylene) and PMMA

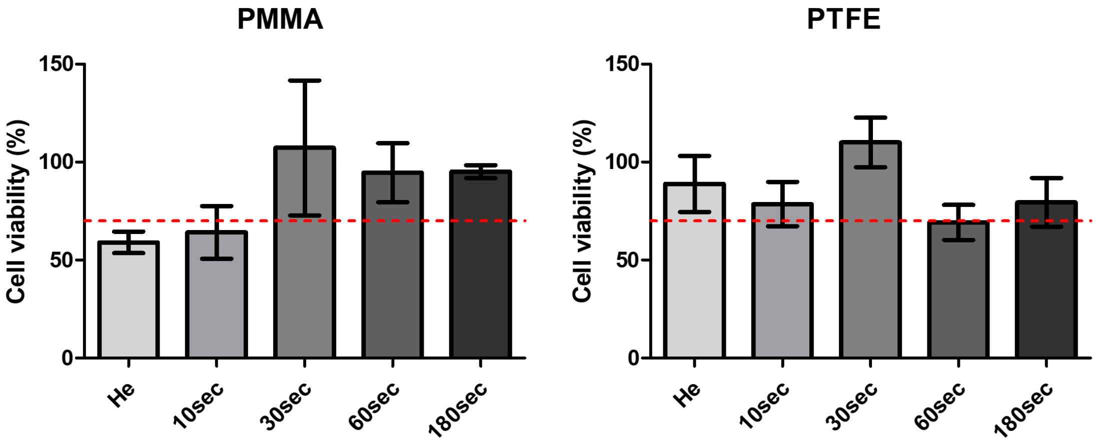

Figure 9.12 – Cellular viability after CAP-2 treatment assessed by WST-1 for different exposure time after 48h of culture with (a) PMMA and (b) PTFE tubing. The red line indicates the toxicity threshold set at 70% **of unexposed control survival.**

(Poly(methyl methacrylate)) indicates the tubing material used, "r" stands for CAP-2 device, "co-flow" note means that co-flow was on. CAP-2 treatment of 10 and 30 sec was done with co-flow. On the scale of 24h, PMMA tubing shows a very slight decrease in cell viability which becomes more pronounced after 48h. After 48h, He co-flowed control for any tubing shows more toxic conditions than any CAP-2 treatment. More precisely, Figure 9.12 illustrates cellular viability assessed by WST-1 following 48h of culture after CAP-2 with co-flow exposure with (a) PMMA and (b) PTFE tubing of different times. Poor survival rate of He flow control clearly shows toxic character of devices' PMMA tubing on DPSCs.

Lactate dehydrogenase (LDH) is a cytosolic enzyme present in many different cell types that is released into the cell culture medium upon damage to the plasma membrane. LDH release is thus served as a mean to track an amount of damage (so-to-say, stress) that cell undergoes. Figure 9.13 presents the data on LDH release assessed by LDH cytotoxic assay for CAP-2 treatment. LDH release was not observed following the plasma treatment, suggesting that the cytotoxic effect of PMMA occurs lately. Following 48h, the LDH release did not show an important increase for any treated condition. It is thus suggested that LDH was released in the medium shortly after the treatment and completely degraded after 48h. This subsection illustrates that the tubing material used for guiding gas to the device should be carefully selected.

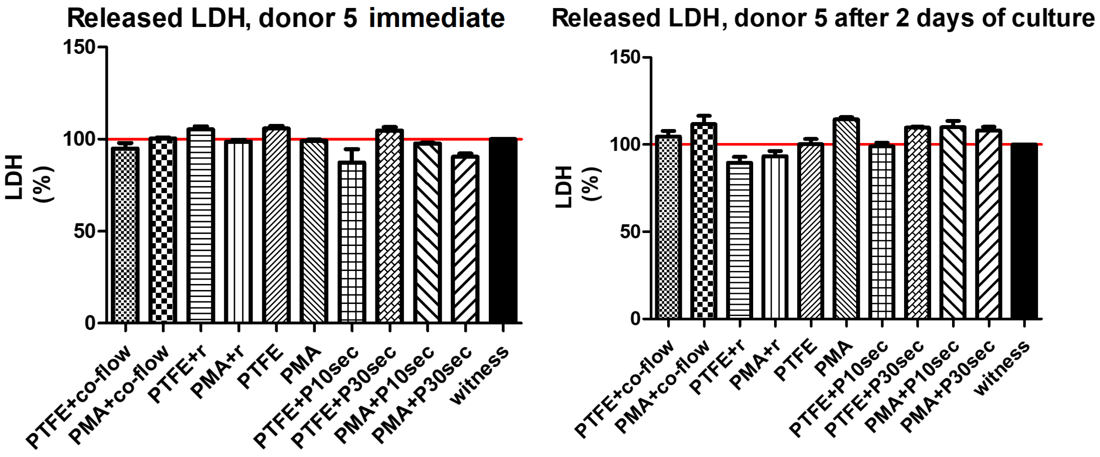

Figure 9.13 – LDH release after CAP-2 treatment assessed by LDH cytotoxic assay for different exposure time and tubing plastic immediately and after 48h of culture. The red line indicates the LDH release of unexposed control.

Changes in cellular morphology 6 days after treatment: cytoskeleton and nuclei fluorescent imaging

For this test, CAP-2 stimulated cells were culture on coverslip glass of 14 mm × 14 mm size. After 6 days, cells were washed from nutritive media and stained by DAPI and phalloidin staining to differentiate cell nuclei and cytoskeleton, respectively. Figure 9.14 presents fluorescent microscopy images of the cells treated by CAP-2 (on the left) *versus* their respective environmental control (on the right). CAP exposure time is indicated at the left from each line. Figure 9.15 shows unexposed cells (on the left) and 3 min He flow control (on the right).

As it can be seen, cell morphology overall was not altered following plasma treatment. Both exposed and control cells that were still adhered on the glass after 6 days kept their elongated morphology. No round-shaped (apoptotic or necrotic) cells were observed. For CAP treatment time 1 minute and less, the cytoskeleton is rather constant and occupies the majority of the surface while cell nuclei are bright, numerous and present a normal round shape. For 3 min CAP treatment, cell monolayer seems disturbed probably due to a weak number of cell that survived in culture. This indicates that 3 min CAP exposure seems to govern a more important amount of damage to the cells so that they do not recover even in 6 days.

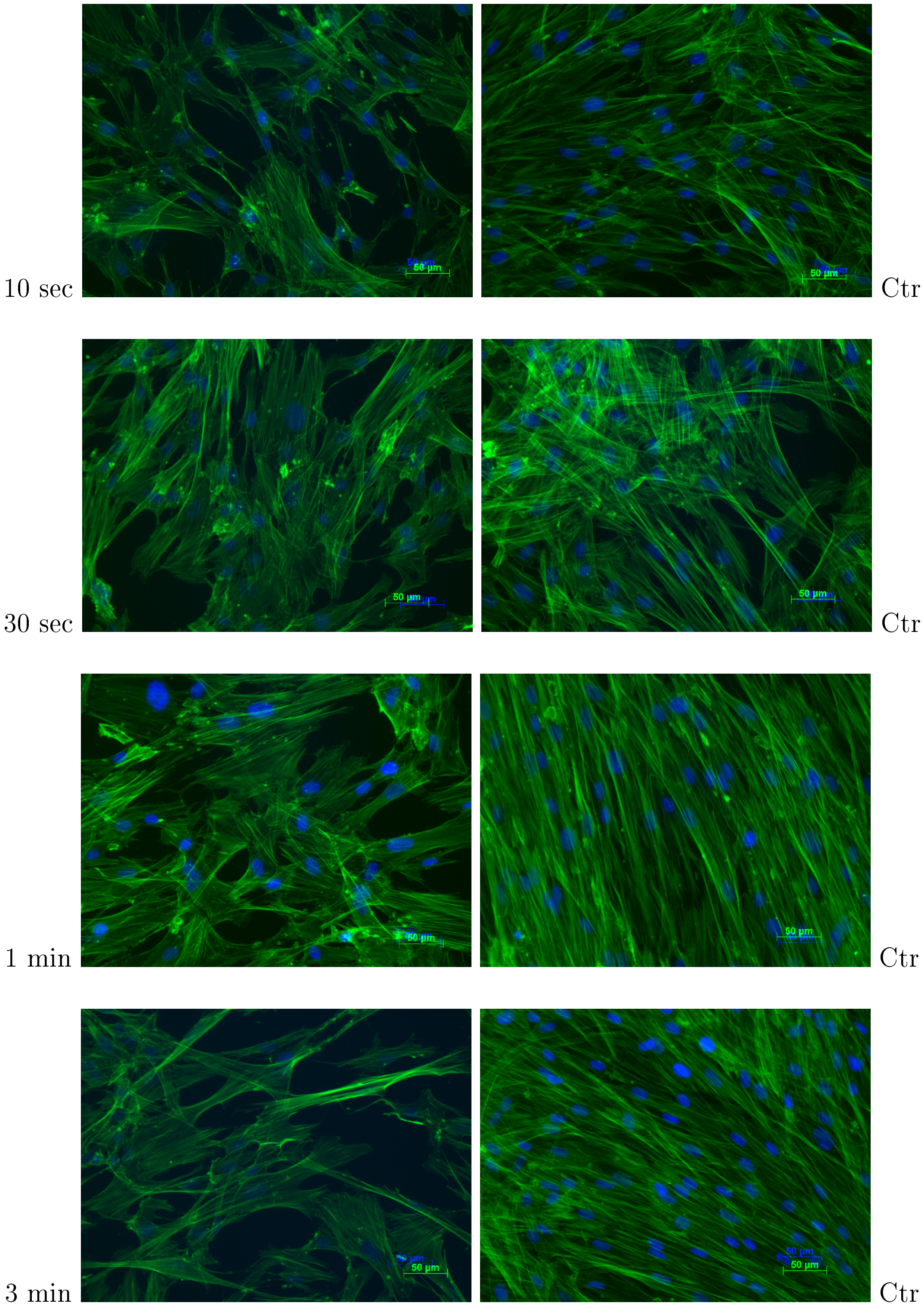

Figure 9.14 – Fluorescent microscopic images of cells treated by CAP-2 (left column) *versus* control (right column). CAP exposure time is indicated at the left. Cell nuclei (blue) were differentiated by DAPI staining while cytoskeleton (green) - by phalloidin staining.

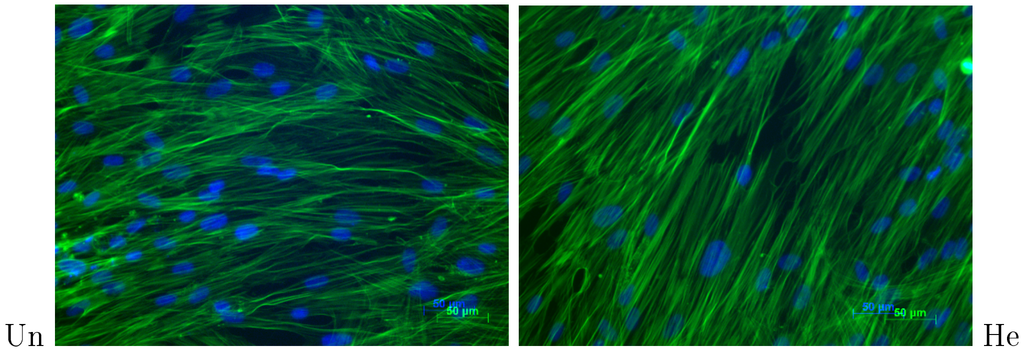

Figure 9.15 – Fluorescent microscopic images: unexposed cells (left) and 3 min He flow control (right). Cell nuclei (blue) were differentiated by DAPI staining while cytoskeleton (green) - by phalloidin staining.

9.5 Conclusions

A cold atmospheric plasma (CAP) device was developed and tested for non-toxicity within the framework of current PhD. Obtained preliminary biological results showed that stem cells and inflammatory cells can be stimulated with CAP without inducing cell damage and necrosis nor in short-term (24h test) nor in long-term scale (6 days test). Cells exposed to less than 1 min kept their proliferative capabilities and fibroblastic morphology. ROS intracellular accumulation seems to show a donor-dependent behavior.

Chapter 10

Conclusions

The present work was focused on the influence of specific deposited energy on plasma kinetics in nanosecond pulsed discharges at high reduced electric fields and had studied a possibility of nanosecond plasma biological application.

The time-resolved longitudinal component of electric field E in the front of fast ionization wave (FIW) was measured by electric field induced second harmonic generation (E-FISH) technique for the first time. The technique was calibrated against recognized electrical techniques such as back current shunt (BCS) and capacitive probe (CP) for the first time as well. Temporal sampling as high as 200 ps attained due to single laser shot data treatment allowed to fully resolve the E waveform measured in nanosecond pulsed discharge with low specific deposited energy 10^{-3} eV/molecule in range of pressures from 20 mbar to 100 mbar in N_2. The absolute calibration of E-FISH signal against validated electrical tools such as back current shunts and capacitive probe was performed for the first time. The E peak value, $8-10$ kV/cm, did not show pressure dependence. Full width at half maximum of the transient electric field peak in the wave front monotonously increases from 1 ns at 20 mbar to 3 ns at 100 mbar. The speed of FIW propagation deduced from plasma emission imaging by ICCD camera shows a monotonous decrease from 1.6 cm/ns at 20 mbar to 0.4 cm/ns at 100 mbar. The length of FIW front is equal to $\sim$ 1.5 cm at 20, 40 and 70 mbar and reduces to 1.2 cm at 100 mbar. Peak reduced electric field E/N reached the value of 2 kTd at 20 mbar pressure.

The E-FISH technique itself was found to provide an excellent spatio-temporal resolution while being simple compared to alternative laser-using electric field measurement techniques. Based on generation of second harmonic signal, E-FISH potentially enables electric field measurements in any optically thin material (solid, liquid, gaseous) with non-zero third order susceptibility χ_3 using an arbitrary wavelength focused laser beam of ns duration or shorter. The experimentally measured E-FISH signal is constituted of second harmonic light generated by materials encountered along the laser beam propagation, and the main contribution to E-FISH signal might originate from the region out of laser focus. Such property, on one hand, rises questions concerning absolute calibration and data interpretation, but on the other hand makes possible electric field measurements in low-χ_3 media (*exempli gratia*, He) through an intermediary in the face of a high-χ_3 admixture or an optical window.

As it has been shown through comparison of numerically modeled and experimentally measured data, in nanosecond pulsed capillary discharge where conditions of high specific deposited energy, 1 eV/molecule, and high reduced electric fields, $\sim$ 200 Td, are satisfied, reactions between charged and/or excited species become dominant. Time and space resolved measurements of N-atom number density with noble gas absolute calibration by TALIF technique in nanosecond capillary discharge allowed to reveal that the stepwise dissociation mechanism *via* electronically excited $\mathrm{N_2(A^3\Sigma_u^+, B^3\Pi_g, C^3\Pi_u)}$ triplet states is an additional source behind the unusually high dissociation rate of N_2. Limits of validity of optical actinometry technique have been tested in nanosecond capillary discharge for O-atom number density measurements with Ar as an actinometer. Experimentally measured emission waveforms of $\mathrm{O(3p^3P_{1,2,0}) \rightarrow O(3s^3S_1)}$ at 844.6 nm and $\mathrm{Ar(2p_1) \rightarrow Ar(1s_2)}$ at 750.4 nm actinometric transitions helped to identify that reaction of 3-body recombination of O^+ and Ar^+ ions with electron as a third body become dominant in the early afterglow.

Comparison of N-atom number densities measured by TALIF technique in nanosecond pulsed discharges at the same high reduced electric field value and different specific deposited energies had shown that the production rate of reactive (nitrogen) species increases significantly with specific deposited energy ω. At $\sim$ 200 Td, N-atom number density was measured to be $5.5\cdot10^{12}$ cm^{-3} at $\omega = 10^{-3}$ eV/molecule and $1.3\cdot10^{17}$ cm^{-3} at $\omega = 1$ eV/molecule corresponding to N_2 dissociation fraction of 10^{-5} and 10%, respectively. The possibility to control the rate of plasma produced reactive species by a single parameter is an interesting feature for applications.

Overall, nanosecond pulsed capillary discharge with high specific deposited energy, 1 eV/molecule, and high reduced electric fields, $\sim$ 200 Td, had shown high dissociation rates for molecules. The N_2 dissociation fraction of 10% in the afterglow of the nanosecond discharge has been reported for the first time; O_2 dissociation fraction reached 23% already during the discharge.

Treatment of stem cells by nanosecond plasma has been done for the first time. On the example of dental pulp derived stem cells it has been shown that plasma can provide a stimulation to stem cells without inducing cell damage, regression in proliferative capabilities, change of fibroblastic morphology and necrosis nor in short-term (24h) nor in long-term scale (6 days).

Perspectives and future work

The present work had reported the time resolved longitudinal component of electric field in the front of FIW with the E/N value as high as 2 kTd at 20 mbar pressure. However, according to the theory of FIW formation, the main electric field component is the radial one since it is responsible for the connecting of the displacement current through FIW to the tube shielding. E-FISH technique can be as well applied to probe the radial electric field component using the same setup but with laser beam of different polarization.

The demonstrated possibility of reactive species production control by tuning the value of specific deposited energy at constant high reduced electric fields is worth of further investigation. In view of potential applications, it would be important to identify the conditions needed for production of required number densities of reactive species. Thus an investigation of the effect of variant high reduced electric fields and specific deposited energy on reactive species production and molecular species dissociation in N_2:O_2 mixtures is foreseen. Based on observations of the present work, it is expected that N and O atomic species number density calibrated TALIF measurements at high specific deposited energies would reveal never seen before dominant reactions between excited and/or charged species and efficient dissociation pathways while low specific deposited energy measurements would allow to validate cross-section set essential for kinetic modeling.

Controlled reactive oxygen and nitrogen species production presents interest in particular for biological applications. A potential increase in accumulation of the intracellular ROS without inducing a cell toxicity could be a good strategy for cell preconditioning. For a long time, ROS have been considered to trigger cellular dysfunction and death *via* the destructive oxidation of intra-cellular components. However, in recent years there has been an accumulating understanding of ROS role as signaling molecules and that only unregulated levels of ROS are harmful. In regenerative medicine, the regulation of the basal level of ROS is advantageous for maintenance of cell functions, such as proliferation, differentiation, and survival [140]. Thus, cold atmospheric plasma (CAP) exposure of stem cells before stem cell administration to the damaged cite could improve cell engraftment and survival through the regulation of the intracellular level of ROS. It has been reported recently [199] that CAP promotes bone formation though an increase in pre-osteoblastic cell commitment in bone forming cells (osteoblasts). It will thus be interesting to study the effect of CAP on differentiation of DPSCs into several lineage such as osteoblasts and cartilage forming cells (chondrocytes).

List of Figures

Bibliography

[1] Adamovich I V, Choi I, Jiang N, Kim J H, Keshav S, Lempert W R, Mintusov E, Nishihara M, Samimy M and Uddi M 2009 Plasma assisted ignition and high-speed flow control: non-thermal and thermal effects *Plasma Sources Science and Technology* **18** 034018

[2] Starikovskiy A, Aleksandrov N and Rakitin A 2012 Plasma-assisted ignition and deflagration-to-detonation transition *Philosophical Transactions of the Royal Society of London A: Mathematical, Physical and Engineering Sciences* **370** 740–773

[3] Houpt A W and Leonov S B 2016 Charge Transfer in Constricted Form of Surface Barrier Discharge at Atmospheric Pressure *Journal of Thermophysics and Heat Transfer* 1–9

[4] Junkin M and Wong P K 2011 Probing cell migration in confined environments by plasma lithography *Biomaterials* **32** 1848–1855

[5] Donnelly V M and Kornblit A 2013 Plasma etching: Yesterday, today, and tomorrow *Journal of Vacuum Science & Technology A: Vacuum, Surfaces, and Films* **31** 050825

[6] Flamm D L and Auciello O 2012 *Plasma deposition, treatment, and etching of polymers: the treatment and etching of polymers* (Elsevier) ISBN9780122004308

[7] Kováčik D, Zahoranová A, Černák M, Mazúr M *et al.* 2005 Surface modification of polypropylene non-woven fabrics by atmospheric-pressure plasma activation followed by acrylic acid grafting *Plasma chemistry and plasma processing* **25** 427–437

[8] Aanesland A, Rafalskyi D, Bredin J, Grondein P, Oudini N, Chabert P, Levko D, Garrigues L and Hagelaar G 2014 The PEGASES gridded ion-ion thruster performance and predictions *IEEE Transactions on Plasma Science* **43** 321–326

[9] Klämpfl T G, Isbary G, Shimizu T, Li Y F, Zimmermann J L, Stolz W, Schlegel J, Morfill G E and Schmidt H U 2012 Cold atmospheric air plasma sterilization against spores and other microorganisms of clinical interest *Applied and environmental microbiology* **78** 5077–5082

[10] Duchesne C, Frescaline N, Lataillade J J and Rousseau A 2018 Comparative study between direct and indirect treatment with cold atmospheric plasma on in vitro and in vivo models of wound healing *Plasma medicine* **8**

[11] Keidar M, Walk R, Shashurin A, Srinivasan P, Sandler A, Dasgupta S, Ravi R, Guerrero-Preston R and Trink B 2011 Cold plasma selectivity and the possibility of a paradigm shift in cancer therapy *British journal of cancer* **105** 1295–1301

[12] Liu B, Honnorat B, Yang H, Arancibia J, Rajjou L and Rousseau A 2018 Non-thermal DBD plasma array on seed germination of different plant species *Journal of Physics D: Applied Physics* **52** 025401

[13] Starikovskii A Y, Nikipelov A A, Nudnova M M and Roupassov D V 2009 SDBD plasma actuator with nanosecond pulse-periodic discharge *Plasma Sources Science and Technology* **18** 034015

[14] Takashima K, Yin Z and Adamovich I V 2012 Measurements and kinetic modeling of energy coupling in volume and surface nanosecond pulse discharges *Plasma Sources Science and Technology* **22** 015013

[15] Rusterholtz D L, Lacoste D A, Stancu G D, Pai D Z and Laux C O 2013 Ultrafast heating and oxygen dissociation in atmospheric pressure air by nanosecond repetitively pulsed discharges *Journal of Physics D: Applied Physics* **46** 464010

[16] Mintoussov E I, Pendleton S J, Gerbault F G, Popov N A and Starikovskaia S M 2011 Fast gas heating in nitrogen-oxygen discharge plasma: II. Energy exchange in the afterglow of a volume nanosecond discharge at moderate pressures *Journal of Physics D: Applied Physics* **44** 285202

[17] Leonov S B, Adamovich I V and Soloviev V R 2016 Dynamics of near-surface electric discharges and mechanisms of their interaction with the airflow *Plasma Sources Science and Technology* **25** 063001

[18] Starikovskiy A 2015 *Physics and chemistry of plasma-assisted combustion* (The Royal Society Publishing)

[19] Ju Y and Sun W 2015 Plasma assisted combustion: Dynamics and chemistry *Progress in Energy and Combustion Science* **48** 21 – 83

[20] Starikovskaia S M 2014 Plasma-assisted ignition and combustion: nanosecond discharges and development of kinetic mechanisms *Journal of Physics D: Applied Physics* **47** 353001

[21] Graves D B 2014 Low temperature plasma biomedicine: A tutorial review *Physics of Plasmas* **21** 080901

[22] Phelps A V and Pitchford L C 1985 Anisotropic scattering of electrons by N_2 and its effect on electron transport *Physical Review A* **31**(5) 2932–2949

[23] Braginskiy O V, Vasilieva A N, Klopovskiy K S, Kovalev A S, Lopaev D V, Proshina O V, Rakhimova T V and Rakhimov A T 2005 Singlet oxygen generation in O_2 flow excited by RF discharge: I. Homogeneous discharge mode: α-mode *Journal of Physics D: Applied Physics* **38** 3609

[24] Hagelaar G J M and Pitchford L C 2005 Solving the Boltzmann equation to obtain electron transport coefficients and rate coefficients for fluid models *Plasma Sources Science and Technology* **14** 722–733

[25] BOLSIG+ solver, http://www.bolsig.laplace.univ-tlse.fr/

[26] Alexandrov N L and Son E E 1980 Energy distribution and swarm parameters of electrons in gases under the action of electric field (in Russian) *Plasma Chemistry, edited by B M Smirnov, Atomizdat* 35–75

[27] Capitelli M, Celiberto R, Colonna G, Esposito F, Gorse C, Hassouni K, Laricchiuta A and Longo S 2015 *Fundamental aspects of plasma chemical physics: kinetics* vol 85 (Springer Science & Business Media)

[28] Starikovskiy A and Aleksandrov N 2013 Plasma-assisted ignition and combustion *Progress in Energy and Combustion Science* **39** 61 – 110

[29] Thomson J J 1893 *Notes on recent researches in electricity and magnetism: intended as a sequel to Professor Clerk-Maxwell's Treatise on electricity and magnetism* (Clarendon Press)

[30] Snoddy L B, Dietrich J R and Beams J W 1937 Propagation of potential in discharge tubes *Physical Review* **52** 739

[31] Mitchell F H and Snoddy L B 1947 Ionization processes in a long discharge tube with application to lightning mechanism *Physical Review* **72** 1202

[32] Loeb L B 1965 Ionizing waves of potential gradient *Science* **148** 1417–1426

[33] Fowler R G 1974 Non-linear electron acoustic waves, Part I vol 35 (Elsevier) pp 1–86

[34] Fowler R G 1976 Non-linear electron acoustic waves, Part II *Advances in Electronics and electron physics* vol 41 (Elsevier) pp 1–72

[35] Asinovskii E I, Vasilyak L M, Markovets V V and Tokunov Y M 1982 Existence of a minimum of the attenuation factor of ionizing potential-gradient waves **263** 1364

[36] Vasilyak L M, Kostyuchenko S V, Kudryavtsev N N and Filyugin I V 1994 Fast ionisation waves under electrical breakdown conditions *Physics-Uspekhi* **37** 247

[37] Ionikh Y Z 2020 Electric Breakdown in Long Discharge Tubes at Low Pressure *Plasma Physics Reports* **46** 1015–1044

[38] Starikovskaia S M 2000 Pulse discharge at high overvoltages: features of development and excitation of internal degrees of freedom of gas (Dr. Sc. thesis in Russian)

[39] Takashima K, Adamovich I V, Xiong Z, Kushner M J, Starikovskaia S, Czarnetzki U and Luggenhölscher D 2011 Experimental and modeling analysis of fast ionization wave discharge propagation in a rectangular geometry *Physics of Plasmas* **18** 083505

[40] Osmokrovic P, Krivokapic I and Krstic S 1994 Mechanism of electrical breakdown left of Paschen minimum *IEEE Transactions on Dielectrics and Electrical Insulation* **1** 77–81

[41] Korolev Y D and Mesyats G A 1998 *Physics of pulsed breakdown in gases* (URO-press Ekaterinburg)

[42] Babich L P and Stankevich Y L 1972 Criterion of transition from streamer mechanism of gas-discharge to continuous electron acceleration (in Russian) *Journal of Technical Physics* **42** 1669–1673

[43] Starikovskaia S M, Anikin N B, Pancheshnyi S V, Zatsepin D V and Starikovskii A Y 2001 Pulsed breakdown at high overvoltage: development, propagation and energy branching *Plasma Sources Science and Technology* **10** 344

[44] Lepikhin N D, Klochko A V, Popov N A and Starikovskaia S M 2016 Long-lived plasma and fast quenching of $\mathrm{N_2(C^3\Pi_{\mathit{u}})}$ by electrons in the afterglow of a nanosecond capillary discharge in nitrogen *Plasma Sources Science and Technology* **25** 045003

[45] Anikin N B, Pancheshnyi S V, Starikovskaia S M and Starikovskii A Y 1998 Breakdown development at high overvoltage: electric field, electronic level excitation and electron density *Journal of Physics D: Applied Physics* **31** 826

[46] Pancheshnyi S V, Starikovskaia S M and Starikovskii A Y 1999 Population of nitrogen molecule electron states and structure of the fast ionization wave *Journal of Physics D: Applied Physics* **32** 2219

[47] Favre M, Chuaqui H, Leñero A M, Wyndham E and Choi P 2001 A miniature capacitive probe array for transient high voltage capillary discharges *Review of Scientific Instruments* **72** 2186–2190

[48] Takashima K, Adamovich I V, Czarnetzki U and Luggenhölscher D 2012 Development of Fast Ionization Wave Discharges at High Pulse Repetition Rates *Plasma Chemistry and Plasma Processing* **32** 471–493

[49] Huang B D, Carbone E, Takashima K, Zhu X M, Czarnetzki U and Pu Y K 2018 The effect of the pulse repetition rate on the fast ionization wave discharge *Journal of Physics D: Applied Physics* **51** 225202

[50] Zhu W, Huang B, Zhu X, Chen W and Pu Y 2020 Investigation on the streamer propagation in atmospheric pressure helium plasma jet by the capacitive probe *Plasma Science and Technology* **22** 052001

[51] Klochko A 2014 *Excited species chemistry in homogeneous nanosecond discharges with high specific energy deposition* Ph.D. thesis Ecole Polytechnique

[52] Stark J 1913 Observation of the separation of spectral lines by an electric field *Nature* **92** 401–401

[53] Stark J 1914 Beobachtungen über den Effekt des elektrischen Feldes auf Spektrallinien. I. Quereffekt (in German) *Annalen der Physik* **348** 965–982

[54] Epstein P S 1916 Zur theorie des Starkeffektes (in German) *Annalen der Physik* **355** 489–520

[55] The Nobel Prize in Physics 1919. NobelPrize.org. Nobel Media AB 2020. Tue. 20 Oct 2020, https://www.nobelprize.org/prizes/physics/1919/summary/

[56] Sivuhin D V 2005 *General physics course (in Russian)* vol 5 (Fizmatlit)

[57] Delone N B and Krainov V P 1999 AC Stark shift of atomic energy levels *Physics-Uspekhi* **42** 669

[58] Hicks W W, Hess R A and Cooper W S 1972 Combined Zeeman and High-Frequency Stark Effects, with Applications to Neutral-Helium Lines Useful in Plasma Diagnostics *Physical Review A* **5**(2) 490–507

[59] Booth J P, Derouard J, Fadlallah M and Sadeghi N 1993 Time-resolved electric-field measurements in 30 kHz hydrogen discharges by optical emission Stark spectroscopy *Journal of Applied Physics* **74** 862–867

[60] Kuraica M, Konjević N and Videnović I 1997 Spectroscopic study of the cathode fall region of Grimm-type glow discharge in helium *Spectrochimica Acta Part B: Atomic Spectroscopy* **52** 745 – 753

[61] Preppernau B L and Ganguly B N 1993 Time-resolved electric field measurements in a 15 kHz helium glow discharge *Review of Scientific Instruments* **64** 1414–1417

[62] Kuraica M M and Konjević N 1997 Electric field measurement in the cathode fall region of a glow discharge in helium *Applied Physics Letters* **70** 1521–1523

[63] Sismanoglu B, Grigorov K, Santos R, Caetano R, Rezende M, Hoyer Y and Ribas V 2010 Spectroscopic diagnostics and electric field measurements in the near-cathode region of an atmospheric pressure microplasma jet *The European Physical Journal D* **60** 479–487

[64] Alam R C, Fletcher S J, Wasserman K R and Hüwel L 1990 Time-resolved emission spectroscopy in laser-generated nitrogen plasmas *Physical Review A* **42**(1) 383–390

[65] Kampschulte T, Schulze J, Luggenhölscher D, Bowden M and Czarnetzki U 2007 Laser spectroscopic electric field measurement in krypton *New Journal of Physics* **9** 18

[66] Czarnetzki U, Luggenhölscher D and Döbele H F 1998 Sensitive Electric Field Measurement by Fluorescence-Dip Spectroscopy of Rydberg States of Atomic Hydrogen *Physical Review Letters* **81**(21) 4592–4595

[67] Böhm P, Kettlitz M, Brandenburg R, Höft H and Czarnetzki U 2016 Determination of the electric field strength of filamentary DBDs by CARS-based four-wave mixing *Plasma Sources Science and Technology* **25** 054002

[68] Demtröder W 2010 *Atoms, molecules and photons* vol 3 (Springer)

[69] Lempert W R and Adamovich I V 2014 Coherent anti-Stokes Raman scattering and spontaneous Raman scattering diagnostics of nonequilibrium plasmas and flows *Journal of Physics D: Applied Physics* **47** 433001

[70] Bigio I J, Finn R and Ward J 1975 Electric-field induced harmonic generation as a probe of the focal region of a laser beam *Applied Optics* **14** 336–342

[71] Shelton D P and Rice J E 1994 Measurements and calculations of the hyperpolarizabilities of atoms and small molecules in the gas phase *Chemical Reviews* **94** 3–29

[72] Dogariu A, Goldberg B M, O'Byrne S and Miles R B 2017 Species-independent femtosecond localized electric field measurement *Physical Review Applied* **7** 024024

[73] Simeni M S, Tang Y, Frederickson K and Adamovich I 2018 Electric field distribution in a surface plasma flow actuator powered by ns discharge pulse trains *Plasma Sources Science and Technology* **27** 104001

[74] Chng T, Ding C, Naphade M, Goldberg B, Adamovich I and Starikovskaia S 2020 Characterization of an optical pulse slicer for gas-phase electric field measurements using field-induced second harmonic generation *Journal of Instrumentation* **15** C03005

[75] FID GmbH company, http://www.fidtechnology.com/

[76] Huang B, Zhang C, Adamovich I, Akishev Y and Shao T 2020 Surface ionization wave propagation in the nanosecond pulsed surface dielectric barrier discharge: the influence of dielectric material and pulse repetition rate *Plasma Sources Science and Technology* **29** 044001

[77] Orr K, Tang Y, Simeni M S, Van Den Bekerom D and Adamovich I V 2020 Measurements of electric field in an atmospheric pressure helium plasma jet by the E-FISH method *Plasma Sources Science and Technology* **29** 035019

[78] Lepikhin N D, Luggenhöelscher D and Czarnetzki U 2020 Electric field measurements in a He:N_2 nanosecond pulsed discharge with sub-ns time resolution *Journal of Physics D: Applied Physics*

[79] Cui Y, Zhuang C and Zeng R 2019 Electric field measurements under DC corona discharges in ambient air by electric field induced second harmonic generation *Applied Physics Letters* **115** 244101

[80] Goldberg B M, Reuter S, Dogariu A and Miles R B 2019 1D time evolving electric field profile measurements with sub-ns resolution using the E-FISH method *Optics Letters* **44** 3853–3856

[81] Meehan K C, Starikovskiy A and Miles R 2020 Two Component Electric Field Dynamics of a ns-SDBD Plasma with Sub-Nanosecond Resolution by Femtosecond EFISH *AIAA Scitech 2020 Forum* p 1747

[82] Chng T L, Naphade M, Goldberg B M, Adamovich I V and Starikovskaia S M 2020 Electric field vector measurements via nanosecond electric-field-induced second-harmonic generation *Optics Letters* **45** 1942–1945

[83] Chng T L, Starikovskaia S M and Schanne-Klein M C 2020 Electric Field Measurements in Plasmas: How Focusing Strongly Distorts the E-FISH Signal *Plasma Sources Science and Technology*

[84] Oksuz L, Soberón F and Ellingboe A R 2006 Analysis of uncompensated Langmuir probe characteristics in radio-frequency discharges revisited *Journal of Applied Physics* **99** 013304

[85] Oyama K 2015 DC Langmuir probe for measurement of space plasma: A brief review *Journal of Astronomy and Space Sciences* **32** 167–180

[86] Andreussi T, Saravia M and Andrenucci M 2019 Plasma characterization in Hall thrusters by Langmuir probes *Journal of Instrumentation* **14** C05011–C05011

[87] Popov T K, Dimitrova M, Ivanova P, Kovačič J, Gyergyek T, Dejarnac R, Stöckel J, Pedrosa M A, López-Bruna D and Hidalgo C 2016 Advances in Langmuir probe diagnostics of the plasma potential and electron-energy distribution function in magnetized plasma *Plasma Sources Science and Technology* **25** 033001

[88] Cherrington B E 1982 The use of electrostatic probes for plasma diagnostics - A review *Plasma chemistry and plasma processing* **2** 113–140

[89] Demidov V I, Ratynskaia S V and Rypdal K 2002 Electric probes for plasmas: The link between theory and instrument *Review of scientific instruments* **73** 3409–3439

[90] Brisset A, Gazeli K, Magne L, Pasquiers S, Jeanney P, Marode E and Tardiveau P 2019 Modification of the electric field distribution in a diffuse streamer-induced discharge under extreme overvoltage *Plasma Sources Science and Technology* **28** 055016

[91] Leonov S B, Petrishchev V and Adamovich I V 2014 Dynamics of energy coupling and thermalization in barrier discharges over dielectric and weakly conducting surfaces on μs to ms time scales *Journal of Physics D: Applied Physics* **47** 465201

[92] Engeln R, Klarenaar B and Guaitella O 2020 Foundations of optical diagnostics in low-temperature plasmas *Plasma Sources Science and Technology* **29** 063001

[93] Bruggeman P, Cunge G and Sadeghi N 2012 Absolute OH density measurements by broadband UV absorption in diffuse atmospheric-pressure He–H_2O RF glow discharges *Plasma Sources Science and Technology* **21** 035019

[94] Wijaikhum A, Schröder D, Schröter S, Gibson A R, Niemi K, Friderich J, Greb A, von der Gathen V S, O'Connell D and Gans T 2017 Absolute ozone densities in a radio-frequency driven atmospheric pressure plasma using two-beam UV-LED absorption spectroscopy and numerical simulations *Plasma Sources Science and Technology* **26** 115004

[95] Ko J H, Choi S, Park H W and Park D W 2013 Decomposition of Nitrogen Trifluoride Using Low Power Arc Plasma *Plasma Science and Technology* **15** 923–927

[96] Stancu G D, Janda M, Kaddouri F, Lacoste D A and Laux C O 2010 Time-Resolved CRDS Measurements of the $N_2(A^3\Sigma_u^+)$ Density Produced by Nanosecond Discharges in Atmospheric Pressure Nitrogen and Air *The Journal of Physical Chemistry A* **114** 201–208

[97] Röpcke J, Lombardi G, Rousseau A and Davies P B 2006 Application of mid-infrared tuneable diode laser absorption spectroscopy to plasma diagnostics: a review *Plasma Sources Science and Technology* **15** S148–S168

[98] O'Keefe A and Deacon D A G 1988 Cavity ring-down optical spectrometer for absorption measurements using pulsed laser sources *Review of Scientific Instruments* **59** 2544–2551

[99] Laux C O, Spence T G, Kruger C H and Zare R N 2003 Optical diagnostics of atmospheric pressure air plasmas *Plasma Sources Science and Technology* **12** 125

[100] Boffard J B, Lin C C and Jr C A D 2004 Application of excitation cross sections to optical plasma diagnostics *Journal of Physics D: Applied Physics* **37** R143–R161

[101] d'Agostino R, Cramarossa F, De Benedictis S and Ferraro G 1981 Spectroscopic diagnostics of CF_4-O_2 plasmas during Si and SiO_2 etching processes *Journal of Applied Physics* **52** 1259–1265

[102] d'Agostino R, Colaprico V and Cramarossa F 1981 The use of "actinometer" gases in optical diagnostics of plasma etching mixtures: SF_6-O_2 *Plasma Chemistry and Plasma Processing* **1** 365–375

[103] Walkup R E, Saenger K L and Selwyn G S 1986 Studies of atomic oxygen in O_2+CF_4 rf discharges by two-photon laser-induced fluorescence and optical emission spectroscopy *The Journal of Chemical Physics* **84** 2668–2674

[104] Pagnon D, Amorim J, Nahorny J, Touzeau M and Vialle M 1995 On the use of actinometry to measure the dissociation in O_2 DC glow discharges: determination of the wall recombination probability *Journal of Physics D: Applied Physics* **28** 1856–1868

[105] Conway J, Kechkar S, Connor N O, Gaman C, Turner M M and Daniels S 2013 Use of particle-in-cell simulations to improve the actinometry technique for determination of absolute atomic oxygen density *Plasma Sources Science and Technology* **22** 045004

[106] Booth J P, Joubert O, Pelletier J and Sadeghi N 1991 Oxygen atom actinometry reinvestigated: Comparison with absolute measurements by resonance absorption at 130 nm *Journal of Applied Physics* **69** 618–626

[107] Ivanov V V, Klopovskii K S, Lopaev D V, Rakhimov A T and Rakhimova T V 2000 Nonlocal nature of the electron energy spectrum in a glow-discharge in pure O_2: II. Actinometry of O(3P) atoms in a plasma at low gas pressures *Plasma Physics Reports* **26** 980–990

[108] Czerwiec T, Greer F and Graves D B 2005 Nitrogen dissociation in a low pressure cylindrical ICP discharge studied by actinometry and mass spectrometry *Journal of Physics D: Applied Physics* **38** 4278–4289

[109] Levaton J, Ricard A, Henriques J, Silva H R T and Amorim J 2006 Measurements of $N(^4S)$ absolute density in a 2.45 GHz surface wave discharge by optical emission spectroscopy *Journal of Physics D: Applied Physics* **39** 3285–3293

[110] Thomaz J C, Amorim J and Souza C F 1999 Validity of actinometry to measure N and H atom concentration in N_2-H_2 direct current glow discharges *Journal of Physics D: Applied Physics* **32** 3208–3214

[111] Jenq J S, Ding J, Taylor J W and Hershkowitz N 1994 Absolute fluorine atom concentrations in RIE and ECR CF_4 plasmas measured by actinometry *Plasma Sources Science and Technology* **3** 154–161

[112] Lopaev D V, Volynets A V, Zyryanov S M, Zotovich A I and Rakhimov A T 2017 Actinometry of O, N and F atoms *Journal of Physics D: Applied Physics* **50** 075202

[113] Maiman T H 1960 Stimulated optical radiation in ruby *Nature* **187** 493–494

[114] Kinsey J L 1977 Laser-induced fluorescence *Annual Review of Physical Chemistry* **28** 349–372

[115] Kossyi I A, Kostinsky A Y, Matveyev A A and Silakov V P 1992 Kinetic scheme of the non-equilibrium discharge in nitrogen-oxygen mixtures *Plasma Sources Science and Technology* **1** 207

[116] Niemi K, von der Gathen V S and Döbele H F 2005 Absolute atomic oxygen density measurements by two-photon absorption laser-induced fluorescence spectroscopy in an RF-excited atmospheric pressure plasma jet *Plasma Sources Science and Technology* **14** 375–386

[117] Pindzola M S 1978 Two-photon excitation of atomic oxygen *Physical Review A* **17**(3) 1021–1027

[118] Dixit S N, Levin D A and McKoy B V 1988 Resonant enhanced multiphoton ionization studies in atomic oxygen *Physical Review A* **37**(11) 4220–4228

[119] Miller J C 1989 Two-photon resonant multiphoton ionization and stimulated emission in krypton and xenon *Physical Review A* **40**(12) 6969–6976

[120] Aldén M, Westblom U and Goldsmith J E M 1989 Two-photon-excited stimulated emission from atomic oxygen in flames and cold gases *Optics Letters* **14** 305–307

[121] Tserepi A D, Wurzberg E and Miller T A 1997 Two-photon-excited stimulated emission from atomic oxygen in rf plasmas: detection and estimation of its threshold *Chemical Physics Letters* **265** 297 – 302

[122] Buijsse B, van der Zande W J, Eppink A T J B, Parker D H, Lewis B R and Gibson S T 1998 Angular distributions for photodissociation of O_2 in the Herzberg continuum *The Journal of Chemical Physics* **108** 7229–7243

[123] Tonokura K, Shafer N, Matsumi Y and Kawasaki M 1991 Photodissociation of oxygen molecules at 226 nm in the Herzberg I system *The Journal of Chemical Physics* **95** 3394–3398

[124] Wysong I J, Jeffries J B and Crosley D R 1989 Laser-induced fluorescence of $O(3p^3P)$, O_2, and NO near 226 nm: photolytic interferences and simultaneous excitation in flames *Optics Letters* **14** 767–769

[125] Hasson V and Nicholls R W 1971 Absolute spectral absorption measurements on molecular oxygen from 2640-1920 AA. II. Continuum measurements 2430-1920 AA *Journal of Physics B: Atomic and Molecular Physics* **4** 1789–1797

[126] Stancu G D 2020 Two-photon absorption laser induced fluorescence: rate and density-matrix regimes for plasma diagnostics *Plasma Sources Science and Technology* **29** 054001

[127] Goehlich A, Kawetzki T and Döbele H F 1998 On absolute calibration with xenon of laser diagnostic methods based on two-photon absorption *The Journal of Chemical Physics* **108** 9362–9370

[128] Niemi K, von der Gathen V S and Döbele H F 2001 Absolute calibration of atomic density measurements by laser-induced fluorescence spectroscopy with two-photon excitation *Journal of Physics D: Applied Physics* **34** 2330–2335

[129] Klochko A V, Lemainque J, Booth J P and Starikovskaia S M 2015 TALIF measurements of oxygen atom density in the afterglow of a capillary nanosecond discharge *Plasma Sources Science and Technology* **24** 025010

[130] Wang Y, Capps C and Kulatilaka W D 2017 Femtosecond two-photon laser-induced fluorescence of krypton for high-speed flow imaging *Optics Letters* **42** 711–714

[131] Dumitrache C, Gallant A, Stancu G D and Laux C O 2019 Femtosecond two-photon absorption laser induced fluorescence (fs-TALIF) imaging of atomic nitrogen in nanosecond repetitive discharges *AIAA Scitech 2019 Forum* p 1507

[132] Es-Sebbar E T, Sarra-Bournet C, Naudé N, Massines F and Gherardi N 2009 Absolute nitrogen atom density measurements by two-photon laser-induced fluorescence spectroscopy in atmospheric pressure dielectric barrier discharges of pure nitrogen *Journal of Applied Physics* **106** 073302

[133] Cosby P C 1993 Electron-impact dissociation of nitrogen *The Journal of Chemical Physics* **98** 9544–9553

[134] Matsumoto T, Wang D, Namihira T and Akiyama H 2010 Energy efficiency improvement of nitric oxide treatment using nanosecond pulsed discharge *IEEE Transactions on Plasma Science* **38** 2639–2643

[135] Gherardi N, Sebbar E E, Bournet C S, Naudé N, Massines F, Tsyganov D, Ségur P and Pancheshnyi S 2008 Acive species generation of homogeneous DBD in N_2 experimens and modelling *Proceedings of the XI International*

Symposium on High Pressure Low Temperature Plasma Chemistry, Oléron Island

[136] Popov N 2013 Dissociation of nitrogen in a pulse-periodic dielectric barrier discharge at atmospheric pressure *Plasma Physics Reports* **39** 420–424

[137] Akishev Y, Grushin M, Karalnik V, Trushkin N, Kholodenko V, Chugunov V, Kobzev E, Zhirkova N, Irkhina I and Kireev G 2008 Atmospheric-pressure, nonthermal plasma sterilization of microorganisms in liquids and on surfaces *Pure and Applied Chemistry* **80** 1953–1969

[138] Niemira B A 2012 Cold plasma decontamination of foods *Annual review of food science and technology* **3** 125–142

[139] Vandamme M, Robert E, Lerondel S, Sarron V, Ries D, Dozias S, Sobilo J, Gosset D, Kieda C, Legrain B, Pouvesle J M and Le Pape A 2012 ROS implication in a new antitumor strategy based on non-thermal plasma *International journal of cancer* **130** 2185–2194

[140] Li Q, Gao Z, Chen Y and Guan M X 2017 The role of mitochondria in osteogenic, adipogenic and chondrogenic differentiation of mesenchymal stem cells *Protein & Cell* **8** 439–445

[141] Gorbanev Y, Privat-Maldonado A and Bogaerts A 2018 Analysis of short-lived reactive species in plasma–air–water systems: the dos and the do nots

[142] Sousa J S, Niemi K, Cox L, Algwari Q T, Gans T and O'Connell D 2011 Cold atmospheric pressure plasma jets as sources of singlet delta oxygen for biomedical applications *Journal of Applied Physics* **109** 123302

[143] Girard P M, Arbabian A, Fleury M, Bauville G, Puech V, Dutreix M and Sousa J S 2016 Synergistic effect of H_2-O_2 and NO_2 in cell death induced by cold atmospheric He plasma *Scientific Reports* **6** 29098

[144] Ratajczak M Z, Zuba-Surma E K, Wysoczynski M, Wan W, Ratajczak J, Wojakowski W and Kucia M 2008 Hunt for pluripotent stem cell–regenerative medicine search for almighty cell *Journal of autoimmunity* **30** 151–162

[145] Horwitz E M, Gordon P L, Koo W K K, Marx J C, Neel M D, McNall R Y, Muul L and Hofmann T 2002 Isolated allogeneic bone marrow-derived mesenchymal cells engraft and stimulate growth in children with osteogenesis imperfecta: Implications for cell therapy of bone *Proceedings of the National Academy of Sciences* **99** 8932–8937

[146] Murphy J M, Fink D J, Hunziker E B and Barry F P 2003 Stem cell therapy in a caprine model of osteoarthritis *Arthritis & Rheumatism* **48** 3464–3474

[147] Lazović S, Puač N, Miletić M, Pavlica D, Jovanović M, Bugarski D, Mojsilović S, Maletić D, Malović G, Milenković P and Petrović Z 2010 The effect of a plasma needle on bacteria in planktonic samples and on peripheral blood mesenchymal stem cells *New Journal of Physics* **12** 083037

[148] Miletić M, Mojsilović S, Đorđević I O, Maletić D, Puač N, Lazović S, Malović G, Milenković P, Petrović Z L and Bugarski D 2013 Effects of non-thermal atmospheric plasma on human periodontal ligament mesenchymal stem cells *Journal of physics D: Applied physics* **46** 345401

[149] Lepikhin N D 2017 *Fast energy relaxation in the afterglow of a nanosecond capillary discharge in nitrogen/oxygen mixtures* Ph.D. thesis Université Paris-Saclay

[150] Raizer Y P 1991 *Gas Discharge Physics* (New York: Springer)

[151] Lepikhin N D, Popov N A and Starikovskaia S M 2018 Fast gas heating and radial distribution of active species in nanosecond capillary discharge in pure nitrogen and N_2:O_2 mixtures *Plasma Sources Science and Technology* **27** 055005

[152] Mueller J L and Siltanen S 2012 *Linear and Nonlinear Inverse Problems with Practical Applications* (SIAM)

[153] ISTEQ company, https://www.isteq.nl/

[154] Kramida A, Ralchenko Y, Reader J and Team N A NIST Atomic Spectra Database (version 5.8), [Online] [Feb 2020] National Institute of Standards and Technology, Gaithersburg, MD.

[155] Radtsig A and Smirnov B 1980 Handbook on atomic and molecular physics *Atomizdat, Moscow* 240

[156] Zhu Y 2018 *Numerical Study of Nanosecond Capillary and Surface Dielectric Barrier Discharges : Kinetics, Transport and Fluid Responses* Ph.D. thesis Université Paris-Saclay

[157] Zhu Y, Lepikhin N D, Orel I S, Salmon A, Klochko A V and Starikovskaia S M 2018 Optical actinometry of O-atoms in pulsed nanosecond capillary discharge: peculiarities of kinetics at high specific deposited energy *Plasma Sources Science and Technology* **27** 075020

[158] Rauf S and Kushner M J 1999 Dynamics of a coplanar-electrode plasma display panel cell. I. Basic operation *Journal of Applied Physics* **85** 3460–3469

[159] Pancheshnyi S, Eismann B, Hagelaar G and Pitchford L 2008 Computer code ZDPlasKin, University of Toulouse, LAPLACE Tech. rep. CNRS-UPS-INP, Toulouse, France www.zdplaskin.laplace.univ-tlse.fr

[160] Bacri J and Medani A 1982 Electron diatomic molecule weighted total cross section calculation: III. Main inelastic processes for N_2 and N_2^+ *Physica B+C* **112** 101 – 118

[161] Dutton J 1975 A survey of electron swarm data *Journal of Physical and Chemical Reference Data* **4** 577–856

[162] Kucukarpaci H N and Lucas J 1979 Simulation of electron swarm parameters in carbon dioxide and nitrogen for high E/N *Journal of Physics D: Applied Physics* **12** 2123–2138

[163] Fletcher J and Reid I D 1980 The transport parameters of an electron swarm in nitrogen at elevated E/N *Journal of Physics D: Applied Physics* **13** 2275–2283

[164] Moruzzi J L and Price D A 1974 Ionization, attachment and detachment in air and air-CO_2 mixtures *Journal of Physics D: Applied Physics* **7** 1434–1440

[165] Rao C R and Raju G R G 1971 Growth of ionization currents in dry air at high values of E/N *Journal of Physics D: Applied Physics* **4** 494–503

[166] Flitti, A and Pancheshnyi, S 2009 Gas heating in fast pulsed discharges in N_2-O_2 mixtures *The European Physical Journal Applied Physics* **45** 21001

[167] Capitelli M, Ferreira C M, Gordiets B F and Osipov A I 2001 *Plasma kinetics in atmospheric gases* vol 31 (Springer Science & Business Media)

[168] Lawton S A and Phelps A V 1978 Excitation of the $b^1\ \Sigma_g^+$ state of O_2 by low energy electrons *The Journal of Chemical Physics* **69** 1055–1068

[169] Yamabe C, Buckman S J and Phelps A V 1983 Measurement of free-free emission from low-energy-electron collisions with Ar *Physical Review A* **27**(3) 1345–1352

[170] Klochko A, Salmon A, Popov N, Booth J P, Kushner M J, Xiong Z and Starikovskaya S 2014 *Experimental and numerical study of fast gas heating and O atom production in a capillary nanosecond discharge*

[171] Pancheshnyi S, Starikovskaia S and Starikovskii A 2000 Collisional deactivation of $N_2(C^3Pi_u$, v=0, 1, 2, 3) states by N_2, O_2, H_2 and H_2O molecules *Chemical Physics* **262** 349 – 357

[172] Chng T L, Orel I S, Starikovskaia S and Adamovich I V 2019 Electric field induced second harmonic (E-FISH) generation for characterization of fast ionization wave discharges at moderate and low pressures *Plasma Sources Science and Technology* **28** 045004

[173] FlexPDE solver, https://www.pdesolutions.com/

[174] Carter R G 2018 *Emission and Breakdown Phenomena* (Cambridge University Press) pp 694–734 The Cambridge RF and Microwave Engineering Series

[175] Bourdon A, Darny T, Pechereau F, Pouvesle J M, Viegas P, Iséni S and Robert E 2016 Numerical and experimental study of the dynamics of a μs helium plasma gun discharge with various amounts of N_2 admixture *Plasma Sources Science and Technology* **25** 035002

[176] Shcherbanev S A, Ding C, Starikovskaia S M and Popov N A 2019 Filamentary nanosecond surface dielectric barrier discharge. Plasma properties in the filaments *Plasma Sources Science and Technology* **28** 065013

[177] Preda V C 1982 The Student distribution and the principle of maximum entropy *Annals of the Institute of Statistical Mathematics* **34** 335–338

[178] Bening V E and Korolev V Y 2005 On an application of the Student distribution in the theory of probability and mathematical statistics *Theory of Probability & Its Applications* **49** 377–391

[179] de Chatellus H G and Freysz E 2001 Measurement of the third-order susceptibility of glasses by EFISH of femtosecond pulses *Optics Express* **9** 586–591

[180] Gubler U and Bosshard C 2000 Optical third-harmonic generation of fused silica in gas atmosphere: Absolute value of the third-order nonlinear optical susceptibility $\chi^{(3)}$ *Physical Review B* **61**(16) 10702–10710

[181] Anikin N B, Starikovskaia S M and Starikovskii A Y 2002 Polarity effect of applied pulse voltage on the development of uniform nanosecond gas breakdown *Journal of Physics D: Applied Physics* **35** 2785

[182] Anikin N, Starikovskaia S and Starikovskii A 2004 Study of the oxidation of alkanes in their mixtures with oxygen and air under the action of a pulsed volume nanosecond discharge *Plasma Physics Reports* **30** 1028–1042

[183] Klochko A V, Starikovskaia S M, Xiong Z and Kushner M J 2014 Investigation of capillary nanosecond discharges in air at moderate pressure: comparison of experiments and 2D numerical modelling *Journal of Physics D: Applied Physics* **47** 365202

[184] Goldberg B M, Chng T L, Dogariu A and Miles R B 2018 Electric field measurements in a near atmospheric pressure nanosecond pulse discharge with picosecond electric field induced second harmonic generation *Applied Physics Letters* **112** 064102

[185] Chng T L, Lepikhin N D, Orel I S, Popov N A and Starikovskaia S M 2020 TALIF measurements of atomic nitrogen in the afterglow of a nanosecond capillary discharge *Plasma Sources Science and Technology* **29** 035017

[186] Marshall T 1962 Surface Recombination of Nitrogen Atoms upon Quartz *The Journal of Chemical Physics* **37** 2501–2502

[187] Adams S F and Miller T A 1998 Two-photon absorption laser-induced fluorescence of atomic nitrogen by an alternative excitation scheme *Chemical Physics Letters* **295** 305 – 311

[188] Galvão B R L, Varandas A J C, Braga J P and Belchior J C 2013 Electronic Quenching of N(^{2}D) by N_2: Theoretical Predictions, Comparison with Experimental Rate Constants, and Impact on Atmospheric Modeling *The Journal of Physical Chemistry Letters* **4** 2292–2297

[189] Dvořák P, Šimek M and Prukner V 2019 Evolution of N(^{4}S) atoms produced under nitrogen streamer conditions: time-resolved TALIF study at reduced pressures *Plasma Sources Science and Technology* **28** 125004

[190] Fresnet F, Baravian G, Pasquiers S, Postel C, Puech V, Rousseau A and Rozoy M 2000 Time-resolved laser-induced fluorescence study of NO removal plasma technology in N_2/NO mixtures *Journal of Physics D: Applied Physics* **33** 1315–1322

[191] SIGLO database, http://lxcat.laplace.univ-tlse.fr/

[192] Jans E, Raskar S, Yang X and Adamovich I V 2020 Kinetics of metastable $N_2(A^3\Sigma_u^+,v)$ molecules in high-pressure nonequilibrium plasmas *Plasma Sources Science and Technology*

[193] Herron J T 1999 Evaluated chemical kinetics data for reactions of N(^{2}D), N(^{2}P), and $N_2(A^3\Sigma_u^+)$ in the gas phase *Journal of Physical and Chemical Reference Data* **28** 1453–1483

[194] Kalghatgi S U, Fridman G, Cooper M, Nagaraj G, Peddinghaus M, Balasubramanian M, Vasilets V N, Gutsol A F, Fridman A and Friedman G 2007 Mechanism of Blood Coagulation by Nonthermal Atmospheric Pressure Dielectric Barrier Discharge Plasma *IEEE Transactions on Plasma Science* **35** 1559–1566

[195] Yan D, Talbot A, Nourmohammadi N, Cheng X, Canady J, Sherman J and Keidar M 2015 Principles of using cold atmospheric plasma stimulated media for cancer treatment *Scientific Reports* **5** 18339

[196] Keidar M, Shashurin A, Volotskova O, Ann Stepp M, Srinivasan P, Sandler A and Trink B 2013 Cold atmospheric plasma in cancer therapy *Physics of Plasmas* **20** 057101

[197] Kogelschatz U 1988 *Advanced Ozone Generation* (Boston, MA: Springer US) pp 87–118 ISBN 978-1-4684-8556-1

[198] Hoffmann-Jorgensen J and Pisier G 1976 The Law of Large Numbers and the Central Limit Theorem in Banach Spaces *Annals of Probability* **4** 587–599

[199] Tominami K, Kanetaka H, Sasaki S, Mokudai T, Kaneko T and Niwano Y 2017 Cold atmospheric plasma enhances osteoblast differentiation *PLOS ONE* **12** 1–15

ECOLE
DOCTORALE

Titre : Mesure du champ électrique et de la densité de particules dissociées dans des décharges nanosecondes pour des applications de cinétique et de biologie

Mots clés : plasma froid, E-FISH, TALIF, actinometrie, biologie cellulaire

Résumé : La thèse présente des mesures absolues et résolues en temps des densités d'atomes O et N (techniques d'actinométrie optique et de fluorescence induite par laser à absorption à deux photons, TALIF) et du champ électrique (technique de la génération de deuxième harmonique induite par champ électrique, E-FISH) en fonction de l'énergie déposée spécifique dans des décharges pulsées nanosecondes à des champs électriques réduits élevés qui se développent sous la forme d'onde d'ionisation rapide. Il a été montré que dans des conditions à la fois de champ électrique réduit élevé et d'énergie spécifique déposée élevée, les réactions entre espèces chargées et/ou excitées définissent le comportement du plasma. Le champ électrique dans l'onde d'ionisation rapide mesuré avec une résolution de 0,2 ns a révélé une valeur de crête indépendante de la pression d'environ 10 kV/cm et une durée 1-3 ns qui augmente avec la pression. Le pic mesuré d'[O], $7,5 \cdot 10^{16}$ cm^{-3}, correspond à un taux de dissociation de 23% pendant la décharge. Pour 1 eV/molécule pour la décharge capillaire, [N] atteint la valeur de crête de $1,3 \cdot 10^{17}$ cm^{-3} 1 μs après le début de la décharge. [N] reste constante jusqu'à 1 ms, puis diminue exponentiellement jusqu'à atteindre la limite de détection à 20 ms. La valeur de crête de [N] correspond à une fraction de dissociation de 10% et à un coût énergétique de production effectif de N de 10 atomes/100 eV. La thèse aborde également l'intérêt des décharges ns dans des applications biologiques. Un dispositif à plasma atmosphérique froid (CAP) a été développé pour le traitement des cellules souches mésenchymateuses dérivées de la pulpe dentaire. L'effet CAP sur les cellules a été évalué par analyse morphologique des cellules, test de viabilité, test de cytotoxicité, test prolifératif, cytométrie en flux marqué pour les mesures de l'accumulation intracellulaire de ROS et microscopie à fluorescence pour l'imagerie du cytosquelette et des noyaux qui ont conduit à l'établissement d'un protocole non toxique de traitement cellulaire par CAP.

Title : Measurements of electric field and dissociated species in nanosecond discharges for kinetic and biological applications

Keywords : cold plasma, E-FISH, TALIF, actinometry, cellular biology

Abstract : The thesis presents absolute and time resolved measurements of O and N atom densities (optical actinometry and two photon absorbed laser induced fluorescence, TALIF, techniques) and electric field (electric field induced second harmonic generation, E-FISH technique) as a function of specific deposited energy in nanosecond pulsed discharges at high reduced electric fields that develop in form of fast ionization wave. It has been shown that in conditions of both high reduced electric field and high specific deposited energy, reactions between charged and/or excited species define plasma behavior. The electric field in the fast ionization wave measured with 0.2 ns resolution had revealed the pressure-independent peak value of about 10 kV/cm and 1-3 ns duration that increases with pressure. The peak measured [O], $7.5 \cdot 10^{16}$ cm^{-3}, corresponds to 23% dissociation fraction in the discharge. For 1 eV/molecule at capillary discharge, N-atoms density reaches the peak value of $1.3 \cdot 10^{17}$ cm^{-3} at about 1 μs after the initiation of the discharge. [N] stays at the peak value up to 1 ms and then decreases exponentially until reaches the detection limit at 20 ms. [N] peak value corresponds to 10% dissociation fraction and to effective N-atom production energy cost of almost 10 atoms/100 eV. The thesis also discusses the interest of ns discharges in biological applications. Cold atmospheric plasma (CAP) device was developed for treatment of dental pulp derived mesenchymal stem cells. CAP effect on cells was assessed by morphological cell analysis, viability test, cytotoxicity test, proliferative test, labelled flow cytometry for measurements of intracellular reactive oxygen species accumulation and fluorescence microscopy for cytoskeleton and nuclei imaging that had led to establishment of non-toxic protocol of cell treatment by CAP.

Institut Polytechnique de Paris
91120 Palaiseau, France